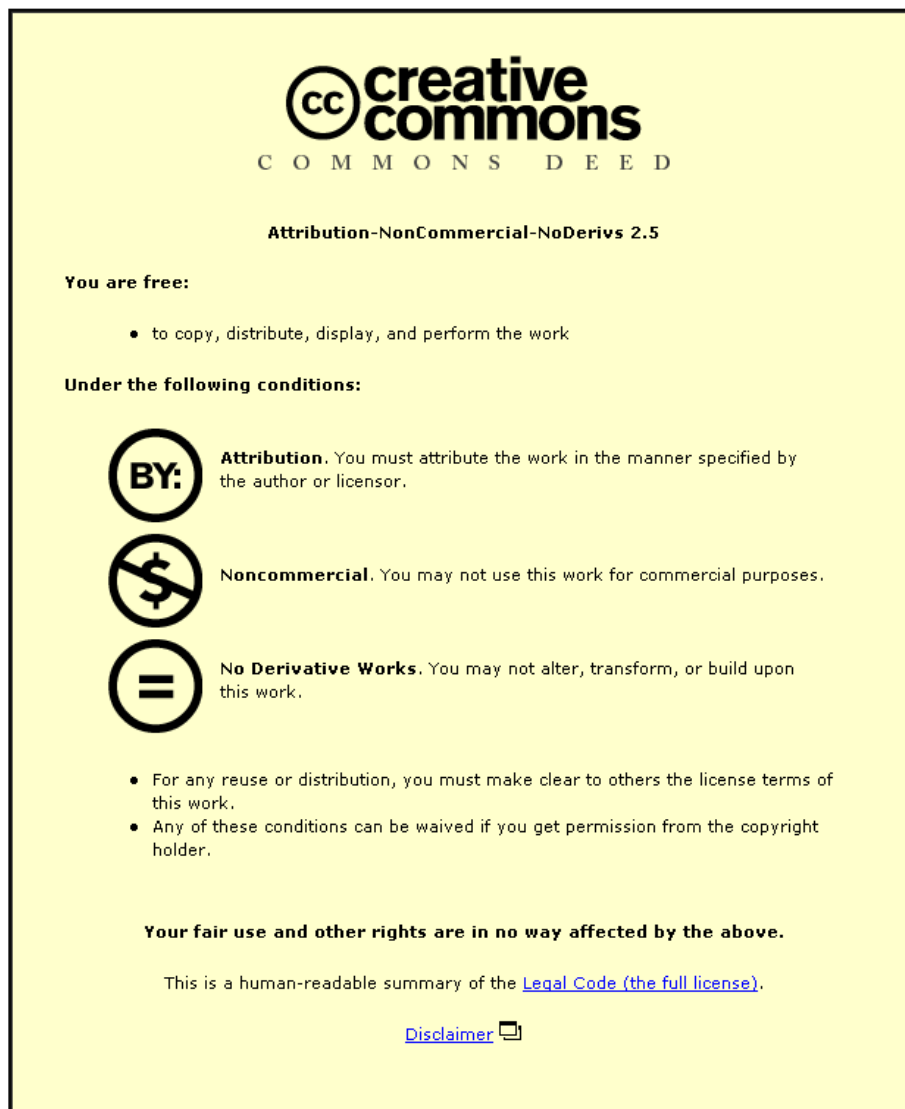


This item was submitted to Loughborough University as a PhD thesis by the author and is made available in the Institutional Repository (<https://dspace.lboro.ac.uk/>) under the following Creative Commons Licence conditions.



For the full text of this licence, please go to:  
<http://creativecommons.org/licenses/by-nc-nd/2.5/>



# **Hot Ultrasonically Assisted Turning of Ti-15V3Al3Cr3Sn: Experimental and Numerical Analysis**

**Riaz Muhammad**

A Doctoral Thesis

Submitted in partial fulfilment of the requirements for the award of Doctor of

Philosophy of Loughborough University

Wolfson School of Mechanical and Manufacturing Engineering

Loughborough University

© 2013 R. Muhammad

## Abstract

Titanium alloys have outstanding mechanical properties such as high hardness, a good strength-to-weight ratio, excellent fatigue properties and high corrosion resistance. However, several inherent properties including their low thermal conductivity and high chemical affinity to tool materials impairs severely their machinability with conventional machining techniques. Conventional machining of Ti-based alloys is typically characterized by low depths of cuts and relatively low feed rates, thus adversely affecting the material removal rates during the machining process. Recently, a non-conventional machining technique known as *ultrasonically assisted turning* (UAT) was introduced to machine modern alloys, in which low-energy, high-frequency vibration is superimposed on the movement of a cutting tool during a conventional cutting process. This novel machining technique results in a multi-fold decrease in the level of cutting forces with a concomitant improvement in surface finish of machined modern alloys. Also, since the late 20<sup>th</sup> century, machining of wear resistant materials that soften when heated has been carried out with hot machining techniques.

In this work, a new hybrid machining technique called *Hot Ultrasonically Assisted Turning* (HUAT) is introduced for processing of a Ti-based alloy Ti-15V3Al3Cr3Sn. In this technique, UAT is combined with a traditional hot machining technique to gain combined advantages of both schemes for machining of intractable alloys. HUAT of the studied alloy was analysed experimentally and numerically to demonstrate its benefits in terms of reduction in cutting forces over a wide range of industrially relevant speed-feed combinations. Thermal evolution in the cutting process was assessed, and the obtained results were compared with FE simulations to gain knowledge of temperatures reached in the cutting zone. The developed novel turning process appeared to improve dry turning of the Ti alloy with significant reduction of average cutting forces without any substantial metallurgical changes in the workpiece material. Nano-indentation, light microscopy and SEM studies were performed to get an insight into the development of hardness in a zone near the machined surface in the workpiece. Backscatter electron microscopy was also used to evaluate the formation of  $\alpha$ -Ti

during the novel HUAT. No grain changes or  $\alpha$ -precipitation were observed in machined workpieces in conventional and hybrid turning processes.

3D elasto-plastic thermomechanically coupled finite-element models for the orthogonal turning process were developed for conventional turning (CT), hot conventional turning (HCT), UAT and HUAT, followed by a more realistic novel 3D finite-element model for the oblique turning process. These 3D models were used to study the effects of cutting parameters (cutting speed, feed rate and depth of cut, ultrasonic vibration, ultrasonic frequency, rake angle and tool nose radius) on cutting forces, temperature in the process zone and stresses. The later model was used to analyse the effect of vibration and heat on the radial and axial components of cutting forces in HUAT, which was not possible with the developed 3D orthogonal-turning model. Comparative studies were performed with the developed CT, HCT, UAT and HUAT finite-element models and were validated by results from experiments conducted on the in-house prototype and in literature.

The HUAT for the Ti-15333 was analysed experimentally and numerically to demonstrate the benefits in terms of a significant reduction in the cutting forces and improvement in surface roughness over a wide range of industrially relevant speed-feed combinations.

**Keywords:** Finite-Element; Machining; Turning; Hybrid Machining; Aerospace Alloys; Dry Cutting; Ti Alloys; Hot Ultrasonically Assisted Turning; Vibration Assisted Turning; Ultrasonic.

# Acknowledgement

I would like to thank my supervisor Professor Vadim V. Silberschmidt and Dr. Anish Roy for their enthusiastic guidance, time, encouragement, support at all levels and source of funding throughout my PhD. Their knowledge, suggestions, understanding of the problem, motivation and continuous guidance were the source of great inspiration to me.

I am also grateful to all staff members of Wolfson School of Mechanical and Manufacturing Engineering for their encouragement and support.

I would also like to express many thanks to my office colleagues, especially to Dr. Agostino Maurotto, Dr. Murat Demiral, Mr. Simin Li, Mr. Abolfazle al Zahedi and Dr. Himayat Ullah for the encouragement and useful suggestions towards the improvement of my research work. Special thanks to Dr. Allan Meadows and Dr. Bob Temple for their support in my research work.

Support of the MaMiNa academic and industrial partners is also much appreciated, I am thankful to MaMiNa and all ESRs for their collaboration and advice on many different issues.

Special thanks to my friends Dr. Mohammad Saleem, Mr. Sajjad Wali Khan, Mr. Aamir Ehsan, Mr. Asmat Ullah, and Mr. Abdul Shakoor for their support and courage. And finally I want to express my respect to my family especially to my mother, wife and elder brother for their support and patience during my studies.

**Dedicated to my beloved mother Humdia Bibi**

# Publications

1. **R. Muhammad**, A. Maurotto, A. Roy and V. V. Silberschmidt: Analysis of forces in vibro-impact and hot vibro-impact turning of advanced alloys, *Applied Mechanics and Materials* 70, 315-320, 2011.  
[doi:10.4028/www.scientific.net/AMM.70.315](https://doi.org/10.4028/www.scientific.net/AMM.70.315)
2. **R. Muhammad**, A. Maurotto, A. Roy and V. V. Silberschmidt: Hot ultrasonically assisted turning of  $\beta$ -Ti alloy, *Procedia CIRP* 1, 353-358, 2012.  
<http://dx.doi.org/10.1016/j.procir.2012.04.060>
3. **R. Muhammad**, N. Ahmed, A. Roy and V. V. Silberschmidt: Numerical modelling of vibration assisted turning of Ti-15333, *Procedia CIRP* 1, 364-369, 2012.  
<http://dx.doi.org/10.1016/j.procir.2012.04.062>
4. A. Maurotto, **R. Muhammad**, A. Roy and V. V. Silberschmidt: Comparing machinability of Ti 15-3-3-3 and Ni 625 alloys in UAT, *Procedia CIRP* 1, 347-352, 2012.  
<http://dx.doi.org/10.1016/j.procir.2012.04.059>
5. **R. Muhammad**, A. Maurotto, M. Demiral, A. Roy and V. V. Silberschmidt: 3D finite element analysis of ultrasonically assisted turning of modern alloys, *International Conference on Computational and Experimental Engineering and Sciences (ICCES, 11)*, 2011, China.  
[doi/10.3970/icces.2011.019.095.pdf](https://doi.org/10.3970/icces.2011.019.095.pdf)
6. **R. Muhammad**, N. Ahmed, A. Roy and V. V. Silberschmidt: Turning of advanced alloys with vibrating cutting tool, *Solid State Phenomena*, 188, 277-284, 2012.  
[doi:10.4028/www.scientific.net/SSP.188.27](https://doi.org/10.4028/www.scientific.net/SSP.188.27)
7. **R. Muhammad**, N. Ahmed, M. Demiral A. Roy and V. V. Silberschmidt: Computational study of ultrasonically-assisted turning of Ti alloys, *Advanced Materials Research* 223, 30-36, 2011

doi:10.4028/www.scientific.net/AMR.223.30

8. **R. Muhammad**, A. Maurotto, A. Roy and V. V. Silberschmidt: Ultrasonically assisted turning of Ti-6Al-2Sn-4Zr-6Mo, Journal of Physics: Conference Series 382 (2012).  
doi:10.1088/1742-6596/382/1/012016
9. A. Maurotto, C. Siemers, **R. Muhammad**, B. Zahra, A. Roy and V. V. Silberschmidt: Ultrasonically assisted turning of enhanced machinability of Ti-alloy, Submitted to International Journal of Precision Engineering and Manufacturing.
10. **R. Muhammad**, M.S. Hussain, A. Maurotto., C. Siemers, A. Roy and V. V. Silberschmidt: Analysis of free machining of  $\alpha + \beta$  Ti-alloy using ultrasonically assisted turning, submitted to Journal of Materials Processing and Technology.
11. A. Maurotto, **R. Muhammad**, A. Roy and V. V. Silberschmidt: Enhanced ultrasonically assisted turning of  $\beta$ -Ti-alloy, Ultrasonic, 53 (6), 1242-1250, 2013.  
<http://dx.doi.org/10.1016/j.ultras.2013.03.006>
12. **R. Muhammad**, A. Maurotto, A. Roy and V. V. Silberschmidt: Enhanced deformability of a beta-Ti alloy in hybrid machining, Will be submitted to International Journal of Material Science and Engineering-A.
13. **R. Muhammad**, A. Maurotto, M. Demiral, A. Roy and V. V. Silberschmidt: Thermally enhanced ultrasonically assisted turning of titanium alloys, under review in CIRP Journal of Manufacturing Science and Technology.
14. **R. Muhammad**, A. Roy and V. V. Silberschmidt: Finite element modelling of 3D oblique ultrasonically assisted turning of titanium alloy: Procedia CIRP 8, 509-514, 2013.  
<http://dx.doi.org/10.1016/j.procir.2013.06.142>
15. **R. Muhammad**, M. Demiral A. Roy and V. V. Silberschmidt: Modelling the dynamic behaviour of hard-to-cut alloys under vibro impact loading conditions, Journal of Physics: Conference Series 451, 1-11, 012030, 2013.  
doi:10.1088/1742-6596/451/1/012030

# Conferences Contribution

1. 20th International Workshop on Computational Mechanics of Materials (IWCMM 2010): 2010, UK.
2. 13<sup>th</sup> CIRP Conference on Modelling of Machining Processes, Sintra, Purogal, 2011.
3. International Conference on Advances in Experimental Mechanics: Integrating Simulation and Experimentation for Validation (ISEV), Edinburgh, UK.
4. International Conference on Computational and Experimental Engineering and Sciences (ICCES, 11), 2011, China
5. 21th International Workshop on Computational Mechanics of Materials (IWCMM 2011): 2011, Ireland.
6. 4th International Conference on Advanced Materials and Structures (AMS'11), Romania, 2011.
7. 5<sup>th</sup> CIRP Conference on High Performance Cutting (HPC), ETH Zurich, Switzerland, 2012.
8. 3<sup>rd</sup> Macro, Micro and Nano Aspect of Machining (MaMiNa) Conference, Braunschweig, Germany, 2012.
9. The Modern Practice in Stress and Vibration Analysis (MPSVA) Conference, Glasgow, UK, 2012.
10. 1st Annual EPSRC Manufacturing the Future Conference, Loughborough, UK, 2012.
11. 14<sup>th</sup> CIRP Conference on Modelling of Machining Processes, Italy, 2013.
12. Conference on Dynamic Deformation and Fracture of Advanced Materials (D2FAM), Loughborough, UK, 2013.
13. Loughborough University Conference, Research That Matters, Loughborough, UK, 2013.

# Table of Contents

<b>Abstract .....</b>	<b>i</b>
<b>Acknowledgement.....</b>	<b>iii</b>
<b>Publications .....</b>	<b>v</b>
<b>Conferences Contribution .....</b>	<b>vii</b>
<b>List of Figures .....</b>	<b>xiv</b>
<b>List of Tables .....</b>	<b>xxiii</b>
<b>Notation and Abbreviations .....</b>	<b>xxiv</b>
<b>Acronyms .....</b>	<b>xxviii</b>
<b>CHAPTER-1 .....</b>	<b>1</b>
<b>Introduction</b>	
1.1 Introduction.....	1
1.2 Aim and Objective of Present Work.....	4
1.3 Research Methodology.....	5
1.4 Thesis Outline .....	7
<b>CHAPTER-2 .....</b>	<b>9</b>
<b>Basic Theory of Metal Cutting</b>	
2.1 Introduction.....	9
2.2 Kinematics of the Turning Process .....	12
2.2.1. Cutting Tools .....	12

2.2.1.1.	Geometry of a Single Point Cutting Tool.....	13
2.2.1.2.	Cutting Tool Materials.....	14
2.2.2.	Types of Cutting Operations .....	15
2.2.3.	Types of Chip in Turning Operations .....	16
2.2.4.	Chip Formation .....	20
2.2.5.	Cutting Forces in Metal Cutting .....	21
2.2.6.	Heat in Metal Cutting.....	26
2.3	Experimental Force Measurement in Turning .....	29
2.3.1.	Displacement Measurement Based Dynamometer .....	30
2.3.2.	Strain Measurement Based Dynamometer .....	32
2.3.3.	Piezoelectric Dynamometer .....	32
2.4	Temperature Measurement in the Turning Process .....	34
2.5	Summary.....	36

## **CHAPTER-3 ..... 37**

### **A Review of Experimental and Computational Methods Used for Conventional and Assisted Machining Processes**

3.1.	Introduction.....	37
3.2.	Ultrasonically Assisted Turning .....	38
3.3.	Hot Machining .....	44
3.4.	Hybrid Machining Processes.....	52
3.5.	Historical Developments in Simulation of Machining Processes .....	54
3.5.1.	Chip Separation from the Workpiece in Machining Processes .....	54
3.5.2.	Friction at the Tool-Tip-Interface.....	59
3.5.3.	Modelling of Cutting Tool in FE Simulations.....	63

3.6. Summary.....	64
-------------------	----

## **CHAPTER-4 ..... 67**

### **Experimental Study of Conventional and Hybrid Oblique Turning Processes**

4.1. Introduction.....	67
4.2. Application of Modern Alloys .....	68
4.3. Properties of Ti-15333 .....	69
4.4. Cutting Force Measurements .....	72
4.4.1. Experimental Methodology .....	77
4.4.2. Results and Discussion .....	79
4.5. Thermal Analysis of Conventional and Assisted Turning Processes.....	83
4.5.1. Introduction .....	83
4.5.2. Experimental Setup for Infra-Red Thermography .....	84
4.5.3. Calibration of Thermal Camera.....	86
4.5.4. Methodology.....	87
4.5.5. Experimental Results and Discussion .....	88
4.6. Surface Quality .....	93
4.6.1. Introduction .....	93
4.6.2. Samples Preparation.....	93
4.6.3. Surface Analysis Using Zygo® Interferometry.....	94
4.6.4. Results and Discussion .....	94
4.7. Metallographic Tests and Chip Shapes.....	97
4.7.1. Light Microscopy of Machined Samples .....	97
4.7.2. Methodology.....	97
4.7.3. Results and Discussions .....	99

4.7.4.	SEM Analysis of the Machined Specimens .....	101
4.7.5.	Chip Analysis .....	103
4.8.	Surface Hardness Evaluation of Machined Specimens .....	107
4.8.1.	Experimental Methodology .....	107
4.8.2.	Results and Discussions .....	109
4.9.	Summary.....	111

## **CHAPTER-5 ..... 113**

### **Finite-Element Modelling of the Orthogonal and Oblique Turning Processes**

5.1	Introduction.....	113
5.2	Finite-Element Modelling .....	114
5.2.1.	FE Modelling of 3D Orthogonal Turning .....	114
5.2.2.	Assumptions and Restrictions.....	116
5.2.3.	Model Description and Features .....	116
5.2.4.	Material Model for Ti-15333 .....	117
5.2.5.	Model Geometry and Boundary Conditions.....	123
5.2.6.	Oblique Turning of CT, UAT, HCT and HUAT.....	127
5.3	Summary.....	133

## **CHAPTER-6 ..... 134**

### **Results and Discussions: Parametric Study of Orthogonal Turning Modelling**

6.1	Introduction.....	134
6.2	Cutting Forces.....	135
6.3	Stresses in Process Zone.....	136
6.4	Thermal Results .....	138
6.5	Effect of Cutting Conditions.....	141

6.5.1.	Effect of Depth of Cut .....	141
6.5.2.	Effect of Cutting Speed .....	142
6.5.3.	Effect of Vibrations Frequency .....	145
6.5.4.	Effect of Vibration Amplitude .....	148
6.6	Effect of Tool Geometry .....	150
6.7	Contact in UAT.....	152
6.8	Hot Machining .....	153
6.9	Summary.....	162

## **CHAPTER-7 ..... 165**

### **Results and Discussions: Parametric Analysis of Hybrid Oblique Turning**

#### **Model**

7.1.	Introduction.....	165
7.2.	Cutting Force Analysis .....	167
7.3.	Thermal Analysis.....	171
7.4.	Effect of Depth of Cut.....	175
7.5.	Effect of Cutting Speed.....	177
7.6.	Effect of Feed Rate .....	179
7.7.	Effect of Cutting-Edge Radius on Cutting Forces.....	179
7.8.	Stresses in Process Zone.....	180
7.9.	Vibration in Axial and Radial Direction.....	182
7.10.	Summary.....	185

## **CHAPTER-8 ..... 188**

### **Conclusions and Future Work**

8.1.	Introduction.....	188
------	-------------------	-----

8.2. Conclusions.....189

8.1.1. Experimentation of Novel Hybrid Turning Process .....189

8.1.2. Numerical Simulations of HUAT, CT, HCT and UAT .....189

8.3. Contribution to Knowledge .....191

8.4. Future Work.....192

**References: ..... 193**

# List of Figures

Figure 1-1: Thesis layout.....	6
Figure 1-2: Thesis methodology .....	7
Figure 2-1: First wooden lathe machine [24] .....	10
Figure 2-2: Cutting tool geometry [20].....	13
Figure 2-3: Orthogonal cutting process [22] .....	16
Figure 2-4: Oblique cutting process [22] .....	17
Figure 2-5: Four basic types of chips; (a) discontinuous chip; (b) continuous chip; (c) continuous chip with built-up edge and (d) serrated chip [22] .....	17
Figure 2-6: Built up edge formation in the turning process [43].....	18
Figure 2-7: Chip formation in the turning process, (a) Ti-6246 by CT; (b) Ti-6246 by UAT; (c) Ti-676-0.9 by CT and (d) Ti-676-0.9 by UAT. The difference in the length of the chips is clearly visible.....	20
Figure 2-8: Chip formation in Piispanen theory [19, 22, 54].....	21
Figure 2-9: Deformation zones in metal cutting [19, 22] .....	22
Figure 2-10: Simplified model for shear angle analysis [22] .....	22
Figure 2-11: Merchant circle for force analysis [22] .....	23
Figure 2-12: Heat generation zone in metal cutting .....	27
Figure 2-13: Two channel displacement dynamometer [19] .....	31
Figure 2-14: Two channel slotted displacement dynamometer [19].....	31
Figure 2-15: (a) Two channel dynamometer with circular transducer; (b) Two component dynamometer with orthogonal transducer [19] .....	33

Figure 2-16: Three component dynamometer with hexagonal transducer [75, 81, 82] .....	33
Figure 3-1: Tool-workpiece interaction, (a) before chip formation and (b) after chip formation .....	56
[159, 163].....	56
Figure 4-1: Principal vibration directions in ultrasonically assisted turning .....	68
Figure 4-2: DNMG cutting insert used in experimentation [188].....	71
Figure 4-3: Stress strain data of Ti-15333 at room temperature and various strain rates .....	72
Figure 4-4: Stress strain data of Ti-15333 at various temperatures .....	72
Figure 4-5: (a) Schematic diagram of the experimental setup; (b) Experimental setup used in experiments of CT, HCT, UAT and HUAT .....	74
Figure 4-6: Thermocouple, thermocouple probe and thermometer used in experimentation to measure the workpiece temperature in hot experiments.....	76
Figure 4-7: Infra-red image of workpiece in hot machining at 300°C.....	77
Figure 4-8: Force history in experimentation at 300°C ( $V = 10$ m/min; $a_p = 0.3$ mm).....	79
Figure 4-9: Tangential cutting forces at various depths of cut, 10 m/min cutting speed and temperature of (a) 300°C; (b) 200°C and (c) 100°C.....	80
Figure 4-10: Radial cutting forces at various depths of cut, 10 m/min cutting speed and temperature of (a) 300°C; (b) 200°C and (c) 100°C.....	81
Figure 4-11: Reduction in cutting forces at various temperatures ( $V = 10$ m/min; $a_p = 0.3$ mm) .....	82
Figure 4-12: Reduction in cutting forces in HUAT when compared to CT at various depth of cuts, $V = 10$ m/min; $T = 300^\circ\text{C}$ .....	83
Figure 4-13: Schematic of the infra-red thermography .....	84

Figure 4-14: Experimental setup for thermal analysis .....	85
Figure 4-15: Temperature profile of the workpiece specimen after camera calibration for emissivity of 0.32 for Ti-15333 .....	86
Figure 4-16: Protecting thin plastic film used to protect lens from chips.....	87
Figure 4-17: Temperature history of the process zone at 300 $\mu\text{m}$ depth of cut, 10 m/min cutting speed; (a) HCT and (b) HUAT.....	88
Figure 4-18: Temperature of the process zone in CT using a micro - lens.....	89
Figure 4-19: Temperature of the process zone in UAT using a micro - lens .....	89
Figure 4-20: Thermal analysis of the process zone in CT and HCT using a standard lens ( $V = 10$ m/min; $a_p = 0.3$ mm).....	90
Figure 4-21: Thermal analysis of the process zone in UAT and HUAT using a standard lens ( $V = 10$ m/min; $a_p = 0.3$ mm).....	91
Figure 4-22: Temperature magnitude of chip in HCT and HUAT at different depth of cut and cutting speed of 10 m/min .....	92
Figure 4-23: Temperature levels in the chip in HCT and HUAT at different initial temperature of the workpiece material .....	92
Figure 4-24: Sample for surface topography.....	94
Figure 4-25: Experimental setup for surface roughness analysis using Zygo <sup>®</sup> interferometry .	95
Figure 4-26: Surface roughness at various temperatures ( $V = 10$ m/min; $a_p = 300$ $\mu\text{m}$ ) .....	95
Figure 4-27: Contour plot of surface roughness ( $V = 10$ m/min; $a_p = 300$ $\mu\text{m}$ ).....	96
Figure 4-28: Surface roughness at various temperatures; cutting speed $V = 10$ m/min; depth of cut $a_p = 200$ $\mu\text{m}$ .....	96
Figure 4-29: Stuer mounting press and prepared samples .....	98

Figure 4-30: Light microscopy of the sub-surface layers in Ti-15333 after CT, UAT, HCT and HUAT.....	100
Figure 4-31: Light microscopy of machined specimen at higher magnifications.....	100
Figure 4-32: Scanning Electronic Microscope used in experiments.....	101
Figure 4-33: SEM analysis of machined specimen .....	102
Figure 4-34: Backscatter analysis of machined samples .....	103
Figure 4-35: Chip shape in CT and UAT .....	104
Figure 4-36: Chip shape in HCT (a) front side of chip and (b) back side of chip.....	105
Figure 4-37: Chip at higher magnification in HUAT of the chip (a) back side and (b) front side .....	105
Figure 4-38: Chip shape at higher magnification in HCT (a) front side of chip and (b) back side of chip .....	105
Figure 4-39: Chip shape at higher magnification in HUAT (a) back side; (b) front side and (c) Back side at higher magnification.....	106
Figure 4-40: Light microscopy of the chips in (a) CT; (b) UAT; (c) HCT and (d) HUAT.....	106
Figure 4-41: Nano tester (NanoTest NTX3) used in the analysis.....	108
Figure 4-42: Nano-Indentation results obtained at various locations away from machined surface .....	110
Figure 4-43: Micro-hardness of machined specimen.....	111
Figure 5-1: Schematic of the turning process and principal direction of vibration .....	115
Figure 5-2: Process zone used in FE simulation of the orthogonal turning process .....	115
Figure 5-3: Stress-strain diagram of Ti-15333 obtained from Split-Hopkinson tests for different strain rates and room temperature [197] .....	118

Figure 5-4: Temperature dependant material flow stress data at various temperature and strain rate of 3300/s [197].....	118
Figure 5-5: Modified strain-rate-sensitive material model for 600°C [197] .....	119
Figure 5-6: Specific heat capacity of Ti-15333 [197] .....	120
Figure 5-7: Coefficient of thermal expansion of Ti-15333 [197] .....	120
Figure 5-8: Schematic representation of friction model .....	121
Figure 5-9: Element type 7 [202].....	122
Figure 5- 10: Element type 157 [202].....	123
Figure 5-11: Element type 43 [202].....	123
Figure 5-12: A schematic of cutting model .....	124
Figure 5-13: Boundary condition used in FE simulation.....	126
Figure 5-14: Cutting insert position in ultrasonically assisted turning in the forward and backward positions of tool vibration in one cycle tool vibration in one cycle.....	126
Figure 5-15: Mesh Convergence in simulations .....	128
Figure 5-16: Cutting insert used in experimentations.....	128
Figure 5-17: Conceptual model for the oblique turning process; (a) Stage-1; (b) Stage-2; (c) Stage-3 and (d) Stage-4 .....	129
Figure 5-18: Cutting tool geometry in FE simulation .....	130
Figure 5-19: Element Type 133 [202] .....	130
Figure 5-20: Improved version of oblique turning model with actual cutting edge geometry .....	131
Figure 5-21: Schematic diagram of a deformable workpiece in oblique turning .....	132

Figure 6-2: Equivalent von-Mises stress distribution in CT and UAT (at penetration stage and retraction stage of ultrasonic vibration ( $V = 10$ m/min; $a_p = 0.2$ mm).....	138
Figure 6-3: Temperature distribution in cutting region ( $V = 10$ m/min; $a_p = 0.3$ mm) .....	139
Figure 6-4: Temperature distribution along width of tool in CT and UAT at $t = 10$ ms .....	140
Figure 6-5: Temperature distribution along rake face of tool in CT and UAT at $t = 10$ ms.....	141
Figure 6-6: Tangential component of cutting forces in CT and UAT of Ti-15333 at various depths of cuts and $V = 10$ m/min .....	142
Figure 6-7: (a) Tangential component of cutting forces at various cutting speeds in CT and UAT, (b) forces history in UAT at various cutting speeds at $a_p = 0.3$ mm .....	143
Figure 6-8: Tangential component of cutting forces in CT and UAT at various cutting speeds and at $a_p = 0.2$ mm .....	144
Figure 6-9: Reduction in cutting force at various cutting speeds .....	144
Figure 6-10: Average cutting forces at various frequencies of vibration ( $V = 10$ m/min; $a_p = 0.3$ mm).....	146
Figure 6-11: Equivalent plastic strain at various frequencies of vibration.....	146
Figure 6-12: Temperature of process zone at various frequencies of vibration.....	147
Figure 6-13: Average cutting forces at various amplitudes of vibration ( $V = 10$ m/min; $a_p = 0.3$ mm).....	148
Figure 6-14: Plastic Strain at various amplitudes of vibration .....	149
Figure 6-15: Temperature of process zone at various amplitudes of vibration.....	150
Figure 6-16: Effect of rake angle on cutting force in CT and UAT .....	151
Figure 6-17: Plastic strain and temperature of the process zone at various rake angles (at the maximum penetration stage in UAT) .....	152

Figure 6-18: Contact status of tool with workpiece in UAT ( $a_p = 0.3$ mm; $V = 10$ m/min; $f = 20$ kHz and $a = 8$ $\mu$ m) .....	153
Figure 6-19: Tangential components of cutting force in HUAT of Ti-15333 ( $V = 10$ m/min; $a_p = 0.3$ mm).....	155
Figure 6-20: Average tangential cutting forces at various temperatures in HCT and HUAT ( $V = 10$ m/min; $a_p = 0.3$ mm) .....	155
Figure 6-21: Reduction in cutting forces in hot machining at various temperatures ( $V = 10$ m/min; $a_p = 0.3$ mm) .....	156
Figure 6-22: Average cutting forces at various amplitudes of vibration (b) .....	158
Figure 6-23: Average cutting forces at various frequencies of vibration .....	158
Figure 6-24: Temperature in the process zone in CT, UAT, HCT and HUAT .....	159
Figure 6-25: Temperature distribution on rake face of tool along chip width in HCT and HUAT .....	161
Figure 6-26: Temperature distribution on the rake face along line CD in HCT and HUAT.....	161
Figure 6-27: Stress distribution of the process zone in CT, HCT and HUAT .....	162
Figure 7-1: (a) Process zone used in orthogonal turning models; (b) chip geometry in the orthogonal turning model; (c) process zone in the oblique turning; (d) chip geometry in the oblique turning process.....	166
Figure 7-2: Cutting forces in CT ( $V = 10$ m/min; $f_r = 0.1$ mm/rev; $a_p = 0.3$ mm).....	167
Figure 7-3: History of cutting forces in HUAT in one complete cycle ( $V = 10$ m/min; $f_r = 0.1$ mm/rev; $a_p = 0.3$ mm; $T = 300^\circ\text{C}$ ) .....	168
Figure 7-4: Comparison of experimental and numerical results.....	169

Figure 7-5: Cutting forces at various temperatures in (a) HCT and (b) HUAT ( $V = 10$ m/min; $f_r = 0.1$ mm/rev; $a_p = 0.3$ mm) .....	170
Figure 7-6: Force reduction in HUAT (as compared to CT) at various temperatures of workpiece materials .....	170
Figure 7-7: Material accumulation in HUAT at 500°C in axial direction.....	171
Figure 7-8: Calculated temperature distribution in cutting region for CT, HCT and HUAT ( $V = 10$ m/min; $a_p = 0.3$ mm; $f_r = 0.1$ mm/rev; $T = 300^\circ\text{C}$ in hot machining) .....	173
Figure 7-9: Temperature distribution along cutting edge in oblique turning of CT, HCT and HUAT ( $V = 10$ m/min; $a_p = 0.3$ mm; $f_r = 0.1$ mm/rev $T = 300^\circ\text{C}$ in hot machining) .....	174
Figure 7-10: Temperature distributions on the rake face of the tool in CT, HCT and HUAT ..	174
Figure 7-11: Calculated plastic strain distribution in cutting region for (a) CT and (b) HUAT	175
Figure 7-12: Three components of cutting forces at various depths of cut ( $V = 10$ m/min; $f_r = 0.1$ mm/rev; $T = 300^\circ\text{C}$ ).....	176
Figure 7-13: Temperature of process zone at higher depth of cut at $t = 3$ ms .....	177
Figure 7-14: Effect of cutting speed on cutting forces: (a) CT and HCT; (b) HUAT .....	178
Figure 7-15: Temperature in process zone at higher cutting speed (70 m/min) in HUAT at $t = 1$ ms .....	178
Figure 7-16: Effect of feed rate on cutting forces in (a) CT and (b) HUAT .....	180
Figure 7-17: Cutting forces for various levels of cutting-edge radius: (a) CT and (b) HUAT ( $V = 10$ m/min; $f_r = 0.1$ mm/rev; $T = 300^\circ\text{C}$ ; $\alpha = 0^\circ$ ).....	181
Figure 7-18: Stress distribution in process zone in (a) CT; (b) HCT; (c) HUAT at the engagement stage; (d) HUAT at retraction stage.....	182

Figure 7-19: Cutting forces at various modes of vibrations (a) Tangential direction; (b) Radial direction; (c) Axial direction; (d) elliptical vibration (XY-mode); (e) Average cutting forces.. 184

# List of Tables

Table 2-1: Motion of tool and workpiece in machining [20].....	12
Table 3-1: A brief overview of UAT.....	39
Table 3- 2: Historical development of FE modelling of UAT at Loughborough University .....	66
Table 4-1: Chemical composition of Ti-15333 [wt. %] [188] .....	70
Table 4-2: Material properties of Ti-15333 [188].....	70
Table 4-3: Cutting tool properties [188].....	71
Table 4-4: Specifications of lathe machine used in turning experiments.....	73
Table 4-5: Laser vibro-meter specifications .....	75
Table 4-6: Band resistance heater specifications.....	76
Table 4-7: FLIR ThermoCAM system features .....	77
Table 4-8: Cutting conditions used in experiments.....	78
Table 4-9: Features of Nano Test NTX3 used for nano and micro indentations.....	108
Table 6-1: Cutting conditions used in experiments.....	135
Table 6-2: Cutting forces at various cutting conditions in conventional and assisted turning processes .....	187

# Notation and Abbreviations

<u>Symbols</u>	<u>Meaning</u>
$a$	Horizontal Amplitude
$a_c$	Undeformed chip thickness
$a_p$	Depth of cut
$a_w$	Undeformed chip width
$b$	Width of workpiece before machining
$b_1$	Constant
$b_2$	Constant
$b_3$	Constant
$\bar{b}$	Vertical amplitude
$b_c$	Width of chip after machining
$C$	Constant of machining
$\bar{c}$	Amplitude in z-direction
$C_p$	Specific heat
$D$	Measured displacement
$f$	Frequency
$F_c$	Main cutting force
$F_f$	Frictional force along the tool face
$F_n$	Normal frictional force
$F_s$	Shear force component along the shear plane
$F_{s0}$	Normal vector to shear force component along the shear plane
$F_p$	Normal force on shear plane
$F_t$	Thrust force

$F_x$	Tangential component of cutting force
$F_{x(t)}$	Instantaneous tangential component of cutting force
$F_y$	Radial component of cutting force
$F_{y(t)}$	Instantaneous radial component of cutting force
$F_z$	Component of force in feed direction
$F_{z(t)}$	Instantaneous feed component of cutting force
$i$	Inclination angle
$k_l$	Unit vector along z-axis
$K_a$	Constant
$k_r$	Tool cutting edge angle
$k_z$	Shear flow stress
$l$	Tool chip contact length
$l_s$	Length of the sticking zone
$M_r$	Material removal rate
$p$	Normal pressure
$P_m$	Heat generation in machining
$P_{sm}$	Specific heat generation in machining
$P_p$	Heat generation in the primary region
$P_s$	Heat generation in the secondary zone
$P_T$	Displacement of tool
$Q_p$	Heat source due to plastic deformation
$R$	Resultant force
$R_I$	Interface resistance
$R_C$	Chip material resistance

$R_s$	Shear plane resistance
$R_t$	Spreading resistance at shear plane
$R_{T(t)}$	Instantaneous resultant force
$r_d$	Dynamometer efficiency
$\bar{r}_d$	Displacement ratio
$r_t$	Coefficient of chip or chip thickness ratio
$S_z$	Feed per stroke
$T$	Temperature
$T_1$	Initial temperature
$T_2$	Temperature of primary deformation zone
$T_3$	Temperature of secondary deformation zone
$t$	Thickness of uncut chip
$t_c$	Thickness of cut chip
$T_l$	Tool life
$T_s$	Temperature of the shear zone
$V$	Velocity of the uncut chip
$V_c$	Velocity of cut chip
$V_{cr}$	Critical sliding velocity
$V_r$	Relative sliding velocity
$V_s$	Shear velocity vector
$V_{so}$	Unit vector parallel to $V_s$
$\alpha$	Rake angle
$\beta$	Frictional angle
$\sigma$	Surface normal stress

$\sigma_{fr}$	Shear friction stress
$\varphi$	Shear plane angle
$\varphi_y$	Phase difference in y-direction
$\varphi_z$	Phase difference in z-direction
$\mu$	Coefficient of friction
$\mu_{sl}$	Local friction coefficient
$\Delta$	Size of a built up edge
$\delta t_2$	Width of the secondary shear zone
$\theta$	Angle of inclination of resultant cutting force to the shear plane
$\theta_i$	Angle between $R_T$ and normal plane, $P_n$
$\theta_n$	Angle between y-axis and projection of $R_T$ on normal plane
$\vartheta$	Wedge angle
$\pi$	Constant
$\rho_{ca}$	Specific electrical resistance
$\rho_t$	Specific electrical resistance of the tool material
$\rho_c$	Specific electrical resistance of the workpiece material
$\Delta\varepsilon^{pl}$	Increment of the equivalent plastic strain
$\Delta\varepsilon_f^{pl}$	Failure strain
$\tau$	Surface friction stress
$\tau_{th}$	Conventional Coulomb friction stress
$\tau_{SSZ}$	Shear stress in the secondary shear zone
$\xi$	Coefficient controlling the distribution of normal stresses
$\bar{\lambda}$	Apparent friction angle

# Acronyms

<b>Symbols</b>	<b>Meaning</b>
2D	Two-Dimensional
3D	Three-Dimensional
CAD	Computer-Aided Design
CAM	Computer-Aided Manufacturing
CIM	Computer Integrated Manufacturing
CNC	Computer Numerical-Control
CT	Conventional Turning
DOF	Degree of Freedom
DNC	Direct Numerical-Control
ECE	End Cutting Edge
ECM	Electro-Chemical Machine
EDM	Electrical Discharge Machine
FCC	Faced Cubic Centre
FE	Finite-Element
FEA	Finite-Element Analysis
FEM	Finite-Element Method
HCT	Hot Conventional Turning
HPC	High Performance Computing
HUAT	Hot Ultrasonically Assisted Turning

REM	Rare Earth Metals
SCE	Side Cutting Edge
SPH	Smooth Particle Hydrodynamics
TEM	Thermally-Enhanced Machining
UAT	Ultrasonically Assisted Turning

# CHAPTER-1

## Introduction

### 1.1 Introduction

The main characteristics that support a swift and broad introduction of titanium alloys into aerospace, chemical and petroleum industries are their high strength-to-weight ratio, fatigue resistance and superior corrosion resistance. However, they pose considerable challenges for manufacturing industries due to their poor machinability. Machining of titanium alloys using conventional machining processes is a production dilemma due to their low thermal conductivity and high chemical reactivity with many tool materials.

There are various types of machining operations such as turning, drilling, milling and grinding, each of which is capable of generating a certain part geometry and surface texture. Turning, which is one of the most fundamental of machining operations performed on a lathe machine, is used in the modern industry to produce a large number of components. In turning, a single-point cutting tool is mounted on a tool post and fed against a revolving workpiece to achieve a desired shape of components. However, conventional turning (CT) of Ti-alloys generates high cutting forces and high temperature in the process zone due to its high shear strength and poor conductivity, respectively [1].

To make matters worse, many aerospace components are machining-intensive to achieve a desired shape. However, production rates in CT are low because of low cutting speeds (typically in the range of 0.2 to 0.63 m/s for aged alloys) and low feeds resulting in high production costs and poor machined surfaces [2]. Productivity of machined titanium components could be increased by using a cutting fluid for cooling and lubrication for the machining of titanium alloys [3]. Most machining operations benefit from the use of cutting fluids depending on workpiece material, including a reduction in friction at the tool-chip-interaction zone and also dissipation of the excessive amount of heat due to plastic deformation of the material at process zone. Moreover, lubrication also helps to remove chips from the process zone and to improve the surface quality of a machined components [4].

However, in recent years, the growing understanding of environmental problems and increasing cost burdens have led to a critical consideration of conventional cooling lubrication used in most machining operations. The cost related to the use of cutting fluid in a manufacturing operation, depending on workpiece and production structure are 16% of the total costs of the manufacturing process while in machining difficult-to-machine materials they reach 20%-30%, whereas some researchers claimed that the costs associated with cutting fluids are higher than the cost of cutting tools [5, 6]. Most of the costs associated with cutting fluids are predominantly due to environmental concerns; handling of the cutting fluids as well as their disposal must obey strict rules of environmental protections. Hence, a key machining process that signifies cost saving prospects associated with cutting fluids, and concurrently improves the overall performance of machining operations, is assisted dry machining.

Furthermore, as the advancement in machining progressed, new techniques were adopted to improve the machinability of Ti-alloys. Ultrasonically assisted turning (UAT) is a recently developed machining technique, in which up to 20000 low-energy vibro-impacts are superimposed on the cutting tool every second that interact with a workpiece. This novel machining technique offers significant improvement in the processing of modern alloys. In this technique, a considerable reduction in cutting forces as well as significant improvement in the surface finish of a machined workpiece was achieved [4, 7-10]. However, the peak instantaneous force in UAT was equal to the level of cutting forces in CT. Over the last few decades, a significant amount of work has been carried out to improve the experimental setup of UAT as well as to develop numerical models of the process [11-13]. A significant reduction in cutting forces was reported in machining of Ti-15V3Al3Cr3Sn (designated as Ti-15333). In addition to that, new techniques have been proposed to improve machinability of Ti alloys, for instance, cryogenic machining with the use of carbon-dioxide snow [14] and liquid nitrogen [15, 16]. Application of those new techniques affected chip shapes and also improved the surface roughness of the machined components [17].

The shear strength and strain-hardening rate of high-strength materials decrease with an increase in temperature due to thermal softening. Therefore, external heat can be supplied to the workpiece materials to make it softer and easier for a cutting tool to remove a given

amount of material; this technique is called *hot machining* [18]. Several assisted machining techniques for the processing of high-strength alloys have been reported in literature. However, there is still a need to develop new hybrid machining processes to improve its machining. Hence, in a current work, ultrasonic vibrations are superimposed on the cutting tool in hot machining to form a new hybrid machining technique called *Hot Ultrasonically Assisted Turning* (HUAT). The cutting forces, subsurface analysis of a machined workpiece, temperature in the process zone and surface roughness are analysed at various cutting conditions.

Furthermore, a finite-element method (FEM) is a main computational tool for simulation of the process zone and tool-workpiece interaction in metal cutting [19]. Modelling and simulation based on the FEM of machining processes are continuously attracting researchers to gain better understanding of the manufacturing process. Accurate predictions of physical parameters such as temperature, forces and stress distributions play a pivotal role in the predictive process engineering of machining processes. In the current work, both experimental and FEM techniques are applied to study the behaviour of hard-to-cut materials in CT, UAT, hot conventional turning (HCT) and newly developed HUAT. Initially, a 3D FE model of orthogonal turning was developed to understand the material response at various cutting conditions in CT, UAT, HCT and HUAT. The developed 3D FE model of orthogonal turning gives a good prediction of the main cutting force at various cutting conditions, ignoring the radial component of cutting force in the analysis. The process zone of the tool-workpiece interaction zone is simplified in the model in order to save time and computational power in the analysis. Later on, the developed model is extended to a 3D model of oblique turning to analyse the effect of vibrations superimposed on the cutting tool and of external heat applied to the workpiece material on all three components of forces. The newly developed 3D oblique turning models for CT, HCT and HUAT incorporate the radial component of cutting force in the analysis using the actual geometry of tool-workpiece interaction zone in the analysis. The models were used for parametric analysis of the process at various combinations of speeds, feed and depth of cut.

The current work was a part of MaMiNa (Macro-Micro and Nano aspect of machining processes) grant, Marie-Curie sponsored in which three different alloys were analysed for

conventional and assisted turning processes. Those alloys include: Ti 15333, Alloy-625, Ti-6246 and Ti-767-0.9La. However, in the current work, Ti-15333 which is beta titanium alloys, suitable for high temperature application were selected for the analysis of conventional and assisted turning processes.

## 1.2 Aim and Objective of Present Work

The main aim of the current work is to investigate a new dry hybrid turning process for turning of  $\beta$ -titanium alloy (Ti-15333). The developed new hybrid turning process is analysed both experimentally and numerically. For numerical modelling, a thermomechanically coupled 3D finite-element (FE) model of the orthogonal and oblique turning processes are developed in order to suggest suitable cutting parameters for assisted machining of modern alloys. The developed model validates the experimental results and is used for the parametric analysis of the newly developed hybrid turning process – HUAT.

The main objectives of the current work are:

1. to reduce the cutting forces in turning of Ti-15333 to a minimum level;
2. to investigate temperature in the process zone in CT, UAT, HCT and HUAT at various cutting conditions and to study the effect of externally applied heat to the workpiece material on it;
3. to develop a finite-element model of the 3D orthogonal turning for the analysis of principal cutting forces at various cutting conditions in conventional and assisted turning process;
4. to develop a 3D thermomechanically coupled FE model of oblique turning to investigate the effect of vibration and externally applied heat on all three components of cutting forces.
5. to improve surface roughness in turning of Ti-15333.
6. to perform parametric analysis of UAT and HUAT for Ti-15333 based on the developed FE models of orthogonal and oblique turning processes.

### 1.3 Research Methodology

A schematic presentation of the overall thesis layout is given in Figure 1-1. The thesis covers five main areas: introduction, literature review, experimentation, simulations, conclusions and future work. The main focus of the current section is to describe the methodology adopted in the current work (Figure 1-2), whereas the subsequent section will give a brief description of chapters.

A comprehensive literature review was carried out and it was found that UAT and hot machining reduce the cutting forces and significantly improve the surface roughness of machined components. Therefore, to reduce cutting forces to a possible minimum level and to further improve surface roughness, these two processes were used in combination for the turning of Ti-15333, resulted HUAT. The thesis consists of two main parts: experimentation and numerical simulations of conventional and assisted turning processes. The experimentation parts are further subdivided into analysis of cutting force, thermal analysis of the process zone and surface roughness. In the literature review, it was found that Ti alloys are sensitive to oxidation at elevated temperature. Hence, post-machining analyses of the machined specimens were carried out to investigate the effect of vibrations and external heat applied to the workpiece material.

The second part of the thesis deals with numerical simulations of the turning processes. The prime focus of this part was to developed finite-element model for conventional and assisted turning processes to carry out parametric analysis at various cutting conditions. In the current work, two models were developed for the analysis of conventional and assisted turning processes. At the first instant, a 3D FE model of orthogonal turning was developed followed by the one for the 3D oblique turning. In the first model, the principal cutting force (the tangential force component) was analysed at various cutting conditions for CT, HCT, UAT and newly developed HUAT. This model was developed based on certain simplification and assumptions used in the analysis; for instance, the radial component of the force was ignored in the model. Therefore, a novel 3D FE model of the oblique turning process was developed for CT, UAT, HCT and HUAT in order to investigate the effect of heat and vibration on the radial and axial components of cutting forces. A parametric analysis with the newly

developed model was carried for the turning of Ti-15333. The computational results obtained from the orthogonal and oblique turning models were validated by comparison with experimental data.

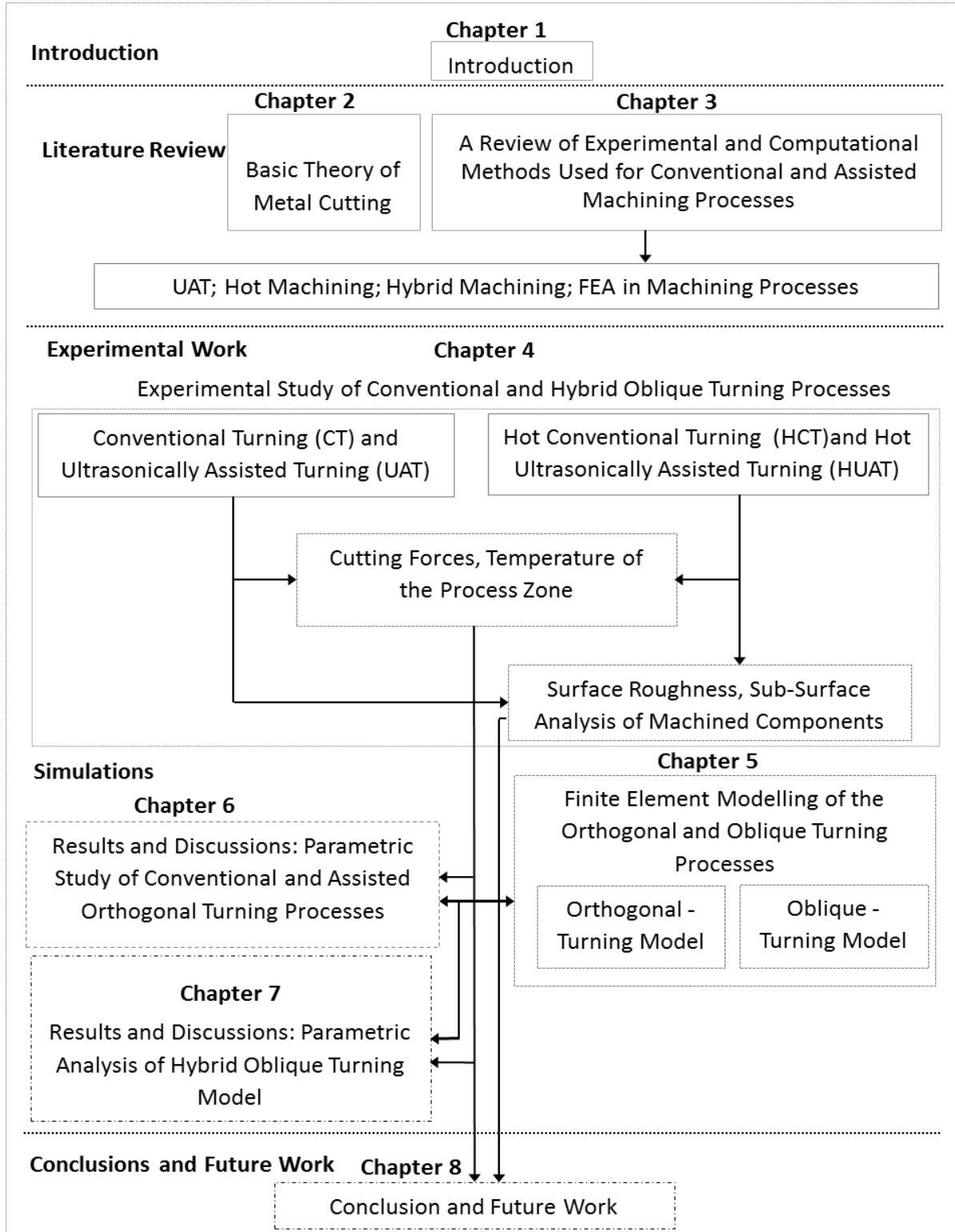


Figure 1-1: Thesis layout

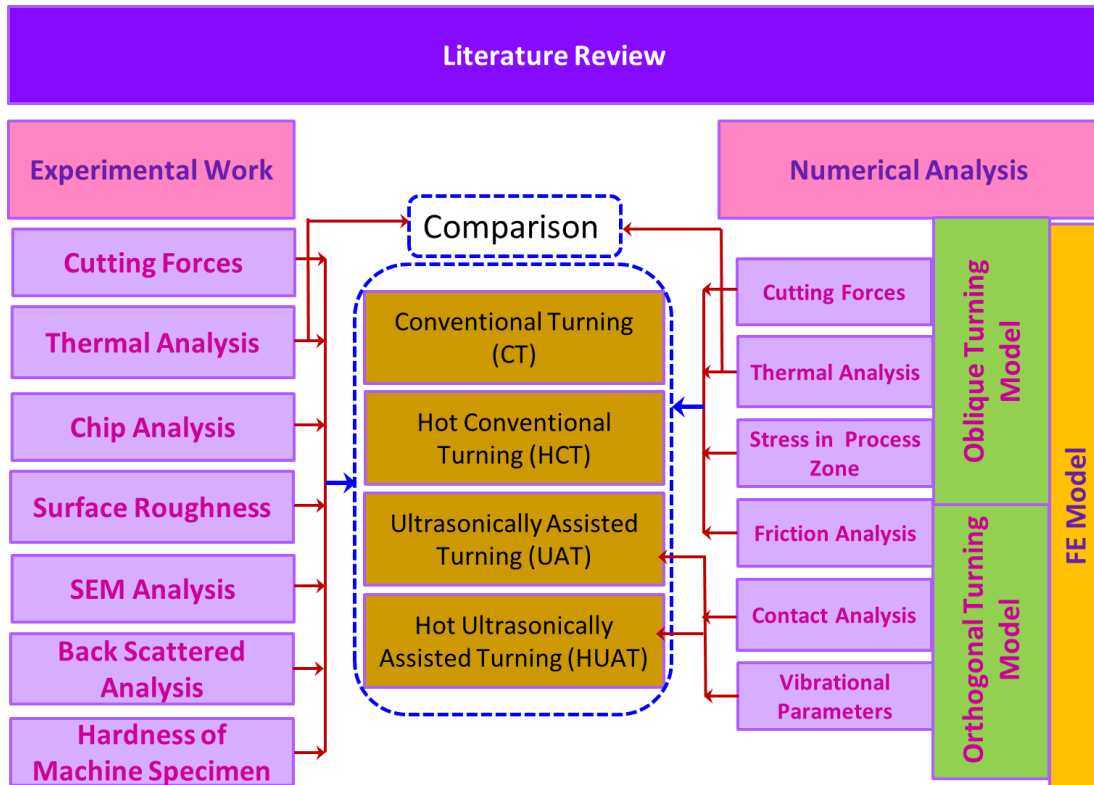


Figure 1-2: Thesis methodology

## 1.4 Thesis Outline

The following part of this report is divided into seven chapters.

**Chapter 2** reviews the basic theory and mechanics of the turning process. The basic concepts of metal cutting, tool nomenclature, chip types and types of the turning processes are discussed. Various analytical models available for analysis of the cutting forces and temperature in the process zone are also summarised in it. The chapter also covers experimental methods used for the analysis of cutting forces and temperature in the process zone.

**Chapter 3** contains the literature review concerning various experimental developments used to implement the assisted turning processes, particularly, ultrasonic vibrations in UAT and pre-heating, followed by the developments in finite-element analysis of machining processes, chip formation mechanism, cutting-tool modelling and three-dimensional (3D) modelling of assisted turning of hard-to-cut materials.

**Chapter 4** highlights the experimental work and measurement procedures for cutting forces, surface roughness and temperature in the process zone in the conventional and assisted turning processes of Ti-15333. Furthermore, microstructure analysis of the machined surface, sub-surface analysis and a study of the materials response to the newly developed turning process are analysed.

**Chapter 5** incorporates various features of a 3D finite-element modelling of the orthogonal and oblique turning processes. A thermomechanically coupled FE model for CT, UAT, HCT and HUAT is developed to investigate the effect of different cutting conditions as well as to study various assisted machining methods in the turning of Ti-15333. The chapter gives information about the material model used in the FE simulations. The mechanism used to incorporate friction between the tool and workpiece material is also discussed in the chapter.

**Chapter 6** presents a detailed discussion of the results obtained with the finite-element model of orthogonal turning and experimentation. The discussion focuses on the comparison of cutting forces (the tangential component), temperature distributions and various parameters of UAT and HUAT such as vibration amplitude, frequency and externally applied heat to the workpiece material.

**Chapter 7** gives a detailed discussion of the results obtained with the finite-element model of oblique turning and experimentation, incorporating the radial component of force into the model. The discussion is focused on the effect of vibration and heat on all the three components of cutting forces. Moreover, the comparison of cutting forces, temperature in the process zone and various parameters of CT, HCT and HUAT such as temperature and direction of vibration are analysed with the developed model. Good agreement between the results of the developed model and experimentation is observed. The chapter also covers various capabilities and features of the developed 3D model of oblique turning to be used in the future for other assisted turning processes.

**Chapter 8** describes conclusions and future work.

## CHAPTER-2

# Basic Theory of Metal Cutting

### 2.1 Introduction

Removing of surplus material in a form of chip from a workpiece to achieved a desire shape, size and surface quality, is one of the leading and major manufacturing processes used in industries. In general, the machining processes ranges from reasonably rough cleaning of casting components to a high precision micro-machining of structures that required narrow tolerances [20]. In machining, a wedge shape tool is used to remove the surplus material from the unfinished workpiece, within the allowable allowances and tolerances. In the early stages, hand-held tools made from bone, stone and sticks were used in machining [20, 21]. Later on, those tools were replaced by bronze and steel tools. The water steam and lately, electricity were used to driven tools in power-driven machines [20].

There are various machining operations used in industries, to shape structural components by removing excessive materials. Those included:

- Turning
- Grinding
- Milling
- Drilling
- Shaping
- Planing
- Broaching

However, turning is most commonly used machining operation, to achieve a desired shape, size and surface quality of a cylindrical machined workpiece. In turning, a single point cutting tool is held stationary in a tool post and fed against a revolving workpiece both in the radial as well as in the axial direction of a workpiece to remove unwanted allowances.

Shaping of materials to a desired shape were started by the ancient Egyptian in 4000 BC to use cylindrical shape metal object to transport stones and quarries to the building sites. In 1300 BC, the Egyptian used the principle of modern lathe machine to cut wooden objects (Figure 2-1). The lathe required two operators, one for revolving the workpiece with a wire rope whereas the other for feeding the cutting tool. The first horizontal bench lathe machine appeared in 1200-1299, based on the principle to use the foot treadle to rotate object [22]. Later on, the first engine lathe machine was introduced in 1820, followed by the introduction of lead screw, gear box and tool post by Maudslay in 1831 [20]. Furthermore, the tail stock, slide ways and automatic feed system were introduced, lately, to give the current shape to the lathe machine. The first turret lathe machine was introduced in 1845 [22, 23], by Fitch and was converted to fully automatic turret lathe machine in 1896, by Spencer. Significant improvements in those machines were brought through the introduction of automatic movement mechanisms, resulted in reduce human labour and improved quality of products.

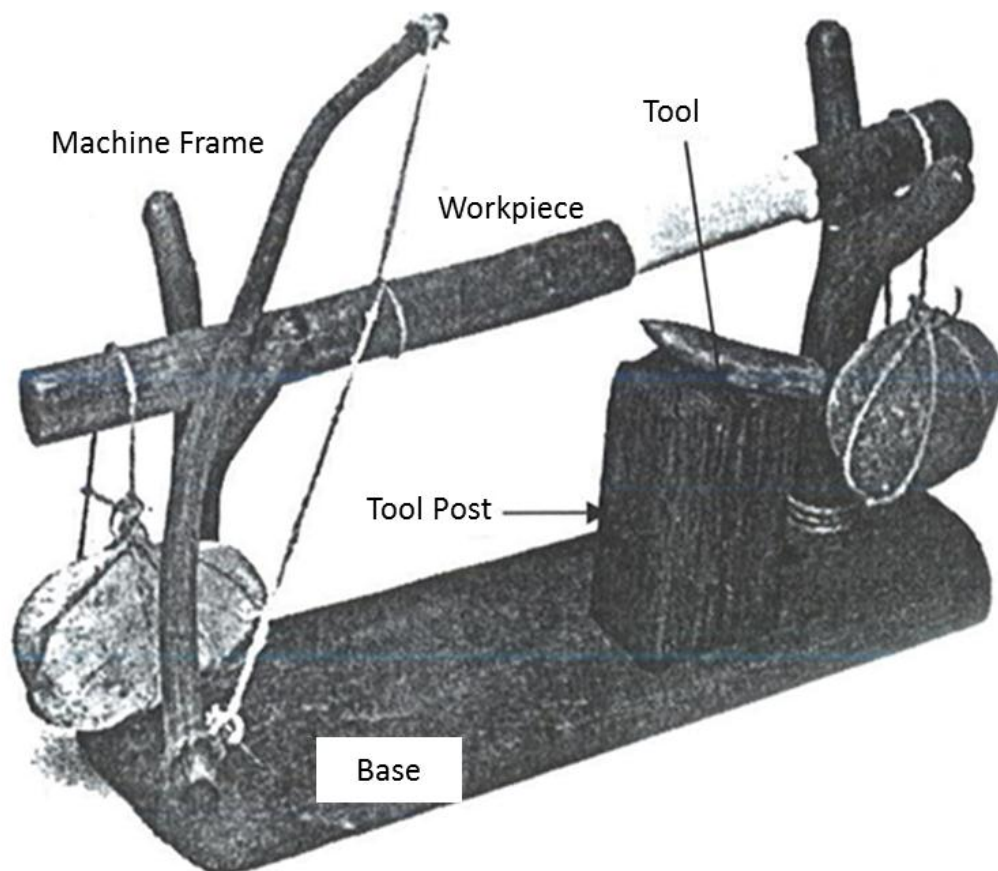


Figure 2-1: First wooden lathe machine [24]

Similarly, non-traditional machining technologies were extensively used in the 20<sup>th</sup> century, for metal cutting operations. In these machining technologies; chemical, mechanical and thermal effects were used to remove the unwanted materials from the workpiece.

Gussef, was credited for the development of Electro-chemical machine (ECM) in 1929 [20], later on, the machine was extensively used in modern automobile and medical engineering industries. Moreover, in 1943, the first electric discharge machine (EDM) was developed by Lazerenko [24]. In 1947, the electron beam was used for the first time, to remove unwanted materials from the workpiece and later on, was mainly attributed to the drilling operation in the modern manufacturing industries.

The introduction of intractable-alloys in aerospace and offshore industries stimulated the development of new machining techniques; the prime reason was the unavailability of sufficiently hard-tool materials to machine those intractable-alloys at economical speed-feed combinations. Therefore, assisted machining techniques were introduced for the machining of those hard-to-cut materials. Thermally-enhanced machining (TEM) was used to soften the workpiece material and make the material removal easier for the cutting tools, as the strength of a material is a function of temperature [25]. Initially, bulk-heating was used to heat up the workpiece materials [26]. Later on, the localized heat sources were used in the hot machining [27].

In 1953, the introduction of computer numerical-control (CNC) and direct numerical-control (DNC) machine centres, opened a new era in machining technology and remarkably improved product quality and accuracy. The computer-aided design (CAD), computer-aided manufacturing (CAM) and computer-integrated manufacturing (CIM) has drastically changed the product accuracy and quality. The introduction of computer technology in machining recognized non-traditional machine-tools in industries [28].

In contrast, researchers were also investigated cryogenic cutting for the processing of hard-to-cut materials. The cryogenic cutting is a new machining technique, in which cryogenic coolant was used to remove heat from the cutting edge [29, 30].

Ultrasonically assisted turning (UAT) was first introduced in 1960s [31]. Initially, UAT was limited to academic research, only. However, DMG/Gildemeister<sup>TM</sup> has recently, developed

ultrasonically assisted milling and drilling machines for the processing of material ranging from soft, hard-to-cut to advanced materials [32]. Therefore, this new machining technology is now available on the industrial floor for the machining of hard-to-cut materials.

## 2.2 Kinematics of the Turning Process

In machine tools, there are two types of motion called the primary motion and secondary motion. The primary motion, mainly contribute of motion of the tool or workpiece called cutting speed. Whereas, motion of the tool or workpiece in either feed or toward a machined surface, is called secondary motion. Table 2-1 listed the type of motion of the tool and workpiece in different machining operations. In many cases, the primary motion is either given to the tool or to the workpiece depending on the type of operation and machine. In the turning operation, the primary motion is given to the workpiece whereas the tool is held stationary in the tool post, followed by the tool movement to a desired position with a secondary motion.

Table 2-1: Motion of tool and workpiece in machining [20]

Workpiece motion	Tool motion			
	Stationary	Linear	Rotary	Spiral
Stationary		Shaping, Broaching	Drilling	Drilling
Linear	Planing		Milling	
Rotary		Turning		

### 2.2.1. Cutting Tools

A cutting tool has one or more than one sharp cutting edge and normally harder than the workpiece materials. The cutting edge is used to remove the excessive machining allowances from the workpiece. The cutting tool is held stationary or moving with appropriate speeds-feed combinations, depending on the cutting operation.

### 2.2.1.1. Geometry of a Single Point Cutting Tool

A single point cutting tool has a wedge shape and all the surfaces are grounded to distinct angles as shown in Figure 2-2 [22]. An angle between a line perpendicular to the shank and end cutting edge of a tool are called edge cutting edge angle (ECE), whereas, the angle between the cutting edge and side of a tool shank are called side cutting edge angle (SCE). The SCE and ECE angles have a primary influence on the chip flow as well as on the surface of a machined workpiece. The tool will observe a maximum force at full depth of cut, when the cutting edge is perpendicular to the workpiece at the time of initial interaction. Whereas, in an inclined cutting edge, the chip width increases and thickness decreases. Therefore, the initial impact at the tool-workpiece-interaction will be gradually increased. However, the excessive SCE angle creates chatter problems in the tool and the recommended angle is  $5^{\circ}$ - $20^{\circ}$  for ordinary materials.

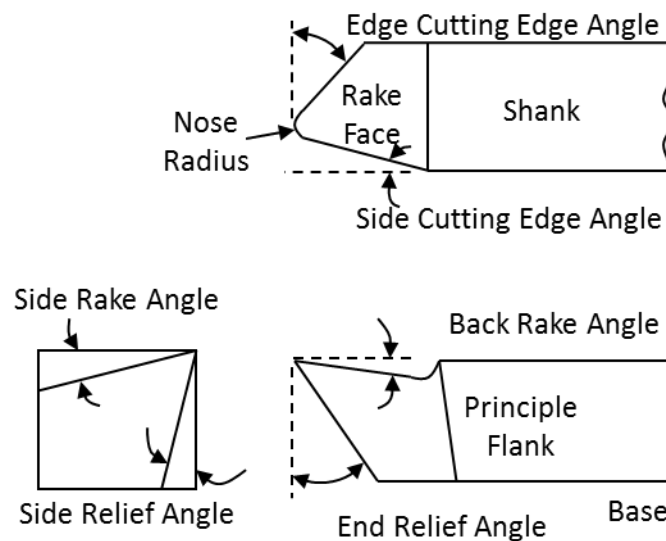


Figure 2-2: Cutting tool geometry [20]

Similarly, the purpose of the ECE angle is to prevent rubbing of the cutting tool on a machined surface. However, a high ECE angle reduces the cutting edge strength and causes tool failure. Therefore, the suggested ECE angle is varied from  $4^{\circ}$  to  $15^{\circ}$  for general cutting conditions.

The intersection of the SCE and ECE generate, nose radius of a cutting tool. It is normally grounded to form an arc to increase the strength of the cutting edge. The strength of a tool is

a direct function of the nose radius and power requirement. The high nose radius tool will generate more chatter in the tool compared to the lower nose tool radius in turning operations [33]. The angle between the face of a tool and a line parallel to the base of a tool formed, back rake angle, measured in a perpendicular plane through the cutting edge. The back rake angle is positive, negative or equal to zero. If the slope of the tool face is downward away from the cutting edge, is called positive rake angle, whereas if the slope is downward toward the cutting edge, the rake angle is negative. Similarly, the side rake angle is an angle between the face of the tool and a line parallel to the base of the tool, measured in a plane perpendicular to the base and side cutting edge. The rake angle controls the flow of chip in a machining operation and also control the wedge angle ( $\vartheta$ ) of a cutting tool. A positive rake angle moves away chips from a machined surface, whereas, a negative rake angle increases the strength of the cutting edge and is normally recommended for the machining of modern high strength alloys [34]. The angle between the end flank and a line perpendicular to the base of the tool, measured at right angles to the side flank is called end relief angle, whereas the side relief angle is formed between the side flank and a line perpendicular to the base of a tool, measured at right angles to the flank. The Relief angles are grounded on the tool to prevent rubbing of a machined surface and to achieve a finish surface.

In the modern standardized world, two systems are used to categorize the cutting inserts based on its geometry. The American National Standard Institute (ANSI) and International Standard Organization (ISO) are using the same nomenclature to identify insert based on their geometry, however, the first one is based on the inch system and the latter is on the metric system. Further details of the cutting insert geometry can be found in the catalogues of SECO.

#### 2.2.1.2. Cutting Tool Materials

The cutting tools are exposed to severe cutting condition with regards to the high cutting forces, excessive temperature, contact stresses and rubbing with machine surface as well as with chip [35, 36]. The selection of appropriate cutting tool material is a prime factor in any machining operation [37, 38]. The basic criteria for the development and selection of a cutting tool material are:

- Strong mechanical properties
- High hardness at room as well as at elevated temperatures
- Resistance to brittle fracture
- Excellent thermal shock resistance properties
- Less wear
- Ease of fabrication
- Economical

It is very hard to develop tools having all above mention properties. However, based on requirement, researchers have introduced various types of tool materials. Various grades of the high speed steel are available in the market, as a tool material. However, in recent years, the coated tools were extensively used in industries for the machining of high-strength alloys due to its high hardness and strength. Those tools were coated with high-strength materials like cemented carbide and tungsten carbides, that are hard, wear resistance, and have a high toughness.

### 2.2.2. Types of Cutting Operations

For an understanding of the mechanics of machining, first a brief knowledge about the type of cutting operation is necessary. In any machining process, there are two types of cutting operation: the orthogonal cutting and oblique cutting. The main difference between the two processes is the orientation of the cutting edge with respect to the cutting velocity. In the orthogonal cutting, the cutting edge of the tool is set in a position perpendicular to the direction of relative work or tool motion and generates a plan parallel to the original work surface. The plane containing both the tool motion-vector and vector normal to a finished surface is described as orthogonal cutting (Figure 2-3). All operations on lathe machine are carried out without feed rate are the orthogonal turning operations.

On the other hand, when the cutting edge rotates at an angle less than  $90^\circ$ , relative to the tool motion, is called oblique turning. The chip does not flow in a plane defined by the tool motion and normal to the finished surface (Figure 2-4). Therefore, the cutting action is no longer two dimensional, and the relation between cutting tool geometry, velocity and cutting force becomes more complex. The orthogonal turning process is mainly used in academia to

elucidate basic characteristics of the machining process avoiding complexity of the process in analysis.

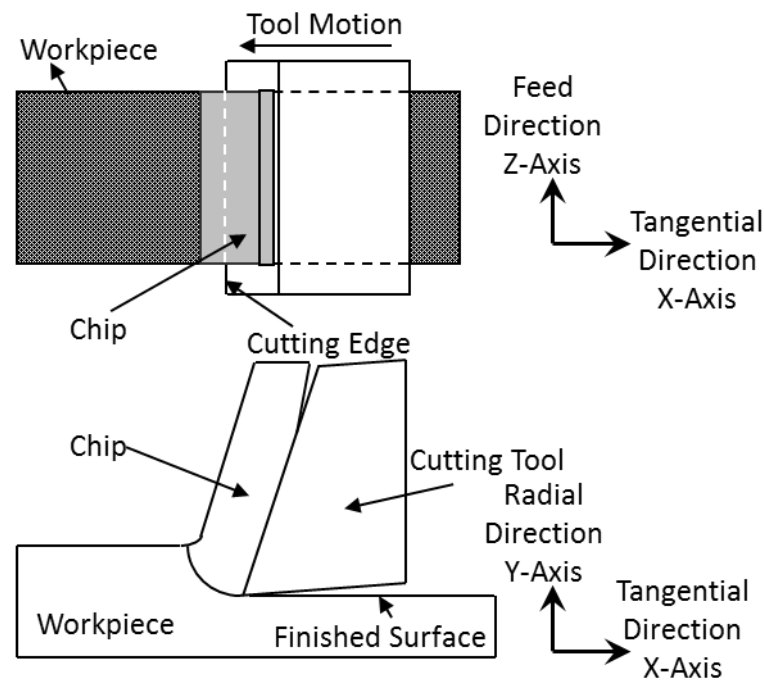


Figure 2-3: Orthogonal cutting process [22]

### 2.2.3. Types of Chip in the Turning Operations

In the metal cutting, the amount of excessive material is removed from a machine surface in a form of a highly deformed material called chips. There are four types of chips that can be formed in metal cutting processes as shown in Figure 2-5. The discontinuous or segmented chips are formed by a fracture mechanism, when brittle metals such as cast iron and hard bronze are cut. The segmented chips are produced when ductile materials are cut under poor cutting conditions, such as low cutting speed, coarse machining feed and small rake angle of a tool that results in a poor surface finish. Some of the ideal conditions that promote the discontinuous chips in metal cutting are higher depth of cut, low cutting speeds and small rake angles. For cutting of ductile material under steady state conditions, results long continuous chips. The continuous chips are like a ribbon flow along the rake face of a tool. In the continuous chips, the flow of metal on the tool face is not constrained either by a built-up edge or friction at the tool-chip-interface.

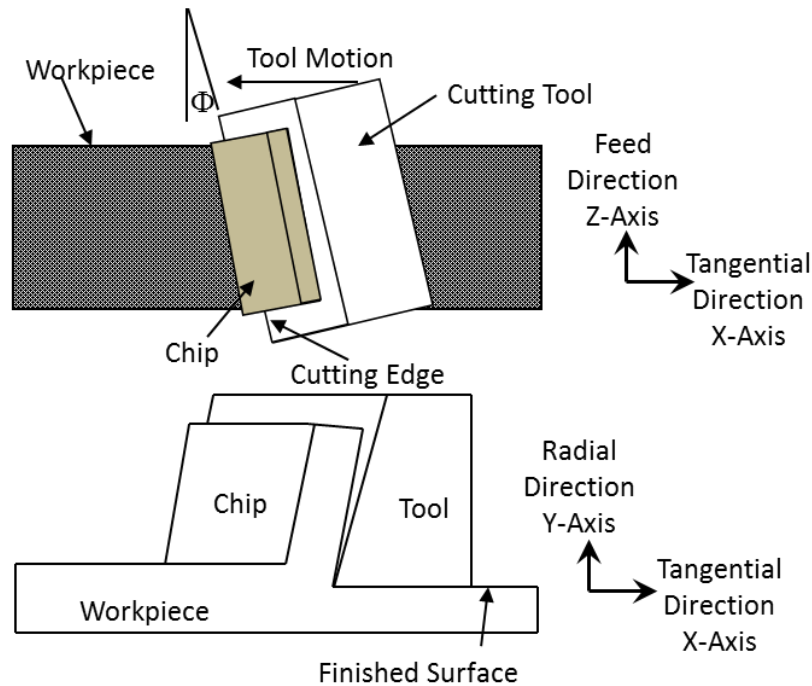


Figure 2-4: Oblique cutting process [22]

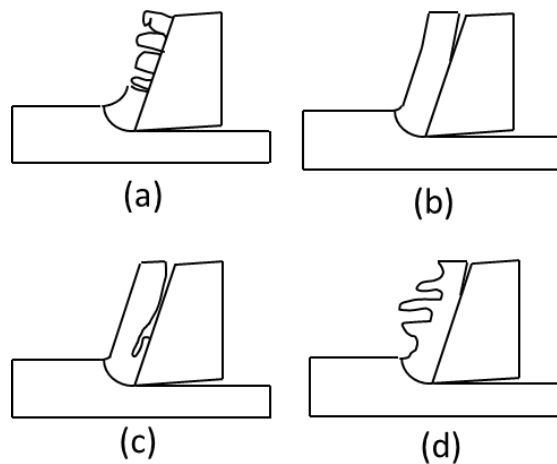


Figure 2-5: Four basic types of chips; (a) discontinuous chip; (b) continuous chip; (c) continuous chip with built-up edge and (d) serrated chip [22]

Some of the ideal conditions that promote continuous chip in metal cutting are: sharp cutting edge, small chip thickness, large rake angle, high cutting speed, ductile work material and less friction between the tool-chip-interface with efficient lubricant. The continuous chips are suitable for better surface finish and smooth cutting process. It also helps in having higher tool life and low power consumption. However, large coils of chips create chip disposal problems. For elimination of that problem, various types of chip breakers have been developed, which are in the form of grooves or steps on the tool rake face. The main

disadvantage of continuous long chip formation in the turning process is the hindrance in mechanized turning processes and high bottle neck time of chip removal from a machine. The chip breaker allows the chip to break into a small segment, so that they can be easily disposed.

In the machining of a ductile material, friction between the rake face-chip is high, resulting, sticking of the chip to the rake face. When a sizeable material is pile-up on the rake face, it acts as a cutting edge in place of the actual cutting edge as shown in Figure 2-6. This accumulation of material is called built-up edges [39-41]. As the size of the built-up edges increases, it becomes unstable and part of it separate from it, whereas part of it adhere to the chip underside, resulting surface roughness, and the chip formed is called continuous chips with built-up edges. Initially most of the work being done on build up edge formation was experimental based, However, in recent times, Childs [41] carried out some numerical analysis of built up edge formation to investigate the main reason of its formation in the turning processes. The numerical results showed that the formations of built-up edges were mainly due to the stagnation zone in front of the tool edge in machining operations. In stagnation zone, the velocity of material atoms became zero and started to accumulate, forming built up edges, in the turning processes [42].

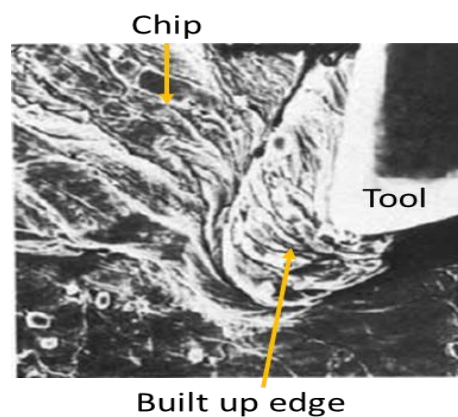


Figure 2-6: Built up edge formation in the turning process [43]

Therefore, the tools with built up edges, in the turning processes, the cutting is being carried out by the built up edges instead of the actual tool, resulting in longer tool life. A microscopically, shear localized chip consisting of a narrow band of heavily deformed materials, alter with relatively larger region of un-deform materials results in segmented chip

formation. Those types of chips occur, when cutting hardened stainless steel and titanium alloy at high cutting speeds. The prime reasons for the serrated chip formation in high strength alloys is its low thermal conductivity, high cutting forces and excessive process zone temperature.

Recently, a new technique has been introduced to achieve the discontinuous chip formation in the turning of high strength alloys even at lower cutting speeds. This novel technique is called free machining. In this process, rare earth metals having a low melting point are doped in to the alloys, resulting the discontinuous chip formation. The prime reason is the melting of those low melting metals in chip formation at the shear band.

Only a few attempts have been made to develop the free-machining titanium alloys. Kitayama *et. al*, [44] have added different rare earth metals (REM) together with phosphorus (P) or sulphur (S) to distribute rare-earth metal sulphides in the titanium alloy. Siemers *et. al*, [45] improved the machinability of Ti 6Al 4V (Ti-64) alloy by the addition of small amounts of cerium (Ce), erbium (Er), lanthanum (La) and neodymium (Nd). It turned out that the addition of 0.9% Ce, La or Nd leads to the formation of short chips during machining due to softening and melting of the metallic rare earth metal precipitates. This results in reduced adhesion between the segments and chip separation during further progress of the tool. The addition of Er does not improve the machinability as its melting point is too high [46-48]. The free-machining alloy of Ti-6Al 4V 0.9La can successfully reduce the production costs of machined components as automated manufacturing is enabled and is now ready for technical application [49]. Whenever tin (Sn) is present in the alloys, the addition of rare earth metals did not improve the machinability as Sn and La form intermetallics like  $La_5Sn_3$  which have softening temperature above 1500°C [50]. In Sn-containing alloys, Sn can be replaced by Zirconium (Zr) ensuring that metallic rare earth metal particles are present in the alloys. Similar attempts have been made on commercially pure titanium (CP-Titanium Grade 2 and Grade 4), Ti 6Al 2Sn 4Zr 2Mo 0.08Si (Ti-6-2-4-2-S), Ti 15V 3Al 3Cr 3Sn (Ti-15-3-3-3) and Ti 5Al 5V 5Mo 3Cr 0.5Fe (Ti-5-5-5-3) [47, 48]. The obtained discontinuous chip formation modified Ti-676-0.9 La is shown in Figure 2-7.

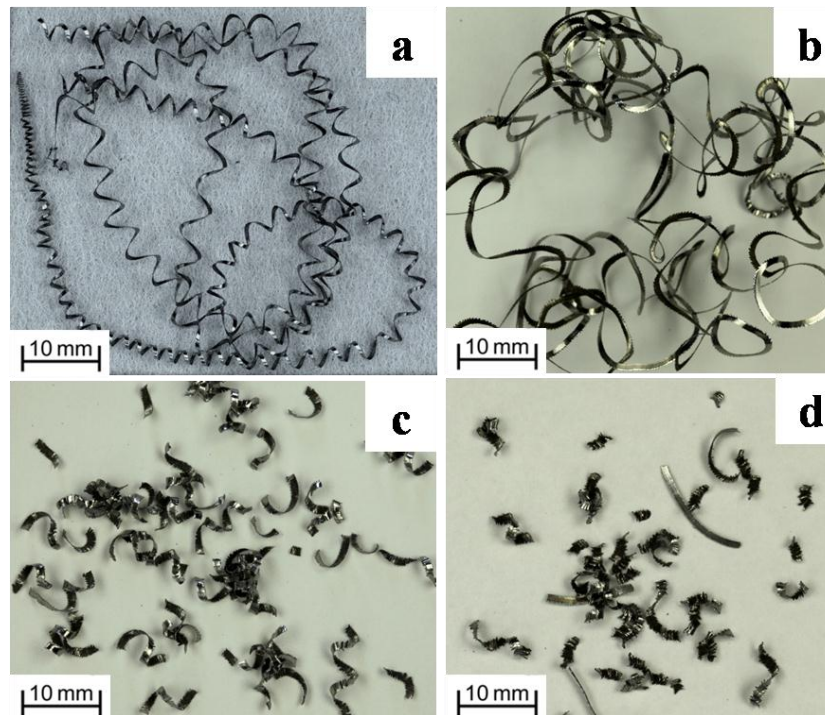


Figure 2-7: Chip formation in the turning process, (a) Ti-6246 by CT; (b) Ti-6246 by UAT; (c) Ti-676-0.9 by CT and (d) Ti-676-0.9 by UAT. The difference in the length of the chips is clearly visible

#### 2.2.4. Chip Formation

Many attempts have been made to analyse and understand the mechanism of chip formation in the turning operations with the introduction of new high-strength alloys and new tool materials [51-53]. However, due to the complex nature of deformation of the process zone, there are two schools of thoughts to explain the chip formation mechanism. The first school of thought adopted the thin plane theory to explain the chip formation mechanism. The first attempt was made by Piispanen [54] to understand the chip formation mechanism. According to Piispanen, the un-deformed metal is just like a stack of cards. The cards slide over one another, when the cutting tool moves toward those cards as shown in Figure 2-8. Later on, Karabacher *et al* [55], has also used the thin plane theory to explain the chip formation mechanism.

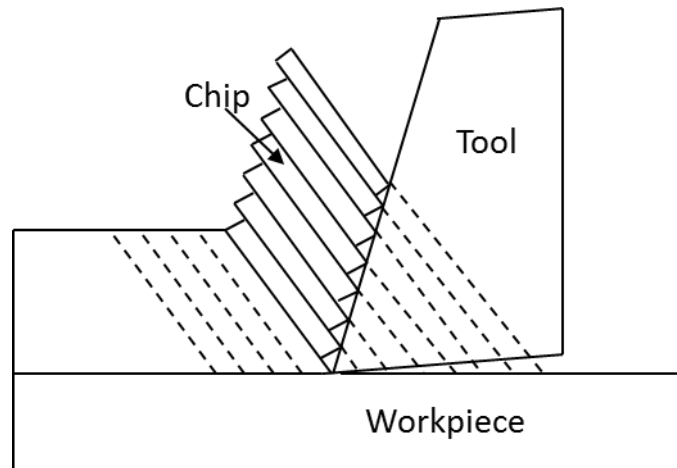


Figure 2-8: Chip formation in Piispanen theory [19, 22, 54]

The second school of thought used the thick deformation plane to explain the complex chip formation mechanism. The prime work carried out using the thick deformation plan include: Palmer [56] and Oxley [57]. However, actual metal cutting is a very complex process. The metal in front of the tool rake face is compressed, first elastically and then plastically. The compressed zone is traditionally called shear zone. The actual separation of the metal starts as a yielding or fracture depending on the cutting conditions. Deformation in machining process is concentrated into two regions close to the cutting tool edge called primary and secondary deformation zones. The primary deformation zone, extend from the tip of the cutting tool to a junction between the surface of the un-deformed work material and the deformed chip. Similarly, a secondary deformation zone may be divided into two regions: sticking region and sliding region as shown in Figure 2-9. Chip formation processes is very complex and depend on various cutting parameters including, speed, feed combination, tool geometry, workpiece material, tool materials, contact conditions and tool coating. Various attempts have been made to study the chip formation process in the turning process using various workpiece and cutting tool materials to understand this complex process [58, 59].

### 2.2.5. Cutting Forces in Metal Cutting

There have been several studies in the literature on modelling of the cutting forces in turning of metals using the different predictive modelling approaches, however, the most commonly used modelling technique is an analytical modelling method. The first attempt to analyse the shear deformation of metal was carried out by Merchant in 1945 [60]. The theory was based

on the minimum energy criterion and a very famous relation was derived for calculating the shear plane angle.

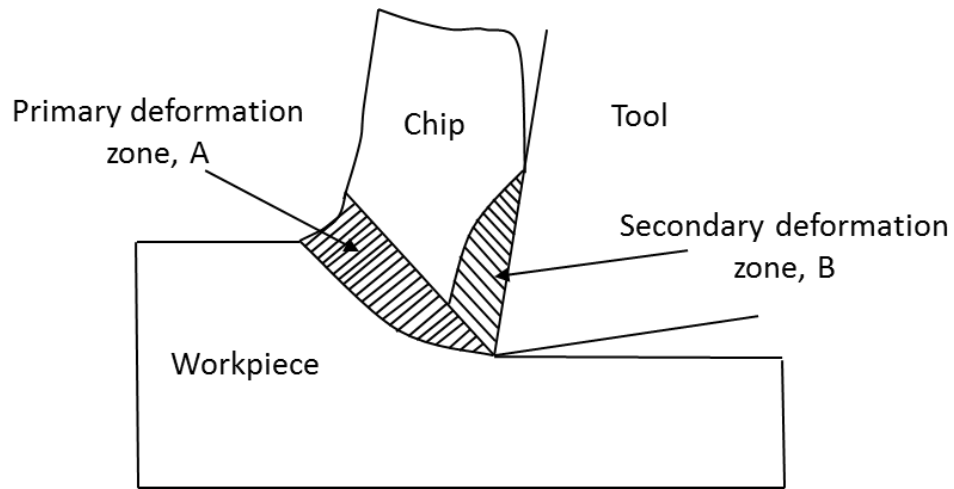


Figure 2-9: Deformation zones in metal cutting [19, 22]

$$\varphi = 45^\circ + \frac{\alpha}{2} - \frac{\beta}{2}, \quad (2-1)$$

where  $\varphi$ ,  $\alpha$  and  $\beta$  are the shear plane angle, rake angle and frictional angle, respectively.

Merchant model will give you a relation for calculating the shear plane angle, resulting in calculating main cutting forces, as shown in Figure 2-10 and Figure 2-11.

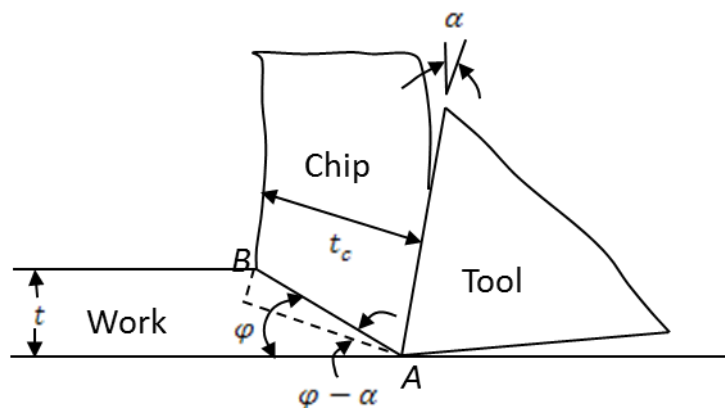


Figure 2-10: Simplified model for shear angle analysis [22]

$R$  = Resultant force

$F_x$  = Experimentally measured force component in the tangential direction

$F_y$  = Experimentally measured force component in the radial direction

$F_s$  = Shear force component along the shear plane

$F_p$  = Normal force on the shear plane

$F_t$  = Frictional force along the tool face

$F_n$  = Normal frictional force

$b$  = Width of chip before machining

$b_c$  = Width of chip after machining

$V$  = Velocity of the uncut chip

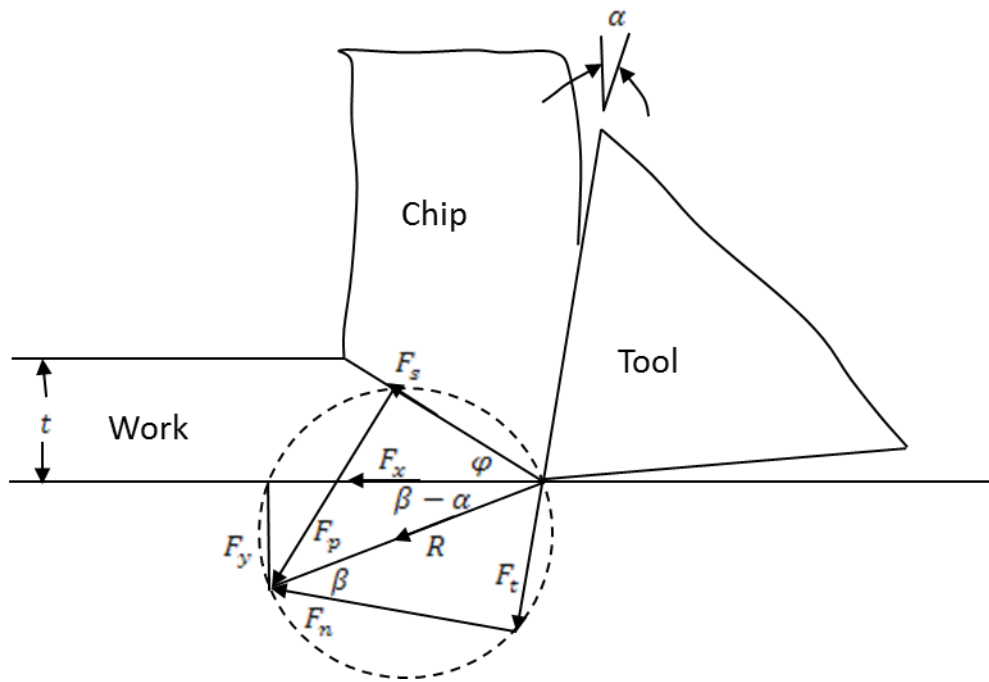


Figure 2-11: Merchant circle for force analysis [22]

$V_c$  = Velocity of the cut chip

$t$  = Thickness of the uncut chip

$t_c$  = Thickness of the cut chip

$\mu$  = Coefficient of friction

© 2013 R. Muhammad

$$F_s = F_x \cos\varphi - F_y \sin\varphi, \quad (2-2)$$

$$F_p = F_y \cos\varphi + F_x \sin\varphi = F_s \tan(\varphi + \beta - \alpha), \quad (2-3)$$

$$F_t = F_x \sin\alpha + F_y \cos\alpha, \quad (2-4)$$

$$F_n = F_x \cos\alpha - F_y \sin\alpha, \quad (2-5)$$

The coefficient of friction  $\mu \sim \tan\beta$  can be calculated as,

$$\mu = \frac{F_t}{F_n} = \frac{F_x \sin\alpha + F_y \cos\alpha}{F_x \cos\alpha - F_y \sin\alpha} = \frac{F_y + F_x \tan\alpha}{F_x - F_y \tan\alpha}, \quad (2-6)$$

$$F_x = \frac{F_s \cos(\beta - \alpha)}{\cos(\varphi + \beta - \alpha)}, \quad (2-7)$$

$$F_x = \frac{\tau_s A_s \cos(\beta - \alpha)}{\sin\varphi \cos(\varphi + \beta - \alpha)}, \quad (2-8)$$

Similarly, the normal stresses can also be calculated as;

$$\sigma = \frac{(F_x \sin\varphi - F_y \cos\varphi)}{bt} \sin\varphi, \quad (2-9)$$

The power required ( $P_m$ ) in any machining operation to remove the given amount of materials is the product of the cutting force and cutting velocity;

$$P_m = F_x V_c, \quad (2-10)$$

The energy consumed in any machining operation, is a sum of shear energy, frictional energy, surface energy and momentum energy. However, the shear energy and friction energy are more dominant as compared to the surface energy and momentum energy [34]. Therefore, it will be neglected and the specific energy ( $P_{sm}$ ) will be;

$$P_{sm} = \frac{P_m}{M_r} = \frac{F_x}{A}, \quad (2-11)$$

where  $M_r$  is the material removal rate and  $A$  is the area of the uncut chip.

Later on, Lee and Shaffer [61] modified Merchant relation for a perfectly plastic material and calculated new relation for the shear angle.

$$\varphi = 45^\circ + \alpha - \beta, \quad (2 - 12)$$

Later, they modified their own model for a cutting condition having built up edge formation as well.

$$\varphi = 45^\circ + \alpha - \beta + \Delta, \quad (2 - 13)$$

where  $\Delta$  is the size of the built up edge formation.

Furthermore, the above two models were further modified by Oxely [62]. A further simplified relation for the shear plane angle, the frictional contact angle and rake angle were derived:

$$\theta = \varphi - \alpha + \beta, \quad (2 - 14)$$

Similarly, an improved oblique model was developed for the turning process taking into account the cutting tool angles and feed velocity by Fang [63]. This model gives us a good approximation of all the three force components.

$$F_s = (a_c \cdot a_w \cdot \tau) / (F_{s0} \cdot k_l) \cdot V_{s0}, \quad (2 - 15)$$

$$R = \left( \frac{|F_s|}{|R_o \cdot F_{s0}|} \right) \cdot R_o, \quad (2 - 16)$$

$$F_z = -(|R| \cdot \sin\beta \cdot V_{s0}), \quad (2 - 17)$$

where  $F_{s0}$ ,  $V_{s0}$ ,  $k_l$ ,  $\tau$ ,  $a_c$  and  $a_w$  are the normal vector to shear force component along the shear plane, unit vector parallel to  $V_s$ , unit vector along z-axis, shear stress, is the undeformed chip thickness measured in the plane perpendicular to the bottom plane of the uncut layer of work material and undeformed chip width, respectively.

Later on, various models were developed for the oblique turning process to understand the process zone of the complex deformation process through parametric study [64-66]. However, most recently, an analytical oblique model was developed for ultrasonically assisted turning to investigate the cutting forces, stresses of the process zone, influence of

tool geometry and vibrational parameters on the output forces [67-69]. The model was also applicable to conventional turning and can be used for parametric study of conventional turning at various speeds-feeds combinations.

$$F_{x(t)} = (-\cos i \cdot \sin k_r \cdot \sin \theta_i + \sin i \cdot \sin k_r \cdot \cos \theta_i \cdot \cos \theta_n + \cos k_r \cdot \cos \theta_i \cdot \cos \theta_n) R_{T(t)}, \quad (2-18)$$

$$F_{y(t)} = (\sin i \cdot \sin \theta_i + \cos i \cdot \cos \theta_i \cdot \cos \theta_n) R_{T(t)}, \quad (2-19)$$

$$F_{z(t)} = (\cos i \cdot \cos k_r \cdot \sin \theta_i - \sin i \cdot \cos k_r \cdot \cos \theta_i \cdot \cos \theta_n + \sin k_r \cdot \cos \theta_i \cdot \sin \theta_n + \cos \theta_i \cdot \cos \theta_n) R_{T(t)}, \quad (2-19)$$

where  $k_r$ ,  $\theta_i$ ,  $i$ ,  $\theta_n$ ,  $R_{T(t)}$ ,  $F_{x(t)}$ ,  $F_{y(t)}$  and  $F_{z(t)}$  are tool cutting edge angle, angle between  $R_T$  and normal plane,  $P_n$ , Inclination angle, angle between y-axis and projection of  $R_T$  on normal plane, instantaneous resultant force, instantaneous tangential component of cutting force, instantaneous radial component of cutting force and instantaneous feed component of cutting force.

### 2.2.6. Heat in Metal Cutting

In metal cutting, a considerable amount of heat is generated, affecting the surface finish of a machined component and also determined the amount of power required to remove the given amount of materials. The main sources of heat in metal cutting are, the plastic deformation in the primary deformation zone (Zone-A), secondary deformation zone (Zone-B) and friction between the tool-tip and a machined surface (Zone-Z) as shown in Figure 2-12.

In metal cutting, the strain rate reaches to a level of  $10^5 \text{ s}^{-1}$  and energy involved in the plastic deformation at high strain rate is converted to heat. Therefore, the frictional heat generation in metal cutting is neglected in most of the analysis and the total heat generated in metal cutting is;

$$P_m = P_p + P_s, \quad (2-20)$$

where  $P_m$ ,  $P_p$  and  $P_s$  are the heat generation in machining, in the primary deformation zone and secondary deformation zone, respectively.

$$P_m = F_x V_c, \quad (2-21)$$

$$P_s = F_s V_s, \quad (2-22)$$

The values of  $F_x$  and  $F_t$  can be determined from experimentation. Therefore, the heat generated in the primary and secondary deformation zone can be determined from equation 2 – 21 and equation 2 – 22, respectively.

Furthermore, the shear zone temperature was calculated by Pandey and Singh [70]. Therefore, the temperature of the shear zone in a turning operation can be calculated by the following relations.

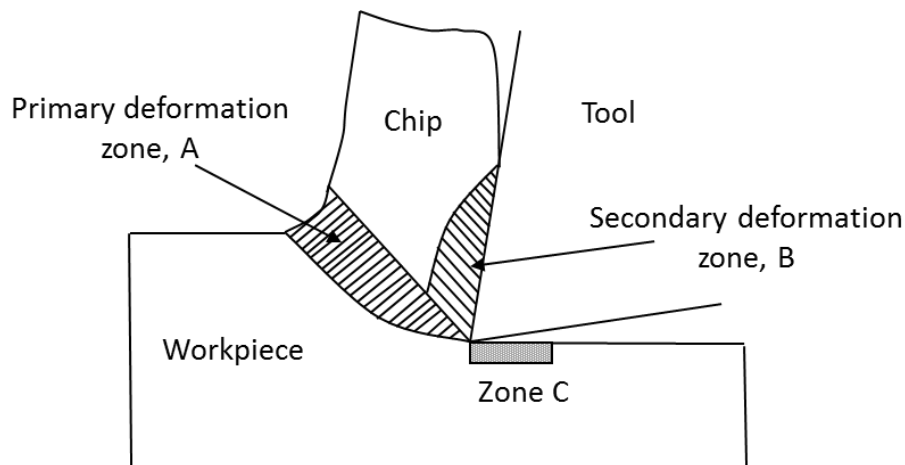


Figure 2-12: Heat generation zone in metal cutting

$$T_s = \frac{0.9F_s V_s}{\rho C_p t V_c b}, \quad (2-23)$$

whereas  $F_s$  is the shear force along the shear plane,  $V_s$  is the shear component of velocity,  $\rho$  is the density,  $C_p$  is the specific heat,  $V_c$  is the cutting velocity and  $b$  is the width of the chip

Furthermore, 70-80% of the heat of the deformation zone were carried away by the chip [34]. Therefore, the temperature of the chip was highest at the exit point of the secondary deformation zone as shown in Figure 2-12. Therefore, the temperature of the chip can be calculated as:

$$T = T_1 + T_2 + T_3, \quad (2-24)$$

where  $T_1$ ,  $T_2$  and  $T_3$  are the initial temperature of the workpiece, temperature rise in the primary deformation and secondary deformation zones, respectively.

The average temperature of the primary and secondary deformation zone can be determined from the following equations for ideal conditions having no frictional effect,

$$T_2 = \frac{P_p}{\rho C_p V_c t_1 b}, \quad (2 - 25)$$

$$T_3 = \frac{P_s}{\rho C_p V_c t_1 b}, \quad (2 - 26)$$

$$T = T_1 + \frac{P_p}{\rho C_p V_c t_1 b} + \frac{P_s}{\rho C_p V_c t_1 b}, \quad (2 - 27)$$

where  $\rho$  and  $C_p$  are the density and specific heat of workpiece material, respectively.

In the literature, various analytical and experimental techniques were used to model, the temperature of the process zone in the turning process [71-74]. Many factors including cutting speed, depth of cut, feed rate, tool geometry and material of the workpiece have a significant influence on temperature of the process zone. An overview of the factors, affecting the temperature of the cutting zone is highlighted.

The temperature of the cutting zone is greatly influenced by the workpiece materials. For high-strength alloys, yield strength of materials is high; therefore, high cutting forces are required to remove the given amount of materials, resulting high cutting zone temperatures [74]. Similarly, the thermal conductivity of the workpiece materials also played an important role in the temperature of the cutting zone. Materials having a high thermal conductivity dissipate higher energy; therefore, the temperature of the cutting zone is lower as compared to the materials having a poor thermal conductivity like titanium alloys.

Moreover, cutting speed, feed rate and depth of cut, control the amount of materials removed from a machined surface and has a considerable influence on the process zone temperature. A rise in feed rate increased penetration into the workpiece. Therefore, the work-leads to higher plastic deformation and resulting higher heat generation in the cutting region.

An empirical relation for the cutting zone temperature in terms of cutting variables are presented in [34].

$$T = k_a \cdot V_c^z \cdot f_r^x \cdot a_p^y, \quad (2 - 28)$$

Where  $k_a, x, y, z, c$  are constant and  $V_c, f_r$ , and  $a_p$  cutting velocity, feed rate and depth of cut, respectively.

Tool geometry also affects the temperature of the cutting region. The most imported are the rake angle, end relief angle and nose radius. Increasing the rake angle and contact length of the chip-tool results, in improvement in heat removal rate from the cutting zone. Similarly, a negative rake angle causes high deformation in the cutting zone and produce high temperature at the cutting zone. An increase in relief angle causes, the frictional heat generation between the tool and finish machined surface. Similarly, the nose radius of the cutting tool also affects the heat generation of the cutting zone. Deformation of the cutting region increases with an increase of a nose radius, resulting high heat generation in the cutting zone [74].

### 2.3 Experimental Force Measurement in Turning

The knowledge of cutting forces under given conditions in various machining processes is an important criterion of material machinability, to the designer-manufacturer of machine tools, as well as to manufacturing industries. Currently, manufacturing industries are continuously concentrating on lower cost solutions with a reduction in lead time and superior surface integrity in order to sustain their efficiency and competitiveness. The newly developed hybrid turning processes and cutting tool grades are intended to allow versatile application in roughing and finishing processes for a wide range of materials. The new developments in the turning processes reduced the induced cutting forces and resulted better surface finish. A wide range of techniques were used to measure the cutting forces in the turning processes.

In current metal cutting practice, dynamometers are extensively used to measure the cutting forces. The basic principle of dynamometer involves measurement of deflection against the applied load, with proper calibrations and is measured with a device called a transducer. In order to obtain accurate results, a dynamometer should be sensitive enough to respond to

the applied load. The recommended accuracy of a dynamometer for metal cutting application is 1% [75]. Furthermore, a dynamometer should be rigid enough so that the cutting operation is not influenced by the accompanying deflections [75, 76]. Other requirements for dynamometer design are its natural frequency, wide frequency response and small cross sensitivity. Additionally, the dynamometer should not be affected by the humidity, temperature, and cutting fluid used, in machining operations.

Various types of dynamometers are available in the literature, to measure the cutting forces, working on the same basic principles. Some of the basic devices that are used as a transducer to measure the cutting forces in metal cutting operation are briefly discussed in the following sections.

### **2.3.1. Displacement Measurement Based Dynamometer**

In these types of dynamometers, displacement or deflection of the cutting tool was measured with a built-in transducer, to calculate the cutting forces. Various designs are available in the literature for displacement transducers to measure the cutting forces are discussed in the subsequent paragraph.

Chisholm designed the two component turning dynamometer in 1955, to analyse the cutting forces in turning operations, experimentally. This dynamometer consists of a cantilever beam, supporting the cutting tool at the free end. Dial gauges were used to monitor the main cutting force in the vertical direction and feed force in the horizontal direction as shown in Figure 2-13. Additionally, the dynamometer was very stiff and consists of one piece of metal to avoid any cross sensitivity.

In the second types of dynamometer, two transducers were mounted on the weakest point of the dynamometer to measure the deflection of the points due to the applied load. Those weakest points are labelled as point A and B as shown in Figure 2-14. The displacement transducers were arranged in such a way to measure the main cutting force in the vertical direction and feed force in the feed direction. The efficiency of the dynamometer was calculated in term of displacement ratio;

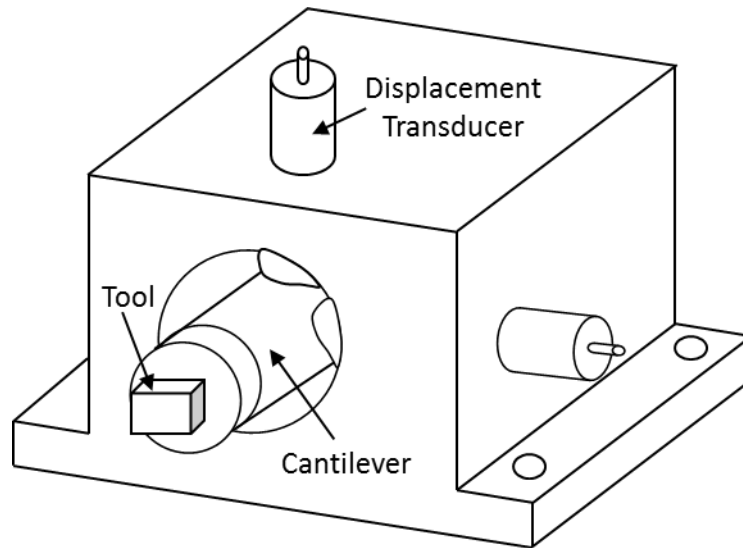


Figure 2-13: Two channel displacement dynamometer [19]

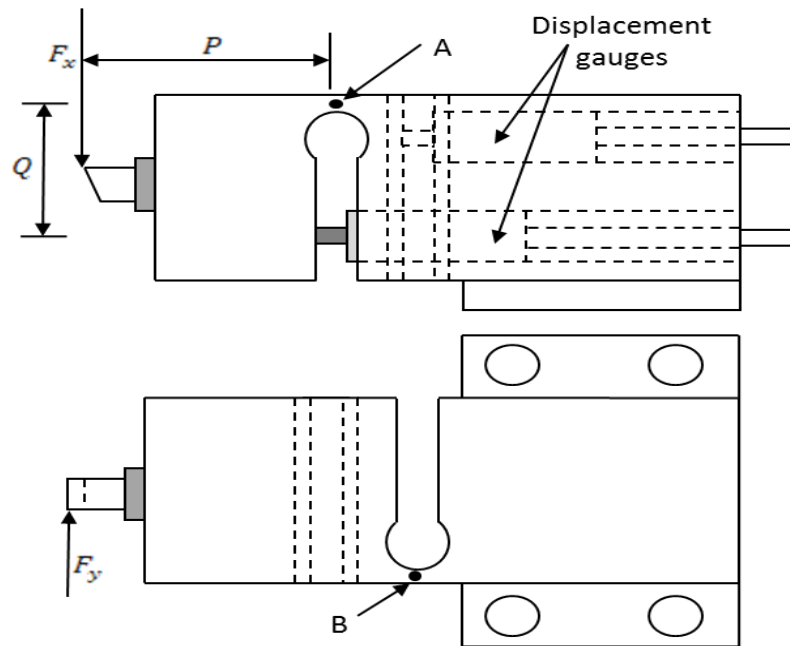


Figure 2-14: Two channel slotted displacement dynamometer [19]

$$\bar{r}_d = \frac{D}{P_T}, \tag{2 - 30}$$

where  $r_d$  is the displacement ratio, representing the efficiency of the dynamometer,  $D$  is the displacement measure by the gauge and  $P_T$  is the displacement of the tool.

There are a lot of customized designs available in the literature for cutting force measurement using the same principle of displacement of the tool. However, the basic approach was the same.

### 2.3.2. Strain Measurement Based Dynamometer

In this type of dynamometer, the resulting deflection was measured by using strain gauges, mounted on the transducers. The strain gauges were mounted on the transducer at specific locations by using recommended epoxy for the strain gauges. The deflection of the transducer was measured with strain gauges, and the resultant forces were calculated based on calibration for dynamometers. Various designs are available in the literature [75, 77-79]. The common types of turning dynamometers used by various researchers in the past are shown in Figure 2-15 and Figure 2-16. The strain gauges mounted on the transducer measured cutting forces in term of deflection. This strain based dynamometers measured deflection of the rings designed on thin and thick ring theories to measure the cutting forces.

### 2.3.3. Piezoelectric Dynamometer

The crystalline, anisotropic piezoelectric materials quartz was used as transducers in the piezoelectric dynamometers. This effect was introduced in 1880, by Curie brothers. The principle of piezoelectric was based on the production of electric charge on the piezoelectric materials with the application of mechanical load. Circular disk of quartz material sensitive to the either pressure or shear, depending on the position, is cut out of the crystal as shown in Figure 2-17.

The basic principle of this type of dynamometer is different from those discussed in previous sections. The piezoelectric dynamometers are more stiff, wide measuring range, compact design and accurate measurement when compared to the displacement and strain gauge based dynamometers [80]. In piezoelectric turning dynamometer, the two peizo-ceramic quartz material measuring  $F_x$  and  $F_y$ , are mounted in such a way that their shear sensitive axis are perpendicular to each other. The third ring is mounted in a separate casing and measuring the  $Z$  -component of force ( $F_z$ ).

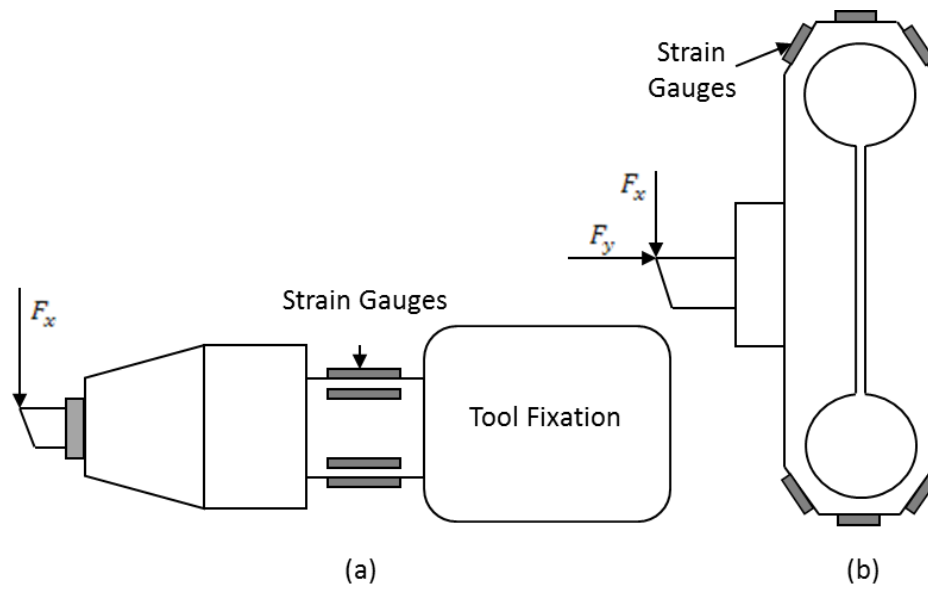


Figure 2-15: (a) Two channel dynamometer with circular transducer; (b) Two component dynamometer with orthogonal transducer [19]

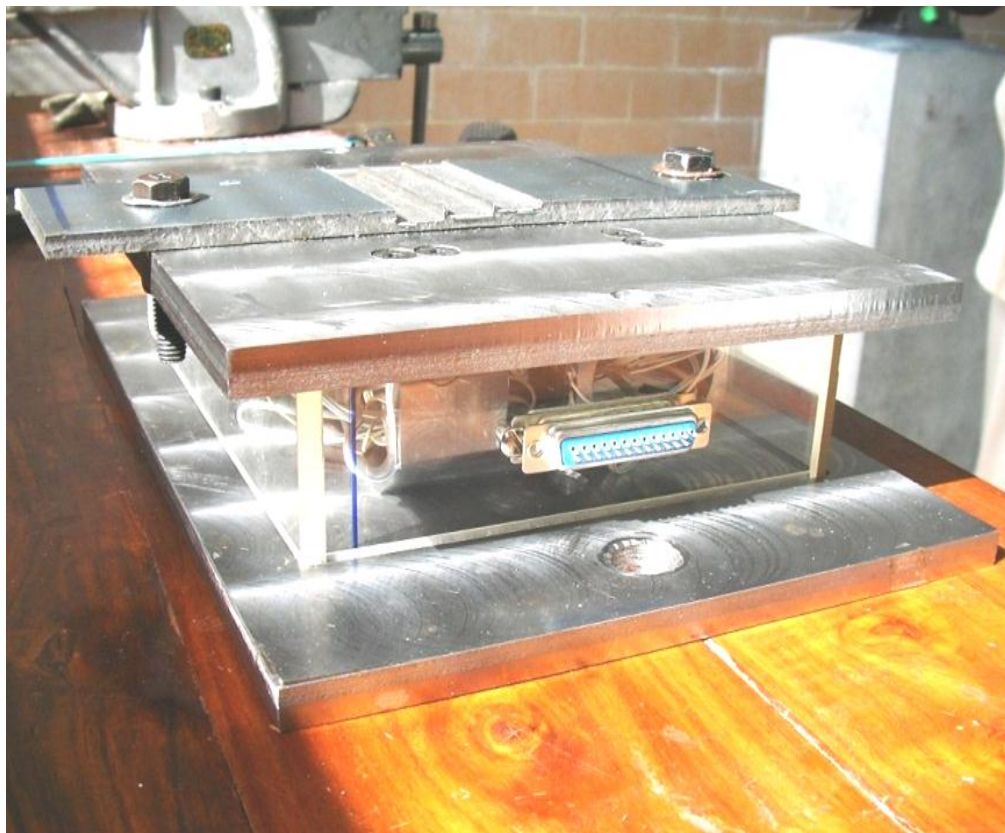


Figure 2-16: Three component dynamometer with hexagonal transducer [75, 81, 82]

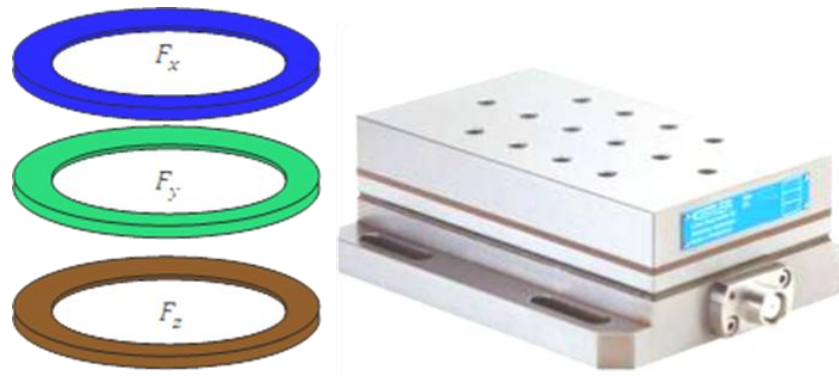


Figure 2-17: Kistler dynamometer and piezoelectric ring used in dynamometer

The piezoelectric dynamometer is extensively used for force measurement in cutting operations. Therefore, in the current study, a Kistler dynamometer was used to measure the cutting forces in all experiments.

## 2.4 Temperature Measurement in the Turning Process

Measuring the process zone temperature and heat prediction in the turning process is very complicated due to complex tool-workpiece-interaction. Considerable attention has been given to temperature measurement in machining processes by researchers in the past. Several analytical and numerical models have been developed based on different simplifying assumptions, which affect the accuracy of those models. In this section, numerous methods for measuring temperature near the cutting tool edge are briefly studied and associated.

Various methods were used in the literature to measure temperature in the process zone in machining operations. Stephenson and Ali [83] have used the tool-work thermocouple technique to measure temperature of the process zone in grey cast iron. In this technique, the tool-workpiece contact area will form a hot junction whereas the tool or workpiece will form a cold junction to produce electromotive force. Later on, the same principle was used to measure temperature of the process zone by Alveild [84] and Lezanski *et al*, [85]. However, the same technique gives us mean temperature values for tool-workpiece interaction zone for a small interval of time.

A well-known technique called embedded thermocouple was also used to measure temperature of the process zone. In this technique the thermocouple was embedded in the

cutting tool or in the workpiece material to measure temperature of the process zone. In the first case, the thermocouple was embedded into the coolant-hole or in the grooves made in tool to monitor the temperature of the tool-work interaction zone. In the second method, a series of thermocouples are embedded in a series of holes close to the cutting edge to monitor temperature of the process zone. The embedded thermocouple was used by Kitagawa *et al*, [86] for temperature measurement in the milling operation. Recently, Muhammad *et al* [81, 87] used the same principle to measure temperature of the process zone in the drilling process of mild steel. The main limitation of this process is a decline in tool strength due to material removal and small distance between the thermocouple and the process zone that gives a predicted temperature of the tool-workpiece interaction zone.

Another important technique for temperature measurement in the process zone was based on metallurgy of a machined specimen called metallographic technique. In this technique; the temperature in the process zone was predicted from the microstructure analysis of the machined specimen. The metallographic pictures were compared with the calibrated curves to obtain the process zone temperature. Typically the accuracy of the temperatures measured by this method was in the range of  $\pm 25^{\circ}\text{C}$  [88]. Therefore, its accuracy was limited. This method cannot be used to record the temperature field in the cutting tool as a function of time [88]. Secondly, this technique was very time consuming and costly.

Additionally, temperature distribution in the rake face of the tool was measured with the help of fine powder, distributed on the rake face of a tool. The amount of temperature was estimated from the melted and un-melted powder in the rake face of a tool [89].

A non-contacting thermo-graphic method, called the radiation technique was used in machining for tool-workpiece temperature prediction. In radiation technique, the surface temperature of a specimen was measured, based on the emitted thermal energy [90]. This technique was used for the measurement of temperature field as well as for a point temperature of the process zone. The radiation technique has many advantages including: no physical contact, fast response and no effects on machined materials. However, the measurement position has to be selected carefully as the accuracy may be significantly affected by chip obstruction. Chip obstruction also makes it difficult to measure the

temperature at the tool-chip interface. In addition, the exact surface emissivity should be known as it strongly affects the measured temperature.

Therefore, the infra-red pyrometer was used to measure temperature of the tool-workpiece interface for ceramics tool by Lin, *et al.*[91]. The infra-red thermal camera is the latest equipment, broadly used in recent time in thermal analysis of machining processes for different tool and workpiece materials [92].

## 2.5 Summary

A brief overview of basic concepts of machining processes was presented in the chapter. The various techniques used in literature to measure the cutting forces as well as the temperature of the process zone were discussed in details. In addition to that, the various analytical models available in the literature for the cutting force predictions were over-viewed. The chapter gives a good understanding of the basic concept used in turning of hard to cut alloys. Various analytical and experimental procedure used in literature for cutting force analysis and temperature measurement were discussed. Based on available literature, experimental and numerical procedures were selected for the analysis of conventional and assisted turning processes of Ti-15333 for cutting forces and temperature in the process zone.

A brief overview of various assisted turning processes used for the machining of hard-to-cut materials is presented in the subsequent chapter. Furthermore, the various finite-element (FE) models developed for different machining processes are discussed in details.

## CHAPTER-3

# A Review of Experimental and Computational Methods Used for Conventional and Assisted Machining Processes

### 3.1. Introduction

In the 20<sup>th</sup> century, cost reduction and product quality have become progressively vital in production industries, when attempting to be competitive in the market. In this circumstance, the manufacturing process plays a key role because it dictates the functional performance and service-life of a machined structure. Selection of appropriate machining operation has a critical consideration in product quality and lifetime.

With the technological advancements continuing in manufacturing industries, turning still remains the most important process used to shape most metals, alloys, polymers and composites. Most of the shapes used in engineering structures are produced by machining and, in terms of size, components from watch parts to aircraft wing parts and ship propeller shafts are machined. Over US \$100 billion is annually spent on finishing processes of metal parts using various machining operations, particularly in turning, milling and boring. Furthermore, it is well known that 10 percent of the produced material goes to waste by the machining industry. This process can be made more economical by using better machining conditions and tools.

In the past, various machining approaches have been used to improve the machinability of high strength alloys. The main aim of those processes was to reduce the expensive post-machining operations in order to improve the final characteristics of the machined product.

In recent decades, the use of titanium alloys has grown considerably, especially in the aeronautic, aerospace, sporting and automotive industries. Titanium alloys are well suited for design applications in which high-strength, good corrosive resistance and low weight is

required. The research activities of titanium machining are going through a transition phase where new machining techniques are introduced to assist its material removal from a finished product.

Up to date, the prime motivation in machining process is to produce economical engineering parts. Most of the material used in aerospace, nuclear and off-shore industries has high tensile strength and wear resistant properties which are difficult to machine. In the machining of hard-to-cut material, the cutting tools encounter extreme mechanical and thermal loads due to high-strength and low thermal conductivity, respectively.

Therefore, many new machining techniques were introduced with the use of:

- Optimization of the cutting tool geometry [93, 94]
- Appropriate cooling methods [5, 95]
- Application of heat source to the workpiece [96-100]
- Superposition of low-energy vibrations on the cutting tool [8, 10-12, 101-106]
- Cryogenic cutting [30, 107-111]

In addition to that, various modelling approaches were used to understand the tool workpiece interaction zone in the turning process. The finite-element is a powerful numerical modelling approach that can provide valuable insight into the behaviour of metal cutting processes. This approach becomes imperative especially in new hybrid and hard-to-cut materials machining paradigms to avoid costly and time consuming experimental methods.

In this chapter, an overview of these processes is given in a summarized form:

### **3.2. Ultrasonically Assisted Turning**

Ultrasonically assisted turning (UAT) is an advanced machining technique in which vibration an excess of 20 KHz is superimposed on the cutting tool. This machining technique results in multi-fold decrease in cutting forces with a concomitant improvement in surface finish in the processing of modern alloys. UAT is an advanced machining process, which has shown several advantages especially in the machining of high strength engineering materials [4, 7, 112]. In

UAT, critical machining parameters are the vibro-impact interaction parameters, namely the frequency, and amplitude of vibration during the machining process.

Therefore, ultrasonically assisted vibration can be superimposed on a cutting tool in the processing of modern alloys to improve its machinability. Table 3-1 listed a brief overview of historical development in UAT. Ultrasonically assisted vibration was first time introduced in cutting operation in late 1960s by Skeleton [31]. Vibrations on the tool was superimposed with the help of a hydraulic vibrator where Oil at 1000 psi was pumped and injected into a device to vibrate the cutting tool at a frequency of 50-125 Hz. Vibrations in tangential and radial direction were used in the study to analyse the cutting forces. A significant reduction in the cutting forces was observed with the introduction of vibration on the cutting tool. However, the reduction in cutting forces was limited to very low cutting speeds.

Table 3-1: A brief overview of UAT

References	Material	Parameter				Coolant
		Vibrational parameters		Cutting parameters		
		Frequency, $f$ (kHz)	Amplitude, $a$ ( $\mu\text{m}$ )	Cutting speed, $V$ , m/min	Depth of cut, $a_p$ , mm	
Skelton. R.C, 1968 [31]	Mild steel	0.05-0.125	0.1016	137-166	0.762	No
Weber. H, <i>et al</i> , 1984 [113]	Steel-C60 Glass ceramics XSCrNiMo18	20	a = 8-12 b = 8-12	0-420	0.1	No
Moriwaka. T, <i>et al</i> , 1991 [114]	Stainless steel- SUS303Se	40	3	1.4-4.2	0.0023	Mineral oil
Kim. D. J, <i>et al</i> , 1993 [115]	CFRP	19.5	15	19-165	0.05-0.3	No
Shamoto. E, <i>et al</i> , 1994 [106]	Copper	0-0.006	a = 5	0.26	0.01	No

			b = 5			
Moriwaka. T, <i>et al</i> , 1995 [116]	Oxygen free-Copper	20	a = 0-8 b = 11-16	5	0.005	No
Kim. D. J, <i>et al</i> , 1997 [117]	CR-39	20	26.4	0-89.4	0.1	No info.
Shamoto. E, <i>et al</i> , 1999 [118]	Steel-SUS-420J2	20	a = 4.5 b = 4.5	3.4	.01	No
Jin. M, <i>et al</i> , 2001	S45C; SUS304; SUS440B; SCM435	21	20	7.9-28	0.05-1	Dry or mineral oil
Liu.C. S, <i>et al</i> , 2002 [119]	Particle reinforced metal matrix composite SiCp/Al	20	15	4.24-12.72	0.1-0.5	No
Xiao. M, <i>et al</i> , 2002 [120]	S45C steel	20	15	58	0.05	
Gao. G.F, <i>et al</i> , 2002 [121]		19.46	15	5.4-44	0.1	Kerosene
Zhou. M, <i>et al</i> , 2002 [120]	Fused silica	40	3	1.1-4.44	0.0004-0.002	No info.
Zhou. M, <i>et al</i> , 2003 [122]	Stainless steel type 304	40	3.6	4.7	0.02	Oil mist
Suzuki. N, <i>et al</i> , 2003 [123]	JIS: SUS420J2	19.6	3-6	0.25-0.7	0.001-0.005	No
Babitsky, V.I, <i>et al</i> , 2004 [124]	Inconel-718	20	15	17	0.8	No
Mitrofinov. A.V, <i>et al</i> , 2004 [9]	Inconel 718	20	15	18.6	0.4	--
Ma. C, <i>et al</i> , 2004 [125]	Al-52S	18.76	a = 4 b = 4	15.75	0.05	No Info.
Mitrofinov. A.V,	Inconel 718	20	13	18.6	1	--

<i>et al</i> , 2005 [126]						
Mitrofinov. A.V, <i>et al</i> , 2005 [112]	Inconel 718	20	7.5	18.6	0.4	--
Shamoto. E, <i>et al</i> , 2005 [127]	JIS: SUS420J2; JIS: NAK80	34.4	a = 8;6 b = 8;6 c = 4;3	1-1.27	0.003	Oil mist
Ma. C, <i>et al</i> , 2005 [128]	Al-52S	18.66	a = 3.5 b = 3.5	3.94-18.93	0.05	
Zhong. W.Z, <i>et al</i> , 2005 [129]	Aluminium-based metal matrix composites	20	23	1.5-3	1-3	No
Ahmed. N, <i>et al</i> , 2006 [130]	Inconel 718	20	15	18.6	0.4	No
Ahmed. N, <i>et al</i> , 2006 [8]	Inconel 718	20	30	38	0.1	No
Ahmed. N, <i>et al</i> , 2007 [7]	Inconel 718	20	15	18.6	0.4	No
Ahmed. N, <i>et al</i> , 2007 [4]	Inconel 718	20	15	5	0.1-0.4	No
Zhang. X, <i>et al</i> , 2011 [131]	Stavax	38	a = 4 b = 2 c = 2	1.414-4.241	0.002-0.01	Air
Nategh. M.J, <i>et al</i> , 2012 [69]	----	20	6-16	31.8-126	1-2	No
Razavi. H, <i>et al</i> , 2012 [68]	----	20	6-16	31.8-126	1-2	No
Razavi. H, <i>et al</i> , 2012 [67]	Aluminium 6061	20	6-16	31.8-126	1-2	No

Moreover, Webler *et al* [113] investigated machining of glass ceramic, XSCrNiMo18 and C60 steel material in the presence of ultrasonic vibration on the cutting tool. An ultrasonic transducer was used, producing vibrations with a frequency of 20 kHz and amplitude of 8-12  $\mu\text{m}$ . A significant reduction in tool wear was observed in the machining of glass ceramic as well as multi-fold increase in the tool life. The prime reason for longer tool life is reduction in cutting forces and removal of powder chips on the rake face of a tool, increases removal of heat from the tool and hence, increase in tool life. Moreover, in machining of C60 steel and XSCrNiMo18, a reduction in build-up edge formation was noted that improved surface roughness of a machined workpiece. No force reduction in UAT was discussed in that work.

Most of the work on UAT was performed in the 1990s by a team in Kobe University, Japan [106, 114, 116, 118, 132]. They developed a wide range of transducers producing one-dimensional vibrations to be superimposed on the cutting tool. The piezo-ceramic rings were used in transducers to produce the required vibration. A significant reduction in the cutting forces was observed with the introduction of vibrations on the cutting tool in machining of various types of materials using diamond tools. A considerable improvement in surface roughness of the machined workpiece was also observed. Similarly, most of their work was limited to experimentation; no other methods were used to verify the results. Additionally, surface roughness analysis was made on the basis of the built up edges formation; and no surface roughness analysis was carried out to validate the claim.

Furthermore, a two dimensional elliptical vibrations were superimposed on the cutting tool in the cutting direction and the feed direction to investigate its effect on copper machining [106, 116]. The piezo-ceramics rings were mounted in such a position to gives elliptical vibration to the cutting tool. The movement of the tools was governed by the following equations.

$$x(t) = a \cos(2\pi ft), \quad (3-1)$$

$$y(t) = \bar{b} \cos(2\pi ft + \varphi_y), \quad (3-2)$$

Where  $a, \bar{b}, f, t$  and  $\varphi_y$  are horizontal amplitude, vertical amplitude, frequency, time and phase difference, respectively.

The elliptical vibration, concept was later on extended to three-dimension elliptical vibrations to investigate its effects on cutting forces and surface roughness in the turning process by using specially designed transducers. The transducers were capable of imposing vibrations in all the three directions resulting three dimensional elliptical tool movements in cutting. The movement of the tool in the third direction was governed by the following equation.

$$y(t) = \bar{c} \cos(2\pi ft + \varphi_y + \varphi_z), \quad (3-3)$$

Where  $\bar{c}$  and  $\varphi_z$  are vibrational amplitude and phase difference in axial direction, respectively. A significant reduction in cutting forces and considerable, improvement in surface roughness was observed in elliptical vibration assisted turning.

Recently, research using uni-directional vibrational assisted machining has still continued. Kim and Choi [117] have used ultrasonically assisted turning for the mirror surface machining of ferrite, glass and optical plastics. UAT has shown significant improvement in mirror shape surfaces compared to CT. Furthermore, ultrasonic vibration was used to suppress tool chatter in the machining of low carbon steel [120]. A significant reduction in in tool chatter was observed when compared to CT, resulting in better surface finish.

Furthermore, Liu *et al* [119] superimposed ultrasonic vibrations on the cutting tool in turning of SiCp/Al composites material. A significant reduction in cutting forces and considerable improvement in surface roughness was observed. Therefore, based on the experimentations of composite materials, UAT can be a useful alternative for precision manufacturing of parts.

A team from Loughborough University [4, 7-10, 112, 124, 126, 130, 133-137] have been working on ultrasonically assisted turning of modern alloys. The group has already developed a state-of-art experimental setup for UAT. Piezo-ceramic material was used in the transducer to produce the required level of vibrations. The system is capable of producing vibrations with 20 kHz and amplitude of 8  $\mu\text{m}$ -30  $\mu\text{m}$ . The experimental setup is in fully functional form and has produced results with a good repeatability. A multi-fold improvement in the surface roughness of the machined surface was reported with the introduction of vibration on the cutting tool [7]. The effect of various vibration parameters, i.e amplitude and frequency of vibrations, on the cutting forces is also reported for various cutting conditions. The system is

capable of producing a significant reduction in cutting forces for a high depth of cut and can be used for high speeds of up to 60 m/min, which are the main advantage of the systems when compared to the previously developed system.

Most recently, an analytical model was developed to analyse the cutting forces in oblique ultrasonically assisted turning [67-69]. The model was validated with experimental results and good agreement between experiments and analytical results were achieved.

To sum up the above discussion, in all simulation work, only one component of cutting force (tangential component of cutting force) was considered in the analysis, ignoring the other two components of cutting forces. Though, that all experiments were carried out for the oblique turning processes and were compared with orthogonal turning to get a good comparisons. The previous study was limited to a few high strength materials, ceramics and composites. Therefore, there is still a need to investigate the effect of UAT on other high strength alloys like titanium alloys and carry out a parametric analysis of this machining technique at various speeds-feed combinations. In addition to that, researchers have used various other assisted machining techniques to improve machinability of hard-to-cut materials. Hot machining is one of the prominent and well known techniques used to improve machinability of hard-to-cut materials. In the subsequent section, a brief overview of the historical development made in hot machining will be discussed below in section 3.3.

### 3.3. Hot Machining

The shear-strength of high-strength materials decreases with an increase in temperature, due to thermal softening. Therefore, hot machining becomes a possibility to cut those high-strength materials with minimal cutting forces on the cutting tool. In hot machining, external heat was used to soften the workpiece material prior to machining, to alleviate the material removal from a machined specimen [18, 96, 100, 138]. Various types of heat sources were used for thermal softening of workpiece materials in hot machining. However, the prime aim was to supply sufficient energy to the workpiece materials to improve the material removal during machining processes of hard-to-cut materials. In this section, hot machining used by various researchers for machining of different materials is discussed in detail;

The oxy-acetylene torch was used by Pal and Basu [100] to heat up the workpiece in shaping of austenitic manganese steel. The strain hardening properties of the studied alloys were investigated through a customize design Rockwell's hardness machine at elevated temperature and it was concluded that the hardness of the machine workpiece reduces with an increase in temperature, as expected. The required surface temperature of the workpiece was achieved in two steps: First, workpiece was pre-heated to a temperature just below a required temperature, followed by adjustment of the flame-torch position, in such a way, to acquire the desired surface temperature in one pass. The surface temperature of the pre-heated workpiece was measured through Tempil-sticks. Based on those experimental observations, the authors derived the following empirical relationships for the cutting force and tool life based on the cutting parameters like cutting speed, depth of cut and feed rate:

$$F_c = C_c S_z^\alpha a_p^\beta, \quad (3-4)$$

$$F_t = C_t S_z^\alpha a_p^\delta, \quad (3-5)$$

$$T_l = 0.636V^{2.06}, \quad (3-6)$$

where  $F_c$  and  $F_t$  are the cutting and thrust force, respectively;  $S_z$  is feed per stroke;  $a_p$  is the depth of cut;  $T$  is the tool life;  $V$  is the cutting speed,  $\alpha$  is the rake angle,  $\beta$  is the friction angle and  $C$  is a constant of machining.

Based on experimental and empirical observation, the cutting forces are independent of the cutting speed in hot machining. Hence, the austenitic manganese alloy can be machined at elevated temperature and at high cutting speed to improve its machinability.

Later on, the flame-torch heating was extended to turning experiments, using the same workpiece material (austenitic manganese steel ) by Ozler *et al* in 2001 [139]. The torch was mounted on the lathe at a fixed distance. A better mechanism was used to control the amount of heat supplied to the workpiece by adjusting a suitable combination of pressure and flow rate of the gases. An Infra-red thermometer was used to monitor surface temperature of the workpiece. A significant improvement in tool life was observed in hot machining when compared to CT.

Furthermore, the authors used factorial regression method to derive an equation for the tool life in hot machining and to validate the experimental results. Taylor's equation 3 – 4 was used to derive an empirical relation for the tool life.

$$C = T_l^\alpha V^\beta f_r^\gamma T^\tau a_p^\varphi, \quad (3 - 7)$$

where  $V$  is the cutting speed (m/min) ,  $f_r$  is the feed rate (mm/rev) ,  $a_p$  is the depth of cut (mm),  $T$  is the workpiece temperature (°C),  $T_l$  is the tool life and  $\alpha, \beta, \gamma, \tau$  and  $\varphi$  are the constants and depend on the tool-workpiece pair.

Rearranging the equation 3 – 7:

$$T_l = K_a V^{b_1} f_r^{b_2} T^{b_3} a_p^{b_4}, \quad (3 - 8)$$

where  $K_a, b_1, b_2, b_3$  and  $b_4$  are the constant. By applying the multiple linear regressions give the following equation;

$$\{a\} = \left[ [Z^{T_l} [Z]]^{-1} \right] [Z]^{T_l} \{Y\}, \quad (3 - 9)$$

where  $a, Z$  and  $Y$  were the correlation co-efficiencies. A program was developed in Matlab To calculate the regression and correlation coefficient. After calculating the coefficient and putting to the governing equation the following relation were derived.

$$T_l = \frac{12.9978V^{-0.9632-0.0947.\log V-0.0238.\log f_r+0.0059.\log T} \cdot T^{4.7687-0.3218.\log T-0.1853.\log V+0.038.\log a_p}}{f_r^{1.3062+0.2449.\log f_r-0.023.\log T} \cdot a_p^{-0.1989-0.0907.\log a_p-0.0258.\log f_r}}, \quad (3 - 10)$$

This empirical relation was used to calculate the tool life at various cutting parameters. The analytical results validated the experimental results.

Moreover, Maity and Swain [140], further extended the work of [100, 139], and carried out an experimental and analytical investigation of hot machining of manganese steel using carbide cutting insert . These authors investigated surface roughness and coefficient of chip thickness additionally, with the tool wear, at elevated temperature. A more precise temperature control sensor, thermocouple with a digital indicator was used to measure the surface temperature of the workpiece. A considerable reduction in cutting forces and improvement in tool life was observed in hot machining when compared to CT.

In addition to that, flame torch was also used to improve the machinability of ceramic material in the CT process [26]. A significant improvement in surface roughness was observed in hot machining. However, a rise in cutting forces was observed with the application of heat to ceramic materials.

The flame-torch, is a simple way to apply heat to a workpiece material; however, in literature, researchers have used other sources of heat as well in hot machining. The following paragraphs describe other heating techniques used in hot machining.

In 1975, direct current (DC) was used as a heat source in the hot machining of steel by Chen and Lo [141], to investigate the dependency of tool life on cutting parameters, tool materials and heating current. In this technique, the electric current passing from a workpiece to a cutting tool, generate heat at tool-tip-workpiece-interface in case of positive polarity. Four types of cutting tools of Coromant Grade S1P, S2, S4 and S6 were used in experimentation. The dependency of cutting speed and heating current as well as polarity and tool material was expressed against a ratio of hot machining tool life to the conventional machine tool life ( $L_h/L_c$ ). It was concluded that  $L_h/L_c$  decreased with the increase in the cutting speed and the possible reason for that was the faster heat removal from tool in the form of chips.

Two years later, Kainth and Chaturvedi [142] investigated the tool-chip-interface temperature analytically and experimentally using DC as a heat source in hot machining. In the analysis, resistance of the workpiece and tool was neglected whereas, the material between the rake face and shear plane is divided into small segments of non-uniform thickness in the model. The summation of chip material's resistance ( $R_c$ ), contact resistance at the chip - tool interface ( $R_t$ ) and spreading resistance at the shear plane ( $R_s$ ) was considered. After deriving the analytical formulation, the following relation was derived to calculate the temperature of the tool

$$R_I = R_c + R_t + R_s, \quad (3 - 11)$$

$$R_c = \frac{\rho_{ca}\theta(\gamma+1)\ln(\gamma)}{2w(\gamma-1)S}, \quad (3 - 12)$$

$$R_t = \frac{1}{4\sqrt{\left(\frac{lw}{\pi}\right)}}(\rho_t + \rho_c), \quad (3 - 13)$$

$$R_s = \frac{S}{4\sqrt{t_1 w / (\pi \sin \varphi)}}, \quad (3 - 14)$$

Where  $\theta$  is the angle between the tool face and shear plane,  $\rho_{ca}$  is the specific electrical resistance of workpiece material at average temperature rise at shear plane and chip-tool-interface,  $\gamma$  is the ratio of shear-plane length to chip-tool contact length,  $w$  is the width of cut,  $S = \sum_{i=m+1}^{i=n} \left( \frac{2}{2i-1} \right)$ ,  $l$  is the chip-tool contact length,  $\rho_t$  is the specific electrical resistance of tool material at tool-chip-interface temperature,  $\rho_c$  is the specific electrical resistance of the workpiece material,  $t_1$  is the uncut chip thickness and  $\varphi$  is the shear-plane angle.

The above relations were used in the temperature relation outlined in [143] to calculate the temperature of the cutting region in hot machining.

Additionally, the theoretical model was validated by using a series of experiments on En-24 steel at a heating current of 200 Ampere. A specially designed thermocouple was used to measure the temperature of the tool-chip-interface. It was concluded from the model that the temperature of the tool-chip-interface increases with the increase in the cutting speed above 26.4 m/min. Similarly, a rise in the electrical resistance between the tool and workpiece was observed with the rise in cutting speed.

Furthermore, in [144], carbide tools were used to increase the tool life and critical velocity in DC hot machining. Experiments were carried out on stainless steel and chilled cast iron to improve cutting speed in DC hot machining. With the introduction of carbide cutting tool, the critical velocity was increased to 7 times when compared to the uncoated tool.

However, the same technique can be very useful in hot drilling because it heated up the region at the tool-tip-interface. The authors used the DC techniques in hot drilling experiments and achieved significant improvement in the process parameters and tool life.

The DC current as heat source can be used to heat up the workpiece to the required temperature; however, this method of heating is limited to low cutting speeds. In the subsequent paragraphs, a brief review of plasma arc as a heating source in hot machining are presented.

Hinds and Almeida used a localized heat source (plasma gun) to investigate the efficiency of the heat source in hot machining [145]. A thermal model was developed for plasma arc moving at a constant velocity, to analyse its effects on the surface layer of the finished workpiece. A special chromel-alumel thermocouple was used to measure the heat intensity of the plasma arc, and radial axi-symmetrically heat-source density was observed. An implicit finite difference method was applied to a super-Gaussian equation for a heat source to predict the temperature of the cut section:

$$q_r = \exp(A - Br^2 + Cr^4 - Dr^6 + \dots), \quad (3 - 15)$$

where  $A$ ,  $B$ ,  $C$  and  $D$  are the constants so that can be determined with a curve fitting technique.

The model was applied to orthogonal cutting as well as to oblique cutting to predict the heat effect of the cut section. It was concluded that the position of the plasma torch affects temperature field of the cutting region in hot machining. Therefore, the model can be used to predict the accurate position of the plasma torch for more efficient results or to minimize the sub-surface damage in hot machining.

Later on, Madhavulu and Ahmed [98] used plasma arc as a heat source in the economical analysis of hot machining of hard-to-cut materials. The surface temperature was controlled by adjusting a distance between the workpiece and the plasma torch. The experiments were carried out on SS 410 and alloy steel at various temperatures and cutting conditions and the reduction in power consumption was calculated in hot machining when compared to the conventional machining. In the former, material removal rate increased 1.8 times when compared to the latter.

A more advanced analysis of the plasma-enhanced machining of modern alloy was presented in [146]. A numerical analysis for the temperature prediction on the workpiece surface was carried out for various cutting parameters, and the results were then verified experimentally by using an in-built experimental setup. A finite difference method was used for temperature calculation considering three modes of heat transfer i. e. Conduction, convection and radiation:

$$\frac{k\partial}{r\partial r}\left(r\frac{\partial T}{\partial r}\right) + \frac{k\partial^2 T}{r^2\partial\varphi^2} + k\frac{\partial^2 T}{\partial z^2} + \rho C V_z \frac{\partial T}{\partial z} + \frac{1}{r}\rho C_p V_\varphi \frac{\partial T}{\partial\varphi} = 0, \quad (3-16)$$

The temperature along the circumference of the workpiece was calculated both numerically and experimentally by varying the cutting speed and current. It was concluded that surface temperature is directly proportional to the current supplied and inversely proportional to the cutting speed. Similarly, the depth of heat source for various cutting condition was also analysed to investigate an optimum current-velocity combination for a required depth of cut.

Furthermore, experiments were carried out to calculate the cutting forces, surface roughness of the machined workpiece and tool wear of the cutting tool. Wide ranges of temperature were used to calculate the cutting forces in the machining of Inconel 718. The maximum reduction of 30% was observed at 700°C. Similarly, the surface roughness of a machined surface reduces by 40% with an increase of surface temperature to 600°C in plasma-enhanced machining at various cutting speeds. That type of machining also increased the material removal rate in the processing of modern alloys. The overall work was a good attempt to analyse the processing of modern alloys with a hot machining technique. However, the re-crystallization temperature of Ni-based alloys is about 800°C. The author did not mention anything about the grain structure changes, which can occur at elevated temperature in Inconel 718.

Plasma arc can be used effectively in hot machining but the plasma arc can heat the workpiece and can cause overheating of materials causing problems in the machined workpiece. Furthermore, overheating of Ti alloys above the recrystallization temperature causes oxidation and burning of Ti alloys which are the main hindrance of hot machining of titanium alloys.

Similarly, another localized heat source used in hot machining for workpiece materials is laser. The next paragraph describes the work related to laser heating in machining.

A S51 1.5 kW CO2 laser system, was used in laser assisted turning and dressing of vitrified CBN grinding wheels with a conventional single point cutting tool by Zhang and Shin [147]. The application of laser heat to the workpiece material improves the economy of the process as well as reduction in tool wear was observed. Furthermore, the efficiency of the laser

assisted turning process was five times better than the conventional counterpart whereas maintaining the same level of accuracy.

Furthermore, high-power diode lasers (CO<sub>2</sub> and Nd-YAG) has been used in laser assisted turning of fully hardened AISI D2 tool steel, a material that is difficult-to-machined, by Dumitrescu, P *et al*, [148]. Individual diode lasers have limitations on their output power due to its size effect. Depending on the total power and beam quality required, high-power diode lasers therefore constitute several diode laser stacks comprising a number of diodes. A significant improvement in tool life, reduction in cutting forces and improvement in surface roughness was reported in laser assisted turning of AISI D2 steel.

Sun *et al* [149] investigated the laser assisted machining (LAM) of Ti alloys to investigate the effect of heating on cutting forces and a chip shape. A 2.5 kW Nd:YAG laser was used to heat up the workpiece. Beam with various power of the laser gun were used to analyse its effect on the cutting forces. A significant reduction in cutting forces was observed in LAM of Ti alloys. The effects of laser power distance between the laser gun and the tool and a distance between the lens and workpiece was investigated experimentally, and it was concluded that the reduction in cutting forces increases with the increase of laser beam power and decreased with the increase in the distance between the laser beam and tool. No changes in grain structure of the machined workpiece were observed.

Recently, Laser was used broadly in hot machining to heat up region in front of the cutting edge in the processing of high-strength alloys. A reduction in cutting forces and effects of heat on the materials was reported by [149]. Furthermore, the effect of laser heating on chip formation [150] followed by the thermal modelling of the heat affected zone [151] and economic analysis [152] of the laser assisted machining was carried out using, laser as a heat source.

The laser and plasma arcs are the most effective sources of localized heating used in hot machining. However, the capital cost and low efficiency (low absorption of energy by metallic surfaces) of laser and plasma arc are the main obstacle in the application of laser and plasma in hot machining. Furthermore, high human skill and closed environment are required in laser assisted turning.

An inductive heating mechanism was also used in hot machining to investigate machining cost and manufacturing time in the machining of AISI D2 hardened steel by [99]. Furthermore, the chatter of tool in end milling of AISI D2 steel was investigated in a vertical machining centre using inductive bulk-heating technique [153].

In literature, new machining techniques were introduced called hybrid machining techniques, in which two or more than two machining techniques are combined to take collective advantages of the two processes. The next section described the available hybrid turning techniques used for the machining of hard-to-cut materials.

### 3.4. Hybrid Machining Processes

In hybrid machining technique, two or more than two conventional or unconventional machining techniques are combined to form a new hybrid machining technique. An overview of assisted machining techniques was discussed in the above sections. Various new hybrid machining techniques were introduced by various researchers in the past are discussed in the following paragraph.

Wang *et al* [154] used a new approach to improve machinability of Inconel 718 by introducing both concept of the hot machining and the cryogenic machining together to combine advantages of both processes. Cryogenic coolant was used in machining to reduce the cutting-tool temperature and increase the tool life by reducing the tool wear. On the other hand, plasma-enhanced machining was used to reduce shear-strength of the workpiece in order to increase the material removal rate in machining of hard-to-cut materials. Those two non-traditional techniques were joined together to get a new machining technique called *hybrid machining*. Results of hybrid machining were compared with those of both conventional machining and plasma-enhanced machining. An increase of 156% and 170% in tool life was observed in hybrid machining when compared to conventional and plasma enhanced machining, respectively. Similarly, a significant reduction in surface roughness was observed in hybrid machining. The reason for the reduction in surface roughness was caused by a decrease in workpiece hardness and temperature of the cutting tool by plasma flame and liquid nitrogen, respectively. A noticeable reduction in the cutting forces was observed in hybrid machining. However, the authors did not mention the dependency of tool wear on

temperature and a suitable way to measure the workpiece temperature in plasma-enhanced machining.

Two years later, Dandekar *et al* [1] used laser assisted machining in combination with cryogenic coolant, to investigate the economical benefit of this novel machining techniques in terms of tool life, energy required to remove machining allowance and material removal rate. The workpiece was heated with a 1.5 kW CO<sub>2</sub> coherent Everlase S51 laser gun and the liquid nitrogen was used to remove heat from the cutting edge of a cutting tool. The amount of heat supplied by a laser was predicted by using a thermal model [155]. Hybrid and laser assisted machining simulations were carried out by using the AdvantEdge finite-element (FE) software package to validate the experimental results. Various temperature levels were used in the FE simulation which were later on used in crater wear rate model [156] to predict the wear rate in the machining of Ti-alloy. Three types of cutting inserts (K68, KC5010 and KC850) were used in experimentation. The crater wear at various temperature levels was analysed at a cutting speed of 107 m/min, and it was concluded that the crater wear is minimum at 250°C. The economic analysis for the above mentioned tool showed that a TiAlN coated tool could cause 30-40% reduction in the overall cost of machining. The scanning electronics microscopy (SEM) of the machined surface was carried out to analyse the effect of pre-heating on microstructure and micro-hardness of the machined workpiece. No discernible difference in the microstructure was observed. The overall work was a good attempt to analyse novel machining techniques both experimentally and numerically.

Several hybrid machining techniques are available for the processing of high-strength alloys with their respective benefit and short-fall. However, there is still a need to investigate the above process in combination with one another to outline the advantages of the above processes.

The work so far presented in the above section was related to experimental analysis of machining processes. The next section described a brief overview of work carried out to analysed machining processes using computational techniques.

### 3.5. Historical Developments in Simulation of Machining Processes

To study and analysed any machining technique, through experimentations is expensive and time consuming when a wide range of parameters is involved, particularly, due to complex disciplines such as contact conditions, friction, plasticity, material non-linearity, heat transfer, lubrication and elasticity are involved. Mathematical simulations are an alternative approach where numerical techniques are used. Among the numerical techniques, Finite-element analysis is one of the most important and frequently used methods in machining processes. The prime aim of the FEA is to develop a parametric model, predicting the response of the material as well as the load on the cutting tool at various cutting conditions.

To date, for accurate and efficient modelling of the machining processes, several finite-element techniques including mesh rezoning, damage model, element separations and material and geometric nonlinear analysis approaches were used. The predictability and validity of the developed FE models were verified by experimental results in many cases [7, 8, 66, 157-159].

In the current section, a brief overview of the published work dealing finite-element analysis of machining processes is presented. The section is organized into three parts. The first section will cover the various techniques used for chip separation in machining processes followed by the available friction models at the tool workpiece interaction-zone. The third section will cover a brief overview of various techniques used to model the cutting tool in FE simulations.

#### 3.5.1. Chip Separation from the Workpiece in Machining Processes

In any machining operation, the separation of chip from the parent material is the most complex phenomena due to large plastic deformation in the tool-workpiece-interaction zone, contact interaction of the chip with tool, friction at the tool rake face and workpiece material. Various techniques were used to separate chips from a parent material. Those include:

Carrol and Strenkowski [160] were the first one to attempt chip formation in the orthogonal turning process in developed computer models. Large updated Lagrangian code was used in

the first model to incorporate elasto-plastic material behaviour. The second model incorporates Eulerian flow behaviour at the vicinity of the tool workpiece and the material passing through the region is considered as viscoplastic. Cutting forces, chip geometry, stress and strain field were determined accurately to have a good agreement with the experimental results. For chip separation from the parent material, an explicit failure criterion was required in the model. On the other hand Eulerian model required good shape element for the modelled material flow. Results obtained from both models showed excellent agreement when compared with measured tool forces for slow cutting speed of aluminium.

Later on, the same approach was used in the modelling of the orthogonal turning of AISI 4340 steel and cutting forces, stresses, chip shape and temperature of the process zone was investigated [161].

In the finite-element (FE) simulation of orthogonal cutting process, a stress-based criteria was used to separate chip from the parent material by Shet and Deng [162]. In the model, a specified distance for the stress-based chip separation was chosen to be equal to one element size (approximately  $50.8 \mu\text{m}$ ). A predefined path was modelled in the FE simulation, with all the nodes bonded to the opposite contact nodes. The chip separation was achieved by de-bonding the nodes in front of the cutting tool when the value of stresses reached to a predefined value. The element above the contact surface moved away from the parent material and formed a chip. Whereas the element below the contact surface moved to the machined surface. The same technique of chip separation was also used in [159, 163]. However, the chip separation criterion was based on the critical distance ( $D$ ) of the tool-tip and workpiece as shown in Figure 3-1.

A plain strain orthogonal turning FE model was developed by Shih and Yang [164]. The chip separation in front of the tool was achieved based on the critical strain value. A prescribed line in front of the tool was used for chip separation and rezoning and adaptive meshing was applied to that line. This technique was capable of adding, refining, combining and deleting element columns on the pre-defined line. The elements and nodal data such as stresses, temperatures were interpolated, deleted, added or translated during mesh rezoning. Although Remeshing and rezoning were introduced in Shih and Yang work, the implementation was still limited to a predefined location.

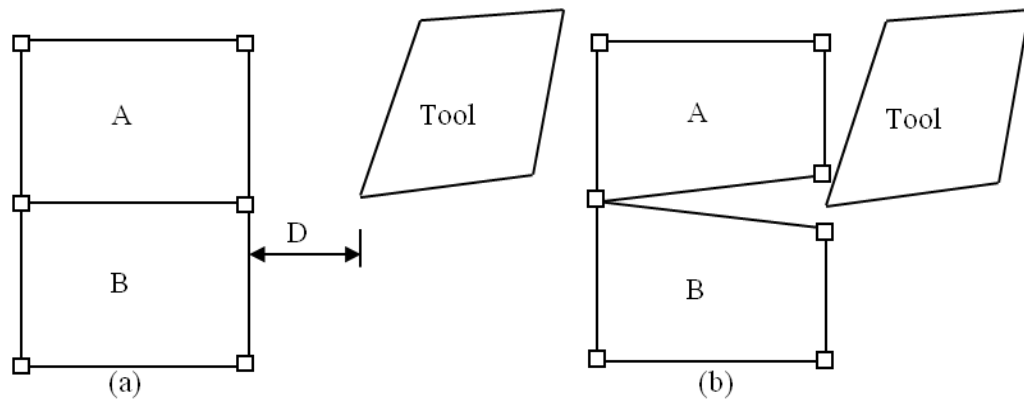


Figure 3-1: Tool-workpiece interaction, (a) before chip formation and (b) after chip formation

[159, 163]

Xie *et al* [165] used the Arbitrary Lagrangian Eulerian (ALE) formulation for the chip separation in finite-element simulation of orthogonal cutting. Commercially available code ABAQUS was used to analyse chip formation, the cutting forces and temperature at the tool tip-workpiece-interface. Lagrangian, Eulerian and Arbitrary Lagrangian Eulerian (ALE) formulation schemes are the well-known methodologies in metal-cutting simulations. However, Lagrangian and ALE approaches are best suited for chip formation in metal-cutting, because, no predetermined separation line is required and the results are independent of the mesh size. Additionally, the mesh is not attached to the material in ALE and thus updates the free chip geometry and avoids excessive distortion. Therefore, ALE was used for the chip formation, with roundup cutting edge tool. A smooth continuous chip separation was achieved with successful implementation of adaptive meshing technique. Moreover, Arrazola and Ozel [166], used the same approach of chip separation to investigate the behaviour of frictional modelling on chip shape, cutting forces and temperature of the process zone.

Another finite-element model was developed for orthogonal cutting of Inconel 718 by Soo *et al* [167]. A strain-rate and temperature dependant workpiece material data were used in the FE model. The material data were achieved with a compression tests on Gleeble-thermomechanical simulator. A user defined subroutine was used to separate chip from the parent material in the developed FE model, based on a shear failure criterion. An equivalent plastic strain (equation 3 – 17) was used as a failure criterion in simulation. A fine mesh was used in the vicinity of the workpiece where the chip was expected to separate from the workpiece, followed by a damage criterion, to delete elements when the damage parameter

exceeded unity. The cutting tool sheared the parent material and gives birth to chip formation. The damage parameter  $w$  was defined as

$$w = \sum \left( \frac{\Delta \varepsilon^{pl}}{\Delta \varepsilon_f^{pl}} \right), \quad (3 - 17)$$

where  $\Delta \varepsilon^{pl}$  is an increment of the equivalent plastic strain and  $\Delta \varepsilon_f^{pl}$  is the strain at failure.

In this methodology, the chip separation was not bound to a predefined line. Additionally, the research extended the application of global remeshing criteria to separate chip, which in earlier attempts, was modelled using pre-defined crack path. Although, the chip separation was achieved, however, some of the elements were not part of the developed chip due to element deletion based on the failure criteria.

In [168], the chip separation was achieved in the FE simulation of the turning process with a control crack propagation technique. A predefined line was used for the chip separation based on plastic strain of a material. Rezoning technique was used to replace the badly distorted element with a consistent one, on the predefined line. Selection of a crack length and time relationship was based on the movement of the cutting tool and a reference point on the machined surface. The need for rezoning was established by monitoring the extent of distortion of elements from the deformed configuration plots. The rezoning was implemented by extracting the current model geometry from the result file. After forming a new mesh, the analysis was continued, using the previous results as new initial conditions. Many rezoning iterations are required to achieve a require convergence in a standard simulation of machining processes. However, in the above described model, rezoning was incorporated based on the tool movement of approximately 0.05 mm into the workpiece. Distributions of strain, strain rate, stress and temperature along the shear zone were presented for machining conditions used in experiments, and the simulation results were in good agreement with experimentations.

Recently, a new method called smooth particle hydrodynamics (SPH), a very promising meshless numerical method for modelling of metal cutting processes was used. The prime aim of the method was to avoid distortion or tangling of the elements at extreme

deformation conditions. Therefore, SPH can be a good alternative to handle large strain and deformation in metal cutting processes. The SPH technique also handles the chip separation from the parent material in a natural way as compared to the ALE based FE model. The particle flows along the rake face of a tool and required no separation criteria. All computational equations are applied on the particles framework.

The SPH method was applied for three dimensional orthogonal turning of AISI H3 steel by [169]. The cutting forces were correctly estimated through a developed orthogonal cutting SPH model. Good agreement between the predicted and experimental cutting forces was observed.

Most recently, the SPH technique was used in the single crystal copper micro-machining by Zahedi *et al* [170] using commercially available FE software ABAQUS/Explicit. SPH was coupled with FEM to avoid excessive computation time and cost. SPH was used in the region where machining simulation taking place. The study is used to gain insight into the effects of crystallographic anisotropy on the machining response of FCC cubic metals.

The advantage of the SPH approach was that the model of the workpiece was not bound to a pre-defined cutting line, and thus chip shapes were better presented in the model. Therefore, the SPH method can be used for machining and other processes where excessive deformation produces errors in the output data. However, the SPH technique cannot be used for thermal and thermomechanically coupled analysis. This restricted the method to structural analysis only.

In addition to SPH, most recently new methods were also used to separate chip from the workpiece material called global remeshing and rezoning. The global remeshing and rezoning technique was extensively used to separate chip from the workpiece material in a two-dimensional (2D) and three-dimensional (3D), thermomechanically coupled, finite-element simulation of ultrasonically assisted turning (UAT) in [4, 7, 8, 130]. A Johnson-Cook material model was used for modelling of material at high strain, strain rates and elevated temperature. Due to plastic deformation of the chip, elements near the tool-tip-interface were distorted badly resulting negative values in the Jacobian matrix; as a result, remeshing techniques was implemented to replace those distorted elements with a consistent one.

Later on, the same technique was used [4, 7, 8, 11, 41, 66, 87, 112, 126, 130, 171-174] for the chip formation in metal-cutting simulation.

Currently, remeshing is one of the well-known methods of chip formation in FE simulation of machining processes. In fact, this technique makes it possible to simulate the chip separation from the workpiece without any arbitrary pre-defined crack line or any path. The remeshing technique also makes it possible to simulate the process from the start to the fully formed chip and for different tool geometries.

The work so far presented in the section above is related to the literature on chip formation in FE simulation. In the next section various friction models used in FE simulation of cutting process are presented.

### 3.5.2. Friction at the Tool-Tip-Interface

In order to simulate machining, it would be desirable to model friction at the tool-workpiece-interaction zone. In literature, various friction models are available to model friction at the interaction of the tool-chip-workpiece interface:

A series of finite-element simulations of an orthogonal metal-cutting process have been performed in [175] by applying a modified Coulomb friction law to model friction along a tool-chip-interface. In the metal-cutting process, the two distinct contact regions are the sticking region and the sliding region. The critical friction stress  $\tau_c$  was in the sticking region while the coefficient of friction  $\mu$  was regarded with the Coulomb friction law in the sliding region. If the value of  $\tau$  was less than the critical frictional stress, then there was no relative motion between the chip and rake face of cutting tool, and a contact point belongs to the sticking region, while if the value of  $\tau$  became equal or exceeded the critical frictional stress value  $\tau_c$ , then sliding occurred and the contact point was in the sliding region. The critical value of the frictional stress value in modified Coulomb friction law was given by

$$\tau = \min(\mu p, \tau_{th}), \quad (3 - 18)$$

where  $p$  is the normal pressure,  $\mu$  is the coefficient of friction and  $\tau_{th}$  is the threshold value for the conventional Coulomb friction stress. When the value of  $\tau_{th}$  was set to infinity,

equation 3 – 18 recovered the original Coulomb friction law. Experiments were performed to validate the simulation results, which were in good agreement. It was found that shear straining was localized in the primary shear zone while material near the tool-tip experienced the largest plastic strain rate. The main idea of the paper was to use a hybrid frictional model by combining two or more than two friction model in FE simulations.

Furthermore, A 3D thermomechanically coupled, elasto-plastic, finite-element model was developed for orthogonal cutting process by Fang and Zeng [176]. At the tool-chip and tool-workpiece-interfaces, a shear friction model was used in the simulation. As the metal - cutting process is a large-deformation process, material in cutting was extremely distorted and, therefore, there is nonlinearity in the material behaviour and boundary conditions.

For non-linear finite-element simulations of metal-cutting two approaches were used: updated Lagrangian and Eulerian formulations. In order to overcome the above problem, a combination of the Coulomb friction model and the shear friction model was used in the analysis:

$$\tau = \begin{cases} \mu\sigma, & \tau < k, \\ k_z, & \tau > k, \end{cases} \quad (3 - 19)$$

Where  $\tau$ ,  $\sigma$  and  $k_z$  are surface friction stress, surface normal stress and shear flow stress, respectively. When the sliding of surfaces started at a fraction of contact pressure  $\sigma$  between the tool-chip surfaces, the Coulomb friction model defined the friction stress  $\tau$ . Otherwise, shear flow stress  $k$  was used to define friction stress, where the contact pressure stress may become very large. In many cases with large deformations, the Coulomb theory provided a critical friction stress at the interface that exceeded the shear flow stress in the material beneath the contact surface.

An analytical model for the friction at the tool-chip interface was presented by Ozel and Zeren in [177]. In this study, maximum and minimum values of normal stresses were observed at the tool-tip-interface and on the chip, at the exit of the rake face, respectively. Similarly, frictional stresses are concentrated in the sticking region and sliding friction occurred in the remaining tool-chip contact area. The frictional shearing stresses were

calculated by measuring the value of  $\mu$ . The normal-stress distribution on the rake face of the cutting tool was described by

$$\sigma_N = \sigma_{N_{mas}} \left[ 1 - \left( \frac{x}{l_c} \right)^z \right], \quad (3-20)$$

where  $x$  is the distance from the cutting edge, and  $z$  is an empirical coefficient that must be calculated [177]. To obtain the value of  $\mu$ , the following relation in terms of  $\sigma_N$  and  $k_{int}$  was used.

$$\mu = \frac{k_{int}}{\sigma_N l_p}, \quad (3-21)$$

The main aim of the paper was to utilize an inverse solution of Oxley's machining theory [57].

Bhahi *et al* [178] formulated a new hybrid friction model for the tool-chip contact length to illustrate the various features of the sliding-sticking region. The Johnson-Cook material model [179], arguments of Child [173] and Molonari *et al* [180] were used to formulate normal pressure on the tool-tip, a local coefficient friction and a heat source model for the sticking and sliding regions:

$$l_c = t_1 \frac{(2 + \xi) \sin(\phi + \bar{\lambda} - \alpha)}{\xi \sin(\phi) \cos(\bar{\lambda})}, \quad (3-22)$$

$$P_o = 4 \frac{(1 + \xi) \cos^2 \bar{\lambda}}{(2 + \xi) \sin(2(\phi + \bar{\lambda} - \alpha))}, \quad (3-23)$$

$$\mu_{sl} = \frac{\tan(\bar{\lambda})}{\left\{ \left( 1 - \frac{a}{l_c} \right)^\xi \left[ (1 + \xi) \frac{a}{l_c} \frac{\bar{\tau}_{st}}{\tau_a} + \left( 1 - \frac{a}{l_c} \right) \right] \right\}}, \quad (3-24)$$

$$Q_p = \tau_{ssz} \frac{V_c}{\delta t_2}, \quad (3-25)$$

$$Q_p = \mu_{sl} V_c p \left( 1 - \frac{x}{l_c} \right)^\xi, \quad (3-26)$$

where  $l_c$  is the tool chip contact length,  $t_1$  is un-deformed chip thickness,  $\xi$  is coefficient controlling the distribution of normal stresses at the tool-chip interface,  $\phi$  is the shear angle,  $\bar{\lambda}$  is the apparent friction angle,  $\alpha$  is the rake angle,  $p$  is the normal pressure,  $\mu_{sl}$  is the local friction coefficient at the sliding zone,  $l_s$  is the length of the sticking zone,  $\bar{\tau}_{st}$  is the shear stress in the sticking zone,  $Q_p$  is the heat source due to plastic deformation in the sticking region,  $\tau_{ssz}$  is the shear stress in the secondary shear zone,  $V_c$  is the chip velocity,  $\delta t_2$  is the width of the secondary shear zone and  $x$  is the distance along the rake face of the cutting tool.

The model was used for a case study of chip formation using numerical analysis. The model demonstrated that the cutting forces reduced with the increase in the cutting speed as expected. The main reason for the reduced cutting forces is the thermal softening of the material caused by temperature generation at the tool tip-workpiece-interface. A reduction in the apparent friction coefficient and contact length with the rise in the cutting speed was also observed, and validating the results in [181, 182]. A rise in temperature in the cutting region with the increase of the cutting speed was observed by using a new hybrid friction model. Whereas stress nullified a temperature trend and gave the minimum values at maximum temperatures due to thermal softening of the machined workpiece materials. These two important parameters caused diffusion wear of the cutting tool by delaminating the tool coating. The tool wear results were verified experimentally by using back-scattered electron micrograph. However, the main deficiency of the model is the total heat generated in the machining process, remains in the chip, which is not the actual case.

A significant difference in various features of conventional turning (CT) and UAT was observed in the analysis by changing the cutting parameters and lubrication conditions. The effect of cutting parameters and lubrication on various features of CT and UAT process using thermomechanically coupled FEA model was investigated in [126]. High-contact stresses were generated at the tool-chip-interface leading to significant friction forces. The classical Coulomb model was unable to adequately reflect friction processes under the conditions, resulting in the unrealistically high friction force. In addition to that, the Coulomb friction model is implemented using approximations for the theoretical step function, because that step function caused numerical difficulties in FEA calculation of the process. The arctangent

function used in the modified shear friction model was used to smooth out the step function in order to avoid numerical difficulties. As a result of the smoothing procedure, a node in contact always had some slipping. The arctan representation of the friction model is a mathematical idealization of non-linear friction behaviour. Therefore, shear friction between the tool and workpiece was modelled with the modified constant shear friction model.

Hence, the shear friction model was chosen for simulations, with the friction force depending on fraction of equivalent stress of a material and not the normal force as in the Coulomb model. Thus, friction stress was introduced in the following form:

$$\sigma_{fr} \leq -\mu \frac{\bar{\sigma}}{\sqrt{3}} \frac{2}{\pi} \operatorname{sgn}(V_r) \arctan\left(\frac{V_r}{V_{cr}}\right), \quad (3 - 27)$$

where  $\bar{\sigma}$  is the equivalent stress,  $V_r$  is the relative sliding velocity,  $V_{cr}$  is the critical sliding velocity below which sticking was simulated. Later on, the modified friction model was used in [9, 10, 126, 130, 172]. The effect of friction in the FE simulation was introduced in terms of  $\mu = 0$  for a fully lubrication case and  $\mu = 0.5$  for dry cutting conditions.

One of the sources of heat generation during a metal-cutting process is friction between the tool-workpiece-interactions, which ultimately affects the material properties of the workpiece. In the present FEA model of modern alloys, a modified shear friction model is used due to the limitation of the Coulomb model at high stress values. The coefficient of friction  $\mu = 0.5$  was used in simulations to incorporate the friction condition at the tool tip-workpiece interface. The following section presents modelling of a cutting tool used in metal-cutting operation.

### 3.5.3. Modelling of Cutting Tool in FE Simulations

In the past, many researchers simplified their FEA problems by assuming the cutting tool as a rigid body to reduce computational complexity of their models [4, 7-10, 130, 159, 162, 174] because, the stress/strain relationship and tool wear of the cutting tool in FE simulations was neglected, it reduced the computational cost as well as the time. To study the thermomechanical behaviour, the tool was modelled as rigid with heat-transfer capabilities in [4, 7-10, 168].

A commercially available finite-element code DEFORM 2D was used for finite-element analysis of tool wear prediction in different phases in [183]. In the first and second phases, a quasi-steady-state-field solution of cutting variables (strain, temperature, stress, etc.), were determined. In Phase 3, local tool wear rates and worn tools geometry were then calculated. Geometry of rake and flank faces of the tool in the FEM model was subsequently updated in Phase 4 with the results obtained in Phase 3. The same procedure was repeated for the next data point after the completion of one entire cycle. The results obtained were in good agreement with the experimental data. However, the main defect in the technique was the introduction of tool wear manually after some interval and was impossible to update the model according to the cutting condition.

Furthermore, In [184] a model of a cutting tool in FEA just before its fracture was presented. The boundary conditions were implemented to a separately modelled cutting tool from the experimental results. Both static and dynamic analyses were conducted for a DNMG 150608 insert and the tool holder. After the static finite-element analysis, the modal and harmonic response analyses were carried on, and the dynamic behaviours of the cutting tool structure were investigated. The equivalent von-Mises stress criterion was used for fracture analysis of the cutting tool. Several aspects of the metal-cutting process predicted by the finite-element model agreed well with experimental results. The harmonic response analysis was performed by including the cutting forces that caused the tool to fracture. Experimental data from the cutting forces were used to validate the model.

### 3.6. Summary

In the past, new techniques have been proposed to improve machinability of hard-to-cut materials as discussed in the above sections [8, 16, 18, 102, 112, 126, 130]. The prime aim of those new techniques was to improved surface roughness of machine specimens and reduced the cutting forces. The maximum reduction in cutting forces and improvement in surface roughness in hot and hybrid machining processes was reported by Leshock *et al* [146] and Wang *et al* [154]. Similarly, a significant reduction in the cutting forces and considerable improvement in surface roughness was reported in UAT [8, 102, 112, 126, 130]. However, no attempts were reported to investigate the effect of supplied heat to the workpiece material in

presence of superimposed vibrations on the cutting tool to form a novel hybrid turning process called HUAT.

Various types of heat sources have been used for thermal softening of the workpiece materials, for instance, gas torch, [99, 100, 139, 140], furnace pre-heating [185], induction heating [153], electric-current heating [132] [144], plasma heating [186] [138, 145, 150] and laser heating [187]. The flame torch is a relatively simple way to heat up a workpiece to a required temperature level. However, this method of heating cannot be used in machining of Ti-based alloys, since the torch deposited carbon particles and produced a carbide layer on the specimen. Similarly, induction heating is not efficient in non-ferrous materials and therefore, cannot be used for Ti-15333. The direct current could be a good alternative for heating; however, the main limitation of direct current was its dependency on cutting speed. Similarly, Laser and plasma arcs are the most effective sources of localized heating used in hot machining. However, the capital cost, requirement of high human skills and health concerns are the main obstacle for a use of these methods in hot machining. Therefore, in the current study, a band resistance heater was used as a heat source in hot machining. The main advantage of the band resistance heater is its low capital cost and more uniform heating of the workpiece material in hot machining. The experimental procedure is very simple and does not require extensive safety precaution as compared to Laser and plasma heat sources. Furthermore, nominal human skill is required for the band resistance heat source in hot machining.

Loughborough University is one of the leading universities of the world working on the development of ultrasonic machining processes. The most prominent is ultrasonically assisted turning and drilling of aerospace materials. The first 2D thermomechanically coupled FE model of CT and UAT was developed by Mitrofanov *et. al.* [10]. The model was used to investigate the process zone in turning of Inconel 718. The model was validated with experimental results and good agreement between the experimental and numerical results were observed. Later, in 2005, Ahmed *et. al.* [130] developed 3D orthogonal model for CT and UAT of Inconel 718. The model possesses a number of advantages compared to 2D model. The model was capable of showing temperature, stress distribution along the chip width. The model was also capable of showing the first 3D chip of UAT. However, the model

was developed for small scale simulation and only 1.5 mm of the workpiece was modelled in the FE simulation. The model was used to validate experimental results and followed by parametric study of the UAT of Inconel 718. Table 5-1 listed the historical development of the UAT models in Loughborough University.

Table 3- 2: Historical development of FE modelling of UAT at Loughborough University

Stage	Year	Reference
2D FE model for UAT	2002-2004	[9, 10, 126]
3D orthogonal model for UAT	2005-2006	[4, 7, 8]

The developed orthogonal turning model of Ahmed *et. al.* [4, 7] was modified and applied to Ti-15333. The model was simulated for CT, UAT, HCT and newly developed HUAT for the first time. However, there was still a need to investigate CT, UAT, HCT and HUAT by developing a complete 3D oblique turning model using actual tool geometry and process zone. The prime reason was that all experiments were carried out for the oblique turning process. In 3D orthogonal turning model, the radial component of cutting force was ignored that has a significant effect on the machined components quality, Additionally, the tool geometry significantly affects the radial component of force that was lacked with developed 3D orthogonal turning model. Hence, there was a need to develop a new oblique model to investigate the effect of vibration and external heat to cutting forces and thermal aspect of the conventional and hybrid turning processes. The modelling of oblique turning required high end computational facilities and advancement in FE simulations packages which were lacked in the previous attempts. A new thermomechanically coupled FE models were developed for Ti-15333 in which chip separation was achieved using a more realistic approach of global remeshing and rezoning technique. The cutting tool was modelled as rigid body to reduce the computational cost. Additional details about the developed FE model are presented in chapter 5.

## CHAPTER-4

# Experimental Study of Conventional and Hybrid Oblique Turning Processes

### 4.1. Introduction

Titanium alloys have shown a high strength-to-weight ratio which is maintained at elevated temperatures, and it has exceptional corrosion resistance. These characteristics were the main cause of the rapid growth of the titanium industry over the last 40 years. The major application of the material is in the aerospace, automotive, biomedical and energy sectors owing numerous inherent sets of mechanical and thermal properties. Non-aerospace applications take advantage mainly of their excellent strength properties, for example steam turbine blades, superconductors and computer hard drive. The low thermal conductivity and high-strength of these alloys created problems in the machinability with conventional cutting techniques.

Hence, in the recent past, researchers have adopted novel experimental techniques to improve the machinability of these high-strength alloys. A detailed description of those new hybrid machining techniques was discussed in Chapter 3. This chapter covers experimental procedures adopted for the analysis of CT, HCT, UAT and the newly developed HUAT as mentioned in the methodology of the Author's work.

Loughborough University is one of the leading academic institutes in the area of ultrasonically assisted turning and drilling of high-strength and composite materials. The state of the art experimental setup is capable of performing both CT and UAT on various material. The previous experiment showed the capability of the experimental setup in the improvement of surface roughness and reduction in cutting forces and has been reported [4, 7, 11, 124].

In UAT, vibrations can be superimposed on the cutting tool in tangential, radial and axial direction as shown in Figure 4-1. However, based on experience, vibration in cutting velocity direction yields a better surface finish and reduction in cutting forces compared to vibration

in any other directions. In addition to that, in newly developed HUAT, external heat was supplied to the workpiece material to alleviate the material removal from the workpiece components.

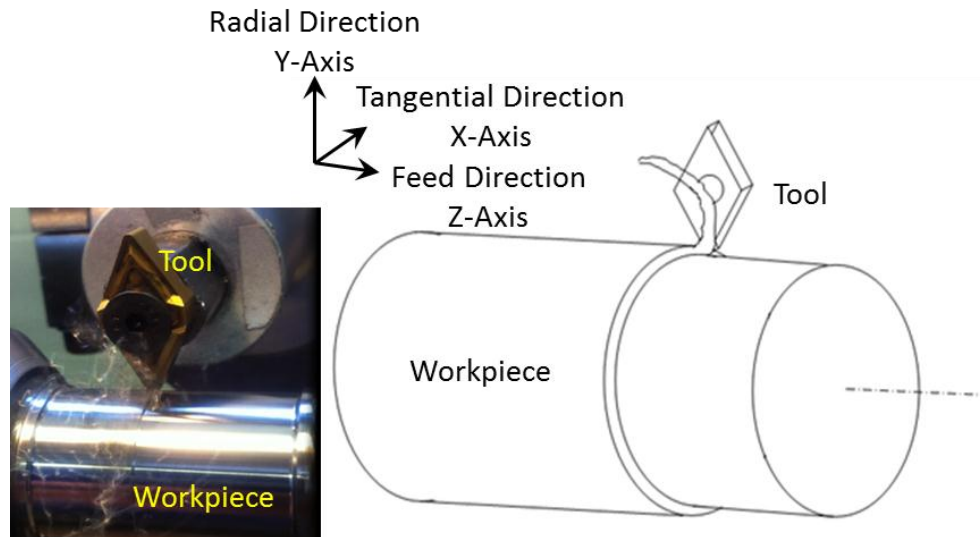


Figure 4-1: Principal vibration directions in ultrasonically assisted turning

#### 4.2. Application of Modern Alloys

High-strength alloys have been the primary material of choice for structural components of aircraft frames, turbine parts and other components exposed to extreme conditions. The wide usage of titanium in industries is growing faster due to its remarkably high-strength to weight ratio. Its low density and high-strength make it exceptionally renowned in all high-strength alloys and make it favourable alloys for aerospace industries. Based on strength and weight, as compared to other high-strength alloys, the same weight of titanium will go twice as far the Ni-based alloys will do. Hence, titanium had established a permanent home in various industries ranging from aerospace, computer industries and chemical engineering.

In power generation industries, titanium is used widely in the production of cooling systems to eliminate the need for corrosion allowance. Titanium offers a good cycle life when compared to nickel and stainless steel, as a result, extensively used in the production of chemical processing industries equipment. The light weight, corrosion resistance to salty water and flexibility of titanium alloy make it an excellent material in petroleum industries,

especially in the explorations of sea oil. Titanium alloys are also widely used in the production of desalination plant worldwide.

Similarly, titanium alloys are also widely used in the production of airframe structure of the aircraft as well as in the landing gear of the modern jet aircraft due to its high strength and light weight. According to the Roll-Roys, 30% of the total weight of modern aircraft engines consists of titanium alloys. These alloys are rapidly replacing all steel parts of a modern aircraft due to cost efficient production and worldwide growing competition of manufacturing industries across the globe. The latest arrival of Boeing, Dreamliner-787 consists of 14% titanium alloys by weight. It's a huge contribution of titanium alloys in passenger aircraft manufacturing.

For hard-drive of modern laptop and computers, titanium is an excellent material in computer industries. Its high-strength, elevated temperature exposure and non-magnetic properties as compared to other material make it a promising material for computer industries. It is also broadly used in the manufacturing of hard-drives in computer industries.

In modern automotive industries, titanium alloys are widely used in the production of piston ring, connecting rods, engine valves, camshaft and airframes of automobile to reduce weight and increase its longevity. Currently, its application in geothermal power generation, human implant and armour industries had drastically increased in the last few decades.

### 4.3. Properties of Ti-15333

A solution treated and aged, Ti-15V3Al3Cr3Sn (designated as Ti-15333), alloy bar ingot having an initial diameter of 65 mm and a length of 500 mm was used in the experiments. The produced 200 mm diameter bars were deformed at 850°C by rotary swaging to a final diameter of approximately 80 mm. The alloy was water-quenched from 790°C. Table 4-1 and Table 4-2 show the chemical composition and material properties of the Ti-15333, respectively.

The cemented-carbide cutting inserts were used in experiments having a coating of ceramic layer of titanium-aluminium-nitride over a layer of titanium-nitride (CP500), suggested for cutting depths, ranges from 200  $\mu\text{m}$  to 300  $\mu\text{m}$  with a feed rate of 50  $\mu\text{m}$  /rev to 250  $\mu\text{m}$  /rev and cutting speed of 45 m/min (as specified by the manufacturer) in machining of high-

strength alloys. The tool has a nose radius of 800  $\mu\text{m}$ , rake angle of approximately  $14^\circ$  and clearance angle of  $0^\circ$ , with a low-depth-of-cut/finishing chip breaker optimized for low feed rates (Figure 4-2). Additional details of the cutting insert are listed in Table 4-3.

Table 4-1: Chemical composition of Ti-15333 [wt. %] [188]

Ti	Al	Cr	Sn	V
~75.52	2.59	3.43	3.07	15.39

Table 4-2: Material properties of Ti-15333 [188]

Workpiece material	Ti-15V-3Al-3Cr-3Sn
Workpiece diameter, $D$ (mm)	68
Workpiece length, $L$ (mm)	500
Producer	GfE Metalle and Materialien GmbH
Heat treatment	Solution-treated and aged
Young's modulus, $E$ (GPa), at room temperature	87
Yield strength, $\sigma_y$ [Mpa]	558.85
Density, $\rho$ ( $\text{kg}/\text{m}^3$ )	4900
Thermal conductivity, $k$ (W/Km)	8.10
Co-efficient of thermal expansion, $\alpha$ [ $\text{K}^{-1}$ ]	8.4e6
Specific heat, $C_p$ [ $\text{J}/\text{g}\cdot^\circ\text{C}$ ]	0.6
Ultimate tensile strength, $\sigma_{ul}$ (Mpa)	1200

Table 4-3: Cutting tool properties [188]

	DNMG-150608-MF1-CP500
Tool maker	SECO
Tool material	Micro-grain cemented carbide
Coating	(Ti,Al)N-TiN
Tool nose radius, $r_n$ ( $\mu\text{m}$ )	800
Nose angle (degree)	55
Rake angle (degree)	14.6
Clearance angle (degree)	0
Cutting edge radius ( $\mu\text{m}$ )	25

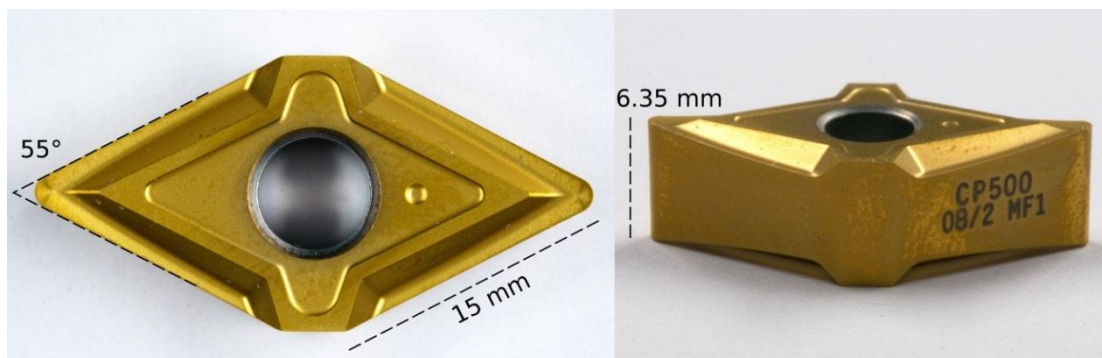


Figure 4-2: DNMG cutting insert used in experimentation [188]

The shear strength of Ti-15333 is a function of temperature and strain rate. Split Hopkinson pressure bar tests were carried out to investigate the material response at various temperatures and strain rate as shown in Figure 4-3 and Figure 4-4.

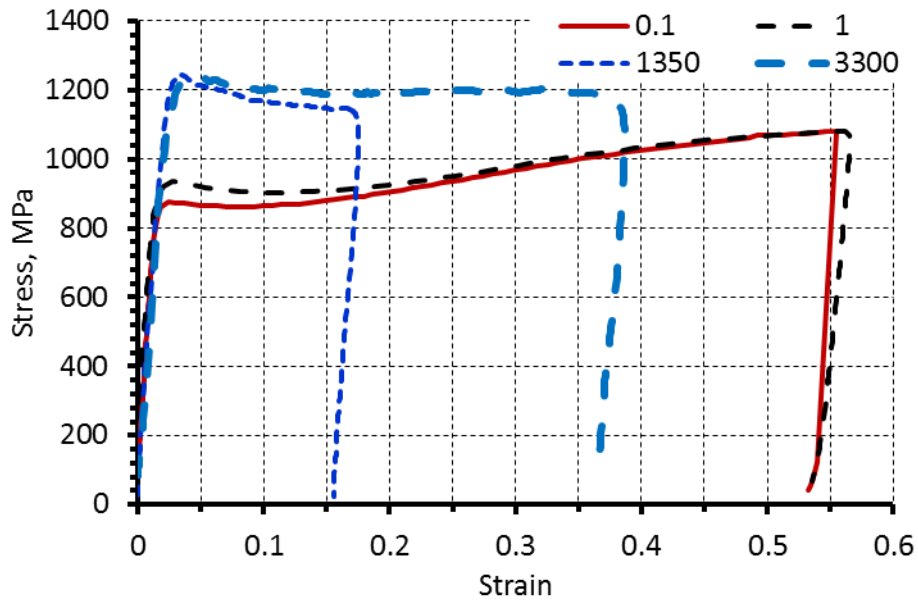


Figure 4-3: Stress strain data of Ti-15333 at room temperature and various strain rates

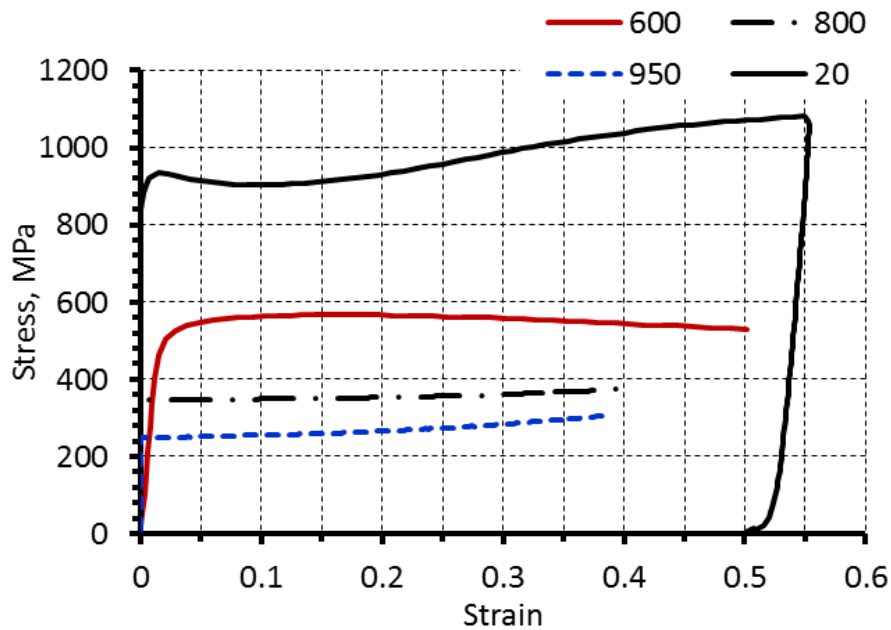


Figure 4-4: Stress strain data of Ti-15333 at various temperatures

#### 4.4. Cutting Force Measurements

Experimental studies were conducted for conventional turning (CT), hot conventional turning (HCT), ultrasonically assisted turning (UAT) and hot ultrasonically assisted turning (HUAT) on universal Harrison M-300 Lathe machine (Table 4-4). The tool post of the lathe machined was modified such that a customized piezo-ceramic transducer was mounted on the cross slid of

the lathe machine having the capability to switch from CT to UAT and from UAT to CT during the turning process.

Table 4-4: Specifications of lathe machine used in turning experiments

Manufacturer	Harrison
Model	M300
Spindle speed ranges (rpm)	40-2500
Feed rate (mm/rev)	0.05-1
Motor power (kW)	2.2
Height of centres (mm)	167
Tailstock quill diameter (mm)	42
Cross slide width (mm)	140
Cross slide X-travel (mm)	190

A Kistler three-component piezo-electric dynamometer (KIAG-SWISS Type-9257A), bolted on the cross slide of the Harrison lathe was used to record the cutting forces. The dynamometers had a sensitivity of  $\pm 0.1$  N and can measure the two components of forces  $F_x$  (Tangential component) and  $F_y$  (Radial component). In experimentations, the dynamometer was unable to measure the axial component of force due some fault in the sensors and was therefore, not included in the experimental results. The dynamometer had a frequency of 3 kHz and was capable of force measurements up to 5 kN. The frequency of the data-acquisition system was significantly lower than the excitation frequency of a transducer applied to the cutting tool in UAT and HUAT. Therefore, the data-acquisition system yielded lower of the forces over a large number of ultrasonic vibrations as recorded from the dynamometer. Hence, average forces were used in the analysis for CT, HCT, UAT and HUAT. Furthermore, an adequate insulation was used between the custom-built tool-holder and dynamometer to shield electrical disturbances, generated during machining operations. A

custom-built tool-holder fixed to an ultrasonic transducer was mounted on the dynamometer is shown in Figure 4-5. A non-contact measurement technique (poly-tech laser vibro-meter) was used to monitor the vibrational parameters in experimentations. The details of the laser vibro-meter are listed in Table 4-5.

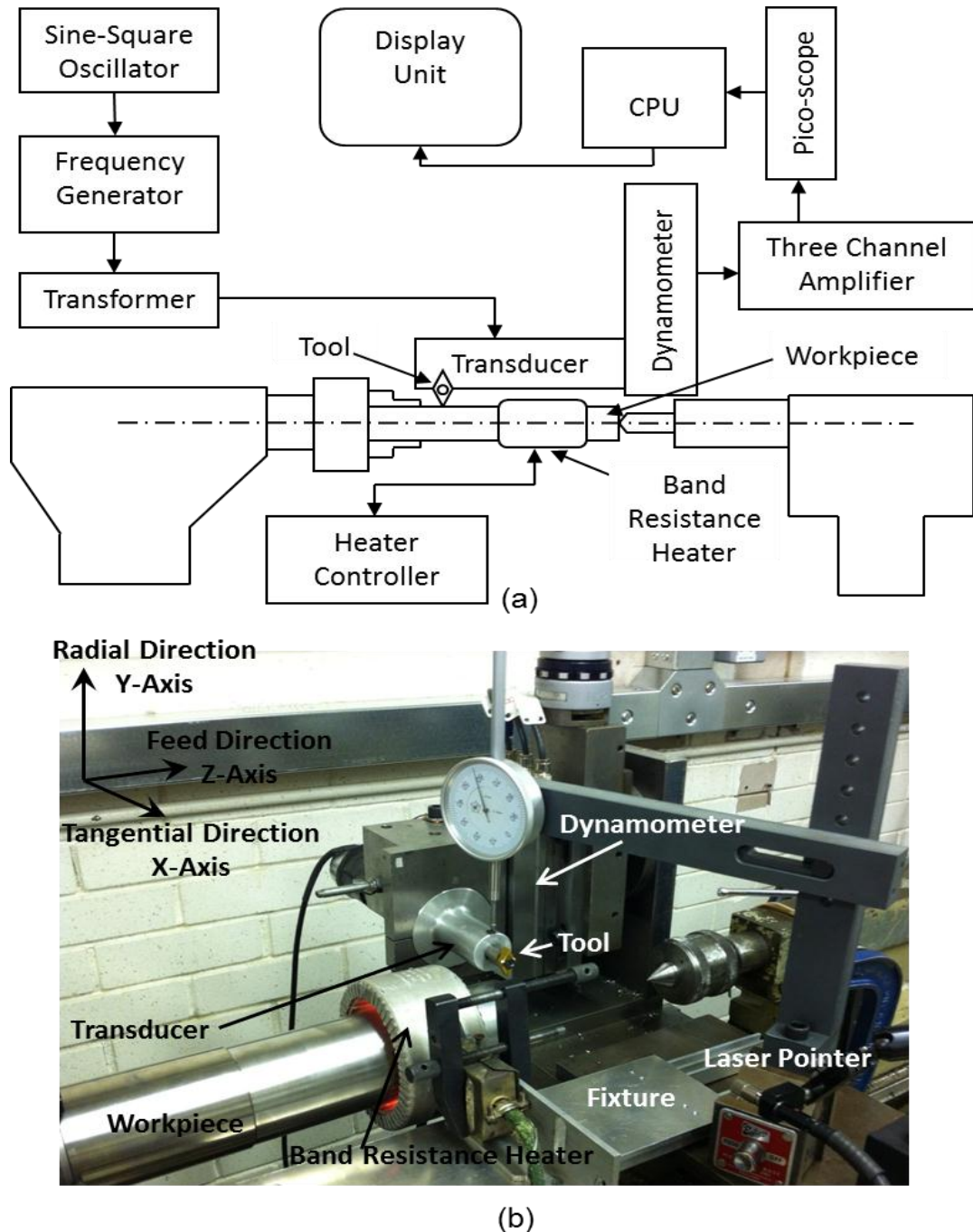


Figure 4-5: (a) Schematic diagram of the experimental setup; (b) Experimental setup used in experiments of CT, HCT, UAT and HUAT

Table 4-5: Laser vibro-meter specifications

Manufacturer	Polytec GmbH
Model number	OFV-3001
Technology	Laser doppler
Resolution ( $\mu\text{m}$ )	0.08
Linearity error	0.1% of full scale
Max velocity (m/s)	10

A bulk heating technique was used to supply external heat to a specimen in hot machining. Therefore, a band-resistance heater (Table 4-5), encapsulating the workpiece, was used as a heat source to increase temperature of the workpiece ( $T_{\text{ext}} \text{ } ^\circ\text{C} \pm 10^\circ\text{C}$ ). Initially, the heater was fixed to a fixture mounted to the cross slid of the lathe machine to supply heat to the workpiece material as shown in Figure 4-5. In machining tests, a slight increase (20 to 30  $\mu\text{m}$ ) in the depth of cut was observed due to deformation of the ultrasonic transducer made of Aluminium. Therefore, the procedure for experiments were modified and the heater was used in the experiments for the application of external heat to the workpiece material and wet cloth and aluminium foil was used to surround the transducer and dial gauge to avoid any thermal expansion in transducer concentrator and ultimately increase in depth of cut during the experiments. However, in the later experiments, the heater was initially used to heat up the workpiece material in experiments and was later on removed it from the machine. However, from experimentation and numerical simulations, it was observed that during removing heater from the machine and adjusting the tool position, a reduction of approximately  $10^\circ\text{C}$  was observed,. Therefore, the workpiece material was initially heated  $10^\circ\text{C}$  higher to a desired temperature to compensate the observed reduction during machine and heater handling.

A Teflon coated, calibrated K-type thermocouple and a *FLIR ThermoCAM<sup>TM</sup> SC3000* infra-red system was used to measure temperature of the workpiece during hot machining. The diameter of the thermocouple was 127  $\mu\text{m}$  and it can measure temperature up to  $1200^\circ\text{C}$ . A

4-channel K-type thermometer HHM290/N was used to record the measured temperature levels as shown in Figure 4-6.

Table 4-6: Band resistance heater specifications

Model number	DE-52641
Power (W)	1100
Internal Diameter (mm)	65
Controller	LE-5023
Max Temperature ( $^{\circ}\text{C}$ )	600

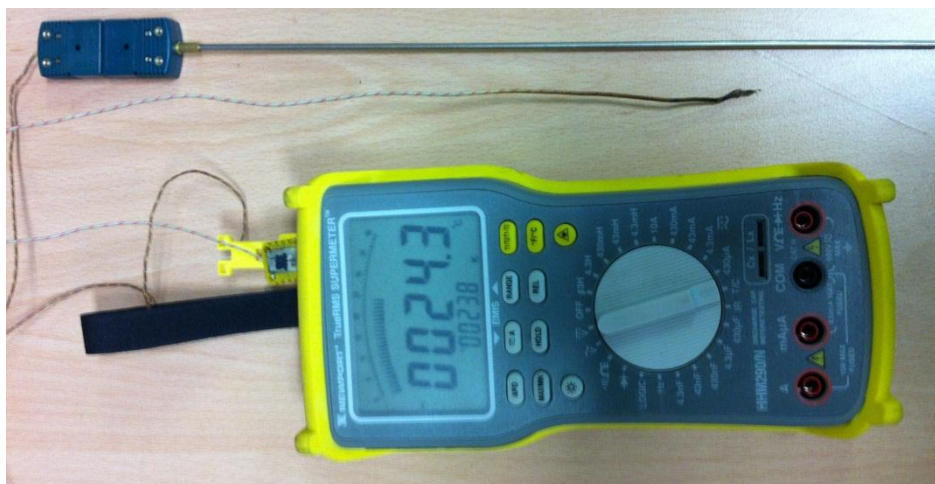


Figure 4-6: Thermocouple, thermocouple probe and thermometer used in experimentation to measure the workpiece temperature in hot experiments

The FLIR ThermoCAM system consists of a built in  $20^{\circ}$  lens, cables, connectors, remote and range of optional hardware and software accessories. The new Stirling-cooled Quantum Well Infrared Photon (QWIP), enabled the system to capture images at low noise detection and high image stability and uniformity. Further details of the system are listed in Table 4-7. In experimentation, continuous mode recording was used to capture thermal resolutions of the process zone in conventional and assisted turning operations. The ThermoCAM<sup>®</sup> QuickView<sup>™</sup> software was used to analyse the data of the *FLIR ThermoCAM<sup>™</sup> SC3000* system. A temperature distribution of the workpiece at  $310^{\circ}\text{C}$  in hot machining is shown in Figure 4-7.

Table 4-7: FLIR ThermoCAM system features

Image format (Pixel)	320 × 240
Temperature range (°C)	-20 to 2000
Emissivity	0.32
Spectral range (μm)	8-9
Image frequency (Hz)	50/60
Accuracy (%)	±2 above 150°C
Power consumption (W)	22
Weight (kg)	3.2

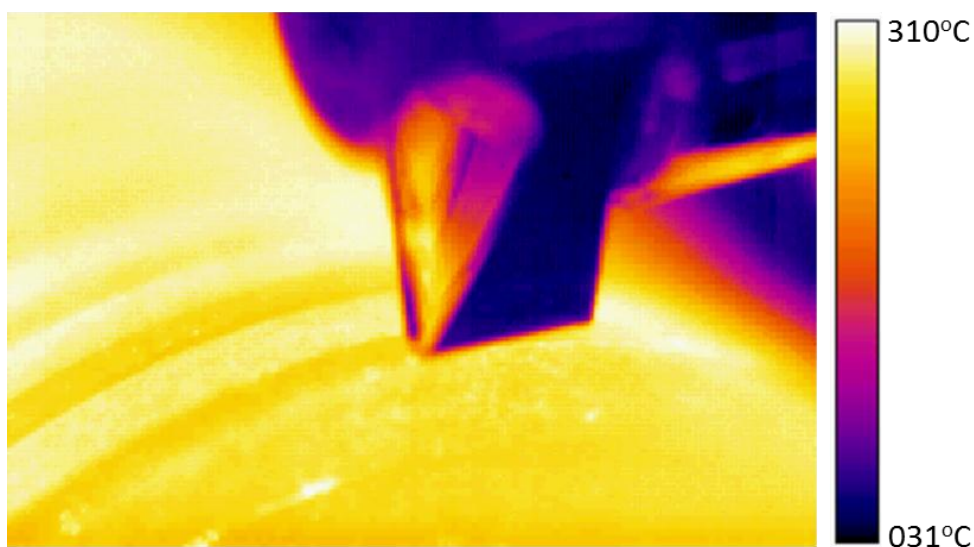


Figure 4-7: Infra-red image of workpiece in hot machining at 300°C

#### 4.4.1. Experimental Methodology

The cutting conditions used in experiments are presented in Table 4-8. These cutting conditions were recommended by the coordinator of the MaMiNa project to achieved synergy in the projects members. The selected temperatures levels were selected based on the metallographic response of Ti-15333 to the applied temperature [189]. A round

Ti15V3Cr3Al3Sn bar, having a length of 500 mm and a diameter of 65 mm was turned on a lathe machine to 63 mm diameter. The ingot bar was mounted on the lathe and the eccentricity was adjusted with the help of mechanical dial gauge. Experiments were carried out for CT, HCT, UAT and HUAT for various depths of cut and cutting forces, imposed on the cutting tool, were measured. In hot machining, external heat was supplied to the workpiece material as discussed above. The experiments were carried out at room temperature and several selected elevated temperatures (Table 4-8). The cutting forces were analysed for the selected temperature levels and various speed-feed combinations in both HCT as well as in HUAT.

Table 4-8: Cutting conditions used in experiments

Parameters	Magnitude
Cutting speed, $V$ (m/min)	10-70
Depth of cut, $a_p$ (mm)	0.1-0.5
Feed Rate, $f_r$ (mm/rev)	0.1
Temperature, $T$ (°C)	20, 100, 200, 300
Frequency, $f$ (kHz)	20
Amplitude, $a$ ( $\mu\text{m}$ )	8

For cutting force analysis, each experimental test lasted for approximately 75 seconds. Within the first 20 seconds the depth of cut was set to the desired magnitude followed by HCT for 20 seconds as shown in the force history taken from the data acquisition system (Figure 4-8). During the tests, ultrasonic vibration was switched on after 40 seconds and lasted for approximately 30 seconds before being switched off to recover HCT for the rest of 5 seconds. Each experiment was repeated at least five times to get a reasonable statistics on experimental data. The error bars represent the standard deviation of obtained experimental results, for each set of experimental conditions.

During UAT, the author observed spurious vibrations in the radial and axial direction with amplitudes of approx.  $0.1 \mu\text{m}$  and  $0.3 \mu\text{m}$ , respectively. This is not surprising as it is arduous to achieve a pure one-dimensional vibration system in transducer design and manufacture. The vibratory amplitude in the primary cutting direction (tangential direction) was observed to be  $8 \mu\text{m}$  for all the cutting depths.

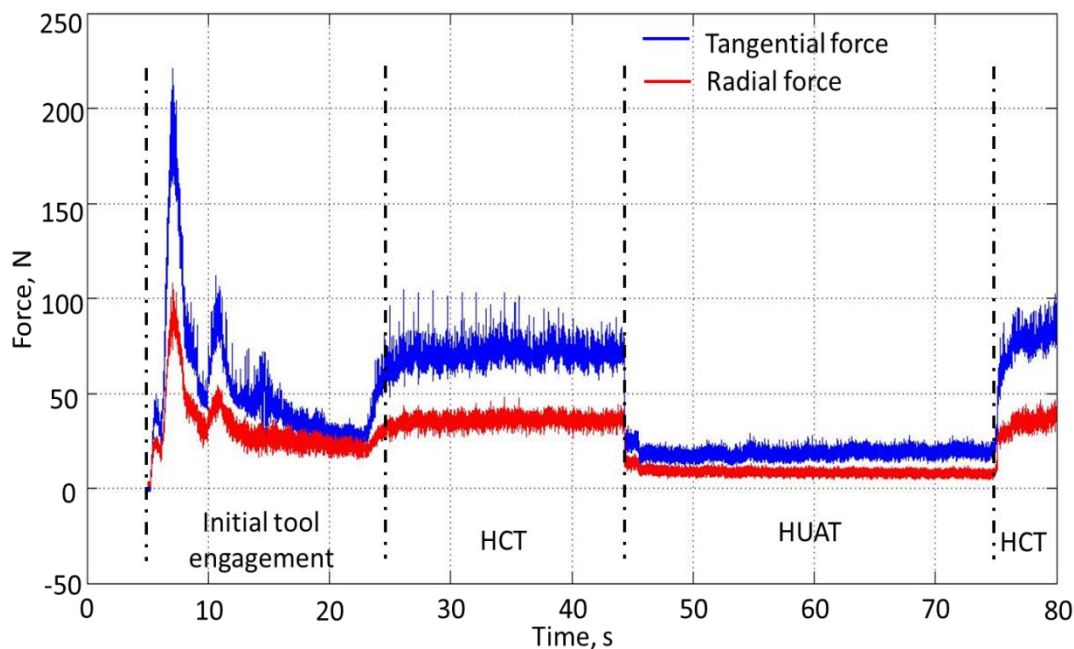


Figure 4-8: Force history in experimentation at  $300^{\circ}\text{C}$  ( $V = 10 \text{ m/min}$ ;  $a_p = 0.3 \text{ mm}$ )

#### 4.4.2. Results and Discussion

Experiments were carried out for CT, HCT, UAT and HUAT and cutting forces were measured for various depths of cut ( $a_p$ ). A substantial reduction in tangential and radial component of forces was seen with the application of ultrasonic vibration in the cutting direction on the cutting tool, as expected in Inconel 718 [7] and Ti-based alloy [103]. Furthermore, with the application of external heat to the workpiece materials, a considerable reduction in tangential and radial components of cutting forces were observed as shown in Figure 4-9 and Figure 4-10, respectively.

The results from experimentations shows that a reduction of 8% (from 98 N to 90 N) and 20% (25 N to 20 N) in the tangential component of cutting force in HCT and HUAT, respectively, was observed at  $100^{\circ}\text{C}$  and  $300 \mu\text{m}$  depth of cut (Figure 4-9c). A further reduction of 3% (from 90 N to 87 N) and 5% (from 20 N to 19 N) in tangential component of forces was observed,

when temperature of the workpiece was further increased by 100°C in HCT and HUAT, respectively (Figure 4-9b). The reduction in HCT and HUAT at 300  $\mu\text{m}$  depth of cut and at 300°C was reached to 20% (from 98 N to 77 N) and 35% (from 25 N to 16 N), respectively, when compared to CT and UAT at room temperature (Figure 4-9a).

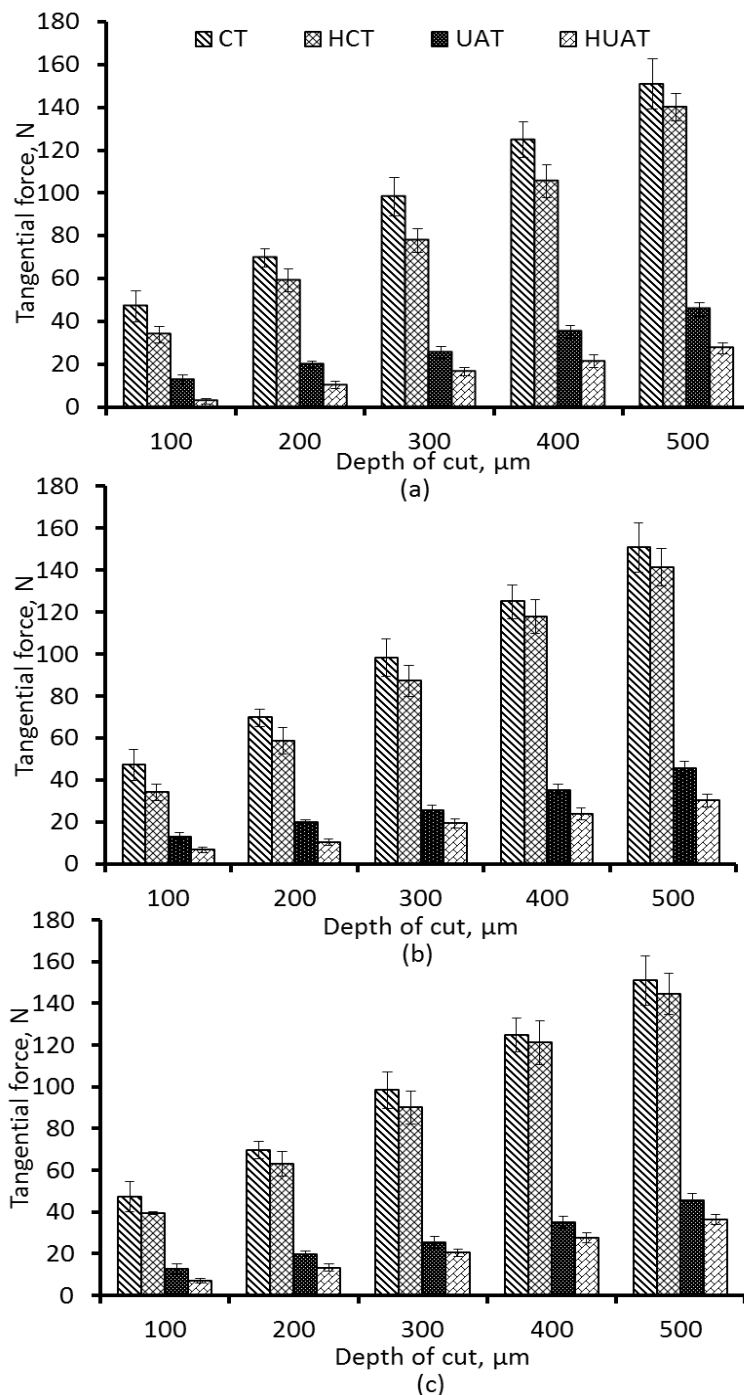


Figure 4-9: Tangential cutting forces at various depths of cut, 10 m/min cutting speed and temperature of (a) 300°C; (b) 200°C and (c) 100°C

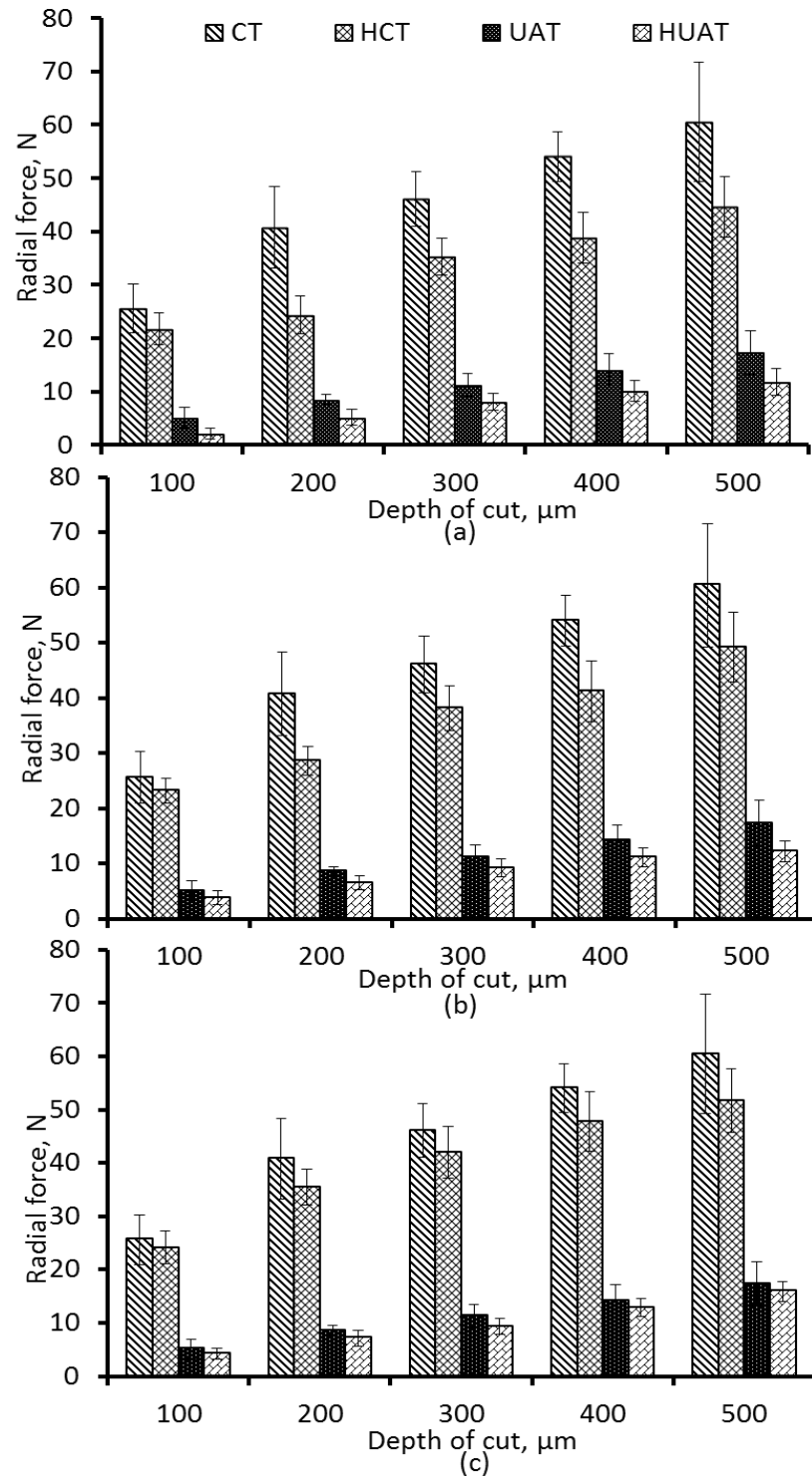


Figure 4-10: Radial cutting forces at various depths of cut, 10 m/min cutting speed and temperature of (a) 300°C; (b) 200°C and (c) 100°C

Application of external heat to the workpiece material not only reduced the tangential cutting forces but also decreased the radial component of forces (Figure 4-10). A reduction of 8% (from 46 N to 42 N) and 17% (from 11 N to 9 N) in radial component of cutting forces was

observed in HCT and HUAT, respectively, at 100°C of the workpiece pre-heated temperature (Figure 4-10c). A further increase of 100°C resulted, a decline of 9% and 11% in HCT and HUAT, respectively (Figure 4-10b). Similarly, the reduction in radial components of cutting forces in CT and UAT at 300°C and 300  $\mu\text{m}$  is 23% (from 46 N to 35 N) and 27% (from 11 N to 8 N), respectively (Figure 4-10a).

Therefore, application of external heat was more effective in UAT when compared to CT. The gradual reductions in cutting forces with application of external heat to the workpiece material are shown in Figure 4-11.

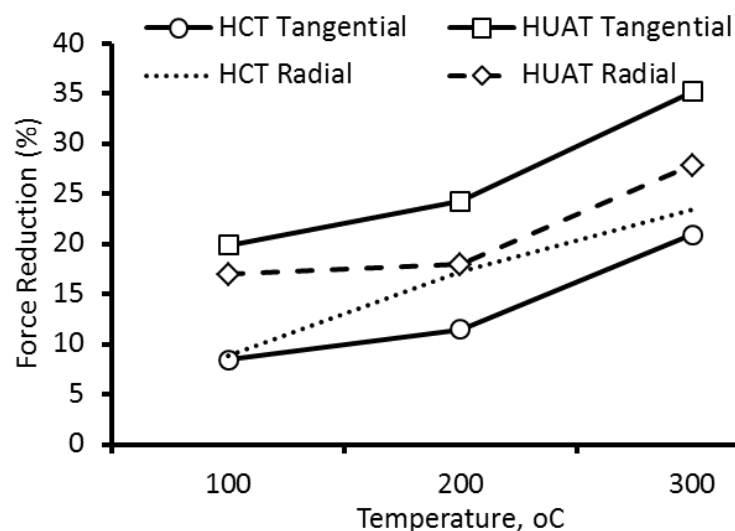


Figure 4-11: Reduction in cutting forces at various temperatures ( $V = 10 \text{ m/min}$ ;  $a_p = 0.3 \text{ mm}$ )

A comparison of this new hybrid machining technique (HUAT) with CT produced a significant reduction in cutting forces (Figure 4-12). At 100  $\mu\text{m}$  the reduction in tangential and radial component of cutting forces was approx. 95% in HUAT. The decline in cutting forces reduced with an increased in depth of cut and ultimately, a steady reduction of 80-85% was observed in HUAT above 200  $\mu\text{m}$  and at 300°C initial workpiece temperature.

In hot machining, reduction in cutting forces was mainly attributed to the decrease in yield strength of Ti15V3Cr3Al3Sn at elevated temperatures [190]. Therefore, the material removal rate in HUAT is higher when compared to CT for the same depth of cut and cutting conditions. As the cutting force on the tool was 47 N at 100  $\mu\text{m}$  depth of cut, whereas at 500  $\mu\text{m}$ , the observed cutting force was 30 N in HUAT (Figure 4-9a). Therefore, for the same level

of cutting forces on the cutting tool, the material removal rate increased considerably, when compared to CT.

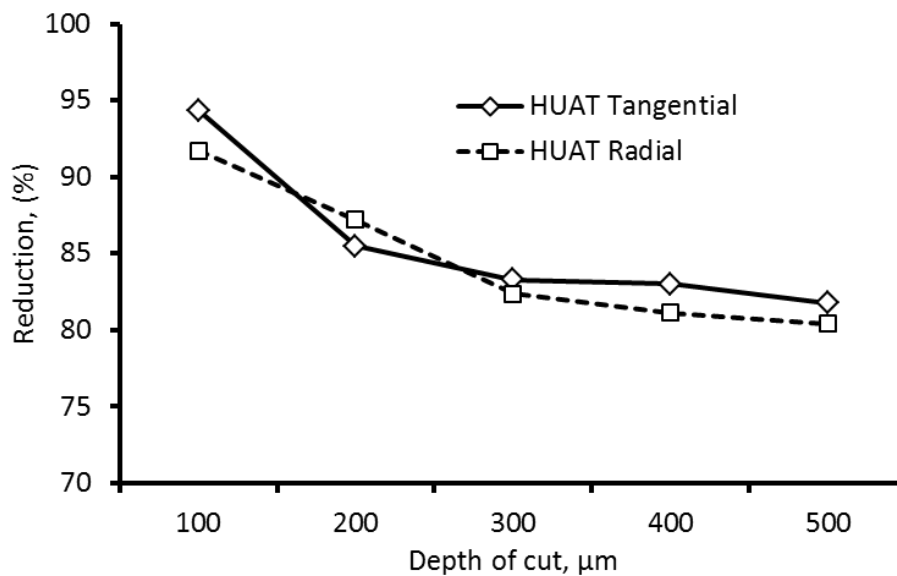


Figure 4-12: Reduction in cutting forces in HUAT when compared to CT at various depth of cuts,  $V=10$  m/min;  $T=300^\circ\text{C}$

## 4.5. Thermal Analysis of Conventional and Assisted Turning Processes

### 4.5.1. Introduction

In many manufacturing processes, it is desirable to have some knowledge of the amount of heat generated and consequent temperature rise (both maximum and average) and its distribution in the conductive medium. For example, the maximum temperature on the tool rake face or the clearance face of a cutting tool can determine the life of a cutting tool. Optimum cutting conditions used, especially the cutting speed, depend on this and the characteristics of the cutting tool material with respect to the work material. Similarly, subsurface deformation and metallurgical structural alterations in the machined surface depend on the maximum temperature, the temperature gradient, and the rate of cooling of parts. The development of new tool materials as well as the advancement of machining technology will depend, to a large extent, on the knowledge and limitations of cutting temperatures that influenced the life and the performance of the tool. To date, many experimental, analytical, and numerical methods have been developed to determine the temperature magnitudes that existed in the process zone during cutting processes.

The frictional conditions between the tool-chip and tool-workpiece are highly complex and also sensitive to the cutting conditions. As a result, the stresses and temperatures at the tool-chip interface and around the cutting edge can be critically high in some cutting conditions and ultimately affect the surface quality of a machined component.

#### 4.5.2. Experimental Setup for Infra-Red Thermography

The infrared thermography is a useful technique used in machining operations to investigate the temperature of the process zone without physical contact. This method is non-destructive, easy and accurate for all those process which cannot be access directly during experimentations. In the current study, FLIR ThermaCAM™ SC3000 infra-red system was used to carry out thermal analysis of the new hybrid turning technique (HUAT), CT, UAT and HCT. The schematic diagram of the thermal system used in the study is shown in Figure 4-13. The system consists of a built in 20° lens, cables, connectors, remote and range of optional hardware and software accessories. The new Stirling-cooled Quantum Well Infrared Photon (QWIP) enable the system to capture images with a spectral response between 8 and 9  $\mu\text{m}$ , temperature range of  $-20^{\circ}\text{C}$  to  $2000^{\circ}\text{C}$ ,  $320 \times 240$  pixel resolution, low noise detection and high image stability and uniformity. The continuous mode recording was used to capture the conventional and assisted turning operations.

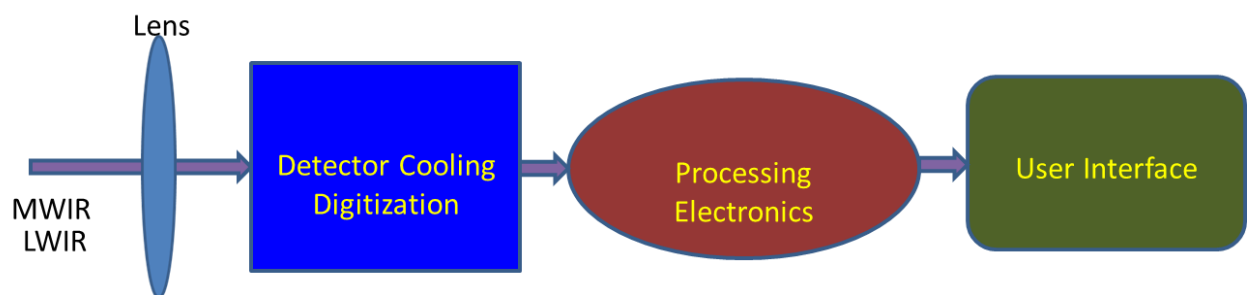


Figure 4-13: Schematic of the infra-red thermography

The ThermaCAM® QuickView™ software was used to analyse the data of the FLIR ThermaCAM™ SC3000 system. The various features of the FLIR ThermaCAM™ SC3000 system are given in Table 4-7. The lens of the thermal camera is made of Silicon (Si) and Germanium (Ge), used for the medium wavelength (MW) range and long wavelength (LW) range infra-red thermography, respectively.

For holding the thermal camera, a special type of fixture was designed to hold the thermal camera on a lathe machine. The special fixture was bolted to a solid mild steel heavy plate mounted on the cross slide of the lathe machine, clamped through a C-clamp. The heavy mild steel plate was used to eliminate the hole on the cross slide of the lathe machine. Similarly, the C clamp was used to eliminate the relative movement of the thermal camera during experimentations (Figure 4-14). The fixture was designed in such way to allow movement of the thermal camera in the forward and backward direction to adjust positions of the camera in such a way to get good quality images. Furthermore, the rotational movement of the fixture along its centre point allowed adjusting the position of the lens to an appropriate position.

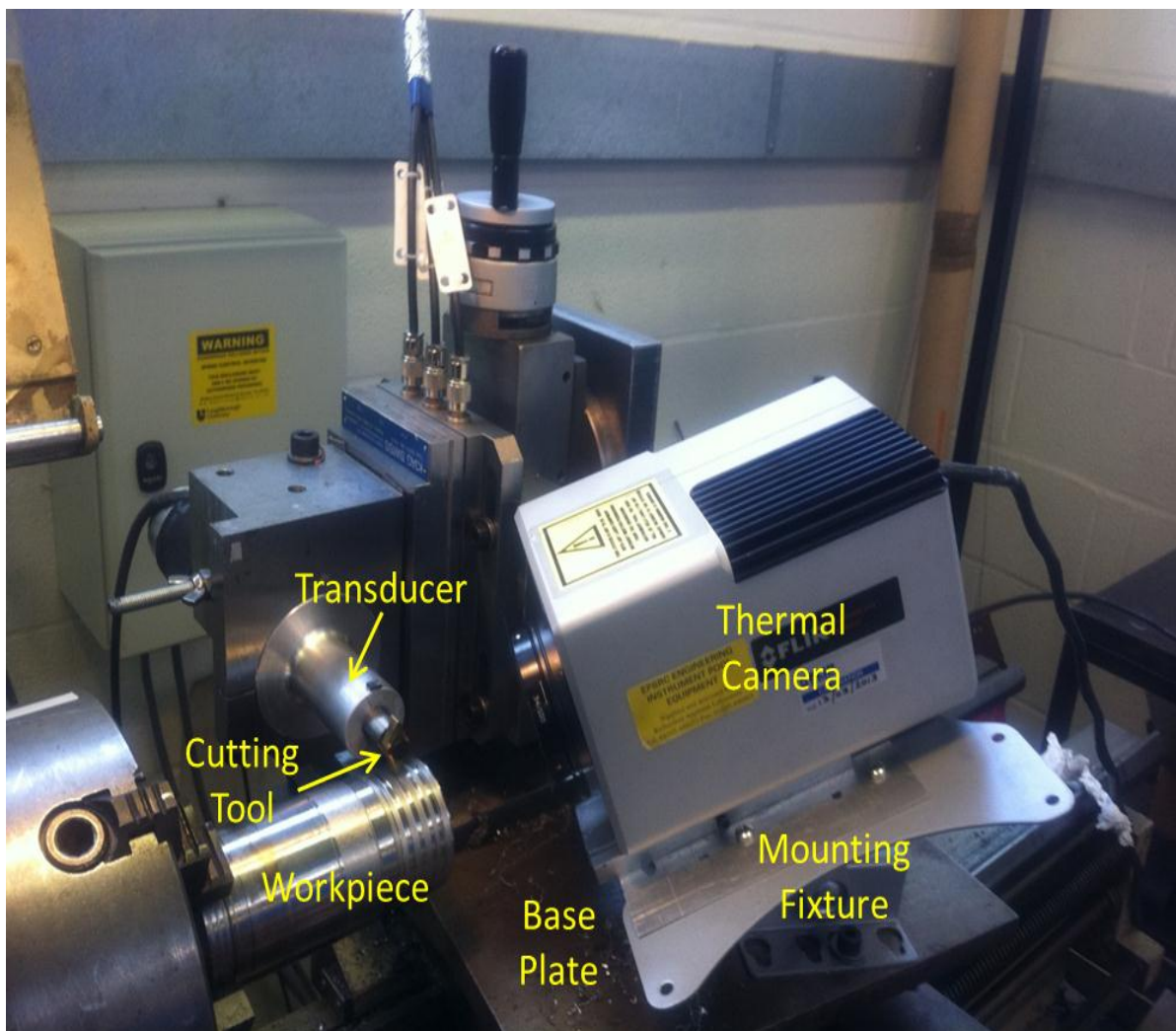


Figure 4-14: Experimental setup for thermal analysis

### 4.5.3. Calibration of Thermal Camera

In the current study, the FLIR ThermaCAM™ SC3000 system was used for the thermal analysis of the process zone in the machining of hard-to-cut alloys. However, the results obtained from the system depend on the emissivity of the object, surface quality, surface shape, humidity and room temperature. Therefore, the system was first calibrated to determine the emissivity of the workpiece material used in turning experiments.

The Ti-15333 rod was heated to elevated temperature (300°C) using a band resistor heater. Standard K-type thermocouples were used to measure temperature of the workpiece. The reading from the thermocouples were recorded with the four-channel thermometer. The distance between the workpiece material and camera was kept the same as used in experiments to get more accurate calibration. All readings were taken using the same distance between the camera and the workpiece material to get more accurate prediction of process zone temperature. Furthermore, the measured temperature of the system is a function of the distance and emissivity. During calculation, the cutting tool edge was the area of interest and the lens was focused on that particular area. The FLIR ThermaCAM™ SC3000 system was mounted on the fixture and the workpiece material was filmed with the camera. Thermal images of a machined workpiece were recorded using ThermaCAM® QuickView™ software. The surface temperature of the workpiece material after calibration is shown in Figure 4-15.

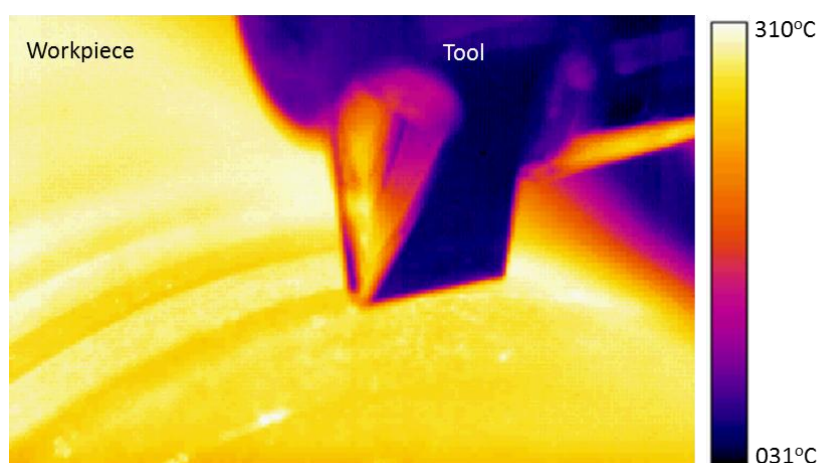


Figure 4-15: Temperature profile of the workpiece specimen after camera calibration for emissivity of 0.32 for Ti-15333

The value of emissivity was calculated using the auto calculate option of the ThermaCAM® QuickView™ software. The default value of emissivity was 0.92 during initial experimentations. The measured temperature level from thermocouple was entered to the software and emissivity of the workpiece material was recorded. The experiment was repeated at least five times and the average emissivity (0.32) of the workpiece materials evaluated from the above experiment and was used in the rest of analysis.

#### 4.5.4. Methodology

The FLIR ThermaCAM SC3000 was used in experimentations to get the thermal analysis of the process zone in CT, HCT, UAT and HUAT. To protect the expensive lens of the thermal camera during experimentations from the flying chips generated during the process, a protecting plastic thin film was used on the camera lens as shown in Figure 4-16. From experimentations, it was observed that no significant difference in results was observed with plastic thin film on the thermal camera lens during the analysis. In hot machining, the movement of the heater was controlled manually. The camera mounted on the cross slide was moved away from the heater to avoid any thermal damage to the infrared system during the heating time, as suggested by the manufacturer. The heater was used to heat up the workpiece to a required temperature and then removed from the workpiece material during the turning tests. The data was analysed using the Quick-view Software to take thermal history data at various cutting conditions as shown in Figure 4-17.

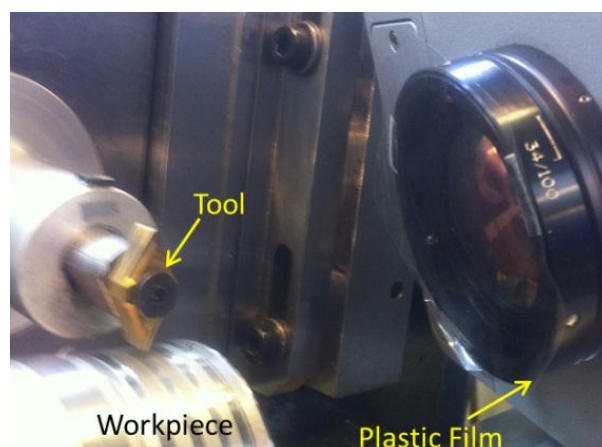


Figure 4-16: Protecting thin plastic film used to protect lens from chips

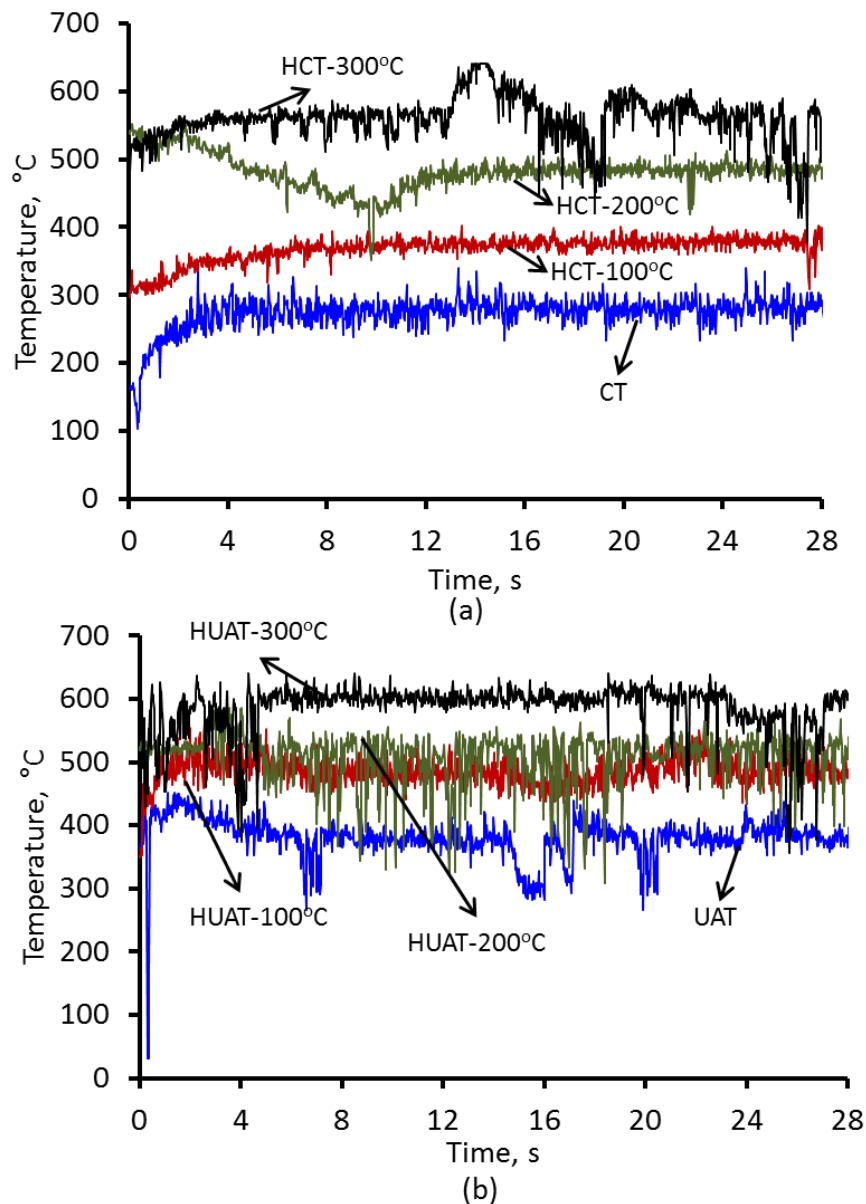


Figure 4-17: Temperature history of the process zone at 300  $\mu\text{m}$  depth of cut, 10 m/min cutting speed; (a) HCT and (b) HUAT

#### 4.5.5. Experimental Results and Discussion

A special study was undertaken to track the process-zone temperatures in CT, HCT and HUAT. In this section, thermal results obtained at various cutting conditions in CT, HCT and HUAT are analysed in detail. The temperature distribution of the process zone in CT and UAT is shown in Figure 4-18 and Figure 4-19, respectively. A relatively higher temperature level was observed in the process zone in UAT when compared to CT. The temperature in the process zone increased with application of external heat to the workpiece material. The temperature in the

cutting region in HCT at 300°C externally applied heat to the workpiece materials and 300  $\mu\text{m}$  depth of cut, was approx. 250°C higher when compared to conventional turning (Figure 4-20). This increased in temperature in the process zone was gradual with the amount of external heat provided to the workpiece material and a rise of approximately 95°C was observed when the temperature of the workpiece material was heated to 100°C. A further increase of 92°C was observed if temperature of the workpiece was increased to 200°C.

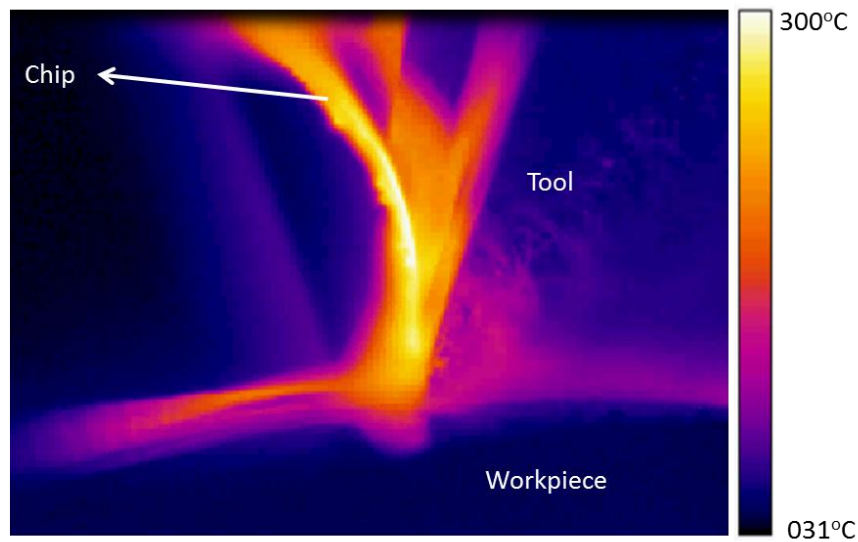


Figure 4-18: Temperature of the process zone in CT using a micro - lens

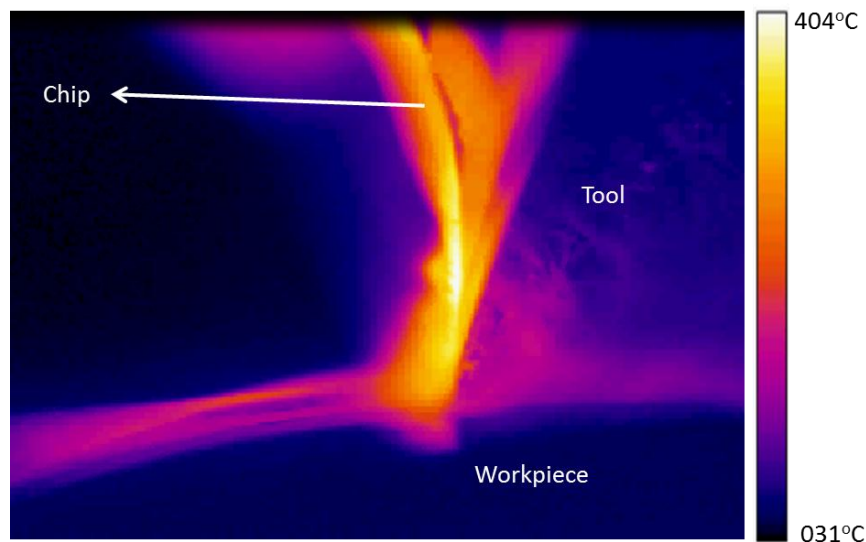


Figure 4-19: Temperature of the process zone in UAT using a micro - lens

A rapid fluctuation in temperature of the process was observed when the tool came in contact with the workpiece in CT, UAT, HCT and HUAT. However, the chip temperature

increased rapidly and finally reached to a steady state level. The thermal history of the process zone for CT, HCT, UAT and HUAT was recorded in experimentation and are shown in Figure 4-17. A marginal increase (less than 15°C in) in chip temperature was observed using micro-lens of the infra-red system. These results were achieved for CT and UAT and showed the effect of relative distance between the process zone and camera lens. However, in the current study, calibrated distance was kept in all tests to get accurate results in conventional and hybrid turning processes for standard lens.

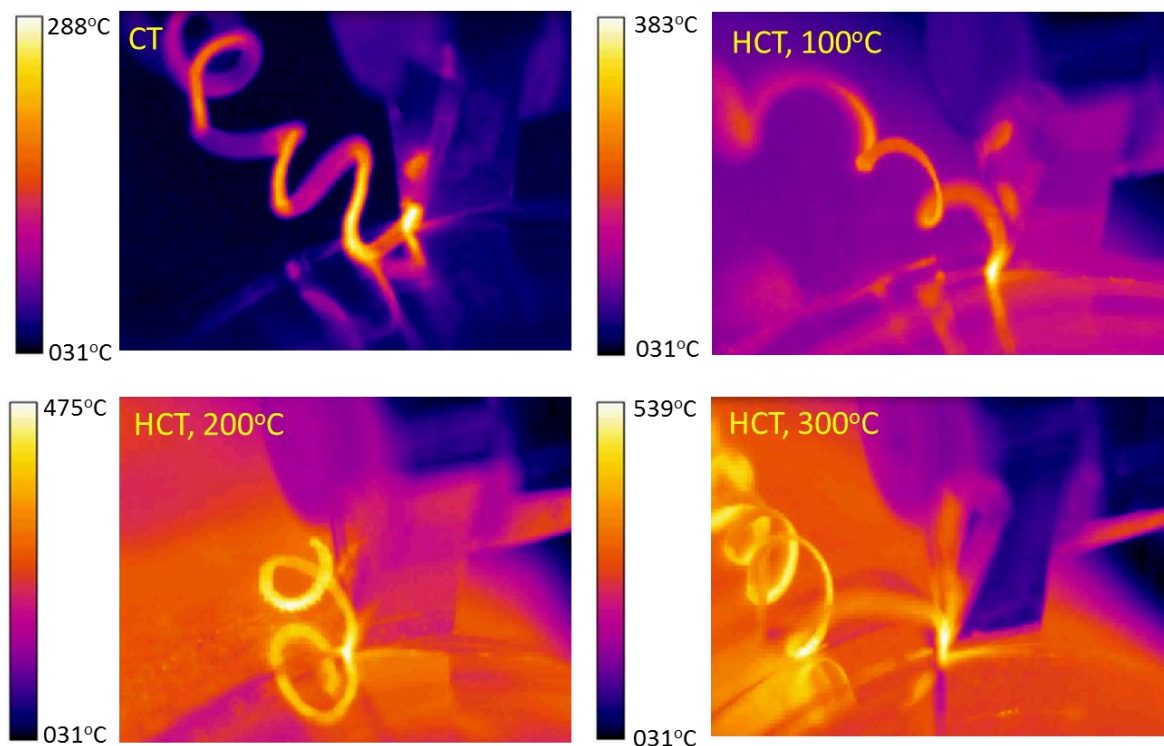


Figure 4-20: Thermal analysis of the process zone in CT and HCT using a standard lens ( $V = 10$  m/min;  $a_p = 0.3$  mm)

Similarly, the temperature of the chip in the cutting region increased with application of ultrasonic vibration in tangential direction in both in UAT and HUAT when compared to CT and HCT, respectively, as shown in Figure 4-21. The possible causes for this are the effect of additional factor linked to dissipation of vibration energy [101]. The temperature of the cutting region in HUAT was approx. 190°C higher at 300°C initial temperature of the workpiece when compared to that observed in UAT. The process zone temperatures in HUAT were 84°C and 115°C higher when compared to those obtained in UAT, at 100°C and 200°C of

initial temperature of the workpiece, respectively, at 300  $\mu\text{m}$  depth of cut and 10 m/min cutting speed.

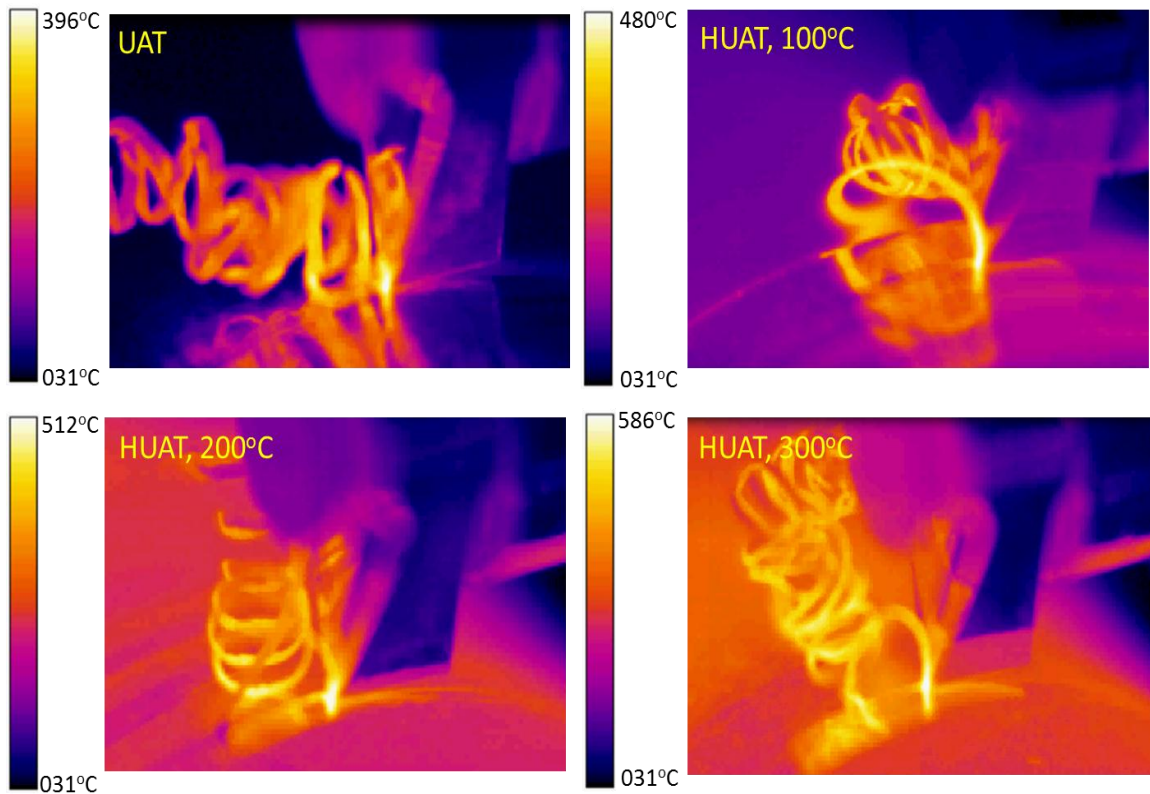


Figure 4-21: Thermal analysis of the process zone in UAT and HUAT using a standard lens ( $V = 10$  m/min;  $a_p = 0.3$  mm)

A noticeable increase in temperature of the cutting region was observed with the increase of cutting speed in conventional and hybrid turning processes, as expected. Furthermore, a rise in temperature of the cutting region with an increase in depth of cut was also observed in CT, HCT, UAT and HUAT (Figure 4-22), as expected.

A reduction in plastic heat generation, both in HCT and HUAT was observed at various pre-heated temperature value. However, at 100°C, the observed reduction was minor. When the temperature of the process zone was increased above 100°C, the plastic heat generation decreased significantly, reducing the amount of work required to remove the given amount of material. The reduction in plastic heat generation was observed in both HCT as well as in HUAT for various cutting conditions as shown in Figure 4-23.

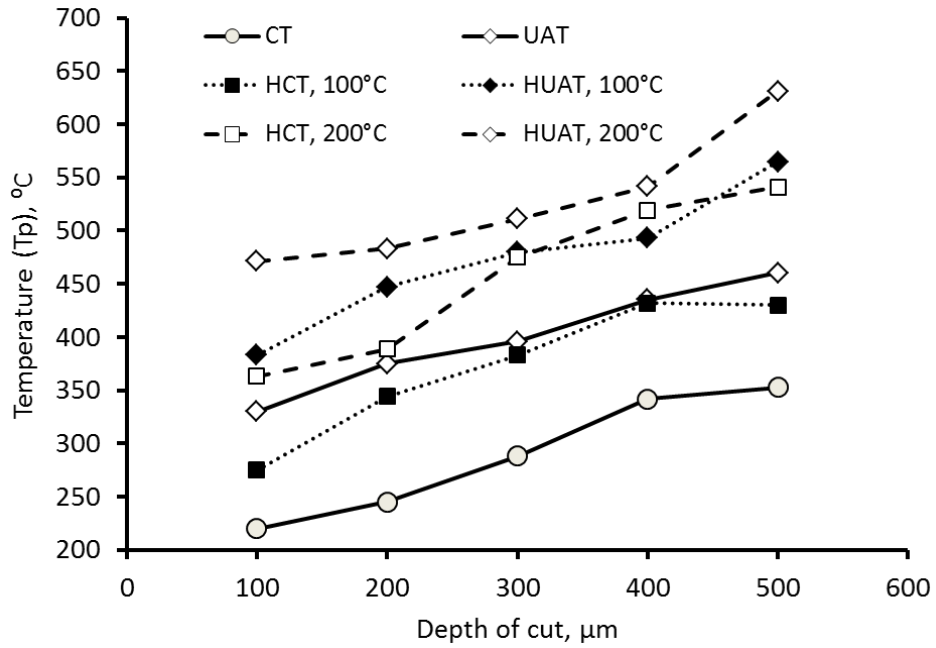


Figure 4-22: Temperature magnitude of chip in HCT and HUAT at different depth of cut and cutting speed of 10 m/min

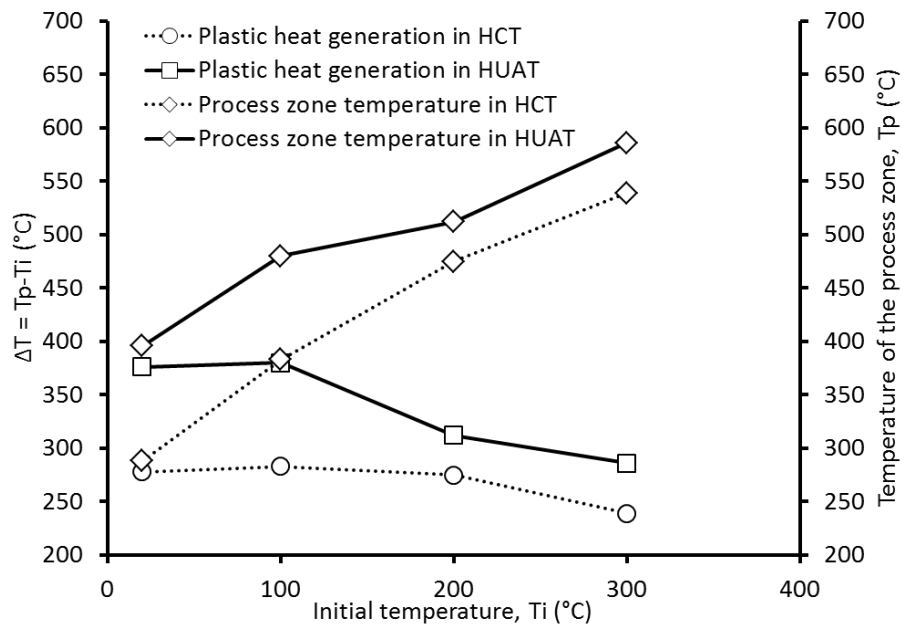


Figure 4-23: Temperature levels in the chip in HCT and HUAT at different initial temperature of the workpiece material

To sum up the above discussion, the temperature in the process zone was analysed using infra-red thermography and it was observed that the temperature in the process zone was approx. 80°C to 100°C higher in UAT when compared to CT. The temperature in the process zone increased with an increased in cutting speed as well as with depth of cut. Similarly, application of external heat to the workpiece material increased the process zone

temperature and decreased the plastic heat generation in HCT and HUAT. In addition to the above, the temperature of the process zone was observed high in HUAT when compared to CT.

One of the main limitations of the above analysis was that the contact region of the tool and workpiece was not visible to the infra-red system. Temperature of the chip closed to the deformation zone was measured in experimental tests. However, a good relative prediction of temperature in the process zone was achieved.

## 4.6. Surface Quality

### 4.6.1. Introduction

Characterisation of surface topography of the finished workpiece is essential in assessing machining quality. Insights into the fatigue strength of the machined component may also be gained from such a study [191]. Most of the cost associated with the machining of Ti alloys comes from the large number of subsequent finishing processes needed to achieve a correct size and finish of the workpiece. The texture formed on a machine surface is generated by the generation of different machining effect including speed, feed, cutting fluid and workpiece material. The Zygo interferometry was used to quantify the improvement in UAT and HUAT in machining of Ti-15333.

### 4.6.2. Samples Preparation

For surface roughness analysis, the experimentation time was increased to get an appropriate surface area for surface topology. A round Ti15V3Cr3Al3Sn bar, having a length of 500 mm and diameter of 65 mm bar of Ti-15333 was turned in the axial direction for a distance of 10 mm (X- axis in Figure 4-24) using CT and UAT as shown in Figure 4-24. Similarly, the same procedure was repeated for HCT and HUAT keeping the same cutting conditions to analyse the surface roughness of machined specimens.

In literature, a large number of surface texture parameters are available to quantify the surface quality of a machine specimen [192]. 2D parameters, such as  $R_a$ , was the most calculated in evaluating the surface of a machined workpiece due to the widespread use of contact instruments, also called stylus profilers. The arithmetic average of filtered roughness

deviations in relation to a center-line along an evaluation length is represented by  $R_a$ . Similarly,  $S_a$  and  $S_q$  are the arithmetic mean and root mean square of roughness parameters evaluated for 3D surface. These three parameters were used to quantify the surface roughness of a machined specimen using conventional and assisted turning processes.

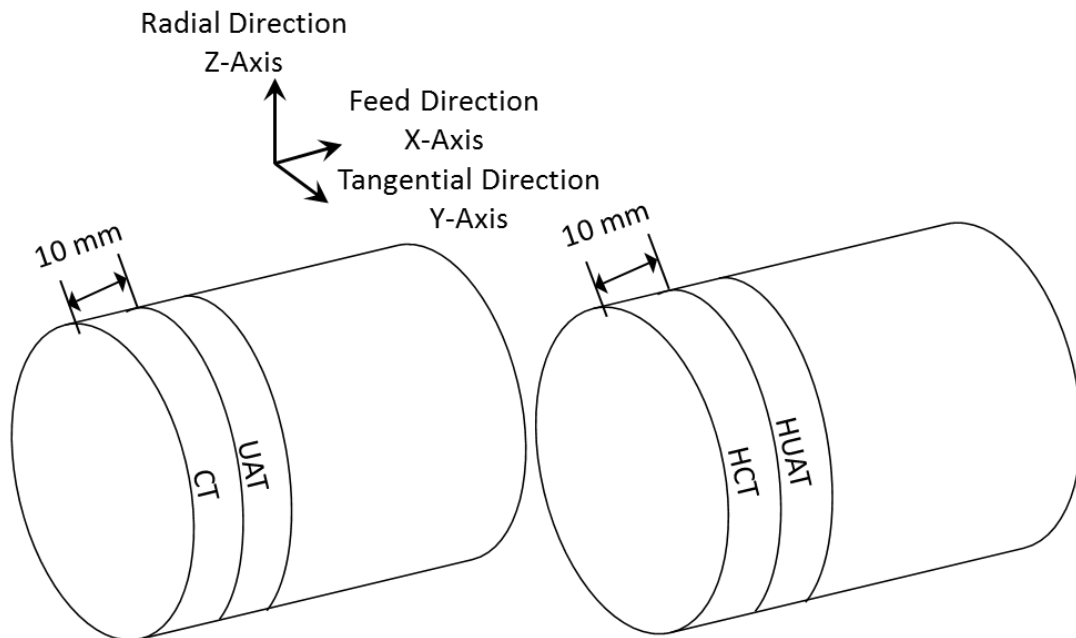


Figure 4-24: Sample for surface topography

#### 4.6.3. Surface Analysis Using Zygo® Interferometry

The Zygo® newview-5000 interferometry equipment was used to analyse surface roughness of machined specimens as shown in Figure 4-25. Special magnets were used to mount the specimen on the machine bed and were moved just beneath the lens for optical scan. The movement of the workpiece on the machine bed was controlled through a X-Y lever of Zygo® equipment. The scan area was focused properly using the Z lever of equipment. Surface scans of machine specimen were obtained for various sections of machined specimen.

#### 4.6.4. Results and Discussion

A significant reduction in all roughness parameters was observed for HUAT and HCT when compared to CT (Figure 4-26). In HUAT, an improvement in surface topography parameters in excess of 50% was found. Therefore, a significantly improved surface quality in the newly developed hybrid machining process was demonstrated. Figure 4-27 compares the underlying texture of typical surfaces machined. These are represented as 2D field plots. Distinct

periodicity can be observed for the conventionally turned surface whereas for the enhanced machining technique this regularity is somewhat curtailed. The surface quality in HCT and HUAT was the same in statistical terms.



Figure 4-25: Experimental setup for surface roughness analysis using Zygo® interferometry

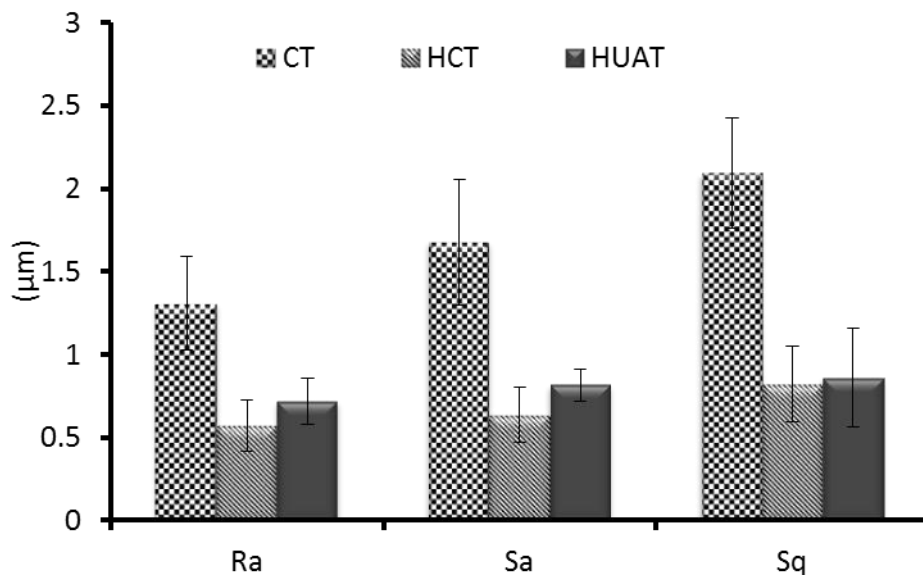


Figure 4-26: Surface roughness at various temperatures ( $V = 10$  m/min;  $a_p = 300$  μm)

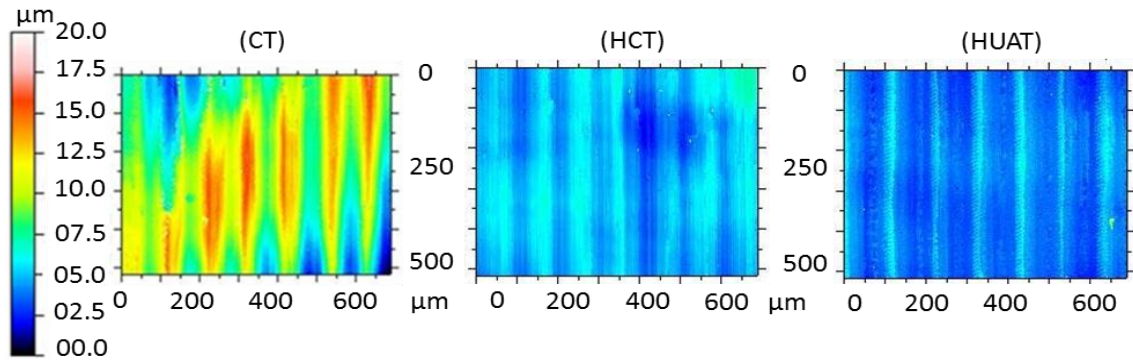


Figure 4-27: Contour plot of surface roughness ( $V = 10$  m/min;  $a_p = 300$   $\mu\text{m}$ )

A significant reduction in universally used centre line average ( $R_a$ ) was observed in UAT, when compared to CT. Zygo scans of the machined surfaces are shown in Figure 4-28 at various temperature and 200  $\mu\text{m}$  depth of cut. A 48% improvement in the  $R_a$  value was observed in UAT when compared to CT for various cutting conditions. However, application of external heat (300°C) to the workpiece materials, further improves it (26%) when compared to UAT (Figure 4-28). Application of external heat source makes the workpiece material 'softer', facilitating easier chip flow relative to the tool surfaces, resulting in an overall improvement in the surface roughness of the machined specimen [17]. Therefore, reduction in the surface roughness was observed in HCT and HUAT when compared to CT and UAT, respectively.

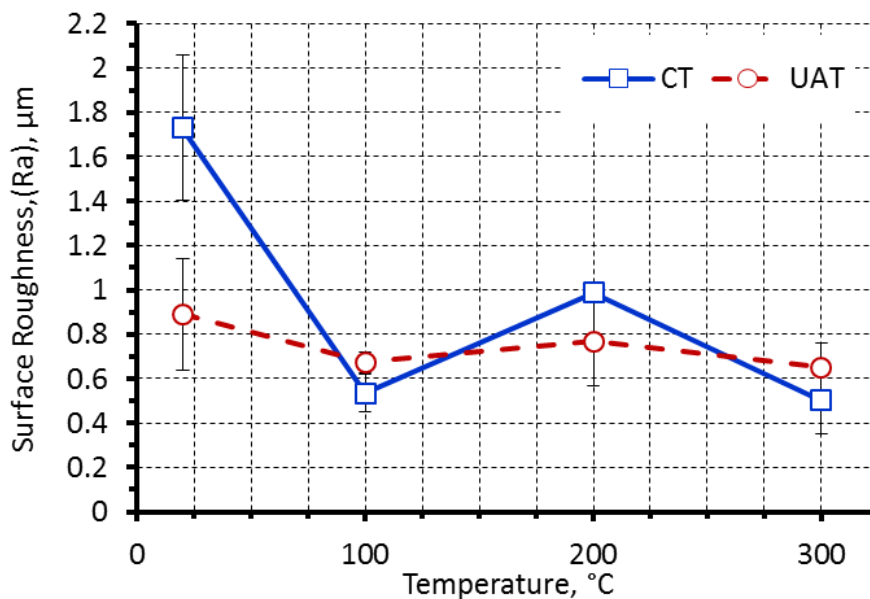


Figure 4-28: Surface roughness at various temperatures; cutting speed  $V = 10$  m/min; depth of cut  $a_p = 200$   $\mu\text{m}$

## 4.7. Metallographic Tests and Chip Shapes

### 4.7.1. Light Microscopy of Machined Samples

The Ti alloys are sensitive to oxidation and metallurgical changes, when exposed to high temperature for an extended period of time (approx. at 450°C for more than 1 hours) [189]. In the current study, the entire tests were carried in open air without protective atmosphere. Additionally, the temperature of the tool-workpiece interaction zone reached up to a couple of hundred degrees centigrade in conventional and hybrid turning processes. Therefore, light microscopy of machined specimens was carried out using Nikon Optiphot, with a GXCAM-5 acquiring system, initially, to investigate the behaviour of the studied material in CT, HCT, UAT and HUAT. The chips produce in the various turning process were also analysed to investigate material response and its shape in conventional and hybrid turning processes.

### 4.7.2. Methodology

The application of external heat and the amount of heat generated during machining of Ti alloys can generate a suitable environment for the oxidation of Ti alloys. From the thermal analysis, it has been observed that the temperature of the cutting region reaches beyond 510°C at some speed-feed combination particularly, in HCT and HUAT. Therefore, the machined specimens were investigated using light microscopy operated at extreme cutting conditions. All the light-microscopic analysis was carried out for 500 µm depth of cut and the 300°C temperature of the workpiece in hot machining. In actual machining, the amount of heat generated at the tool-workpiece interaction zone is for a fraction of time and the chances of getting any oxidation of the Ti-alloys become inconsequential, however, in hot machining, bulk heating methods were used to heat up the workpiece material to a required temperature. Furthermore, the temperature generated in hot machining was higher when compared to CT and UAT. Therefore, investigation of the metallurgy of machined specimens was worth-noting.

A Horizon conventional lathe machine was used to machine a bar of Ti-15333 in the axial direction for a distance of 7-8 mm using conventional turning conditions followed by UAT. The bar was removed from the lathe machine and a new bar of Ti-15333 was mounted on the lathe machine. The workpiece was pre-heated to 300°C and followed by HCT and HUAT in

axial direction for the same cutting conditions. The machined specimens obtained from CT, HCT, UAT and HUAT were cut off from their parent materials and then hot mounting technique was used to mount in a plastic resin. For cutting of specimens for light microscopy and SEM analysis, a shark saw (Shark-281 SXI) was used to cut the specimen at low feed rate (0.001 mm/min), cutting speed (5 m/min) and presence of coolant to eliminate the thermal effect produced by the shark saw.

In the mounting of samples, the initially choice was Buehler Bakelite resin, offering lower shrinkage and superior edge retention. A Struer mounting press, with a mounting pressure of 20 kN at 180°C was used for specimens potting in the plastic resin as shown in Figure 4-29. Initially, an edge retention problem was observed in polishing operation that prevented effective inspection of the specimens. The sample also required high polishing time and high pressure for preparation of mirror surface. In order to overcome the above problem, a layer of very hard Buehler Epomet-G resin was used in combination with Buehler Transoptic as a support resin in the moulding of the specimens. The sample was kept in the Stuer Mounting press for 13 min and applied a constant pressure of 20 kN and temperature of 180°C.

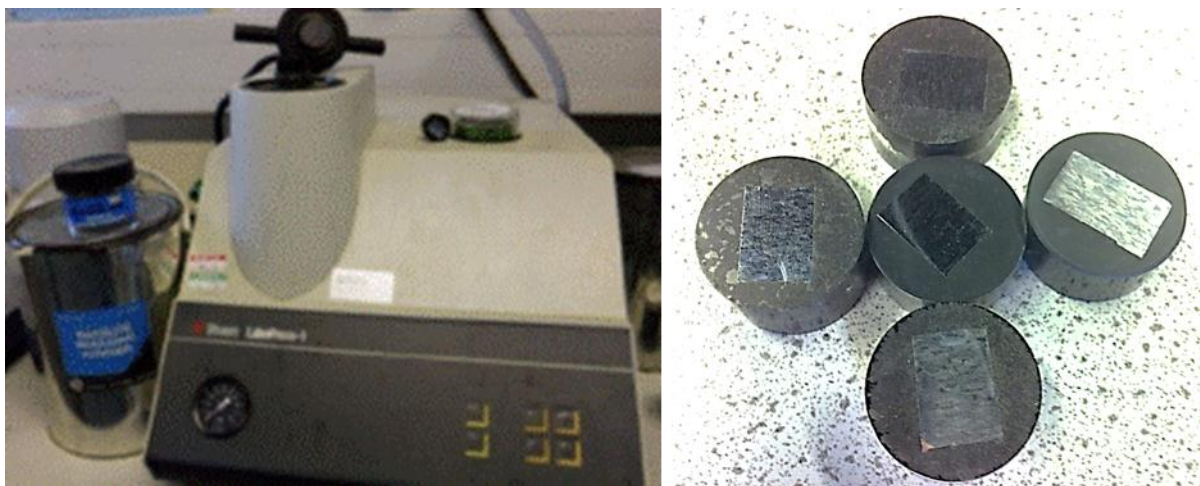


Figure 4-29: Stuer mounting press and prepared samples

A manual polishing of samples was carried out using silicon carbide wet grinding paper with increasing grit sizes up to 4000. The Ti alloy is tougher and required high polishing time compared to other softer materials. The polishing operation was first carried out on Buehler Taxmet 1500 with 6 nm diamond paste. The specimens were washed using tap water and polishing was continued on Buehler microcloth with 1 nm diamond paste and finally Buehler

Chemomet with 20 nm colloidal silica. The polished samples were then washed and etched with Kroll solution consist of 2% HCL, 2% HF and 96% H<sub>2</sub>O. The etching was carried in five steps until the grain becomes visible with a naked eye due to large grain size (approx. 1 mm) as reported by Alexey, *et al* [189]. The etched samples were analysed with optical microscope and images of the samples were taken for further analysis.

#### 4.7.3. Results and Discussions

The light microscopy of the machined specimen showed no signs of oxidation and metallurgical changes even in HCT and HUAT (Figure 4-30). The grain size in Ti-15333 was not uniform and was changing throughout the specimen of the material as reported [189]. According to previous studies, the needle like precipitate was observed in Ti-15333, exposed to temperature above 450°C for more than 1 hour. The specimens were investigated at different magnification and no signs of alpha-precipitate and significant changes in grain size were observed as shown in Figure 4-31. Hence, the applied external heat to the workpiece and plastic heat generation in the process has no significant effect on the grain size as well as on oxidation of the machined specimen. The prime reason for no alteration in the grain structure of the workpiece material was that the generated temperature in the process zone reached somewhat 650°C at 500 µm depth of cut in HUAT. However, the exposure time was much less compared to 1 hours as reported by Alexey, *et al* [189]. Therefore, this new hybrid machining technique produced a considerable reduction in cutting forces and noticeable improvement in surface roughness [97] with no oxidation and metallurgical changes in the workpiece materials.

The light microscopic analysis showed no signs of needle like structure that is typical of  $\alpha$ -Ti and alteration in the sub-surface layers grain structure of CT, HCT, UAT and HUAT machined workpiece as shown in Figure 4-31. Some polishing artefacts were found near the machined surface due to the shrinkage of the mounting resin and the difference in polishing rates. From the optical metallographic analysis, it was not possible to verify any changes in that particular region caused by the turning processes. This result, when associated with the absence of significant hardness changes, could probably rule out the possibility of  $\alpha$ -casing formation in the conventional and hybrid turning processes of Ti 15333.

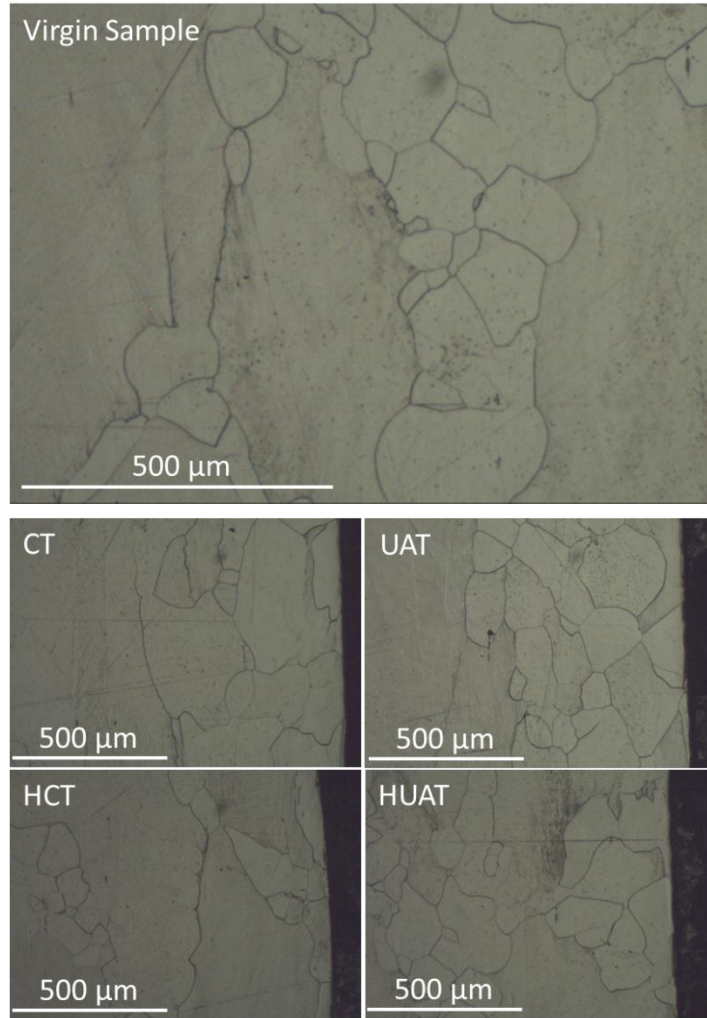


Figure 4-30: Light microscopy of the sub-surface layers in Ti-15333 after CT, UAT, HCT and HUAT

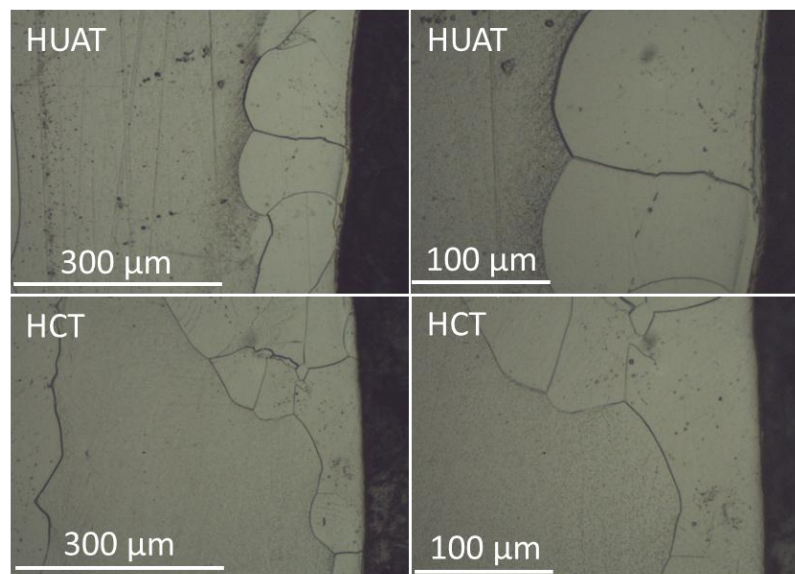


Figure 4-31: Light microscopy of machined specimen at higher magnifications

#### 4.7.4. SEM Analysis of the Machined Specimens

A thin area close to the cutting region was observed differently in light microscopy, the prime reason can be either edge retention problem or affected machined surface during machining process. Therefore, new samples were prepared and polished. The specimens were analysed with the field emission gun scanning electron microscope (FEGSEM) as shown in Figure 4-32. The FEGSEM required high surface quality for analysis; therefore, based on the previous experience, a new technique was used to polish the specimens. During polishing operations, samples were wetted with H<sub>2</sub>O<sub>2</sub> (10% solution) to improve the quality of the polished surface. The obtained surface has much better surface finish compared to the previously obtained specimens.



Figure 4-32: Scanning Electronic Microscope used in experiments

The polished samples were loaded to Carl Zeiss Leo 1530 VP electronic microscope, featuring variable chamber pressure for analysis. The system was capable to analysed specimens at a resolution of 2 nm in optimal conditions. The system was also capable of backscatter capability which was required to investigate the possible phase changes during the turning process. The polished, etched samples were loaded to the SEM machine and analysis of the samples was carried out. During the investigation, a highly deformed layer of approximately,

3-5  $\mu\text{m}$  was observed close to the cutting surface. The region was etched differently and further investigation was needed to identify the possible reason for this region as shown in Figure 4-33. It was reported in literature [189], that a thin layer of alpha-precipitate was observed in Ti-15333, when annealed at a temperatures of 450 °C for one hour, and dense precipitates when annealed at 600 °C. However, in turning, the process temperature of the process zone reaches up to 650°C in extreme conditions for a short period of time as reported in Section 4.5. But still, the specimens need further investigation to analyse the highly deformed region and the possible presence of  $\alpha$ -Ti formation which was still not investigated through the SEM analysis.

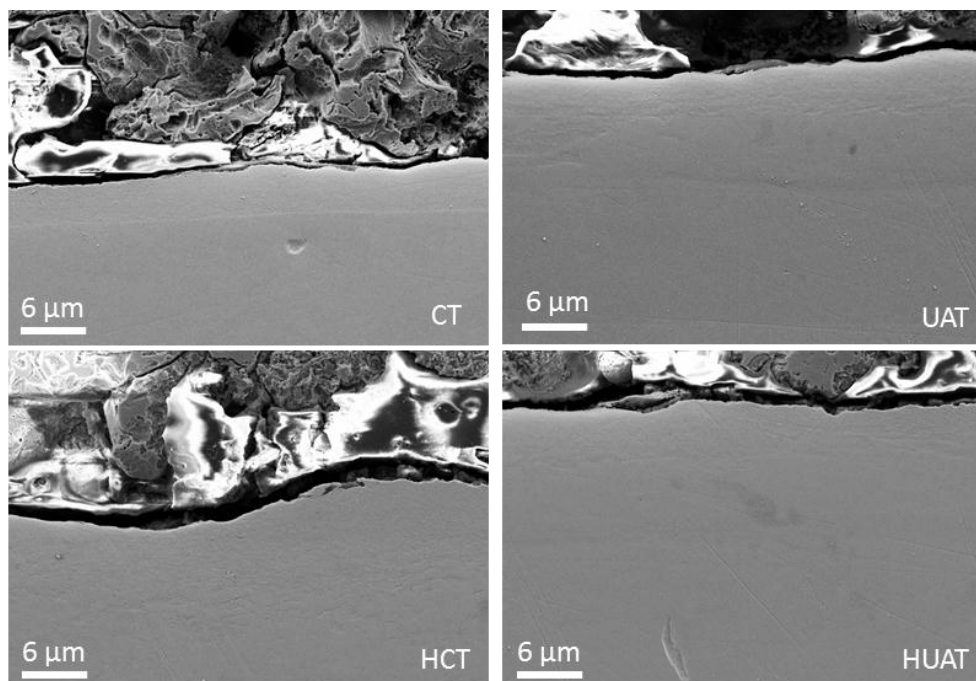


Figure 4-33: SEM analysis of machined specimen

Hence, the backscatter analysis of the samples was carried out. The backscatter effect, is in fact greatly dependent on the average atomic weight of the studied area, the microscope would see areas at different average atomic mass that etched differently, this could be for a number of reasons including the formed  $\alpha$ -Ti. The presence of  $\alpha$ -Ti was excluded by the backscatter analysis as shown in Figure 4-34. No visible signs of  $\alpha$ -Ti were observed in the backscatter analysis. However, it was concluded that the etched area near the cutting edge in CT, HCT, UAT and HUAT was the deformed material observed in the analysis of chip formation of Ti-15333 through a quick stop experiments [189]. However, the deformed

regions in all samples have a thickness of 2-5  $\mu\text{m}$  and were slightly etched in UAT and HUAT when compared to CT and HCT, respectively.

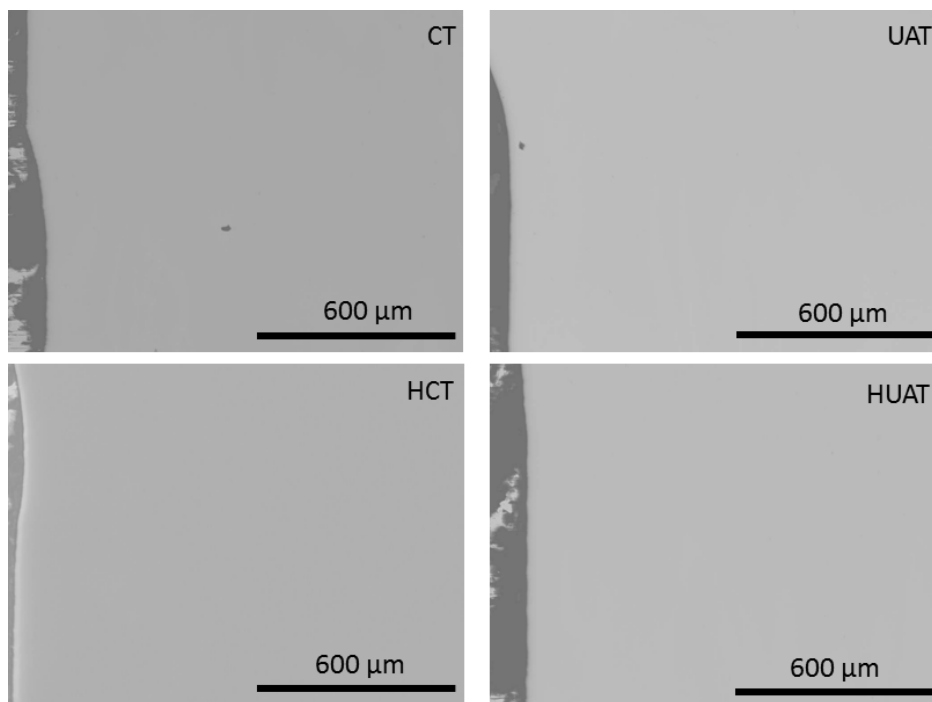


Figure 4-34: Backscatter analysis of machined samples

#### 4.7.5. Chip Analysis

In turning experiments, continuous chips were obtained in turning of Ti-15333 in CT, HCT, UAT and HUAT. The chip samples were collected in turning experiments and was analysed through Carl Zeiss Leo/Cambridge Stereoscan-360 electronic microscope. The chips were mounted on the fixing plate and both sides of the chip (the one in contact with the rake face named as front side and chip surface opposite to it is called back side) were exposed for SEM analysis. The analysis showed continuous chip formation in CT and UAT as shown in Figure 4-35. The chips were generated by material separation in the process zone. The deformed material accumulated in the form of shear planes. The study was carried out to investigate any serration in the chip formation in the turning process. However, the cutting speed was low and no serration in chip formation was observed.

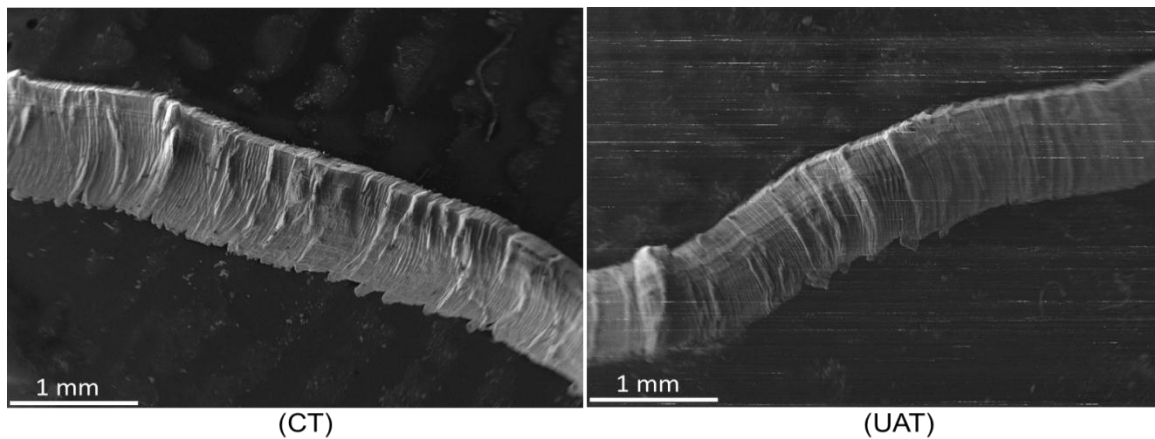


Figure 4-35: Chip shape in CT and UAT

The application of external heat to the workpiece material in HCT and HUAT did not produce any significant difference in the chip morphology. Continuous chips were observed at various cutting condition in HCT and HUAT as shown in Figure 4-36 and Figure 4-37, respectively. The shear deformation of material produced continuous chip with a highly deformed zone. However, in the current study, cutting speed up to 70 m/min was used in the analysis but the observed chips were continuous in HCT and HUAT. The chips were also investigated at higher magnification and continuous line on the front side of the chip was observed in CT and HCT. These lines were generated by the tool edge interaction with the workpiece material. It was observed that the chip in contact with the tool produced continuous lines on the front side of the chip as well as on the machine surface due to severe deformation and shearing of material. These lines are more visible at higher magnification and are shown in Figure 4-38. The overall chip shape was continuous with no visible sign of serration as observed in high speed cutting of beta-titanium alloys [193].

In UAT and HUAT, vibration is superimposed on the cutting tool caused the tool to apply vibro-impact load on the chip-workpiece. In one complete cycle of vibration, the tool penetrated into the workpiece material at approach and penetration stages whereas retracted back during the retraction and withdrawal stages. The vibration imposed on the cutting tool has a frequency of 20 kHz and amplitude of 8  $\mu\text{m}$ . Therefore, in the chip analysis, small indents were observed on the chip surface in contact with the tool material as shown in Figure 4-39. The indents were at regular interval and were due to the vibro-impact of the tool on the workpiece material in the tool forward and backward movement in UAT and HUAT.

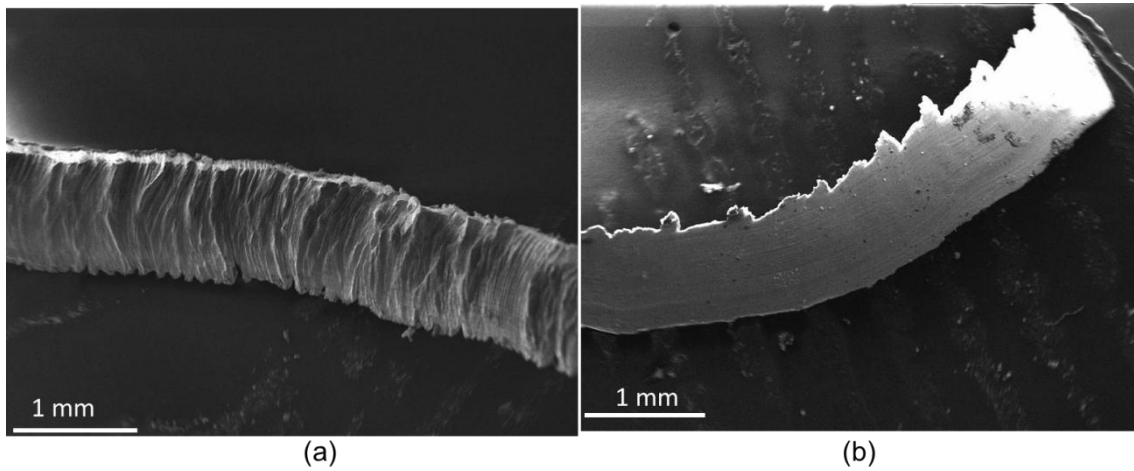


Figure 4-36: Chip shape in HCT (a) front side of chip and (b) back side of chip

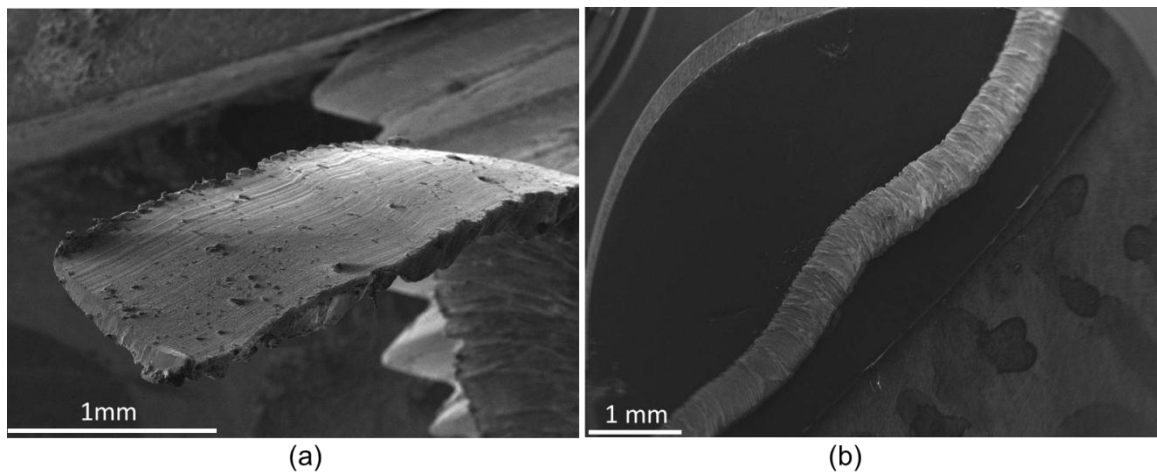


Figure 4-37: Chip at higher magnification in HUAT of the chip (a) back side and (b) front side

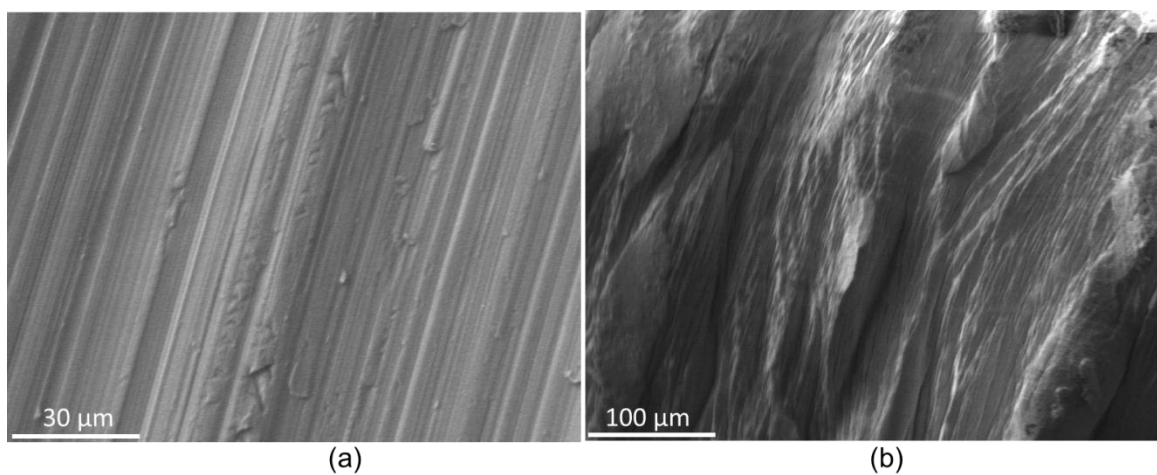


Figure 4-38: Chip shape at higher magnification in HCT (a) front side of chip and (b) back side of chip

In addition to above, some light microscopy of the chips cross-section was also carried out. A continuous chip with uneven thickness was observed in CT and UAT (Figure 4-40a and Figure 4-40b). A sudden increase in the chip thickness was observed at particular location of the chips. The possible reason can be the irregular grain size of the alloys. Whereas in HCT and HUAT, application of external heat made the material softer resulted in a slight increase in the chip thickness when compared to CT and UAT, respectively. A much smoother chip shapes were observed in HUAT and HCT when compared to CT and UAT as shown in Figure 4-40.

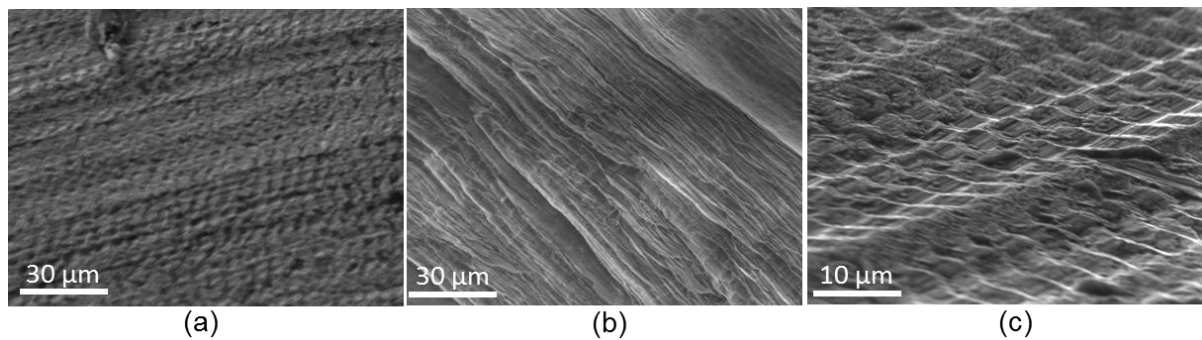


Figure 4-39: Chip shape at higher magnification in HUAT (a) back side; (b) front side and (c) Back side at higher magnification

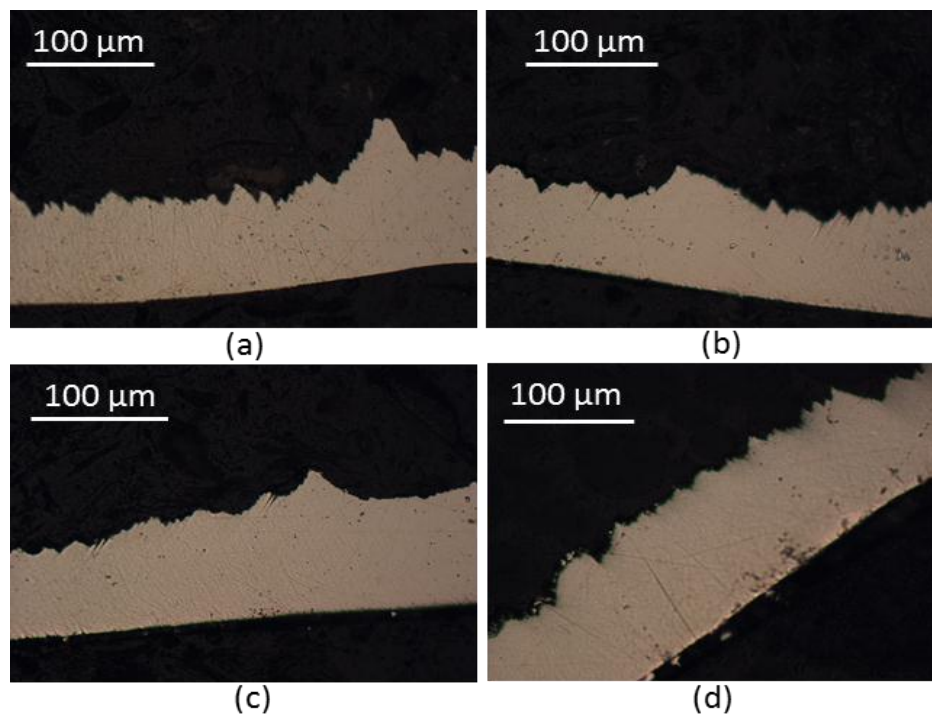


Figure 4-40: Light microscopy of the chips in (a) CT; (b) UAT; (c) HCT and (d) HUAT

Therefore, based on the above analysis, continuous chips were produced in CT, UAT, HCT and HUAT. In literature, the serrated chip formation was reported in the turning process of various Ti- alloys at high cutting speeds. Hence, in simulation of those alloys, various modified material models were used to get a closer resemblance between simulated and actual chip shape, however, in the current work, continuous chips were produced with various cutting conditions and was verified in our numerical model.

#### **4.8. Surface Hardness Evaluation of Machined Specimens**

The thermal analysis of Ti-15333 shows significant temperature rise in the process zone at various cutting conditions. The main sources of heat generation in the process zone are the plastic heat generation and heat due to frictional effect. The high temperature was observed in UAT when compared to CT. Similarly, application of external heat to the workpiece material increased the process zone temperature and higher temperatures levels were observed in HUAT when compared to CT, UAT and HCT at various cutting conditions. The application of external heat in HCT and HUAT, in addition to the heat generated in the process zone generated a thin layer of highly deformed layer as discussed in the previous section. The generated harder layer was proven to the formation of micro cracks, thus reducing the fatigue life of machined components. The possibility of alpha-casing and grain growth was nullified as described in the previous section. However, the hardness of a machined surface was investigated on various specimens. The analysis was carried out using micro-hardness directly on the machined surface and nano-hardness tests on the cross section of a machined specimen. The Vickers indenter was used to investigate the hardness of a machine surface away from the machined edge and analysed the effect of the harder layer formed in CT, UAT, HCT and HUAT.

##### **4.8.1. Experimental Methodology**

The experiments were carried out in two stages, in the first phase; a nono-indenter was used to carry out hardness away from the machined surface at various locations. The samples were mounted in the plastic mould and was polished using different grade of polishing papers to get a mirror shape surface. A second set of experiments was carried on the machined surfaces using different turning processes, using a micro-indenter (Vickers indenter) without

any modification to the machined surface. All experiments were carried out on NanoTest NTX3 as shown in Figure 4-41. Its outstanding versatility and sensitivity allowed performing fully automated tests on several areas of the machined surface. The various features of the NanoTest are listed in Table 4-9

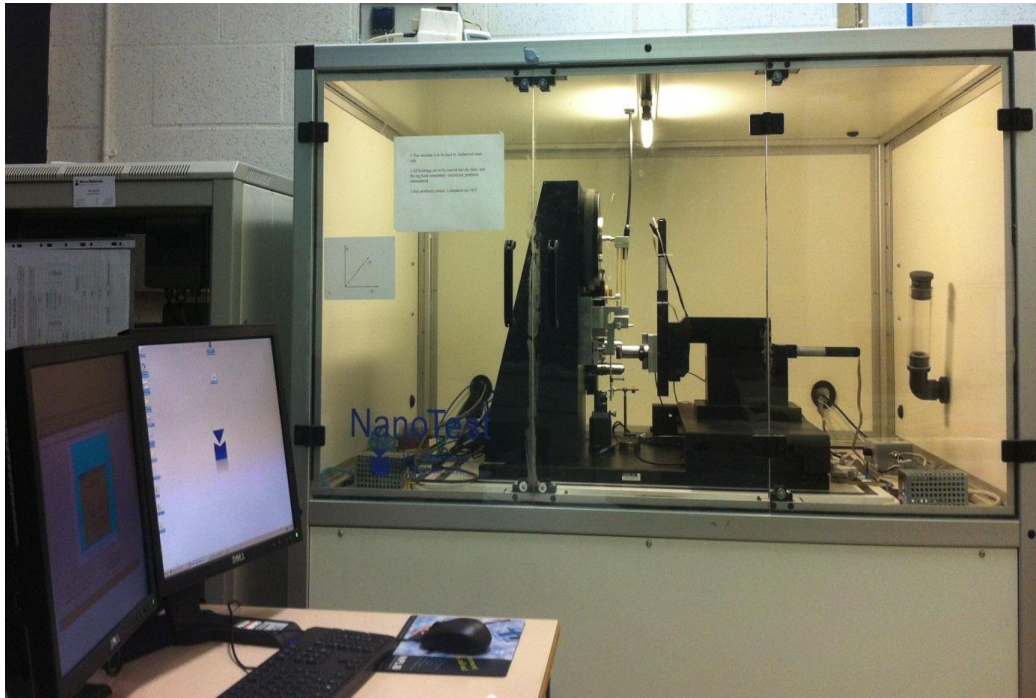


Figure 4-41: Nano tester (NanoTest NTX3) used in the analysis

Table 4-9: Features of Nano Test NTX3 used for nano and micro indentations

Parameters	Magnitude
Maximum load	20 N
Load resolution	$\leq 100$ nN
Maximum displacement resolution	0.05 nm
Force noise floor	100 nN
Maximum displacement	80 $\mu$ m
Thermal drift	$\leq 0.004$ nm/s

In both the tests, the specimen was glued to the sample holder using cyanoacrylic adhesive. The specimen was moved to the built-in microscope in the system to get a good quality

focused image of the surface for appropriate location selection in indentation experiments. In nano-indentation tests, three schedules were defined for the indentation to get reasonable data of the studied region in CT, HCT, UAT and HUAT. The first defined schedule of experiments was carried out in a diagonal path away from the machined surface edge of a workpiece. The purpose of this schedule was to get a maximum number of data points close to the highly deformed layers. The second and third indentation schedules were defined in the vertical direction away from the machined surface.

Similarly, in the micro-indentation test, the sample was cut and glued to the sample holder in the machine. Several indentation tests were carried out at different locations of a machined specimen. The pattern of experiments was linear in shape and the distance between each indentation was 150  $\mu\text{m}$ . Each experiment was repeated two times to get reasonable point data. However, in experimentation, the main problem was the surface roughness. High surface roughness was observed in CT when compared to UAT, HCT and HUAT. Therefore, the indentation on the peak of asperity of a machined surface yield lower hardness values compared to the valley indentation hardness value. A series of experiments were carried out and an average of hardness value was used in the analysis.

#### 4.8.2. Results and Discussions

Nano-indentation tests were carried out on specimens away from the machined surface. Initially, high indentation load was used to get the hardness value of the specimen machined in CT and hybrid turning processes. However, due to edge limitation, lower values were observed closed to the cutting edge. The edge effect in nano-indentation simulation was observed by Demiral *et al* [194]. A 20% reduction in the reaction force on indenter was observed due to edge effect. This effect was observed for different loading conditions. Based on the initial tests loading conditions, however, the same results were observed even at lower load conditions. A lower hardness value was observed close to the machined surface in all tests and the prime reason in reduction of hardness was the edge effect reported in [194]. A gradual rise in the hardness value was observed moving away from the machined edge in all turning processes. The calculated hardness value of the specimens at different indentation points is shown in Figure 4-42. However, it was really hard to predict any effect of the thermal load generated at the process zone in the turning process. Based on the results

obtained from the nano-indentation test, no significant claim can be concluded from the results. Hence, a new set of experiments were carried out using the micro-indenter on the actual machined surfaces without any alteration to the machined surface.

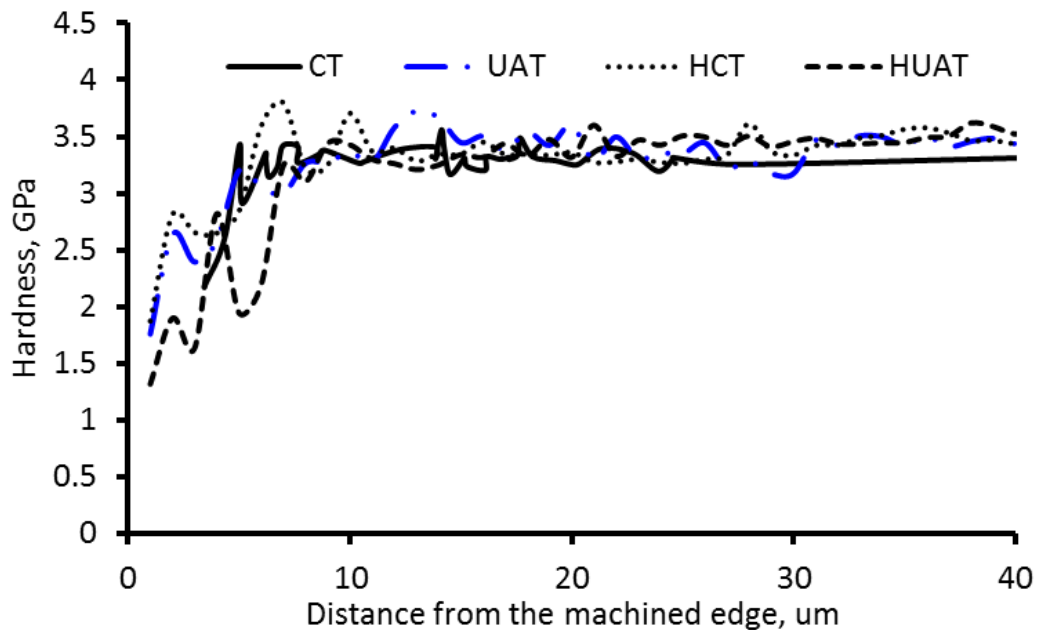


Figure 4-42: Nano-Indentation results obtained at various locations away from machined surface

The bulk properties of the alloy were then investigated to be used as a benchmark against the valued obtained from the machined surface. Furthermore, the sample obtained from workpiece machined during CT, UAT, HCT and HUAT was tested and the results obtained was analysed for further analysis. The main problem faced in macro indentation was the surface roughness. A better surface roughness was observed in the hybrid turning processes when compared to CT. Therefore, the peaks and valleys formed on the machined surface in the turning process produced significant deviation in all test results. The hardness of the machined sample was slightly high compared to the virgin material, however, the standard deviation obtained in tests of machined specimen was high and based on the overall hardness levels, it can be concluded that no significant difference in the hardness value of the workpiece material after CT, UAT, HCT and HUAT was observed.

The surface hardness of HCT and HUAT appeared to be slightly higher; the possible reason can be the work hardening of material during the machining process and additional heat supplied to the workpiece material. In the turning process, the non-linearity of material

resulted, strain hardening of the material, which are well represented in UAT and HUAT. The results obtained in a micro-hardness test of a machined specimen are shown in Figure 4-43.

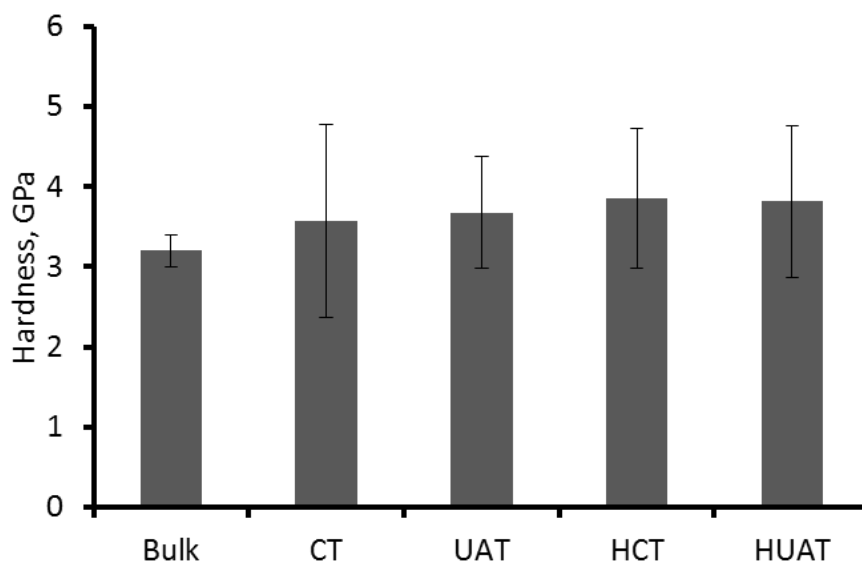


Figure 4-43: Micro-hardness of machined specimen

Since the strain rate to which the material was subjected during UAT and HUAT was higher than in CT and HCT, respectively, due to the lower contact time between the tool and workpiece in one complete cycle of vibration. When compared to the total cumulative time, the induced deformation resulted in a high strain-rate and high strain-hardening. Therefore, a higher surface hardness in the UAT and HUAT surfaces was observed.

Therefore, based on the above discussion, it can be concluded, that the newly developed hybrid turning process at various cutting conditions resulted in no significant increase in hardness value when compared to CT, UAT and HCT. The imposed vibration on the cutting tool can increase the hardness of a machined surface due to the strain hardening effect; however, the difference in hardness was minimal and can be neglected compared to a significant reduction in cutting forces and better surface quality [97].

#### 4.9. Summary

In this chapter, experimental results of a novel hybrid machining technique – *hot ultrasonically assisted turning* (HUAT) – was presented for the machining of  $\beta$ -Ti alloy to

described the advantages in terms of force reduction, temperature of the process zone, metallurgical changes and surface hardness of a machined surface.

Experiments on the turning of Ti-15333 were carried out using conventional and assisted turning techniques. In assisted turning, vibration and heat was applied to the tool and workpiece, respectively. From experimentation the following conclusion was derived:

- A significant reduction in cutting forces was observed with the application of ultrasonic vibration on the cutting tool.
- Application of heat to the workpiece material further reduced the cutting forces, considerably, both in CT and UAT; however, application of an external heat source to the workpiece material was more effective in UAT when compared to CT.
- The temperature of the process zone increases with the application of external heat to a workpiece material. However, temperature of the process zone in HUAT was higher when compared to HCT.
- Externally applied heat to the workpiece material reduced the plastic heat generation making material removal easier for the tool.
- Higher material removal rate was observed in HUAT when compared to CT.
- A significant improvement in surface roughness was observed in HUAT when compared to CT.
- The application of external heat and heat generated at the process zone in CT, HCT, UAT and HUAT does not change the metallurgy of the machined workpiece material.
- In experimentation a continuous chip was observed in CT, HCT, UAT and HUAT.
- No significant difference in the hardness of a machined sample was observed in CT, UAT, HCT and HUAT.

Therefore, this new hybrid turning process (HUAT) can be an effective alternative for the machining of Ti-15333 when compared to CT.

## CHAPTER-5

# Finite-Element Modelling of the Orthogonal and Oblique Turning Processes

### 5.1 Introduction

The use of FE simulation as a practical tool is progressively growing in manufacturing industries due to availability of numerical simulation software, computational power and increase in FE simulation skills. The FE simulations can offer a favourable alternative to expensive and time consuming experimental investigations, if carefully implemented with true insight of physical phenomena to the model. The affordability and reliability of any such simulation provide landmark to determine the usability of the technique. The term affordability here stands for the acceptability of time required for the completion and reliability means the accuracy of the results it produces.

Numerical simulations of machining processes are computationally expensive, partly due to excessive deformation at the process zone and non-linearity of process in term of material modelling, geometric feature of tool/workpiece and contact conditions. In the past, most of the work related to the turning processes was analysed using finite-element simulation with a certain simplifications and assumptions. Most of the work was related to 2D simulation of the orthogonal turning process [10, 101, 158, 165], 3D orthogonal turning process with assumptions and simplifications [4, 7, 8, 167, 174]. Computational time was considerably reduced by those simplifications or assumptions but some time makes the process over simplified particularly in 2D simulations or ignoring at least one force components.

The current FE model of the turning process of Ti-15333 was developed sequentially, first a 2D orthogonal turning FE models were developed for CT and UAT followed by a 3D Orthogonal turning model to study the deformation process in the workpiece under various cutting conditions. Those models were used to understand the characteristics of the process zone, considering two components of forces and ignoring the third component

There is a lack of exhaustive numerical studies in 3D thermomechanically coupled hybrid and conventional oblique turning processes, which can offer more comprehensive knowledge of the stress, strain and temperature distributions in the tool and workpiece. Therefore, a 3D thermomechanically coupled FE model for the oblique turning process was finally developed to include the third component of force in simulation and get an inclusive understanding of the process zone in turning of Ti-15333. This model possesses a number of advantages as compared to our previously developed FE models for the turning processes [7, 8, 126]. This model allows us to study the effects of cutting conditions, actual tool geometry, vibration parameters and friction conditions on the tool tip-workpiece interface in CT, HCT, UAT and HUAT.

A commercially available code MSC MARC/MENTAT was used to carry out simulations of CT, UAT, HCT and HUAT for the processing of Ti-15333.

## 5.2 Finite-Element Modelling

### 5.2.1. FE Modelling of 3D Orthogonal Turning

A 3D fully thermomechanically coupled implicit finite-element model was developed in the commercially available finite-element software, MSC MARC/MENTAT [168]. The model was based on an updated Lagrangian procedure that provides a dynamic transient analysis for an elasto-plastic material and accounts for the frictional contact interaction between the tool and the workpiece.

In the turning process, the workpiece is mounted in the chuck of a lathe machine and is rotated at a certain speed (rpm) in a clockwise and counter-clock-wise direction. In the current study, the workpiece was rotated in the clockwise direction whereas cutting insert was mounted in a tool holder fixed to the tool post, bolted on a cross slide of a lathe machine as shown in Figure 5-1. The current model was developed considering the tool-workpiece-interaction zone keeping the radial direction as a free cutting edge of the workpiece materials as shown in Figure 5-2. This model resulted in a principal tangential component of cutting forces and feed force (the lowest force in finished machining). However, this model possessed a number of advantages compared to the 2D FE model considering the distribution of temperature, strain and stresses along the chip width, resulting a detail understanding of

the process zone. However certain assumptions and simplifications were used in the FE models discussed in the following section.

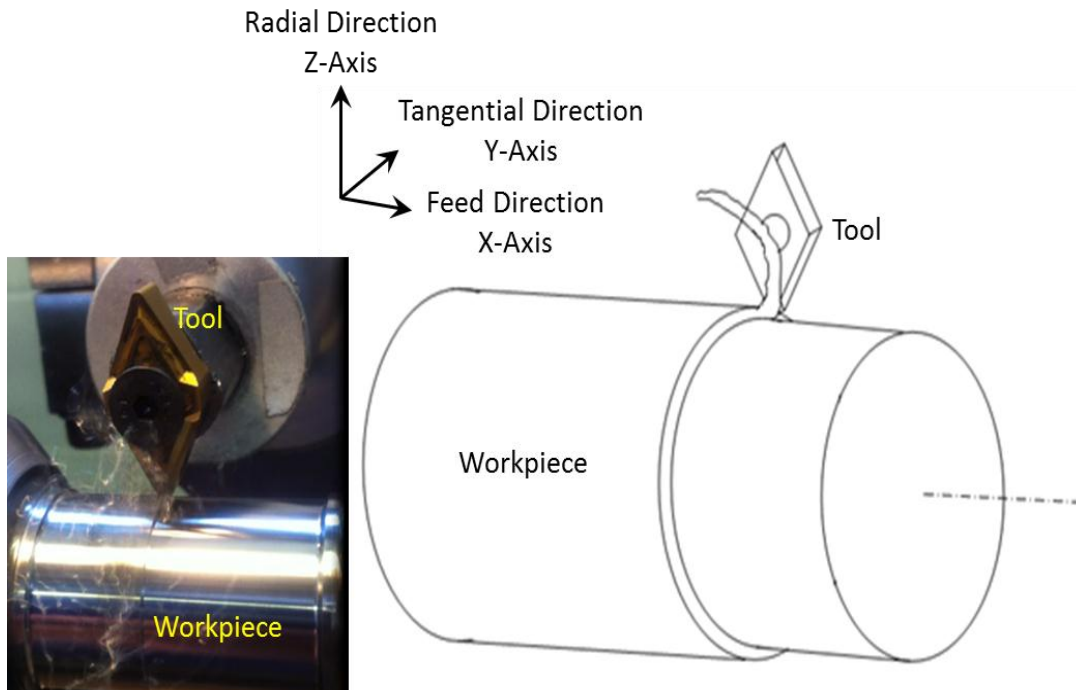


Figure 5-1: Schematic of the turning process and principal direction of vibration

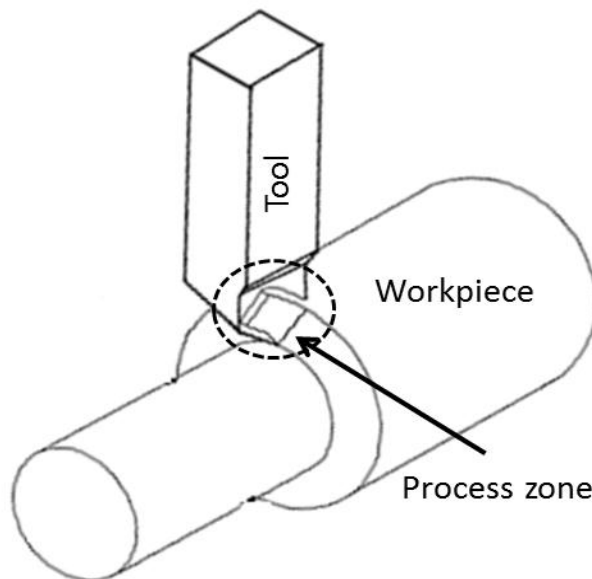


Figure 5-2: Process zone used in FE simulation of the orthogonal turning process

### 5.2.2. Assumptions and Restrictions

In the FEA modelling of CT, UAT, HCT and HUAT, the following assumptions were made.

- The chatter in the cutting tool was neglected.
- The workpiece was rigidly mounted in the chuck.
- Dry cutting condition in FE simulation was defined in terms of friction on the tool-tip interface,  $m_{fr} = 0.5$  was assumed to represent the dry cutting condition (without any lubricant).
- The workpiece and cutting tool material was assumed to be isotropic.
- The tool wear during the turning process was neglected.
- The cutting tool was considered rigid body with heat transfer capabilities.
- Radiations from the chip, workpiece and tool to the environment were neglected in the simulation.

### 5.2.3. Model Description and Features

A finite-element analysis was used to carry out implicit 3D thermomechanically coupled orthogonal turning simulation of CT, UAT, HCT and HUAT. In machining operations, the amount of heat generated due to plastic deformation can significantly increase the temperature of the process zone. The increased in temperature considerably effect mechanical and thermal properties of Ti-15333 owing to non-linear material behaviour at elevated temperatures. The yield strength, specific heat and coefficient of thermal expansion changed with the growth in temperature of the process zone. Therefore, a fully thermomechanically coupled finite-element model was used in simulations of CT, UAT, HCT and HUAT.

A thermal boundary condition was incorporated into the model, by assuming the environmental temperature to be 20°C acquiring heat at a rate of 0.05 N/mm°C, obeying Newton's law of cooling for heat convection.

$$Q = h(T - T_o), \quad (5-1)$$

where  $Q$  is the convective heat transfer,  $T$  is temperature of the process zone,  $T_o$  is the environment temperature or room temperature and  $h$  is the convective heat transfer coefficient.

A conductive heat transfer between the tool and workpiece was also incorporated into the model which allows the transfer of heat from the chip and process zone to the cutting tool, as a result, the temperature of the tool increases with time, following Fourier's law of conduction.

$$\vec{Q} = -k\nabla T , \quad (5-2)$$

where  $\vec{Q}$  is the localized heat flux,  $k$  is the thermal conductivity and  $\nabla T$  is the temperature gradient.

#### 5.2.4. Material Model for Ti-15333

In turning operations, material non-linearity such as its dependency on temperature, strain-rate and strain have a significant influence on cutting forces, heat generations in the process zone, surface roughness, metallurgy of the specimen, tool life and cost of the process. These nonlinearities in material response were observed at the macroscopic and microscopic level. The response of flow stresses of a material increase with the increase of strain rate and strain where as a growth in temperature led to the opposite. Therefore, accurate material characterization was essential in predictive capabilities of FE models.

In the current study, a new material model was used to incorporate the flow stress behaviour of Ti-15333 at elevated temperatures and high strain rates. A series of split-Hopkinson tests for Ti-alloy (Ti15V3Cr3Al3Sn designated as Ti-15333) [195] were carried out at Tampere University of Technology (TUT), Finland, to obtain the flow stress behaviour at known temperatures and strain rates. The material response of the studied alloy at different strain rates and at room temperature obtained in the tests is shown in Figure 5-3. Similarly, the experimental data obtained at various elevated temperatures and for a strain rate of  $3300 \text{ s}^{-1}$  is shown in Figure 5-4. The experimental data were simplified in order to eliminate the variation obtained in the slip-Hopkinson pressure bar tests as shown in Figure 5-5.

In the turning processes, the strain rate reached to  $10^5 \text{ s}^{-1}$  [196] whereas from the Split Hopkinson pressure bar (SHPB) tests at TUT, material data at a maximum strain rate of  $3300 \text{ s}^{-1}$  was obtained. Therefore, an engineering assumption was taken to incorporate high strain rate levels in simulation by considering the stress - strain response for a strain rate level of

$10^5 \text{ s}^{-1}$  is 20% higher than the mechanical response for a strain rate of  $3300 \text{ s}^{-1}$  as shown in Figure 5-5.

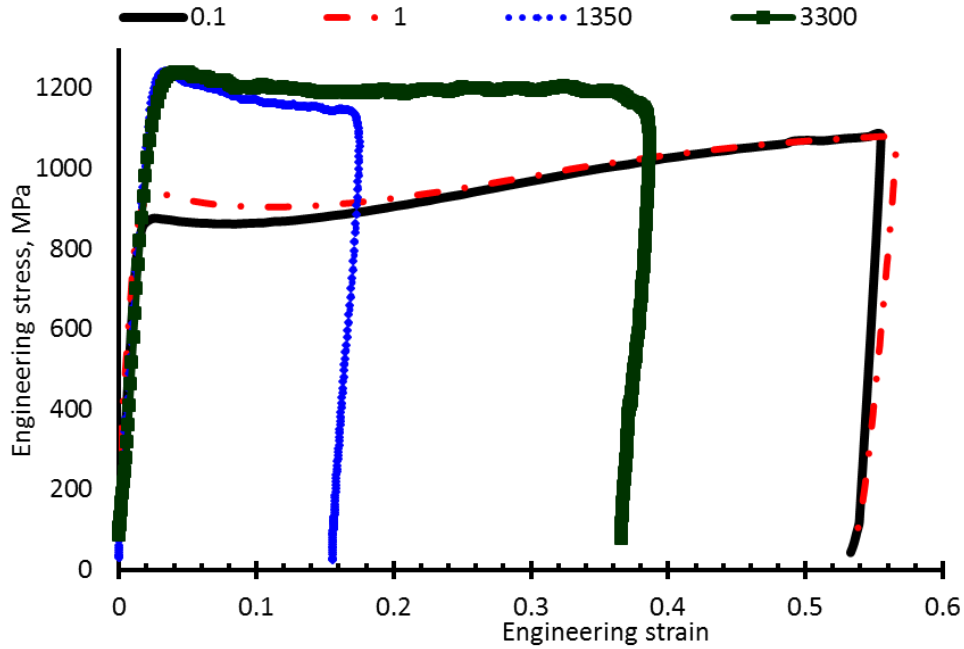


Figure 5-3: Stress-strain diagram of Ti-15333 obtained from Split-Hopkinson tests for different strain rates and room temperature [197]

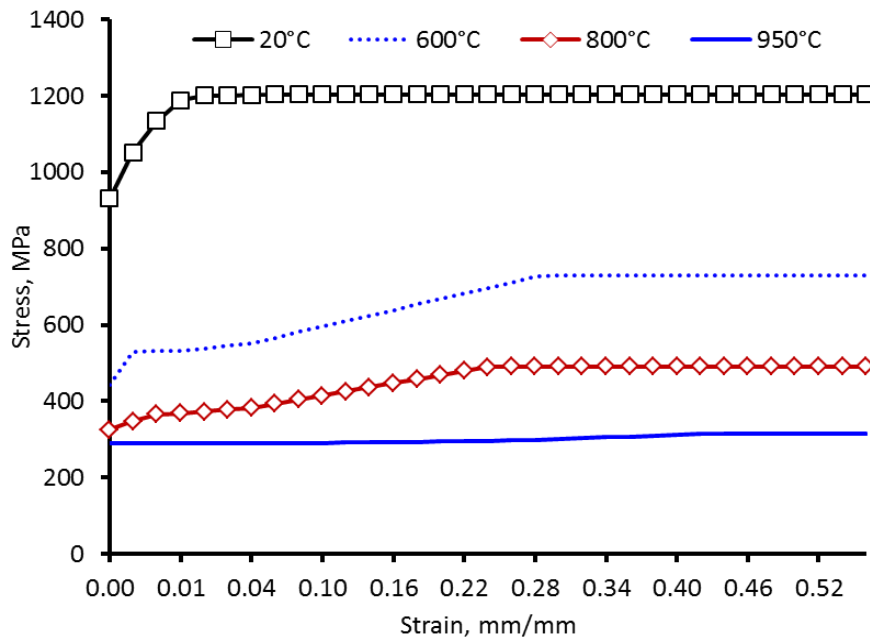


Figure 5-4: Temperature dependant material flow stress data at various temperature and strain rate of 3300/s [197]

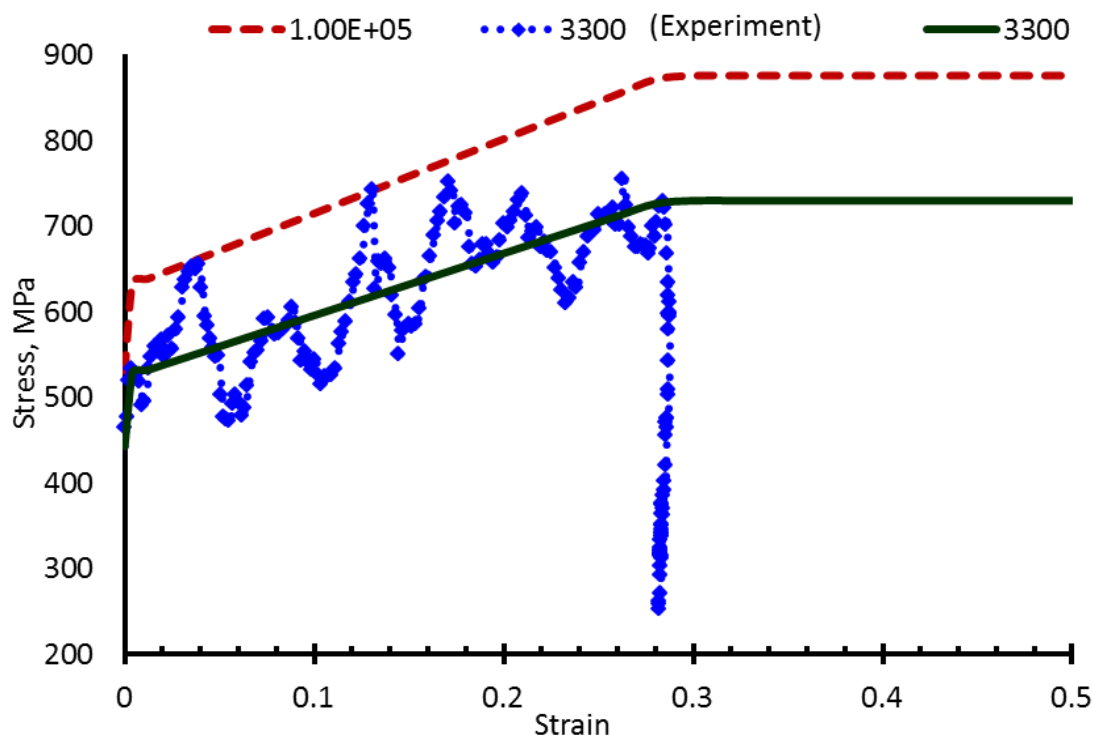
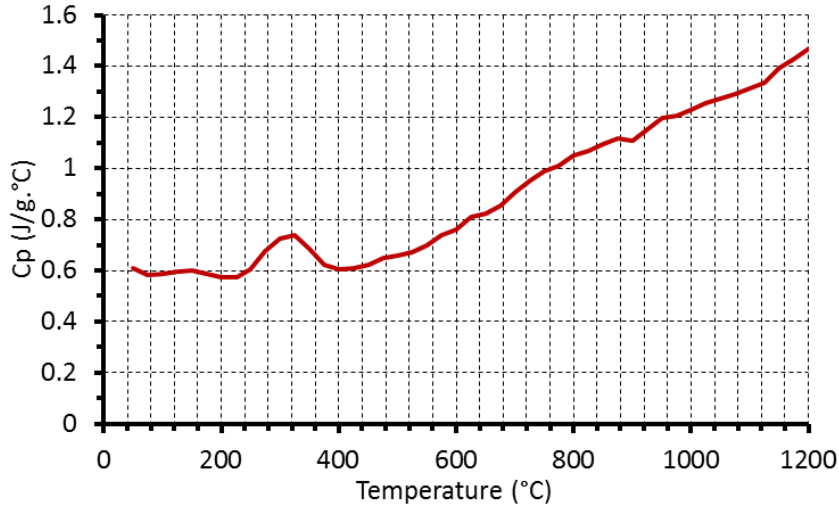


Figure 5-5: Modified strain-rate-sensitive material model for 600°C [197]

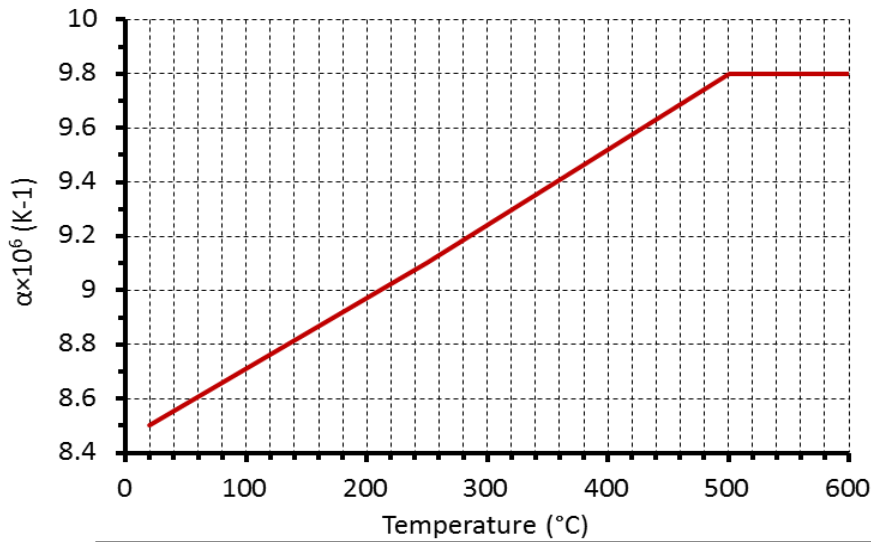
Additionally, the curves were modified in such a way that the magnitudes of stress for high strain levels are limited by the ultimate dynamic tensile stress (UTS). The nonlinear strain-rate and temperature-sensitive material model used in our numerical simulations comprised of different stress-strain curves obtained for a combination of four different strain rates ( $0.1 \text{ s}^{-1}$ ,  $1 \text{ s}^{-1}$ ,  $3331 \text{ s}^{-1}$ ,  $10^5 \text{ s}^{-1}$ ) and four different temperature magnitudes ( $20^\circ\text{C}$ ,  $600^\circ\text{C}$ ,  $800^\circ\text{C}$ ,  $950^\circ\text{C}$ ).

The elastic material properties of the Ti-alloy are  $E = 87 \text{ GPa}$ ,  $\nu = 0.3$ ,  $\rho = 4900 \text{ kg/m}^3$ , where  $E$ ,  $\nu$  and  $\rho$  are the Young's modulus, Poisson's ratio and density of the material, respectively. The thermal conductivity of the Ti-alloy is  $k = 8.08 \text{ W/mK}$ . A temperature-dependent thermal expansion and specific heat ( $C_p$ ) behaviour of the material was incorporated into the model as shown in Figure 5-6 and Figure 5-7, respectively. The thermal characteristics were provided by the Technical University Braunschweig (TUB). The data obtained from TUT is shown in tabulated form



Specific heat of Ti-15333 as function of temperature											
T	Cp	T	Cp	T	Cp	T	Cp	T	Cp	T	Cp
50	0.61	250	0.60	450	0.62	650	0.82	850	1.09	1050	1.27
75	0.58	275	0.68	475	0.65	675	0.85	875	1.12	1075	1.29
100	0.59	300	0.73	500	0.66	700	0.91	900	1.11	1100	1.31
125	0.60	325	0.74	525	0.67	725	0.95	925	1.15	1125	1.34
150	0.60	350	0.69	550	0.70	750	0.99	950	1.20	1150	1.39
175	0.59	375	0.62	575	0.74	775	1.01	975	1.21	1175	1.43
200	0.57	400	0.61	600	0.76	800	1.05	1000	1.23	1200	1.47
225	0.57	425	0.61	625	0.81	825	1.07	1025	1.25		

Figure 5-6: Specific heat capacity of Ti-15333 [197]



Coefficient of thermal expansion at various temperatures				
T	20	250	500	600
$\alpha \times 10^6$	8.5	9.1	9.8	9.8

Figure 5-7: Coefficient of thermal expansion of Ti-15333 [197]

In turning operations, friction plays a vital role, not only determines the amount of power required to remove the surplus amount of material from unfinished specimen but it was also found to affect the surface roughness of machined components and chip shape. Various friction models are available to model the interaction of tool-chip-workpiece interface [198-200]. To simulate the turning process under the applied cutting conditions, a modified shear friction model was incorporated in FE simulation [168]. The modified shear friction model was implemented using approximations of a theoretical step function, because this step function caused numerical difficulties in FEA calculation of the process. The arctangent function used in the modified shear friction model was used to smooth out the step function in order to avoid the numerical difficulties as shown in Figure 5-8. As a result of the smoothing procedure, a node in contact always has some slipping [201]. The arctan representation of the friction model is a mathematical idealization of this nonlinear friction behaviour. Therefore, shear friction between the tool and workpiece was modelled with a modified constant shear friction model (see equation 5 – 3).

$$\sigma_{fr} \leq -m_{fr} \frac{\bar{\sigma}}{\sqrt{3}} \frac{2}{\pi} \operatorname{sgn}(V_r) \operatorname{artan}\left(\frac{V_r}{V_{cr}}\right), \quad (5 - 3)$$

Where  $\sigma_{fr}$  is a friction stress,  $\bar{\sigma}$  is the equivalent stress,  $V_r$  is the relative sliding velocity,  $V_{cr}$  is the critical sliding velocity below which sticking is simulated,  $m_{fr}$  is the friction coefficient and  $\operatorname{sgn}(x)$  is the signum function.

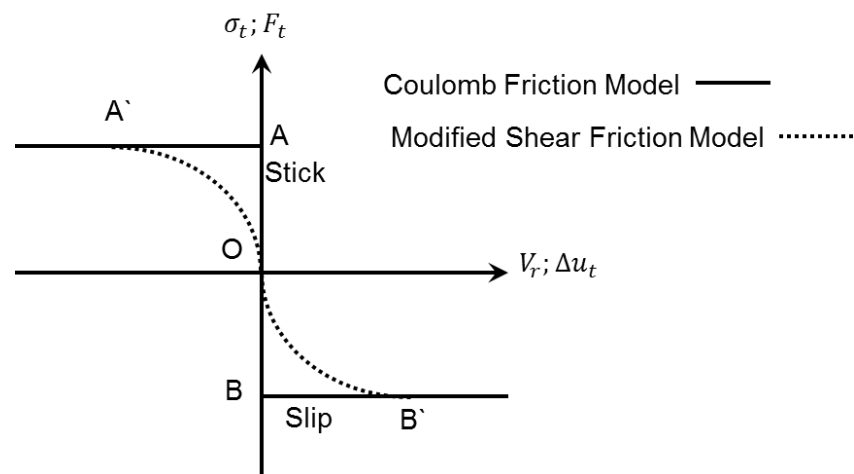


Figure 5-8: Schematic representation of friction model

The workpiece was modelled using MSC MARC element type 7. This class consists of eight nodes, iso-parametric, three-dimensional brick elements with tri-linear interpolation as shown in Figure 5-9. Strain was constant throughout the element, as this element uses tri-linear interpolation functions, resulting in poor representation of shear behaviour [202].

Initially, element type-7 was used in modelling of the workpiece due to its simple shape as compared to element type 157 or 134. However, in actual simulation, element type-7 was replaced by element type-157 because of its poor representation of shear behaviour and lack of support for re-meshing technique. Therefore, at the start of each simulation, the element type-7 was automatically converted in to the tetrahedral element type-157 of MSC MARC, before re-meshing, as shown in Figure 5-10 [202]. Element type-157 is three dimensional, low orders, tetrahedral and Herrmann-82 type element. The shape function for the centre node is a bubble function. Therefore, displacements and coordinates for the element were linearly distributed along the element boundaries. The stiffness of the element was formed using four Gaussian integration points. Element 157 had 5 nodes, with 4 corner nodes and one interior node. There was 1 pressure DOF and 3 displacement DOFs in each corner node while only 3 displacement DOFs in the interior node. The degrees of freedom of the centre node were condensed out on the element level before assembly of the global matrix.

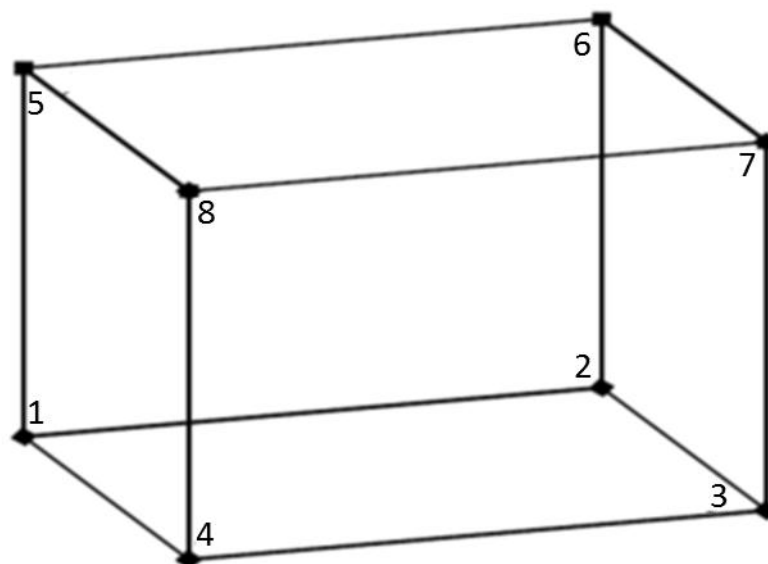


Figure 5-9: Element type 7 [202]

Element type-43 was used for the modelling of the cutting tool [202]. Element type-43 consists of eight nodes, iso-parametric, three-dimensional brick elements with tri-linear interpolation as shown in Figure 5-11. Element type-43 is normally used for three dimensional heat transfer application and recommended for thermomechanically coupled analysis

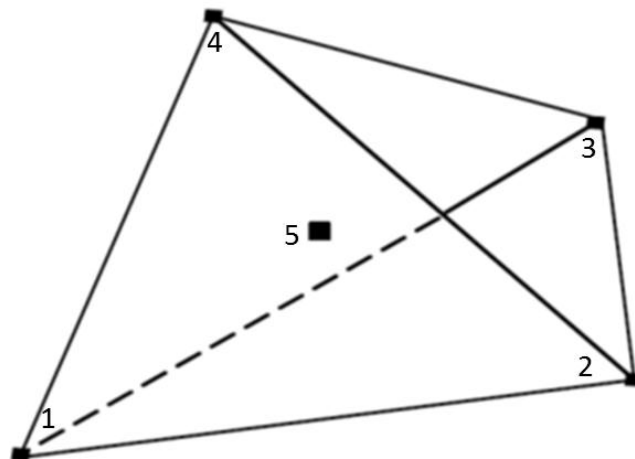


Figure 5- 10: Element type 157 [202]

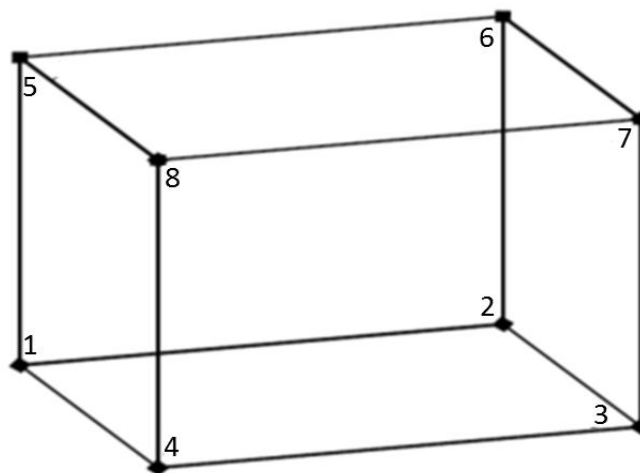


Figure 5-11: Element type 43 [202]

### 5.2.5. Model Geometry and Boundary Conditions

The initial mesh, dimension and relative movement of the workpiece along with the cutting tool of the orthogonal turning process is shown in Figure 5-12. In orthogonal cutting, the tool edge is normal to the cutting direction. In the FE simulation of Ti-alloy, a deformable workpiece with dimension of 3.0 mm in length and 0.7 mm in height was used. The workpiece was given a velocity of  $V$  in the tangential direction (Figure 5-12). Initially, eight-

node hexahedral elements with a minimum and a maximum length of 0.05 and 0.1 mm, respectively, were used to mesh the workpiece. A rigid cutting tool with TiAlN coating was modelled in the FE simulation. Harmonic oscillation of amplitude ( $a$ ) and frequency ( $f$ ) was then superimposed on the cutting tool in the tangential direction in order to model ultrasonic vibration of the tool. The cutting tool has a cutting edge radius of 25  $\mu\text{m}$ , rake angle of 14.6° and end relief angle of 1°. The tool was meshed in such a way, that more refine mesh were used closed to the cutting edge when compared to other parts in the FE simulation of the turning processes. The cutting tool was discretized into eight-node, 8000 iso-parametric, irregular quadrilateral elements with approximately 12000 nodes.

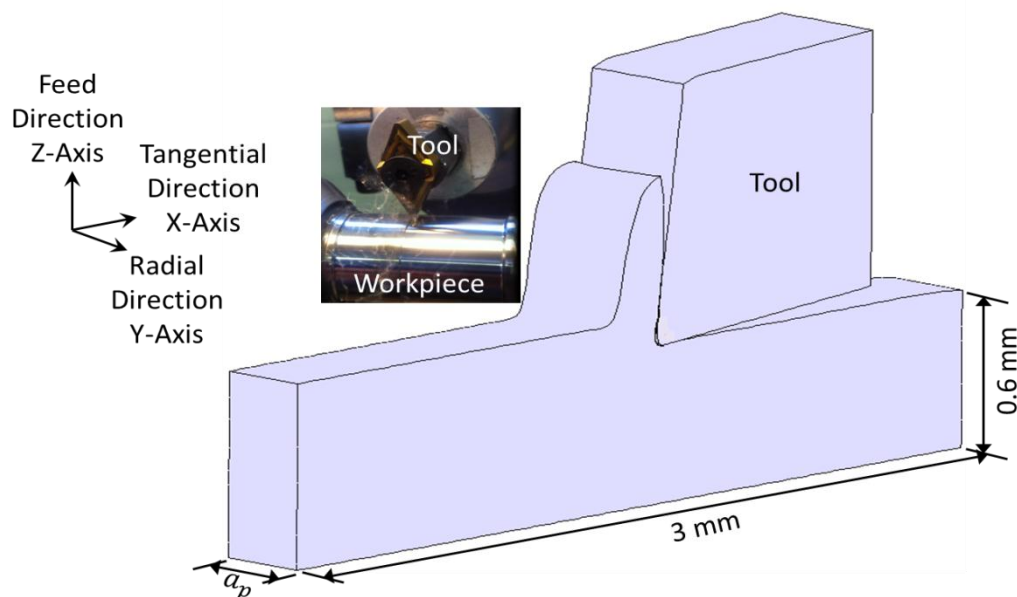


Figure 5-12: A schematic of cutting model

In the literature, researchers have used various techniques to separate chip from the workpiece material as discussed in chapter 3. In the present work, chip separation was achieved with re-meshing technique based on strain change criteria and number of increments, by considering the work piece as a deformable body. Due to the plastic deformation of the chip, elements near the cutting edge of the tool will distort badly and negative values came in the Jacobian matrix as a result re-meshing techniques were used repeatedly to replace those distorted elements with ones of better shape, the current state of deformation, strains and stresses were transferred to the new mesh and the analysis was continued. In strain change criteria, an accumulated incremental strain measure was

recorded after each re-meshing. When this value reached or exceeded the maximum allowed, the re-meshing will be initiated. These criteria's controls the magnitude of deformation between each re-meshing step to get more accurate results and also separate chips from the workpiece material.

In the FE simulation of CT, UAT, HCT and HUAT, the workpiece was moved with a velocity  $V$  along the X-axis (see Figure 5-12). The velocity to the workpiece material was assigned with three rigid surfaces, glued to the workpiece material as shown in Figure 5-13. Therefore, velocity was assigned to the rigid surfaces resulting moving workpiece as per equation 5 – 4,

$$V_{ABCD} = V_{CDEF} = V_{EFGH} = V, \quad (5 - 4)$$

Vibrations were superimposed on the cutting tool in a tangential direction caused the tool to vibrate. Vibrations were defined for the cutting tool and were derived from the following equation,

$$Tool_{path} = a \sin(2\pi ft), \quad (5 - 5)$$

where  $a$  is the amplitude of vibration,  $f$  is the frequency of vibration,  $\pi$  is a constant, and  $t$  is time step in simulation.

The superimposing of those vibrations on the cutting tool in UAT caused the tool to vibrate about its reference point "O" in forward and backward direction as shown in Figure 5-14. The boundary condition of the cutting tool was superimposed in FE simulation using a special feature of MSC MARC to define in coincidence with contact conditions. The contacts were defined between the workpiece-workpiece, workpiece-cutting tool and workpiece-rigid surfaces. Therefore, three contact bodies were defined in the FE modelling of CT, UAT, HCT and HUAT. A contact conditions between the workpiece to cutting tool allowed the chips to move on the rake face of a tool obeying modified shear friction model, whereas contact between the workpiece and the rigid surfaces was glued with no separation.

In the FE simulation of the turning process, incremental iterative Newton-Raphson scheme was used to solve the system of equation. The chosen Full Newton-Raphson scheme updates the stiffness matrix at equilibrium iteration and determines more flexibility to include non-linear material behaviour. Though, more frequent updating of the stiffness matrix needed

larger matrix formulations and inversions, it resulted relatively fast numerical convergence. The matrices obtained from finite-element formulations were usually sparsely populated; therefore, the system of simultaneous equations was solved by using direct sparse matrix solver.

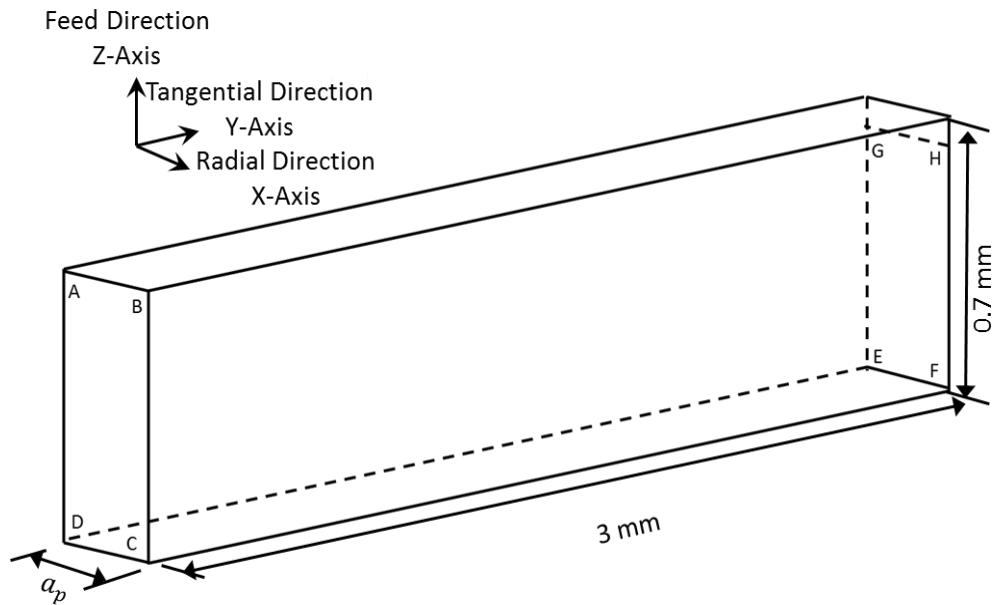


Figure 5-13: Boundary condition used in FE simulation

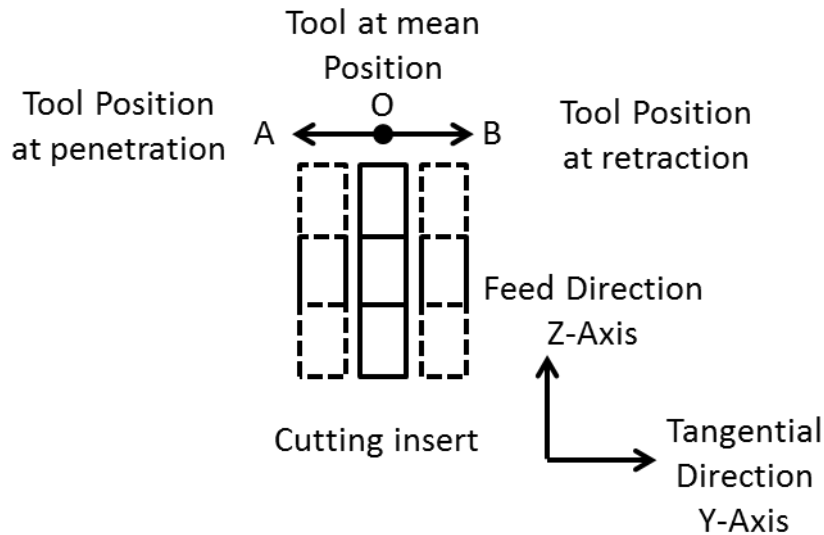


Figure 5-14: Cutting insert position in ultrasonically assisted turning in the forward and backward positions of tool vibration in one cycle tool vibration in one cycle

The number of simulation steps was kept at 5000 with a total time depending on the velocity of the cutting tool. The simulations were carried out on core i7, 2.93 GHz workstation with 8

GB RAM and High Performance Computing (HPC) facility, consisted of A-1956-core 64-bit Intel Xeon cluster supplied by Bull. The HPC facility consists of 161 compute nodes, each having two six-core Intel Westmere-Xeon X5650 CPUs and 24GB of memory. A further two nodes are available with 48GB of memory. The computers nodes are connected by an Infinite-band network. The HPC has around 40TB of user home storage and a further 16TB of Lustre-scratch file space. The total time for one successful FE simulation was 20 hours and was carried out for different cutting parameters for CT, UAT, HCT and HUAT.

In hot machining, thermal boundary conditions were superimposed on the workpiece material using various temperature values in hot turning, to predict the benefit of hot machining in the processing of hard-to-cut material.

#### **5.2.6. Oblique Turning of CT, UAT, HCT and HUAT**

In the current study, an oblique model was developed using the commercially available package MSC MARC/MENTAT. The model was developed sequentially, modifying the orthogonal 2D to orthogonal 3D and orthogonal 3D to oblique 3D model. The final model use in the proceeding analysis was developed after carrying out a number of experiments to develop the first oblique turning model in MSC MARC for CT, UAT, HCT and HUAT. The problems that were faced in the development of the model are discussed herewith.

The main obstacle in the development of the oblique turning process was a requirement of a huge computational facility required for remeshing process. However, it was reduced by applying a localized mesh at the cutting tool edge and workpiece interaction, reducing the computational requirement of the software for the oblique cutting model. The prime reason was that element size has a significant effect on the output results in oblique modelling of the CT and hybrid turning processes. Various element sizes were used in the analysis to get mesh convergence. Initially with reduction in element size from 0.05 to 0.0275 a significant reduction in the output parameters was observed. Figure 5-15 shows all the three components of forces at various element sizes. However, below 0.0275, no considerable decline in solution results was observed. Therefore, in the current model a mesh size of 0.0275 was used in the CT and hybrid simulations of the oblique turning processes.

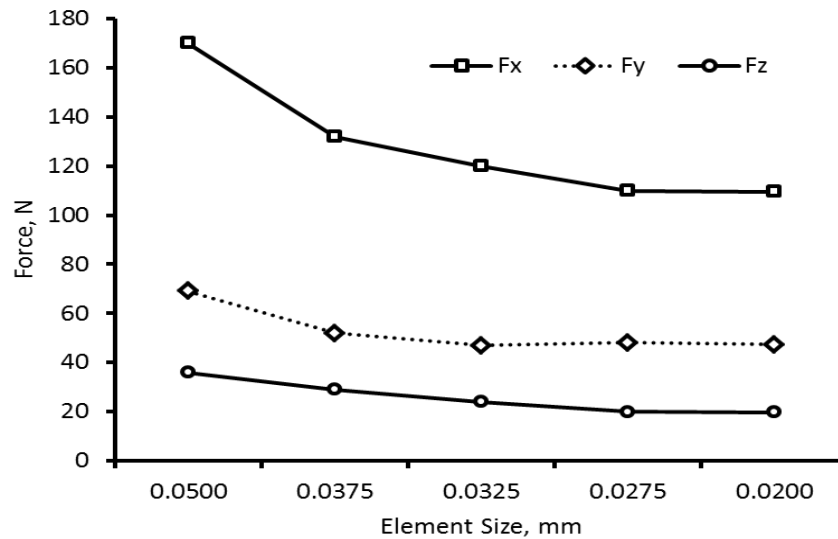


Figure 5-15: Mesh Convergence in simulations

The second difficulty was the actual tool workpiece geometry used in the FE simulation. The tool was modelled using DNMG-150608 tool geometry and only a region of tool in contact with the workpiece material was considered in the FE simulation to reduce the computational cost (Figure 5-16). Similarly, the grooved workpiece geometry was also modelled based on the tool geometry so that the tool removed the actual amount of material during the process. Initially, various conceptual models were developed for the oblique turning process as shown in Figure 5-17. Those models either required very high computational power or it lacked of an actual representation of the tool-workpiece geometries.

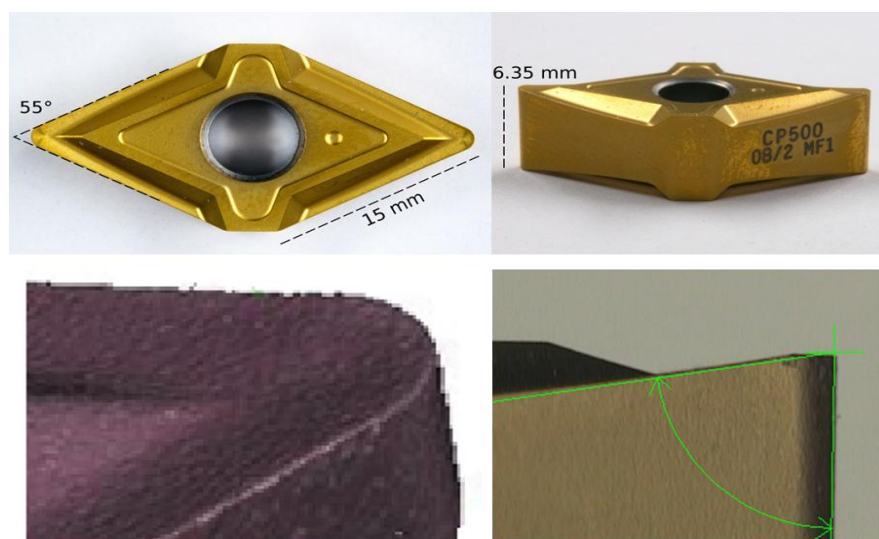


Figure 5-16: Cutting insert used in experimentations

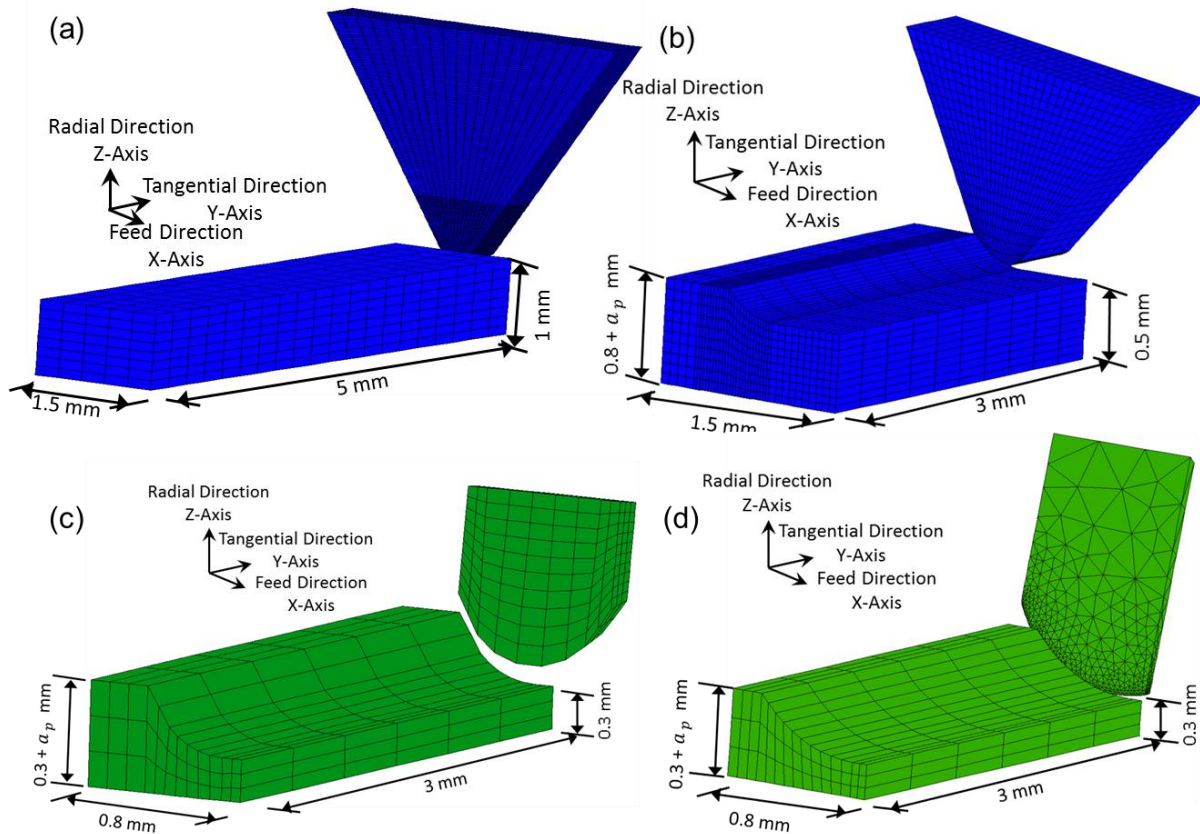


Figure 5-17: Conceptual model for the oblique turning process; (a) Stage-1; (b) Stage-2; (c) Stage-3 and (d) Stage-4

Therefore, the actual cutting edge geometry of the tool was used in the oblique turning process to validate all the three component cutting forces in CT, UAT, HCT and HUAT. The cutting tool was modelled, as a rigid body with heat transfer capabilities. The rake angle of the cutting insert (DNMG-080615 as shown in Figure 5-18) was  $14.6^\circ$ . A nose radius of 0.8 mm and the end relief angle of  $0^\circ$ . The cutting edge radius was  $25 \mu\text{m}$ . The cutting tool was initially modelled in Pro-Engineer and was imported to Patran-3D to discretise it for FE simulation. A Four-noded tetrahedron elements which is a first-order iso-parametric three-dimensional heat transfer element was used to discretise the tool in to 8000 elements (Figure 5-19).

A relatively fine mesh was used in the vicinity of the cutting edge to get more accurate results where as a coarse mesh was used in the regions which have no contribution in the cutting process. Harmonic oscillation of amplitude ( $a$ ) and frequency ( $f$ ) was then superimposed on the cutting tool in the tangential direction in order to model ultrasonic vibration on the tool

in UAT. For the feed rate of the cutting tool in CT, UAT, HCT and HUAT, a feed velocity was given to the cutting tool in the Z-Axis with a feed rate of 0.1 mm/rev as shown in Figure 5-20.

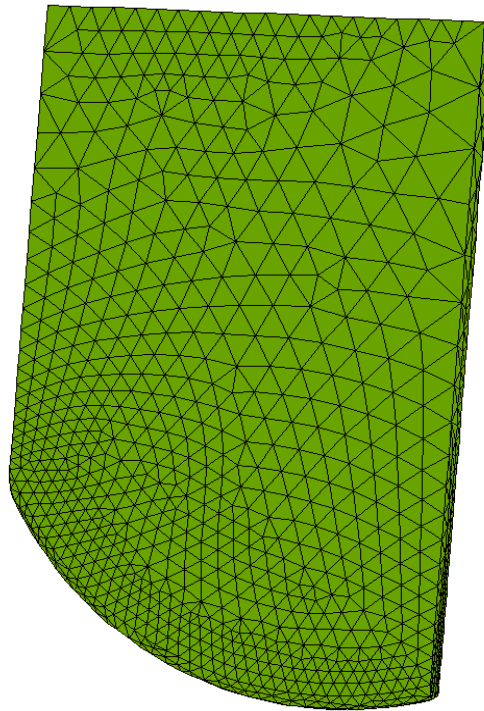


Figure 5-18: Cutting tool geometry in FE simulation

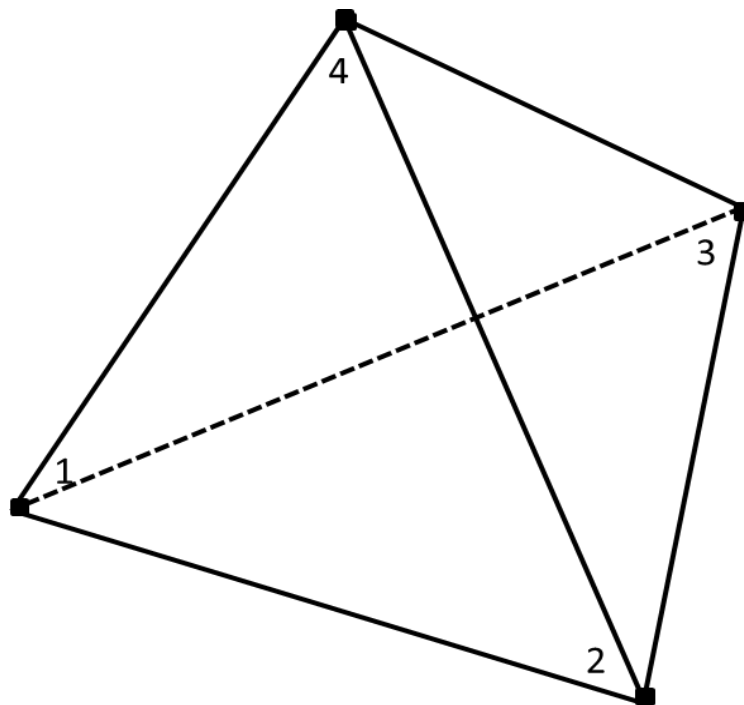


Figure 5-19: Element Type 133 [202]

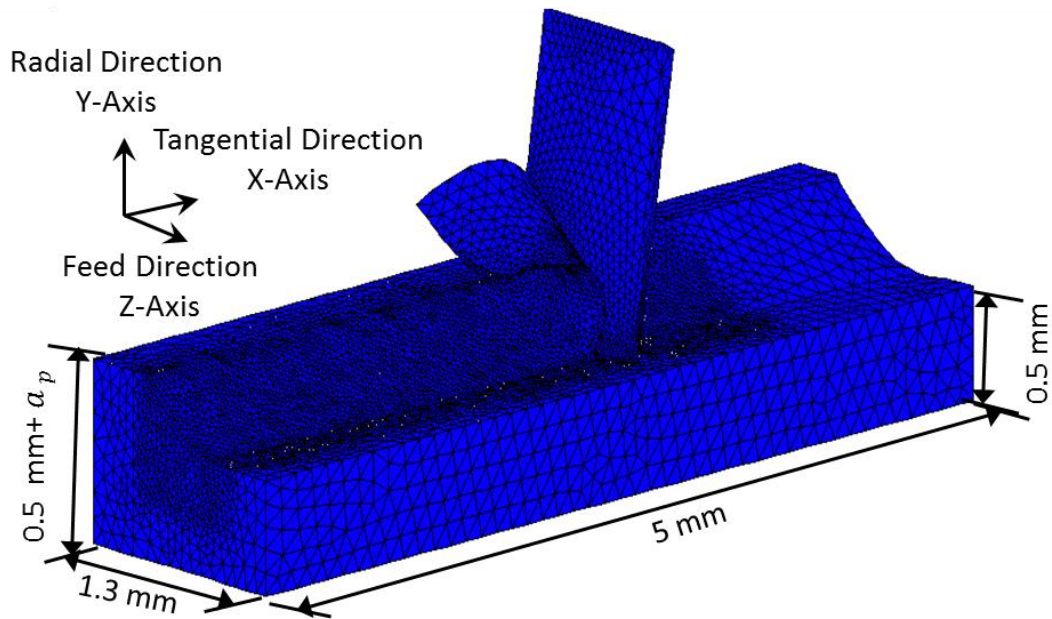


Figure 5-20: Improved version of oblique turning model with actual cutting edge geometry

A deformable workpiece having a length of 5 mm, width of 1.3 mm and height of 0.5 mm +  $a_p$  was modelled in the oblique turning of Ti-15333. Initially, eight-noded hexahedral elements with a minimum length of 0.05 mm were used to mesh the workpiece.

The boundary conditions were superimposed on the workpiece using the special feature of MSC MARC to incorporate at the contact options of the FEA package. The linear velocity of the workpiece was superimposed using a rigid surface ABKL at the bottom of the workpiece material (equation 5-11). The rigid surface ABKL was glued to the workpiece material as shown in Figure 5-21. The separation between the rigid surface and the deformable workpiece was suppressed in the simulation to imposed cutting velocity on the workpiece materials.

$$V_{ABKL_x} = V_{c_x}, \quad (5 - 11)$$

$$V_{ABKL_y} = V_{c_y}, \quad (5 - 12)$$

$$V_{ABKL_z} = V_{c_z}, \quad (5 - 13)$$

As the workpiece material is a deformable body therefore, nodes in the region CDIJ were allowed to move in the X-direction and were restricted in the Y-direction.

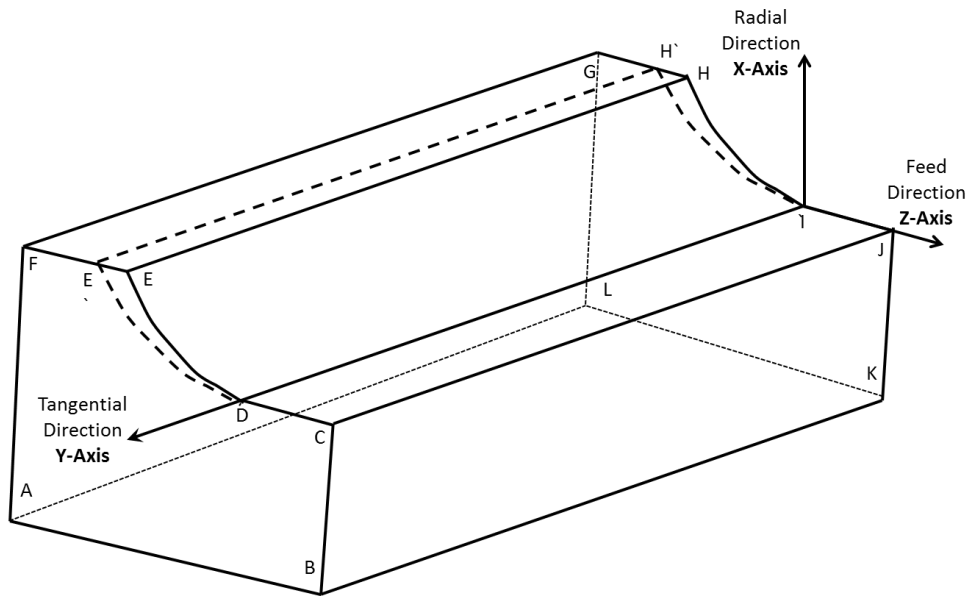


Figure 5-21: Schematic diagram of a deformable workpiece in oblique turning

$$V_{CDIJ_x} = V_{c_x}, \quad (5-14)$$

$$V_{EFGH_x} = V_{c_x}, \quad (5-15)$$

$$V_{CDIJ_z} = 0, \quad (5-16)$$

Global remeshing was defined to achieve local mesh refinement close to the process zone and coarse mesh in the remaining parts of the workpiece material. The localized mesh refinement was incorporated by defining the corner coordinates of the box. In the current study, a refinement level 2 was used to refine the element size to one fourth of the defined one. Therefore, the elements near the process zone have an edge length equal to 0.0275 mm. the coordinate of the refinement box are defined below:

$$X_1 = 1, \quad (5-18)$$

$$Y_1 = -0.2, \quad (5-19)$$

$$Z_1 = 0.2, \quad (5-20)$$

$$X_2 = -5, \quad (5-21)$$

$$Y_2 = 0.7, \quad (5-22)$$

$$Z_2 = -0.7,$$

$$(5 - 23)$$

### 5.3 Summary

General purpose FE code MSC MARC/MENTAT was used to modelled CT, HCT, UAT and HUAT of Ti-alloys. Three-dimensional FE orthogonal turning models were found much less demanding for computational time and data storage, i.e. only almost 40% of the three-dimensional FE oblique model. The 3D orthogonal model was capable of in-depth analysis of the turning process using a simplified geometry of the tool. Similarly, the model also predicts the distribution of temperature, stresses and strain on the chip width which cannot be achieved through 2D FE simulation. Furthermore, a good prediction of tangential and axial force component can be achieved for various cutting conditions, vibrational parameters and lubrication of the process.

A three-dimensional thermomechanically coupled oblique model was developed to simulate the oblique turning process using actual geometry of the cutting insert and workpiece geometry. The model is capable to give a good prediction of all the three components of cutting forces, temperature and stresses of the process zone.

## CHAPTER-6

# Results and Discussions: Parametric Study of Orthogonal Turning Modelling

### 6.1 Introduction

In turning operations, cutting forces, temperature of the process zone, stresses and friction at the tool chip interface depend largely on cutting parameters and geometrical characteristics of the tool. In this chapter, experimental and FEA results obtained with an orthogonal turning model are analysed in detail. Important observations regarding the highest possible force reduction in a newly developed HUAT technique are found through the analysis. In the present work, different turning experiments and FE simulation were conducted, and cutting forces, temperature and stresses in the process zone were recorded at various cutting and vibrational parameters for various special turning processes. The FE simulations were used to investigate those parameters or zones in conventional and assisted turning process, which is impossible or hard to achieve through experimentations.

Various cutting conditions used in the FE model are listed in Table 6-1. The cutting speeds varied from 10 m/min to 70 m/min. Several depths of cuts were used in simulation, ranging from 100  $\mu\text{m}$  to 500  $\mu\text{m}$  to study conventional and assisted turning processes. Furthermore, a range of vibrational parameters was used to investigate their effect on the output results. Additionally, in hot machining, external heat was applied to the workpiece material to study its effect on cutting forces and temperature of the process zone. Various cutting conditions were used in analyses of cutting forces, heat generated and stresses of the process zone in the machining of Ti-15333. The developed FE model was used to analyse the tangential component of cutting forces, which is the highest one in turning of Ti-15333. The experiments have been evaluated based on the criteria of:

- Cutting forces
- Temperature of the process zone

The chapter is organised as follows: in Section 6.2, the cutting forces in CT and UAT at various cutting and vibrational parameters were analysed and reported. Section 6.3 comprises analysis of stresses in the process zone in CT and UAT, followed by thermal analysis at various cutting conditions in Section 6.4. A contact state of the tool in UAT was analysed in Section 6.5. Section 6.6 includes a study of hot machining of high-strength alloys at various cutting parameters. The chapter ends with some concluding remarks in Section 6.7.

Table 6-1: Cutting conditions used in experiments

Parameters	Magnitude
Cutting speed, $V$ (m/min)	10-70
Depth of cut, $a_p$ (mm)	0.1, 0.2, 0.3, 0.4, 0.5
Feed rate, $f_r$ (mm/rev)	0.1
Temperature, $T$ (°C)	20, 100, 200, 300, 500
Coefficient of friction, $m_{fr}$	0.5 (Dry cutting)
Rake angle, $\alpha$ (degree)	-14.6; 0; 14.6
Frequency, $f$ (kHz)	5-25
Amplitude, $a$ ( $\mu\text{m}$ )	3-12

## 6.2 Cutting Forces

A significant reduction in the level of average cutting forces was observed for cases of machining with application of ultrasonic vibrations on the cutting tool. In CT, the cutting tool was in continuous contact with the workpiece, resulting in a constant level of cutting forces after the initial stage of tool engagement. At the initial contact of the tool, the cutting forces increases with time and ultimately reached a constant level after achieving a steady state

condition. In the analysis, the steady state level of force was considered and compared to the average force magnitudes obtained in UAT. In UAT, the vibrating cutting tool caused a cutting force to fluctuate between a maximum (a peak force during penetration) and minimum (no force when the tool was not in contact with the chip) in one complete cycle of vibration. When the tool penetrated the workpiece, the cutting forces gradually increased from zero to the peak force value at maximum penetration (see Figure 6-1 ). The peak-force value was practically equal to the level of force in CT. After reaching to the peak-force value, the tool started to separate its self from the workpiece material in the retraction stage, and the force gradually declined and eventually became zero after being completely separated from the workpiece material. Thus in the repeated cycles in UAT the lower average cutting forces were observed compared to those in CT. In UAT, an average force value with respect to time was calculated and was used in the analysis. A reduction of 65% in a tangential component of the cutting force was observed for Ti-15333 with the introduction of ultrasonic vibration at 300  $\mu\text{m}$  depth of cut as shown in Figure 6-1. The pattern of cutting forces at various depth of cut was the same; however, the peak-force value increased with the increase in the depth of cut, and the average cutting forces were significantly lower in UAT when compared to CT. In experimentation, an average force value was recorded with a Kistler dynamometer. The response time of the data-logging system was much lower compared to the excitation frequency of the tool in UAT. Therefore, the average cutting forces were registered in UAT at various cutting conditions. A nearly constant reduction (by approximately 60-65%) of cutting forces was observed for higher depths of cut. The simulated results validated the experimental results at various cutting conditions.

The fluctuating cutting forces in UAT resulted, a transient deformation in the workpiece material. The resulted stresses generated due to deformation of workpiece material in the process zone in CT and hybrid turning processes are studied in the following section.

### 6.3 Stresses in Process Zone

The calculated distributions of equivalent von-Mises stress in the cutting region of the studied alloy for both CT and UAT are shown in Figure 6-2. In CT, the stresses are concentrated mainly in the primary and secondary shear zones. The first of these regions is between the tool tip and back side of the chip, and the second is on the rake face (front) of the cutting tool. The

character of the stress distribution reached a steady-state condition after the tool came in full contact with the workpiece material. The value of the maximum stress remained almost constant in simulations. In UAT, the distribution of equivalent von Mises stress was transient and changed with the tool movement. The stress values at the tool-workpiece interaction zone reached 1040 MPa in CT and remained constant during the process, whereas in UAT the maximum stress value reached 1050 MPa at the maximum penetration stage and then reduce to 490 MPa in the unloading stage. As soon as the tool came into contact with the chip again at the next penetration stage, the value of stresses reached its peak and thus the cycle was repeated. However, the averaged over time level of the equivalent von-Mises stress in the cutting region in UAT was smaller when compared to those in CT for one complete cycle of vibration.

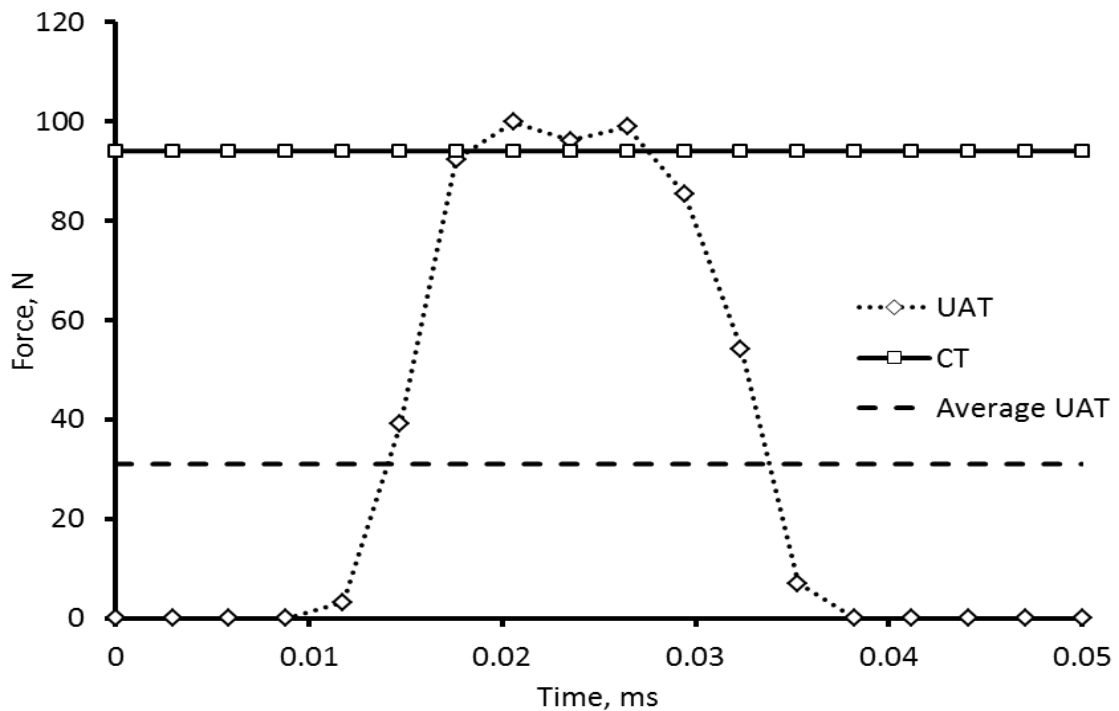


Figure 6-1: Tangential component of cutting force in CT and UAT of Ti-15333 ( $V = 10$  m/min;  $a_p = 0.3$  mm)

The resulted deformation in workpiece material in CT and UAT resulted plastics heat generation in turning of Ti-15333. The amount of heat generated in turning of Ti-15333 was analysed in FE simulations of the orthogonal turning process and are discussed in next section.

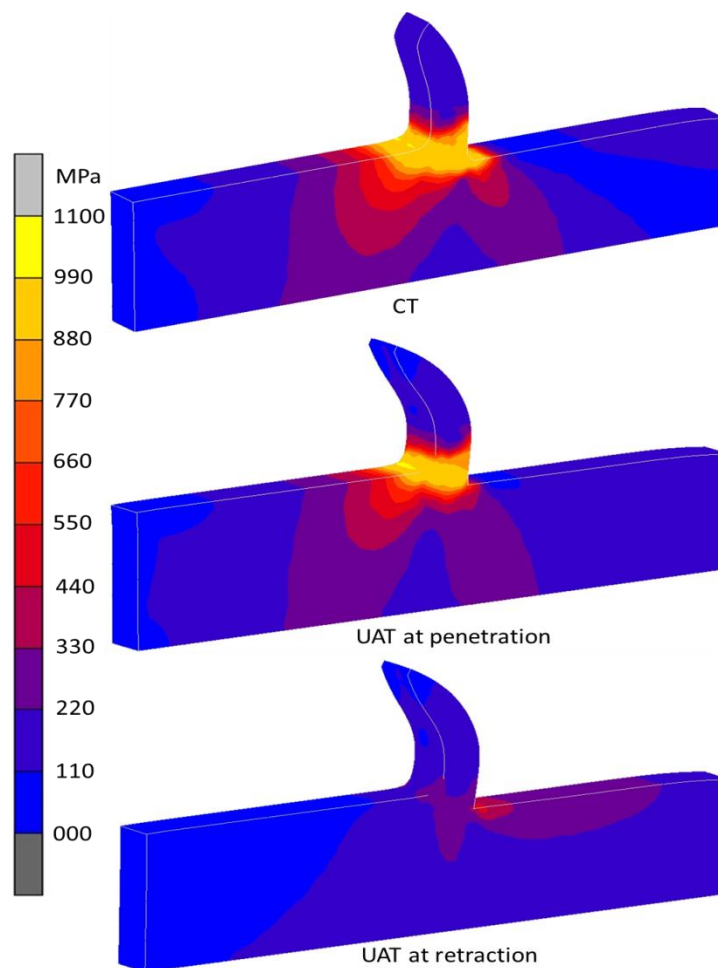


Figure 6-2: Equivalent von-Mises stress distribution in CT and UAT (at penetration stage and retraction stage of ultrasonic vibration ( $V = 10$  m/min;  $a_p = 0.2$  mm))

#### 6.4 Thermal Results

The temperature in the process zone in CT and UAT was also investigated, as shown in Figure 6-3. In simulations of UAT, a relatively higher temperature was observed along the contact area of the tool-workpiece interface. The peak temperature level was observed at penetration stage of vibration. The magnitude of temperature in UAT dropped slightly in retraction stage and relatively higher temperature level was observed in UAT in one complete cycle when compared to CT. The possible cause for this is the effect of additional factor linked to dissipation of vibration energy [4].

The results obtained from experimentations show lower values of temperatures when compared to simulations. The possible reason is the chip obscuring the process zone monitored with the infra-red system. However, one of the main advantages of FE simulations

is its capability to provide in-depth details of the regions that cannot be observed by means of experimentation. Therefore, the temperature of the secondary deformation zone was monitored in the FE simulations that were slightly higher when compared to experimental results. However, the temperature distribution in the chip observed in experiments was in good agreement with FE simulations. The temperature of the process zone in UAT was slightly higher (approximately 80-100°C) when compared to CT.

In turning operations, the cutting tool removes some of the amount of material from the workpiece causes significant plastic deformation in the process zone, resulting heat generation. During the process, the amount of heat transfer from the process zone to the cutting material depends on thermal conductivities of the workpiece and the tool material as well as on the time of contact. In the current study, the temperature distributions along the rake face of the tool in radial direction (width of the tool) and along the chip-flow direction were investigated for CT and UAT.

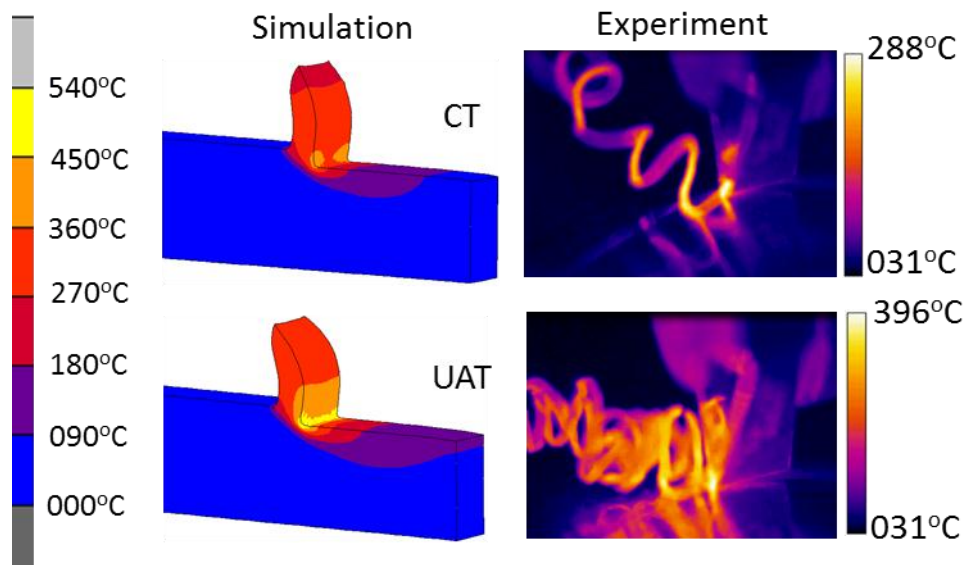


Figure 6-3: Temperature distribution in cutting region ( $V = 10$  m/min;  $a_p = 0.3$  mm)

Analysis of temperature distribution on the rake face of the cutting tool showed that the maximum temperature was reached somewhere in the middle of the cutting edge, with some drops towards the ends of the cutting length (Figure 6-4). This result can be attributed to the convective heat transfer from the rake surface of the tool to the environment.

The temperature distribution on the rake face of tool changes for different stages of the vibration cycle in UAT. At the penetration stage, higher temperature (approx. 90°C) was observed on the rake face due to severe plastic deformation and the frictional effect, whereas during the retraction stage the tool separated from the workpiece, resulting in lower temperatures (approx. 86°C). On the other hand, In CT, a continuous interaction of the tool with the workpiece caused a non-changing distribution of temperature on the rake face. The maximum value observed was 83°C, whereas in UAT the average temperature on the rake face was 88°C. Therefore, temperature distribution on the rake face in UAT was slightly higher (by approx. 5°C) compared to that in CT for 0.3 mm depth of cut, and can be attributed to higher process zone temperature in UAT.

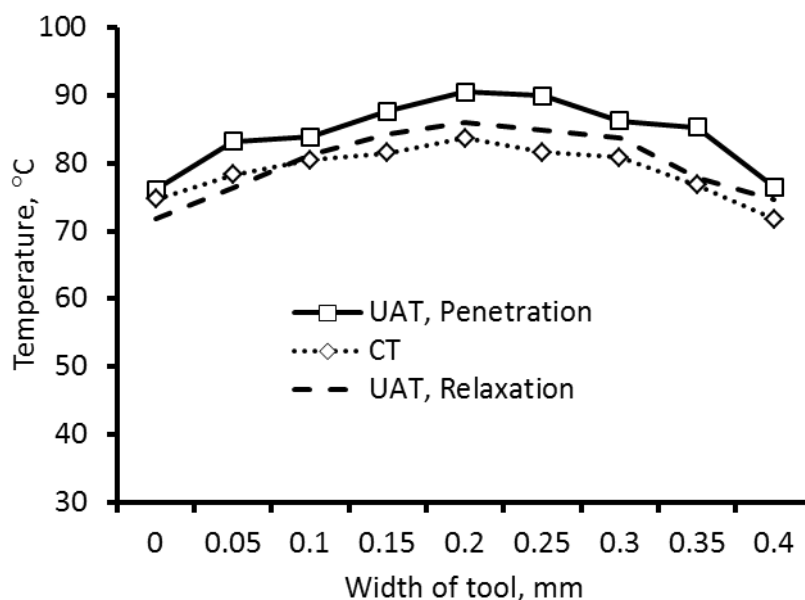


Figure 6-4: Temperature distribution along width of tool in CT and UAT at  $t = 10$  ms

Similarly, a temperature distribution along the rake face (line AB in Figure 6-5) was investigated with the developed model. In UAT at maximum penetration stage, temperature at point-A was higher (by approx. 7°C) compared to CT at maximum penetration stage. Similarly, a maximum temperature of 83°C was observed close to the cutting edge. The magnitude of temperature decreased, moving away from the cutting tool at a given simulation time (10 ms). The tool temperature increased with an increase of time in the turning process; however, the current simulation was carried out for a time interval of 0.0179

s, hence, the tool temperature did not reach a steady state. Still, for comparison purposes, the amount of heat of the cutting tool was discussed in this section.

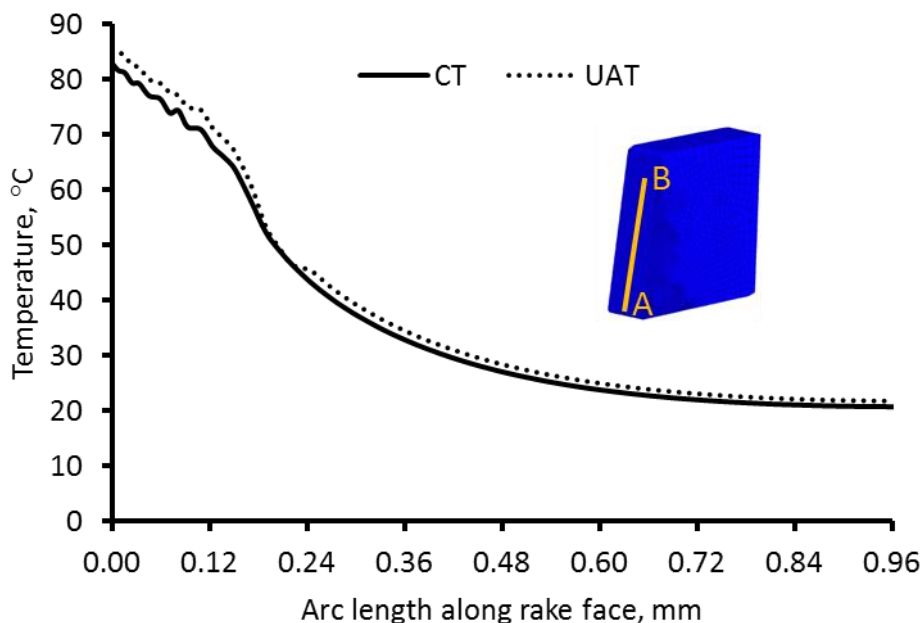


Figure 6-5: Temperature distribution along rake face of tool in CT and UAT at  $t = 10$  ms

## 6.5 Effect of Cutting Conditions

In this section, the effect of cutting conditions on cutting forces and temperature of the process zone was investigated, employing the developed FE model of orthogonal turning together with optimum cutting conditions.

### 6.5.1. Effect of Depth of Cut

The UAT technique was observed to be also effective for higher depths of cut with a consistent reduction (60-65%) in the tangential force component (Figure 6-6). Simulations were carried out for different depths of cut, and it was observed that cutting forces increased with an increase in the depth of cut, as expected. However, for a cutting speed of 10 m/min, a consistent reduction of 60-65% in cutting forces was observed for a depth of cuts exceeding 200  $\mu\text{m}$ . Thus, a higher material removal rates can potentially be achieved in UAT for the same level of cutting forces observed in CT. For instance, the cutting force on the tool at 100  $\mu\text{m}$  depth of cut in CT was 40 N, whereas, at a depth of cut of 500  $\mu\text{m}$  in UAT, the observed cutting force was only 44 N. Therefore, for the same level of cutting forces acting on the cutting tool, the material removal rate can potentially be increased five-fold in UAT when

compared to CT (Figure 6-6). Therefore, UAT is an effective machining technique for the machining of high-strength alloys. Good agreement between experimental and simulations results was observed.

It should be noted that the current trend in machining is to increase the cutting speed as much as possible in order to increase the material removal rate MRR, in this light, it was beneficial to investigate the effect of UAT at higher cutting speed. The succeeding section described in detail the influence of cutting speed on cutting forces in UAT.

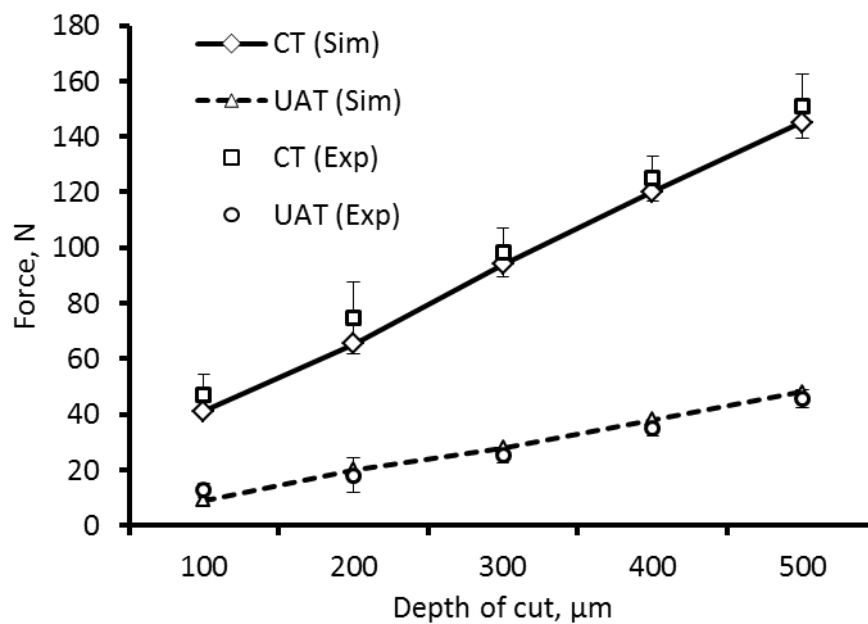


Figure 6-6: Tangential component of cutting forces in CT and UAT of Ti-15333 at various depths of cuts and  $V = 10$  m/min

### 6.5.2. Effect of Cutting Speed

In UAT, for particular vibrational parameters, there is a critical velocity, beyond which reduction in cutting forces vanishes. For the current vibrational parameters of amplitude of  $8 \mu\text{m}$  and frequency of  $20 \text{ kHz}$ , the critical velocity is  $60 \text{ m/min}$ . Therefore, when the cutting speed reaches  $60 \text{ m/min}$ , the tool would not separate from the workpiece material and the effect of UAT will vanish at those particular cutting parameters (Figure 6-7a). The evaluation of forces at various cutting speeds shows that beyond the critical speed, the force levels approach those observed in CT, and the separation between the tool and chip vanished (Figure 6-7b).

In UAT, the cutting forces increased with an increase in cutting speed as shown in Figure 6-8, and the reduction in cutting forces vanished for speed levels beyond 70 m/min (Figure 6-9). However, in CT the cutting forces remain almost the same for various cutting speeds (Figure 6-7a and Figure 6-8). The prime reason for an increase in cutting forces in UAT was that at higher cutting speed, the tool separation in one complete cycle vanished resulting in a nearly constant force level.

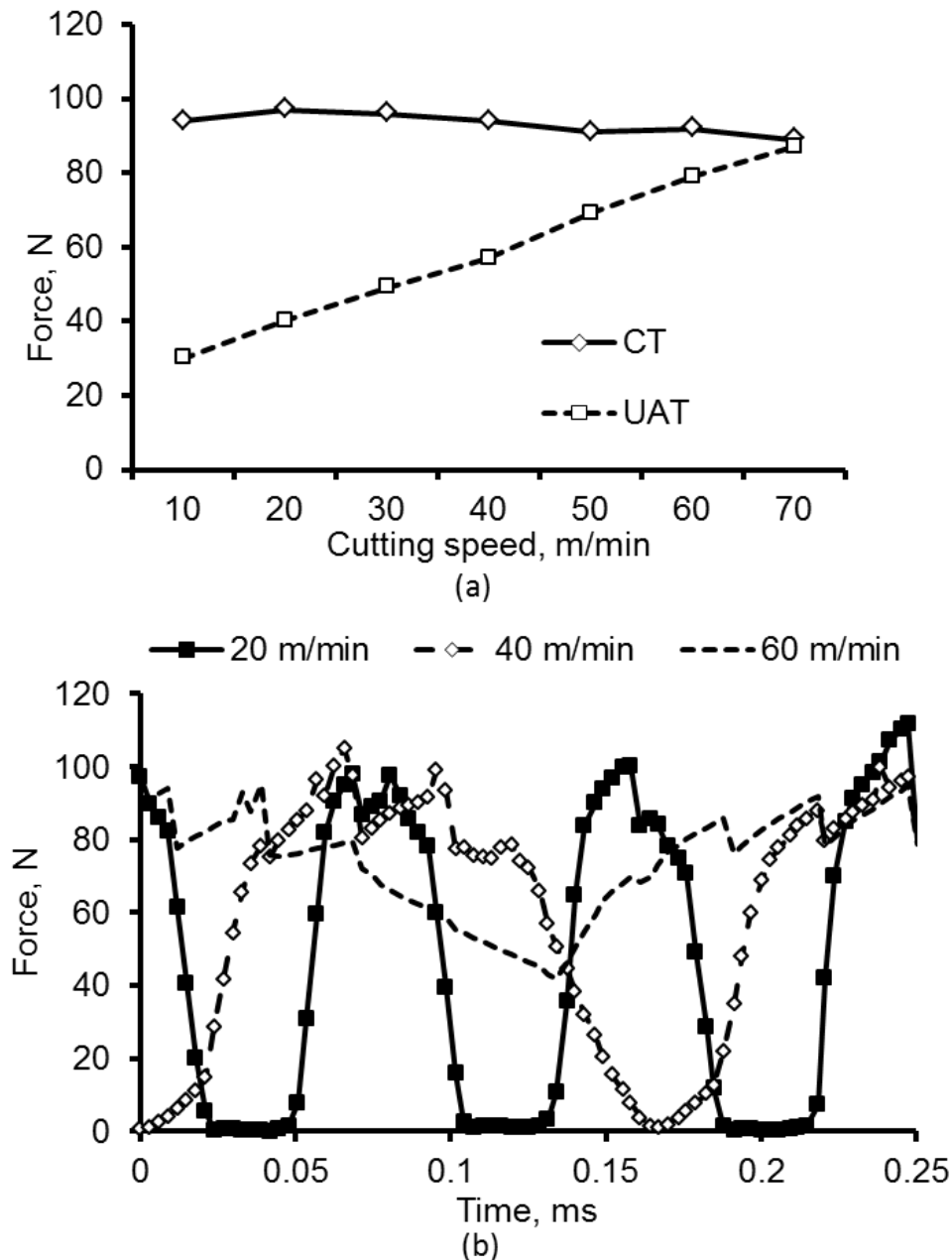


Figure 6-7: (a) Tangential component of cutting forces at various cutting speeds in CT and UAT, (b) forces history in UAT at various cutting speeds at  $a_p = 0.3$  mm

In Figure 6-9, a slight reduction (2%) in the cutting forces was observed at 70 m/min (as well as a 14% reduction at the critical speed (60 m/min)) as shown in Figure 6-7b. During the retraction stage, the tool moved in the backward direction with a relative velocity of 60 m/min whereas the workpiece velocity was 70 m/min. But still some reduction in the cutting forces was observed and can be attributed to the effect of thermal softening of the workpiece material causes by the heat generated at the process zone.

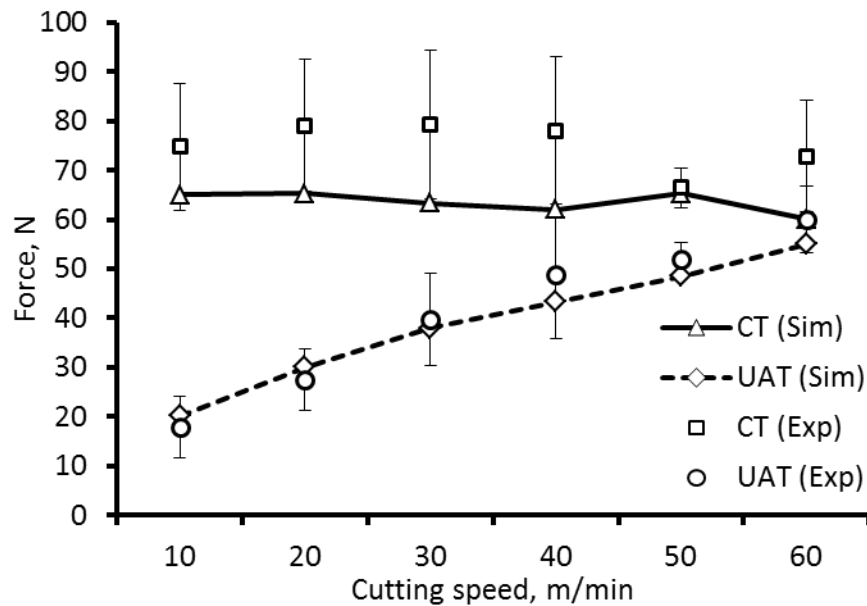


Figure 6-8: Tangential component of cutting forces in CT and UAT at various cutting speeds and at  $a_p = 0.2$  mm

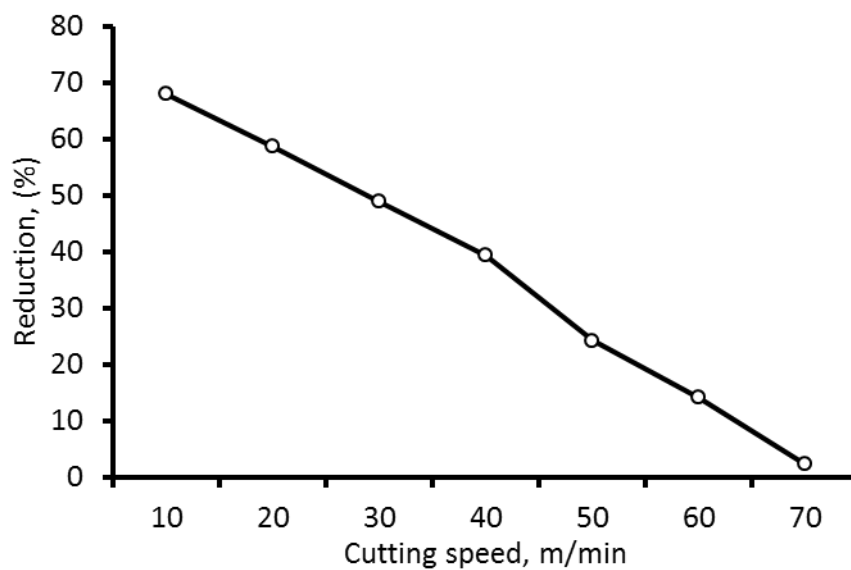


Figure 6-9: Reduction in cutting force at various cutting speeds

Since, cutting speed has a major influence on the cutting forces observed in UAT, whereas it is well known that the relative velocity of the tool in UAT is a function of vibrational parameters. Hence, those parameters will also affect the cutting forces observed in UAT. The following two sections demonstrate the effect of vibrational parameter on the observed cutting forces and temperature of the process zone.

### 6.5.3. Effect of Vibrations Frequency

It is well known that selection of appropriate vibration parameters such as amplitude and frequency of vibration is critical for UAT. This was investigated by means of FE analysis of UAT. Five levels of frequency (5 kHz, 10 kHz, 15 kHz, 20 kHz and 25 kHz) were analysed in FE simulations of UAT of Ti-15333. At lower frequency, the tool separation was very slow which accelerated with an increase in the frequency in UAT. In all the cases, the depth of cut was fixed at 300  $\mu\text{m}$ , the cutting speed at 10 m/min and amplitude of vibration at 8  $\mu\text{m}$ . The relative velocity of the cutting tool is proportional to the vibrational amplitude and frequency:

$$V_r = V + 2\pi f a \cos(2\pi f t), \quad (6 - 1)$$

where  $f$  is the frequency,  $V_r$  is the relative velocity,  $V$  is the cutting speed and  $a$  is the amplitude.

Equation (6 – 1) was verified by using the above set of frequencies to demonstrate the predictability of the model. For all five cases, a reduction in the cutting forces with an increase in frequency is summarized in Figure 6-10. An average reduction of 36 N in the cutting forces was noted with application of 5 kHz frequency on the cutting tool. The decline increased to 55 N and 59 N with the frequency increasing to 10 kHz and 15 kHz, respectively, when compared to CT. A further increase in the frequency to 20 kHz and 25 kHz resulted in an average reduction of 63 N and 64 N when compared to CT, respectively. The effect of frequency growth became very small after 20 kHz. Therefore, in the current study, a frequency of 20 kHz was used for UAT. It is worth noting here that the effect of frequency will be different at various cutting speeds.

The equivalent plastic strain of the workpiece material also increased with an increase in the frequency of the tool in UAT. A nearly linear increase in plastic strain of the process zone was

observed in simulations of UAT with the growing frequency as shown in Figure 6-11. A total increase in plastic strain of 3.5% was noted at the peak frequency when compared to the minimal value of frequency applied in UAT. An increase in plastic strain was mostly due to the increase in temperature of the process zone at higher frequencies.

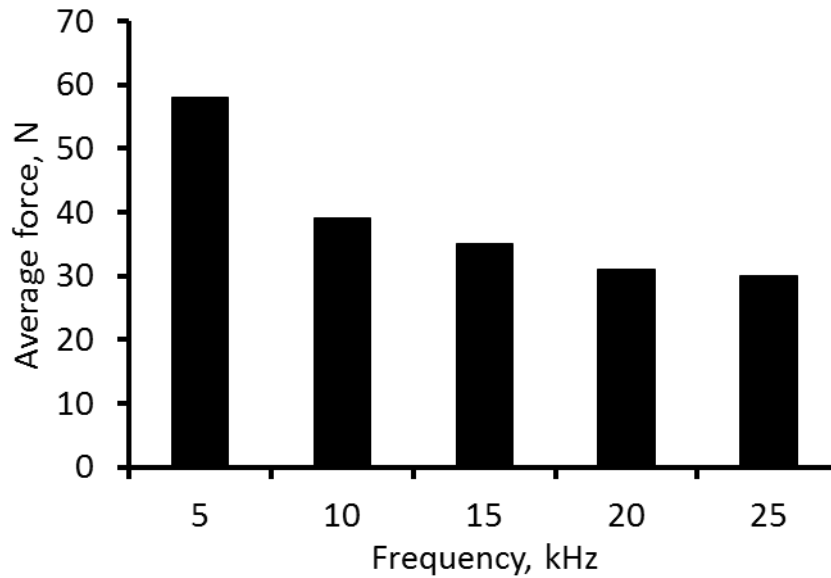


Figure 6-10: Average cutting forces at various frequencies of vibration ( $V = 10$  m/min;  $a_p = 0.3$  mm)

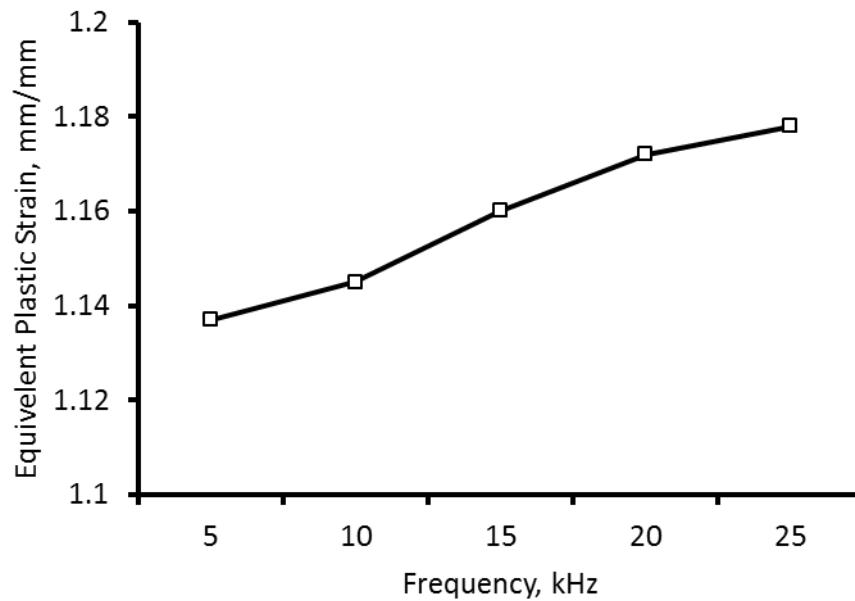


Figure 6-11: Equivalent plastic strain at various frequencies of vibration

The analysis of thermal results was also carried out at various frequencies, and it was found that the temperature of the process zone increased with an increase in the frequency of the cutting tool in UAT (Figure 6-12). In the thermal analysis at various frequencies of vibration, the peak temperature value of the process zone was considered. When ultrasonic vibration was superimposed on the cutting tool, the temperature of the process zone increased as explained in Section 6.4. The effect of frequency on the temperature of the process zone was investigated and it was found that a rise of 36°C was observed for frequency of 5 kHz. A nearly linear increase in temperature of the process zone was achieved with an increase of the frequency of the cutting tool to 20 kHz, and the possible reason is the amount of extra energy due to vibration. However, above 20 kHz, the rise in temperature decreased and a very small increase of temperature was observed at a higher frequency.

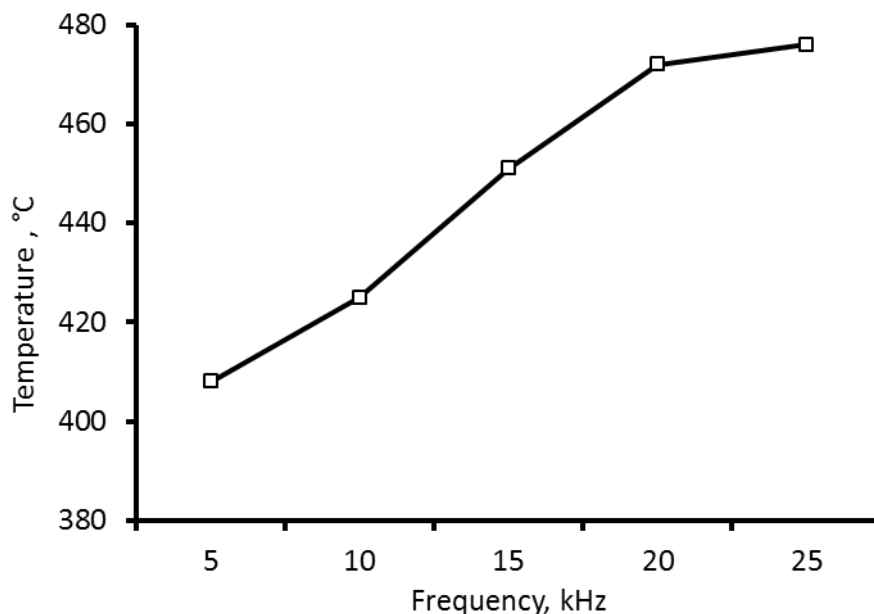


Figure 6-12: Temperature of process zone at various frequencies of vibration

Therefore, with an increase in frequency of the cutting tool, keeping the amplitude constant, a significant reduction in cutting forces, an increase in temperature and plastic strain of the process zone up to a fixed limit, above which the effect of vibration was no longer effective, was observed for the specified cutting speed. However, the values of critical frequency change for different cutting speed and depend on the power of transducer applying vibration to the cutting tool.

Similarly, amplitude of vibration was also analysed with the developed FE model and results obtained from simulations are discussed in the following section.

#### 6.5.4. Effect of Vibration Amplitude

A reduction in cutting forces was observed with the increase in the vibration amplitude for the same frequency. In UAT, the effect of amplitude on the average tangential cutting force, temperature of the process zone and plastic strain of the workpiece material was studied. The cutting depth was fixed at 300  $\mu\text{m}$ , the feed rate at 100  $\mu\text{m}$  and the amplitudes were changed from 3  $\mu\text{m}$  to 12  $\mu\text{m}$  with the frequency set at the optimal level of 20 kHz. From Figure 6-13, it is clear that the tangential component of force declined with an increased in the vibration amplitude.

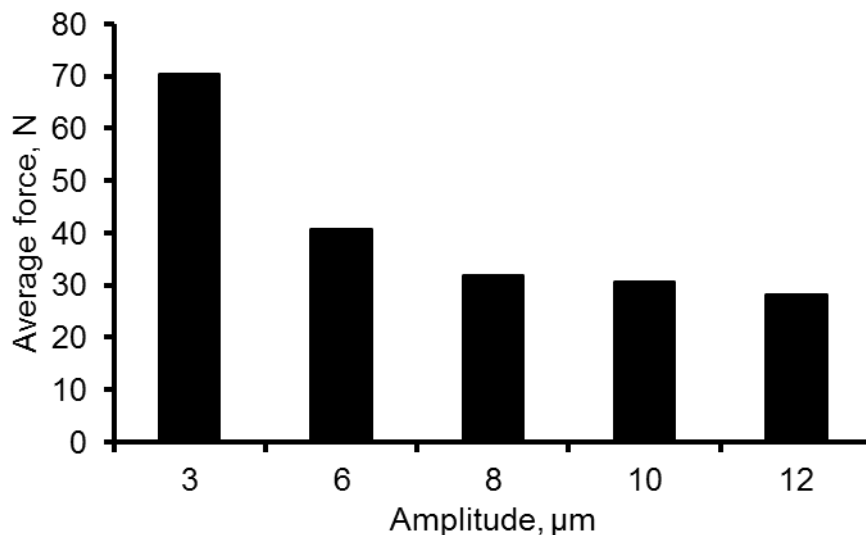


Figure 6-13: Average cutting forces at various amplitudes of vibration ( $V = 10 \text{ m/min}$ ;  $a_p = 0.3 \text{ mm}$ )

As the amplitude of vibration increased, the extent of separation between the tool and workpiece in one complete cycle increased, resulting in a higher force reduction in UAT when compared to interminable tool contact in CT. It was observed that the higher vibration amplitude led to an increase in the force reduction when compared to CT at the same machining parameters. However, high-power transducers are required to produce a stable high amplitude for UAT. In the amplitude analysis, it was observed that a decrease of 25% in the average force level was recorded for an increase in the amplitude from 0  $\mu\text{m}$  to 3  $\mu\text{m}$ . An additional decline of 29 N (41%) and 32 N (54%) was observed when the amplitude was

further increased to 6  $\mu\text{m}$  and 8  $\mu\text{m}$ , respectively (Figure 6-13). The cutting forces declined additionally by 2 N when the amplitude was further increased to 10  $\mu\text{m}$ . However, this reduction lessened above 10  $\mu\text{m}$  (less than 6% from 10  $\mu\text{m}$  to 12  $\mu\text{m}$ ). At higher amplitudes of vibration, the peak force value in a complete cycle increased slightly compared to lower amplitudes. Therefore, in the current study, the amplitude of 8  $\mu\text{m}$  was used in the experimental analysis, resulting in a significant reduction in cutting forces.

Similarly, the amplitude of vibrations has a significant influence on temperature of the process zone and, ultimately, on the plastic strain of the workpiece material. A noticeable change in plastic strain of the process zone was achieved with an increase in the amplitude of vibration (Figure 6-14). An average increase of 5% was observed in plastic strain when the amplitude of vibration was increased from 3  $\mu\text{m}$  to 12  $\mu\text{m}$ . The increase in plastic strain is due to the higher plastic deformation of the workpiece material at transient loading conditions.

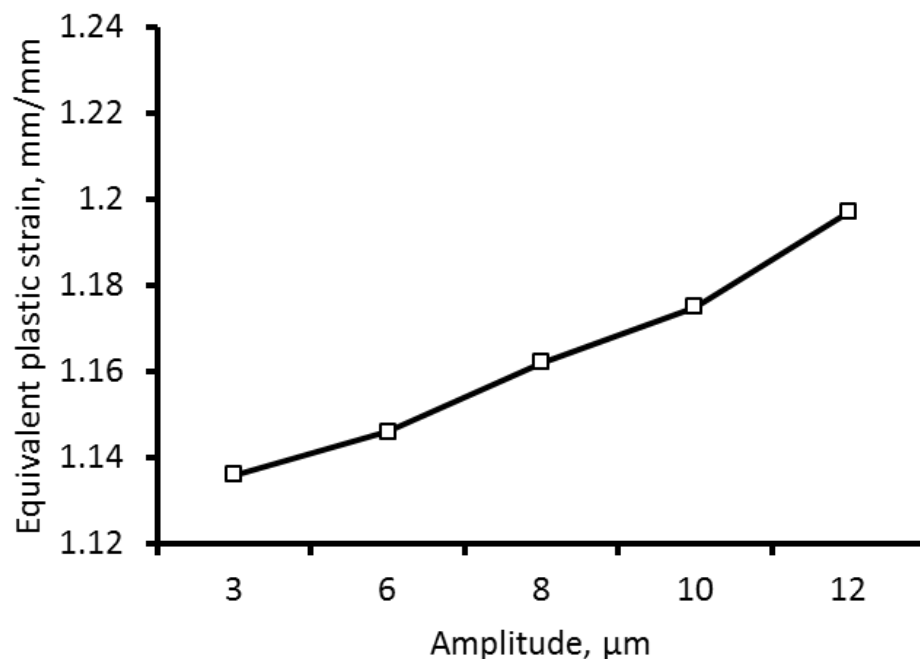


Figure 6-14: Plastic Strain at various amplitudes of vibration

Furthermore, the temperature of the process zone also increased with an increase in the amplitude of vibration (Figure 6-15). An initial increase of 36°C was observed with the application of amplitude of 3  $\mu\text{m}$  on the cutting tool together with a steady rise in temperature with an increase in the amplitude. An average increase of 74°C and 100°C was calculated for 6  $\mu\text{m}$  and 8  $\mu\text{m}$  amplitude of vibration superimposed on the cutting tool. The

process zone temperature grew with an increase in the amplitude, and rises of 23°C and 14°C were observed at the amplitude of vibrations of 10  $\mu\text{m}$  and 12  $\mu\text{m}$ , respectively. The prime reason for the increase in the temperature of the process zone with an increase in the amplitude was the additional amount of energy supplied to the cutting tool in UAT. The imposed vibration on the cutting tool increased the relative velocity of the cutting tool and, eventually, resulted in higher plastic stain and temperature of the process zone.

The analysis of the vibrational parameters on the cutting forces, temperature of the process zone and plastic deformation resulted in-depth understanding of the process. In addition to that, tool geometry has a significant influence on deformation of the process zone and output parameters in the turning process. A separate study was conducted to investigate its effects on deformation in turning of Ti-15333 in the succeeding section.

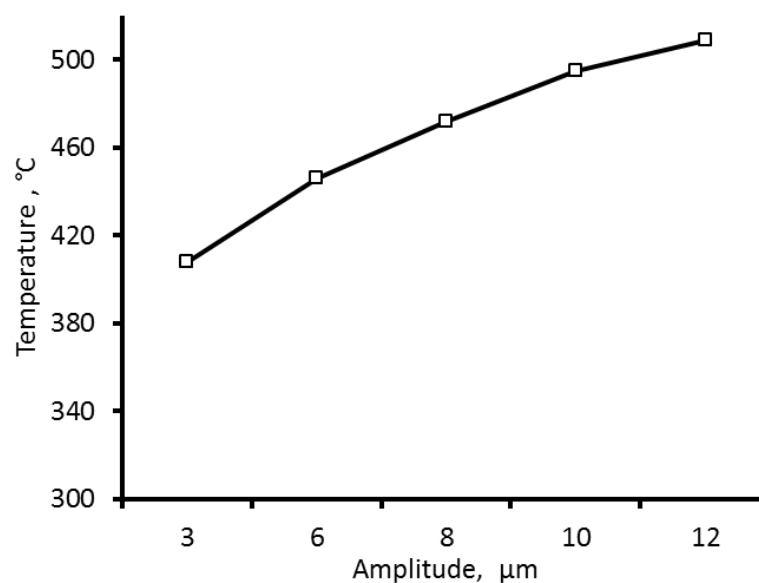


Figure 6-15: Temperature of process zone at various amplitudes of vibration

## 6.6 Effect of Tool Geometry

Three magnitudes of rake angle ( $\alpha$ ) –  $-14.6^{\circ}$ ,  $0^{\circ}$  and  $14.6^{\circ}$ – were used in the FE simulations to investigate the effect of tool geometry on the process parameters. The rake angle not only controls the flow of the chip and the heat generated at the cutting zone but also the magnitude of the cutting forces. A linear increase in cutting forces was observed with a decrease in a rake angle for the same cutting conditions as shown in Figure 6-16. The extent of the increase in the cutting force in CT and UAT with the a maximum decrease in the rake

angle in machining of Ti-15333 was 18% and 31% when compared to the cutting force obtained with the cutting tool having a positive rake angle in CT and UAT, respectively. The possible reason for this is an increase in friction between the tool and the rake face of the tool.

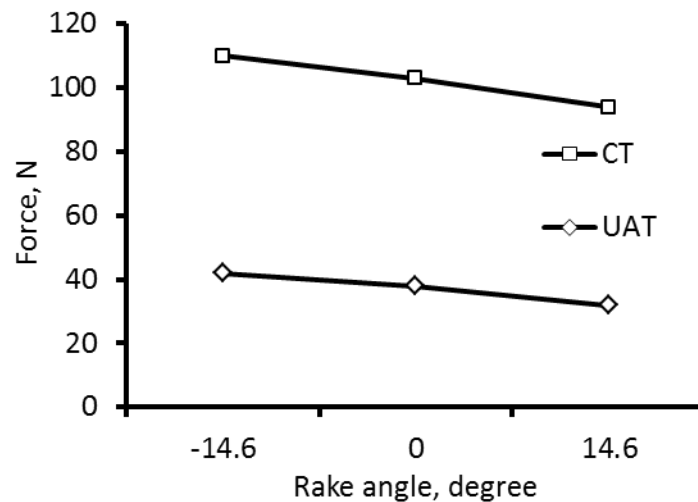


Figure 6-16: Effect of rake angle on cutting force in CT and UAT

In a turning process, a positive rake angle is recommended as the cutting forces are lower in this case compared to tool with the negative and zero rake angles. On the other hand, the strength of the tool is also dependent of the rake angle: a positive rake angle makes the tool sharper and reduces its strength. A negative rake angle increases the forces but makes the tool blunt and increases its strength. Zero rake angle tools are easy to manufacture. However, based on the current study, tool with positive rake angles are recommended for the turning of Ti-15333 in UAT because of lower cutting forces.

Temperature of the process zone was observed to increase with a decrease in the rake angle. This is not surprising, since a reduced rake angle results in increased deformation and work done on the chip; hence, higher temperature in the cutting region was observed. The level of temperature in the cutting region at various rake angles for Ti-15333 is shown in Figure 6-17, during the maximum penetration stage in UAT. A noticeable temperature difference was observed with the decreasing rake angle in UAT. Furthermore, plastic strain also increased with a decrease in the rake angle, as expected (Figure 6-17). In UAT, the vibro-impact behaviour of a tool with workpiece resulted, a significant improvement in output parameters

in the turning process for various tool geometries. In the following section, the contact duration of the tool with the workpiece material in UAT is described in details.

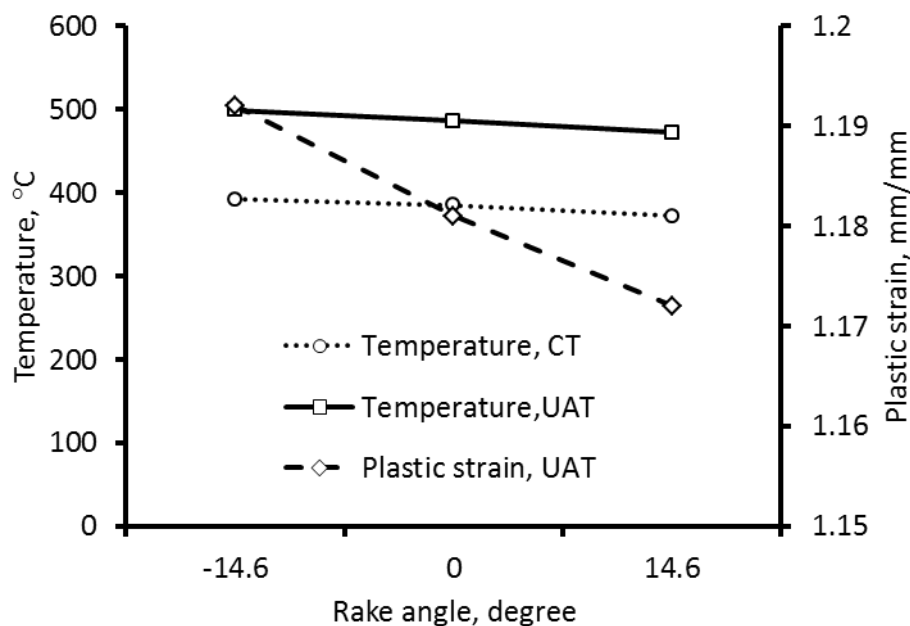


Figure 6-17: Plastic strain and temperature of the process zone at various rake angles (at the maximum penetration stage in UAT)

## 6.7 Contact in UAT

In UAT, vibration in tangential direction was superimposed on the movement of cutting tool causing it to move in forwards and backwards with vibrational parameters superimposed on it. During the penetration stage, the tool came in contact with the workpiece, whereas in the retraction stage, the tool separated from the workpiece material. The separation of the tool from the workpiece material was investigated with the developed FE model. An initial investigation was carried out to investigate the mode of workpiece in contact with the tool in UAT. From the analysis it was concluded that the machining time or time of contact of the tool with the workpiece was approximately 43% in one complete cycle as shown in Figure 6-18. For the rest of the time, the tool is fully separated from the workpiece material. However, in this analysis, the number of nodes in contact with the tool varied during the contact, depending on its position. At the penetration stage of the tool, the number of nodes in contact was maximized. However, the number of nodes changed during the penetration and retraction stage of the tool movement due to the non-linearity of material. So, in the current

contact analysis (Figure 6-18), a full contact was defined as unity if the number of connected nodes between the tool and workpiece exceeded ten. Otherwise, a separation was assumed in the analysis.

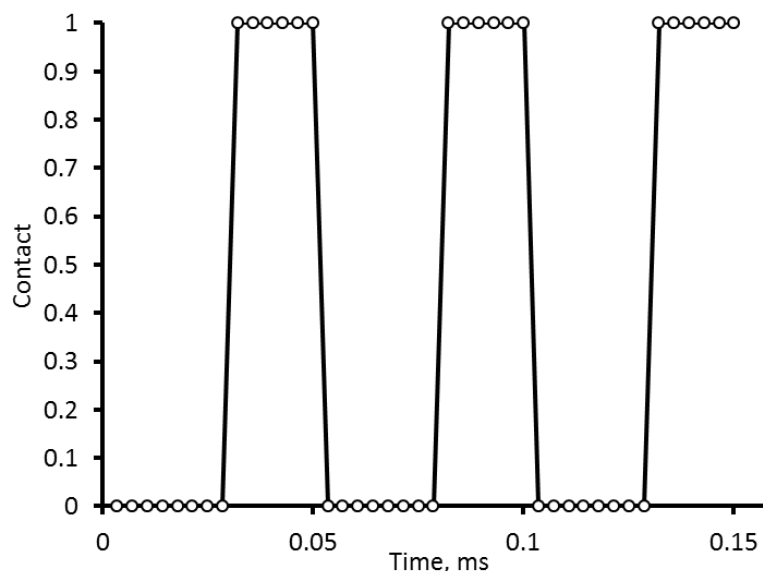


Figure 6-18: Contact status of tool with workpiece in UAT ( $a_p = 0.3$  mm;  $V = 10$  m/min;  $f = 20$  kHz and  $a = 8$   $\mu$ m)

The above sections described the various features of UAT in turning of Ti-15333. The reduction in cutting forces was substantial when compared to CT. The same level of peak force magnitudes were observed in UAT and CT. Though, the interval of time in UAT was significantly lower. In order to minimize the observed peak level of cutting forces and to further minimize the average magnitude of cutting forces, hot machining was combined with UAT to form a new hybrid turning process called hot ultrasonically assisted turning (HUAT). The model was used to analyse the newly developed turning process at various cutting conditions. A detail description of the results obtained from FE simulation of HCT and HUAT are explained in the subsequent section.

## 6.8 Hot Machining

The FE model was developed to investigate ultrasonically assisted turning of Ti-15333 at various cutting conditions. The cutting force observed in UAT was considerably lower when compared to CT. However, the prime aim of the current work was to further reduce the peak-force level. Therefore, the developed FE model was also used to investigate the effect of hot

machining in CT and UAT at various cutting and vibrational parameters, i.e. for two hybrid techniques HCT and newly developed HUAT. Both turning techniques were analysed using the developed FE model to investigate the effect of cutting conditions as well as vibrational parameters. The main purpose of the developed model was to diminish costly experimental efforts and analyse assisted machining techniques at various cutting conditions. Though, all the turning experiments were carried out on a lathe machine using the oblique turning process, the current orthogonal turning model provides a useful prediction for the tangential force component in HUAT when compared to CT at various cutting conditions.

Hence, the FE simulations of HCT and HUAT were carried out at various temperature levels to investigate the effect of externally applied heat on cutting forces, temperature and stresses, at various cutting conditions and vibrational parameters.

Five temperature values  $-20^{\circ}\text{C}$ ,  $100^{\circ}\text{C}$ ,  $200^{\circ}\text{C}$ ,  $300^{\circ}\text{C}$  and  $500^{\circ}\text{C}$  were used in the FE model to investigate the effect of externally applied heat on cutting forces. A gradual reduction in cutting forces was observed with application of heat applied externally to the workpiece material. The force evaluation in one complete cycle of vibration in HUAT is shown in Figure 6-19. The applied heat to the workpiece material reduced yield strength of the advanced alloy and forces required to remove the excess amount of material. In turning Ti-15333 alloy, with both HCT and HUAT, the peak force values reduced with the application of externally applied heat. Hence, the forces required for the cutting tool to remove the given amount of material from the workpiece were significantly lower when compared to CT (see Figure 6-19). The calculated average cutting forces in HCT and HUAT both experimentally and numerically at various temperatures of workpiece are shown in Figure 6-20. The simulated results are in good agreement with the experimental data.

A gradual decline in the level of cutting forces was observed with the application of external heat to the workpiece material. The peak-force value experienced by the tool at the penetration stage of UAT reduced. The extent of reduction in cutting forces was higher in HUAT when compared to HCT for the same level of externally applied heat source to the workpiece material as shown in Figure 6-21.

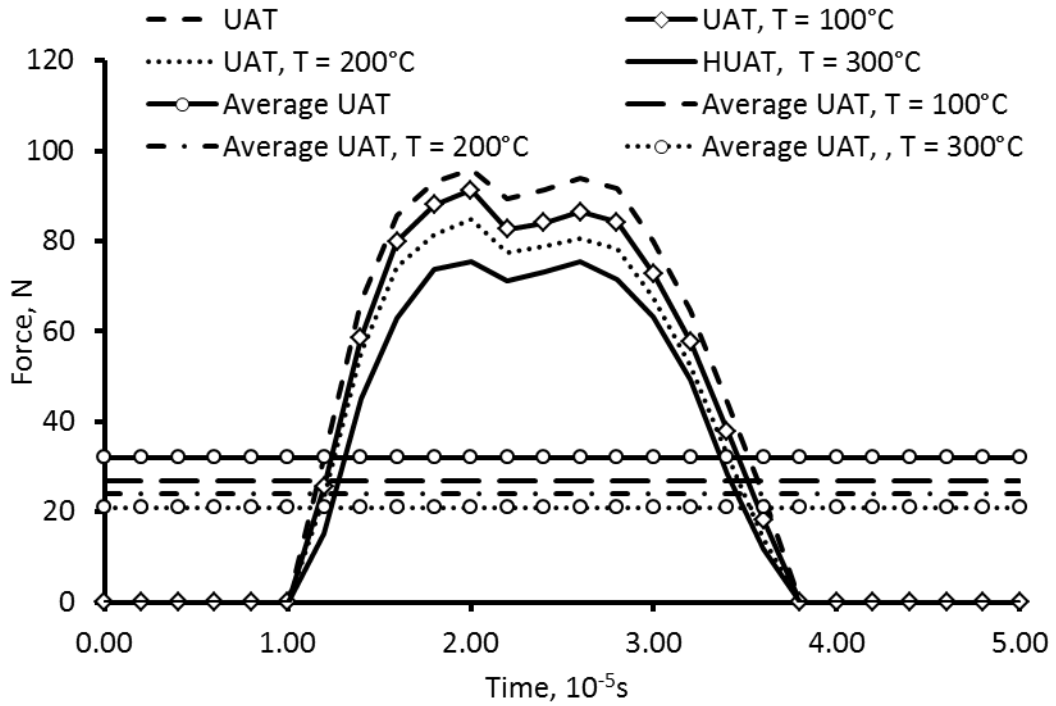


Figure 6-19: Tangential components of cutting force in HUAT of Ti-15333 ( $V = 10$  m/min;  $a_p = 0.3$  mm)

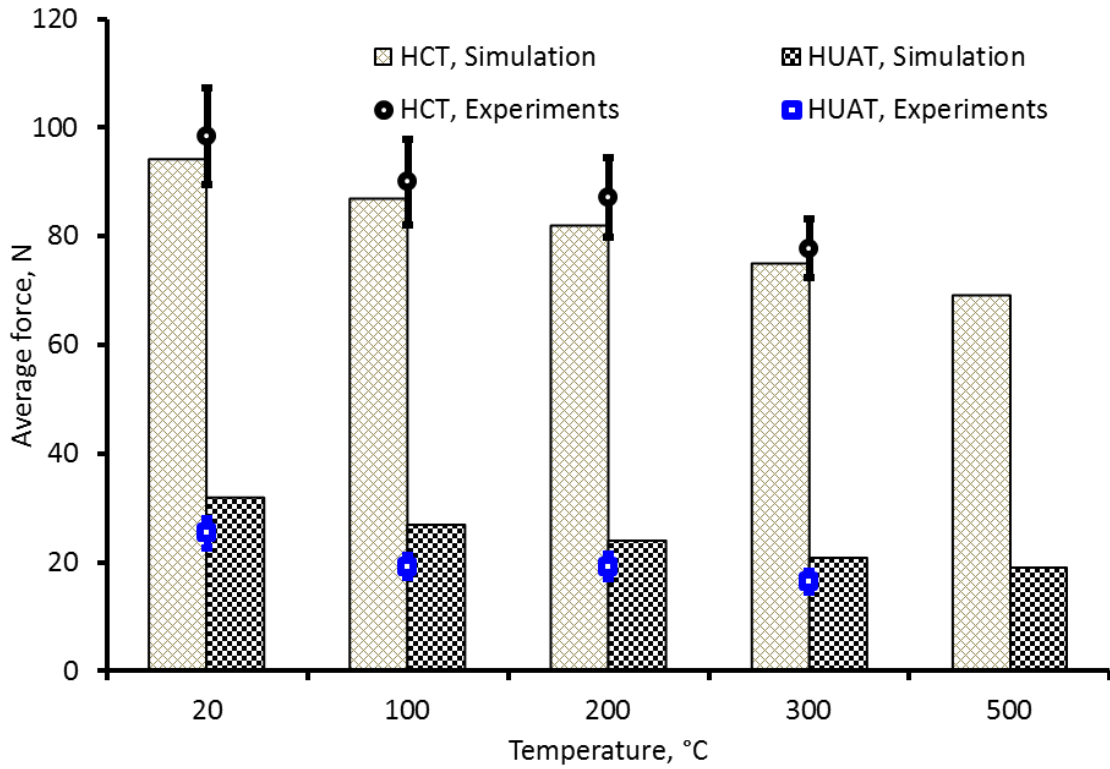


Figure 6-20: Average tangential cutting forces at various temperatures in HCT and HUAT ( $V = 10$  m/min;  $a_p = 0.3$  mm)

At the workpiece temperature of 100°C, the cutting force was 29% of the cutting force obtained in CT whereas in HCT, the reduction in forces was only 7%. The reduction in cutting forces increased in both HUAT and HCT and, ultimately, respective reductions of 80% and 25% in cutting forces was observed at 500°C preheating of the workpiece material. However, when results of HUAT were compared with CT, an interesting observation was obtained from the simulations. The cutting forces were reduced by approximately 78% at 300°C and 80% at 500°C when compared to the forces obtained in CT. The ultimate aim of the newly developed hybrid turning process was to minimize the cutting forces, experienced by the cutting insert in machining of high-strength alloys. However, the main limitation of Ti-15333 is formation of alpha-precipitates if exposed to significantly higher temperatures (above 450°C) for a period of more than one hour. Hence, in experimentation a temperature of 300°C was used to assist the benefits of HUAT. However, once the model was verified for the cutting forces at various cutting conditions and temperature, then their prediction was made based on the developed FE model. The current study indicated that an increase in temperature of hot machining does not necessarily yield tractable benefits with respect to force reductions. At 500°C the reduction in cutting forces is comparable to that for workpiece heating temperature of 300°C. Thus, from the current study, a temperature of 300°C in hot machining of Ti-15333 can be recommended.

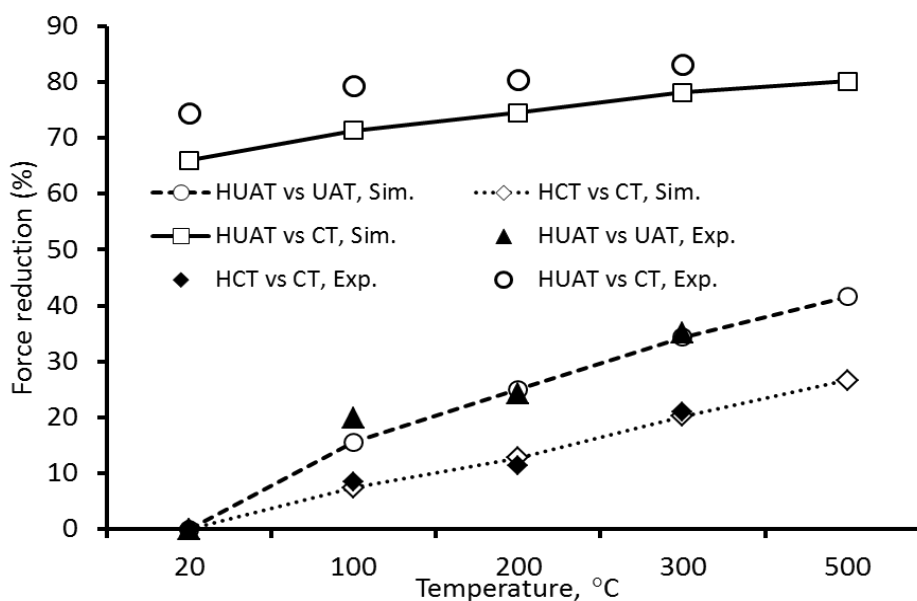


Figure 6-21: Reduction in cutting forces in hot machining at various temperatures ( $V = 10$  m/min;  $a_p = 0.3$  mm)

Similarly, the effect of vibrational parameters on the cutting forces was also investigated with the developed model for HUAT. As discussed in UAT, the application of different amplitude levels resulted in a significant reduction in cutting forces and beyond a certain value of amplitude, the effect vanished and the respective gain in reduction in cutting forces were significantly lower. For that purpose, the developed FE model is an effective tool to study the process at different amplitude values and select the optimized magnitudes of vibration parameters for HUAT. The developed model for HUAT was used for frequency and amplitude analysis to suggest the optimized values for turning of Ti-15333. In the FE simulation of HUAT, it was observed that the cutting forces reduced with increase in the amplitude of vibrations as expected. As amplitude increased, the non-contact time between the tool and the workpiece increased causing lower forces in one complete cycle of HUAT as shown in Figure 6-22. A linear reduction in cutting forces was observed with the amplitude increasing from 0  $\mu\text{m}$  to 8  $\mu\text{m}$  in HUAT. However, the extent of reduction in cutting forces with the application of external heat also decreased above the amplitude of vibration of 8  $\mu\text{m}$  for a cutting speed of 10 m/min and depth of cut of 300  $\mu\text{m}$  (Figure 6-22). A possible reason for diminishing the reduction of cutting forces above 8  $\mu\text{m}$  amplitude was a slight increase in the peak-force level in each cycle in HUAT. Though the amplitude of vibration was increased further, the decline in cutting forces was significantly lower and hence, in the current study of HUAT of Ti-15333, the amplitude of 8  $\mu\text{m}$  was chosen as an optimal value for enhanced force reduction and was used in the analysis.

Additionally, the effect of frequency on the cutting forces was also investigated, and a nearly linear reduction in cutting forces was observed with an increase in the vibration frequency. The average cutting forces at various frequencies of vibrations are shown in Figure 6-23. When compared to the results obtained for UAT, a significant reduction in cutting forces was observed with the application of an external heat to the workpiece material. The reduction in cutting forces ranging from 15% to 35% in HUAT at 5 kHz and 20 kHz respectively was found when compared to the cutting forces in UAT. However, the additional reduction in cutting forces was minimal above frequency of 20 kHz in HUAT. The possible reason for the reduction in cutting forces is a slight increase in peak-force level and reduced separation between the tool and the workpiece. Therefore, the suggested vibrational parameters for Ti-15333 in

HUAT were amplitude of 8  $\mu\text{m}$  and frequency of 20 kHz for a cutting speed of 10 m/ min and depth of cut of 300  $\mu\text{m}$ .

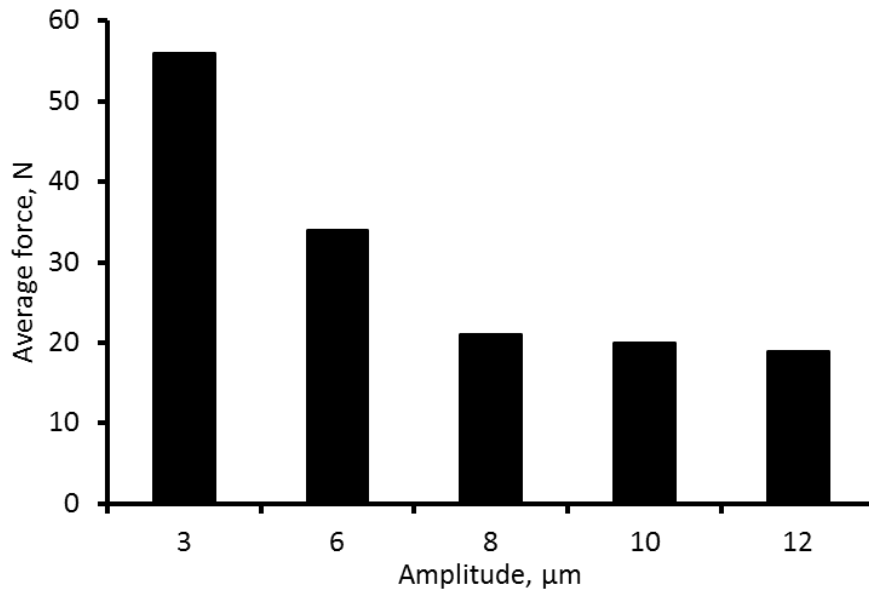


Figure 6-22: Average cutting forces at various amplitudes of vibration (b)

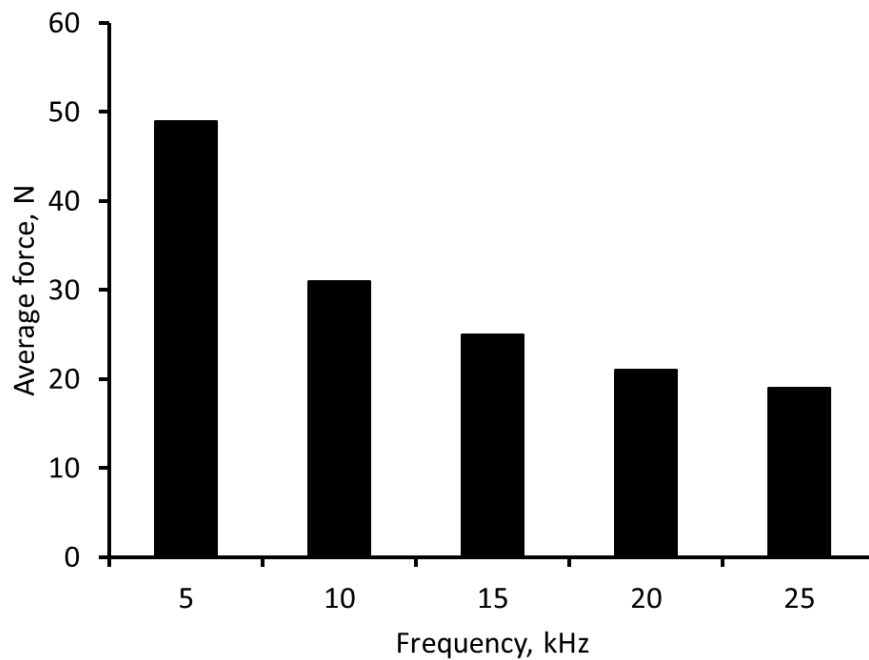


Figure 6-23: Average cutting forces at various frequencies of vibration

The temperature of the cutting region was also analysed numerically at various cutting conditions in HUAT, and the results were compared with those for CT, UAT and HCT. The temperature of the cutting region increased with the increase of external applied heat to the

workpiece material in HUAT. It increased additionally the process zone temperature and resulted in relatively high temperature magnitudes compared to those for all other turning processes studied. The temperature distributions in the process zone in the novel turning process (HUAT) are shown in Figure 6-24.

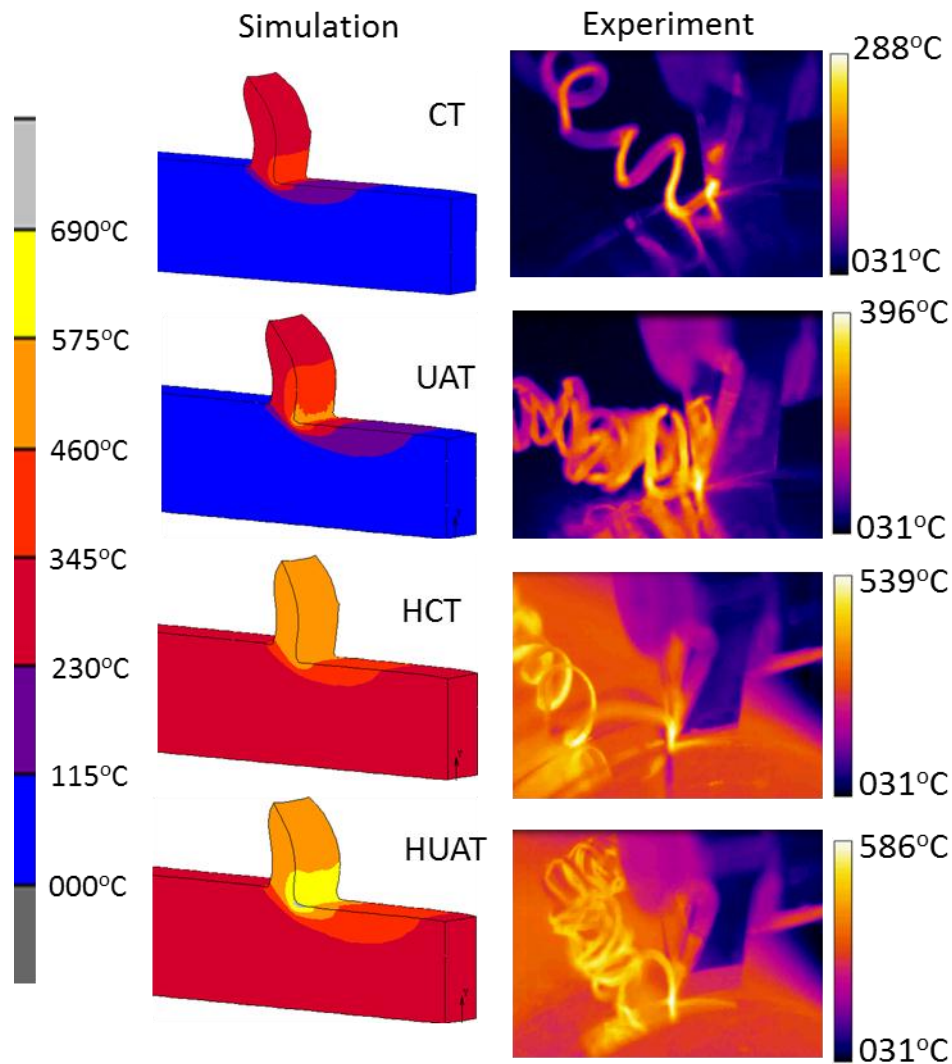


Figure 6-24: Temperature in the process zone in CT, UAT, HCT and HUAT

In turning experiments, infra-red thermography was used to carry out thermal analysis of the process zone for novel HUAT and other turning processes, However, the temperature of the process zone was not visible clearly due to limitations of the complex tool-workpiece interaction zone. Relatively lower values were observed in experiments when compared to the FE results, however, the value of the temperature of the parts visible to the thermal camera in the performed tests are in good agreement with the obtained numerical results.

Hence, in the FE results, the peak temperature value of the deformation zone is discussed in comparison with that of the other turning processes. In HUAT, a relatively higher temperature of the process zone was observed: the peak temperature was 660°C. The overall increase in temperature of the cutting region at the maximum penetration stage of the tool in HUAT (288°C) was 43% more than in CT. A comparative analysis of newly developed HUAT with other turning processes is shown in Figure 6-24. The increase in the temperature of the process zone was due to the application of external heat to the workpiece material and superposition of vibration on the cutting tool. However, from the previous section it is clear that the increase in temperature of the process zone, due to vibration was approximately 100°C (from 372°C to 472°C). Hence, the rise in temperature of the process zone is mainly attributed to the externally applied heat to the workpiece material. The applied heat to the workpiece material reduced the heat generation in the process zone due to plastic deformation. The rise in the process zone temperature was significantly lower when compared to the externally applied heat to the workpiece material.

Similarly, the temperatures of the deformation zone in UAT and HCT are 21% and 37% higher when compared to CT. However, the maximum reduction in the cutting forces was observed in HUAT when compared to the other turning processes.

In addition to above, the amount of heat transfer to the cutting tool from the process zone in HUAT was also investigated. A significantly higher temperature on the rake face in chip-thickness and flow direction was observed. A maximum temperature of 318°C was found on the rake face in HUAT at the penetration stage. A slight reduction of 7°C in temperature was observed in the retraction stage, and the average temperature in one complete cycle was 314°C. The reduction in temperature at the retraction stage in HUAT can be attributed to the convective heat transfer from the cutting tool. However, the temperature in HUAT was nearly equal to the rake-face temperature in HCT (309°C). Hence, in both HCT and HUAT, the rise in rake-face temperature was almost the same when compared to CT; however, the maximum reduction in cutting forces was observed in HUAT. The distributions of temperature along the rake face in the chip-width and flow directions are shown in Figure 6-25 and Figure 6-26, respectively.

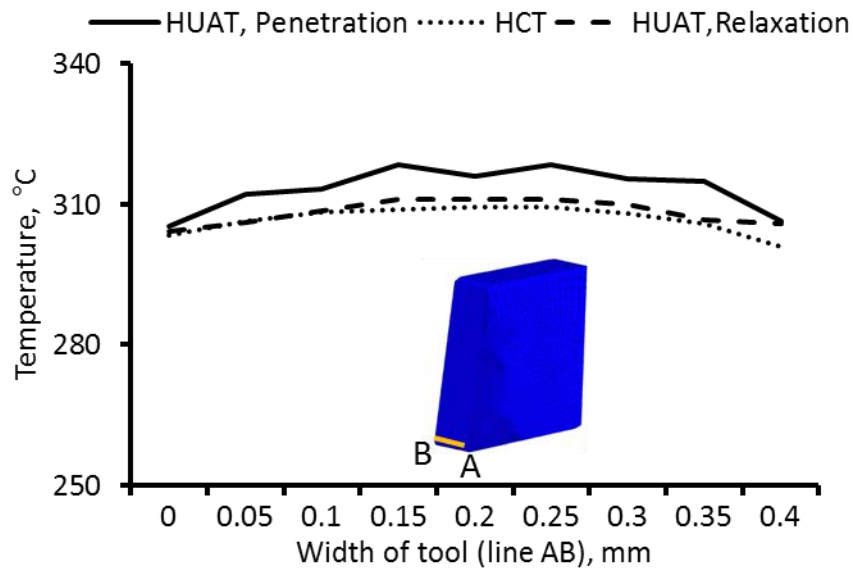


Figure 6-25: Temperature distribution on rake face of tool along chip width in HCT and HUAT

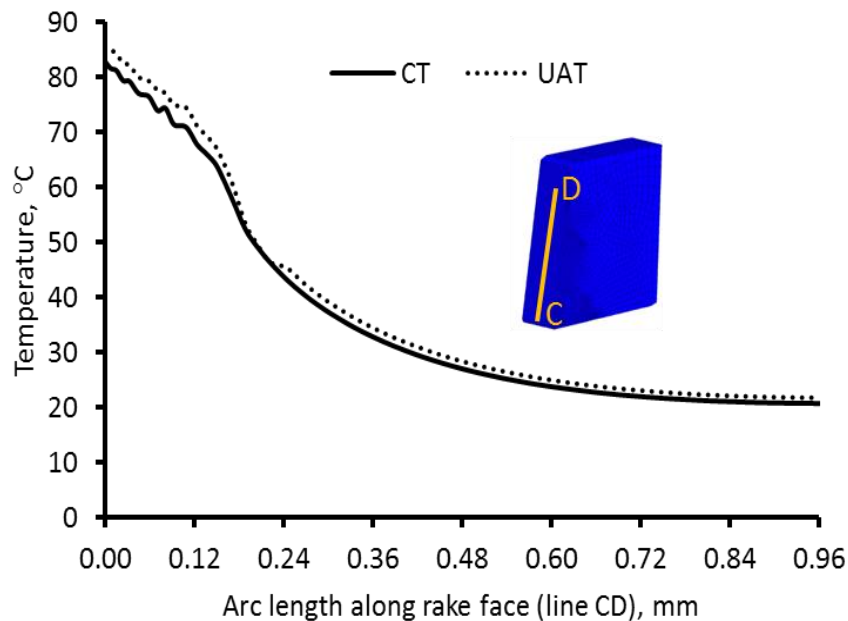


Figure 6-26: Temperature distribution on the rake face along line CD in HCT and HUAT

The calculated distributions of von-Mises stresses in the cutting regions of the studied alloy for both UAT and HUAT are shown in Figure 6-27 with the tool position at the maximum penetration stage (maximum stress). In CT and HCT, the stresses were concentrated in two main regions called *primary* and *secondary deformation region*, while in UAT and HUAT; the distribution of von Mises stress was transient and changed with the tool movement.

In HUAT, the stress values reduced due to the thermal softening of material thanks to the externally applied heat. The stress level at the cutting region at the maximum penetration in HUAT (300°C) reached 800 MPa, then dropping significantly at the retraction stage when the tool separated from the workpiece in HUAT. The stress value in HCT was approximately 800 MPa same as the peak-force value in HUAT. As soon as the tool came into contact with the chip again at the next penetration stage, the value of stresses reached the maximum and thus the cycle was repeated. The values of the von-Mises stress averaged after time in the cutting region in HUAT were smaller when compared to those in CT and HCT due the externally applied heat.

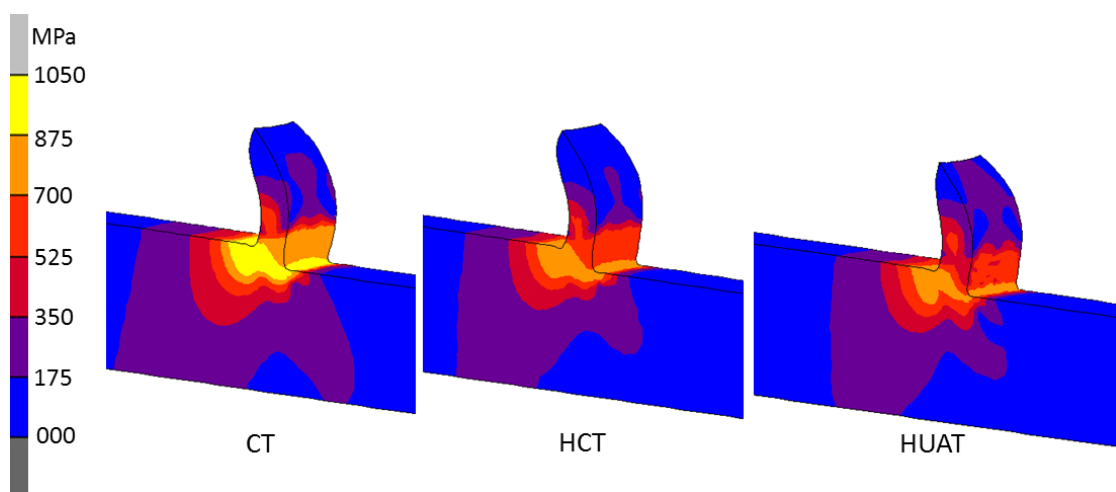


Figure 6-27: Stress distribution of the process zone in CT, HCT and HUAT

## 6.9 Summary

A fully parametric 3D FE model of orthogonal turning was developed to simulate CT, HCT, UAT and HUAT of Ti-15333. The model was used to simulate the cutting process for various cutting parameters, such as depth of cuts, cutting speed and different vibrational parameters. The model allowed the interaction between the tool and workpiece, to be studied, therefore enabling the assessment and optimization of the cutting procedure. The chip-formation process was studied to predict distributions of stresses, cutting forces in conventional turning (CT) and assisted turning (HCT, UAT and HUAT). A piece-wise material model based on the results obtained from the split Hopkinson pressure bar tests was used in the cutting simulations.

Initially, the model was used to study the effect of various cutting conditions on cutting forces, stresses and temperatures of the process zone in CT and UAT. The results were also validated experimentally. The model was later on extended to model a novel hybrid machining process –*HUAT*– for the first time.

When subjected to ultrasonic vibration, the material experienced a varying stress state depending on the motion and location of the tool in each vibration cycle. The average over the cycle stress level in the material in UAT was lower than that produced in CT. The level of cutting forces in numerical simulations was affected by tool geometry and cutting conditions. A comparison of results for various depths of cut showed that cutting forces and temperature of the process zone increased of this parameter for both CT and UAT. However, UAT was still effective at higher depths of cut and a consistent reduction of 60-70% reduction in cutting forces was observed at various depths of cut.

The material removal rate and extent of vibrational parameters were the main factors responsible for the variation of the cutting force. The model was used to provide basic understanding of the effects of the process parameters and tool geometry on the cutting force in conventional and hybrid turning processes. In simulations, changing the cutting speed within the studied interval was found to have no effect on the cutting force, particularly in CT, which was consistent with our experimental results for cutting speeds up to 70 m/min. However, in UAT, the force increased with an increasing cutting speed, and a reduction in cutting forces vanished for speeds above 70 m/min. A significant rise in temperature of the process zone was observed with an increase in the cutting speed, as expected, in HUAT, CT, HCT and UAT.

Furthermore, the vibrational parameter (amplitude and frequency) also significantly affect the cutting forces and temperature of the process zone. FE analyses for various vibrational parameters were carried out and optimum parameters were suggested for UAT.

The current model can also be used to analyse various hybrid machining techniques. With the developed model, various ranges of temperature can be used to analyse the effect of external heat on main cutting forces and temperature of the process zone. However, all the experiments were carried out for the oblique turning process, and the current model is limited to orthogonal turning simulations. In addition to the above, a reduction in the radial

component of cutting forces was also observed in HUAT that was ignored in the orthogonal turning model. Therefore, a new oblique model was developed for CT, UAT, HCT and HUAT to analyse the process zone in detail for the actual tool and workpiece geometries. This model is the first developed for HUAT, to the best knowledge of the author. The results obtained with that model will be presented in the next chapter.

## CHAPTER-7

# Results and Discussions: Parametric Analysis of Hybrid Oblique Turning Model

### 7.1. Introduction

The oblique turning process is a commonly used machining process. Most of the turning operations taking place on industrial floors are the oblique turning processes. The study and analysis of oblique turning are of substantial interest to the manufacturing sector. To date, various techniques were used for its analysis including costly and time-consuming experimental methods, analytical techniques and to less extent finite-element analysis [64, 69].

Finite-element simulation is a powerful tool to study deformation processes in modern alloys. To date, most of the developed 2D and 3D finite-element models are for the orthogonal turning process. In orthogonal turning models, two components of cutting forces were incorporated in the analysis, ignoring the third component. Whereas the experimental work carried out on lathe machines are an oblique turning process. The tool movement and interaction with the workpiece in both processes are different. In the current study, an orthogonal turning model was developed and the principal (tangential) cutting force, temperature and stresses generated in the process zone were analysed (see Chapter 6). The model can be used to analyse the process zone in detail with some limitations. The process of the tool-workpiece interaction was simplified, including the tangential and axial direction, disregarding the radial component of force, which was the second largest force in turning of Ti-15333. The material removed by the cutting tool from the workpiece was in the form of rectangular shape (Figure 7-1b). Whereas in the oblique turning process the thickness of material removed from the workpiece material is changing along the cutting edge as shown in Figure 7-1d.

The developed novel oblique turning model possesses a number of advantages compared to the three-dimensional orthogonal turning models. This model allows us to study the effects of vibration amplitude, frequency and friction conditions in CT, HCT and HUAT, incorporating

the actual tool and workpiece geometries. The tool was allowed to move in the feed direction that was not the case in orthogonal models. In addition to the type of feed, the tool geometry has a great influence on the output parameters. The most important parameter in oblique turning is the cutting edge radius, which has a strong effect on cutting forces. Dimensions of the DMNG-150608 cutting insert were used for the cutting tool in the developed FE model.

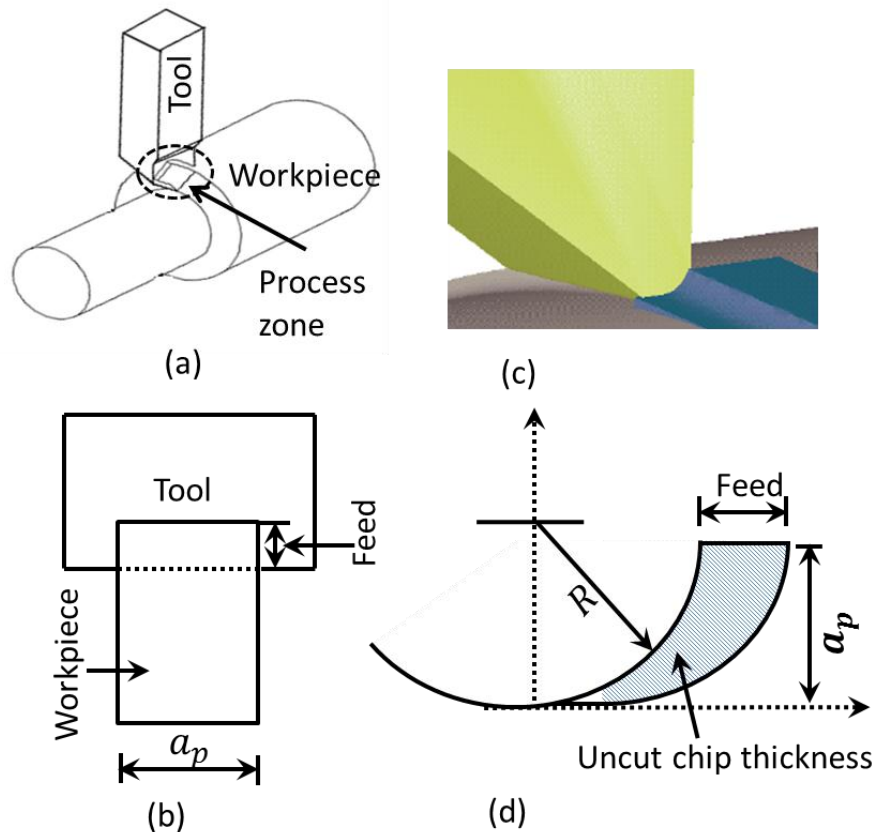


Figure 7-1: (a) Process zone used in orthogonal turning models; (b) chip geometry in the orthogonal turning model; (c) process zone in the oblique turning; (d) chip geometry in the oblique turning process

The model was additionally extended to simulate hot turning and the newly developed hybrid turning technique – hot ultrasonically assisted turning. The model was used to carry out a study of the effect of vibration on all three components of forces, temperature in the process zone, stresses and strains. The most important observation is the effect of vibration on the radial component of force, which was ignored in the previously developed 3D orthogonal turning model. The effect of externally applied heat source was also investigated with the developed model and reduction in cutting forces was reported in respective sections.

Similarly, in hard-to-cut alloys, the radius of cutting tool edge had a promising effect on the radial component of the cutting force.

## 7.2. Cutting Force Analysis

The developed oblique model gives all the three components of cutting forces. The tangential cutting force ( $F_x$ ) of magnitude 110 N was observed in CT at a cutting velocity of 10 m/min, feed rate of 0.1 mm/rev and depth of cut of 300  $\mu\text{m}$  as shown in Figure 7-2. A radial component ( $F_y$ ) was 48 N and an axial component ( $F_z$ ) 20 N. At the start of the simulated cutting process, the level of cutting forces on the cutting tool was zero. The magnitudes of cutting forces increased rapidly with an initial tool contact with the workpiece. After initial engagement, a steady-state level of cutting forces was observed in CT. In the model, global remsehing and rezoning technique was used for chip separation from the workpiece material; as a result, small fluctuations in all three components of cutting forces were observed.

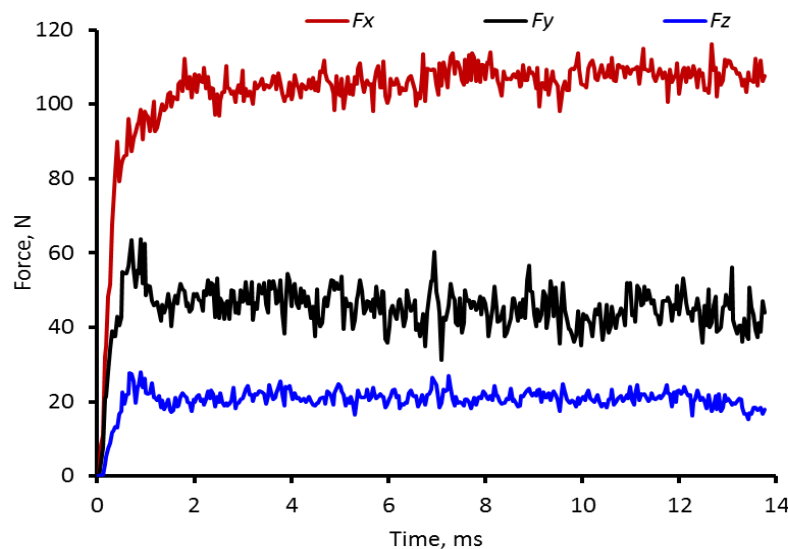


Figure 7-2: Cutting forces in CT ( $V = 10$  m/min;  $f_r = 0.1$  mm/rev;  $a_p = 0.3$  mm)

Application of ultrasonic vibration on the cutting tool and external heat to the workpiece material produces significant reduction in the cutting forces. The external heat supplied to the workpiece material reduced the peak force value as the shear strength of these high-strength alloys is a function of temperature, whereas the superposition of vibrations on the cutting tool separated the tool from the chip during machining process. The combined effect of these two factors resulted in a considerable reduction in cutting forces in HUAT when

compared to CT. During the penetration stage of the tool in HUAT, the tool indents the workpiece material and reaches peak forces in tangential, radial and axial directions at maximum penetration. The resulted peak force values were lower in magnitude than those in CT, but almost equal to the level of cutting forces in HCT. After the peak, the cutting forces start to decline and ultimately become equal to zero during the retraction stage (see Figure 7-3). The traces of minor forces, less than 2 N in the radial and axial direction were recorded on the cutting tool at the retraction stage. This rubbing of the tool with the workpiece material in the retraction stage resulted in better finish when compared to that in CT.

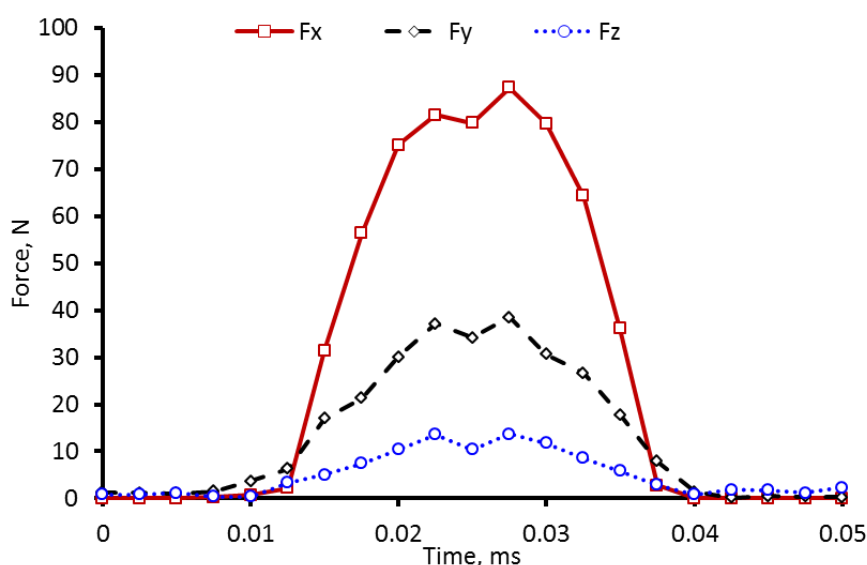


Figure 7-3: History of cutting forces in HUAT in one complete cycle ( $V = 10$  m/min;  $f_r = 0.1$  mm/rev;  $a_p = 0.3$  mm;  $T = 300^\circ\text{C}$ )

A significant reduction in tangential component of force ( $F_x$ ) – 80% – was calculated for HUAT. The simulation was carried out for an initial temperature of  $300^\circ\text{C}$ . The average levels of cutting forces dropped from 48 N to 11 N and from 20 N to 6 N in radial and axial direction, respectively. The developed new turning process resulted in an enormous reduction in cutting forces when compared to CT. Therefore, superposition of ultrasonic vibration on the cutting tool and application of external heat to the workpiece material in HUAT reduces all the three components of cutting forces significantly. On the other hand, a reduction in  $F_x$ ,  $F_y$  and  $F_z$  in HCT was 20%, 22% and 40%, respectively, when compared to CT at room temperature.

In the oblique turning model, the levels of cutting forces were slightly higher when compared to those found in the orthogonal turning simulations. The prime reason is the amount of material removed from the workpiece material and the complex character of tool-workpiece interaction in the oblique turning model. Additionally, a free surface was assumed in the orthogonal turning model ignoring the chip separation from the parent material in radial direction that resulted in lower levels of cutting forces. However, the former model incorporated the radial direction and resulted in marginally higher force magnitudes compared to those obtained in orthogonal turning simulations. The calculated cutting forces are in good agreement with the experimental results (see Figure 7-4.). An average error up to 10% was found for the numerical results.

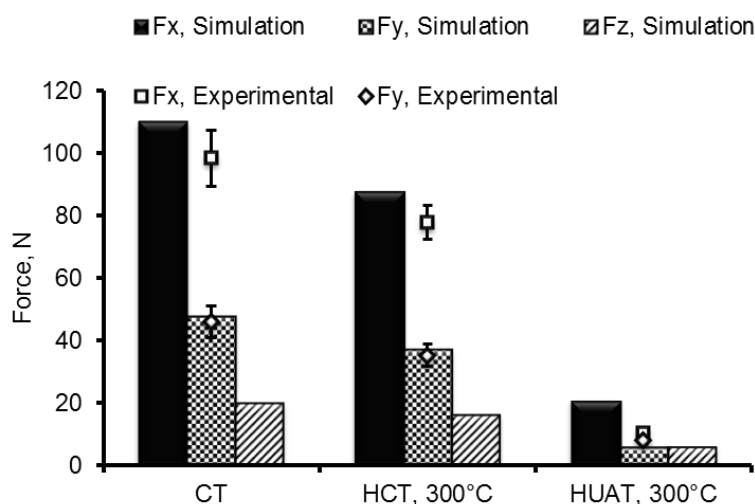


Figure 7-4: Comparison of experimental and numerical results

In addition to the above, the model of oblique turning was used for various externally applied temperature magnitudes in HUAT and HCT ranging from 100°C to 500°C. A gradual reduction in cutting forces was recorded with an increase in temperature of the workpiece material in both HCT and HUAT (Figure 7-5). A reduction of 28% (from 110 N to 79 N) and 82% (110 N to 19 N) in the tangential component of cutting force in HCT and HUAT, respectively, was observed at 500°C. Similarly, a reduction of 28% and 78% in the radial component of cutting force and 44% and 63% in the axial component was calculated for HCT and HUAT, respectively (see Figure 7-6).

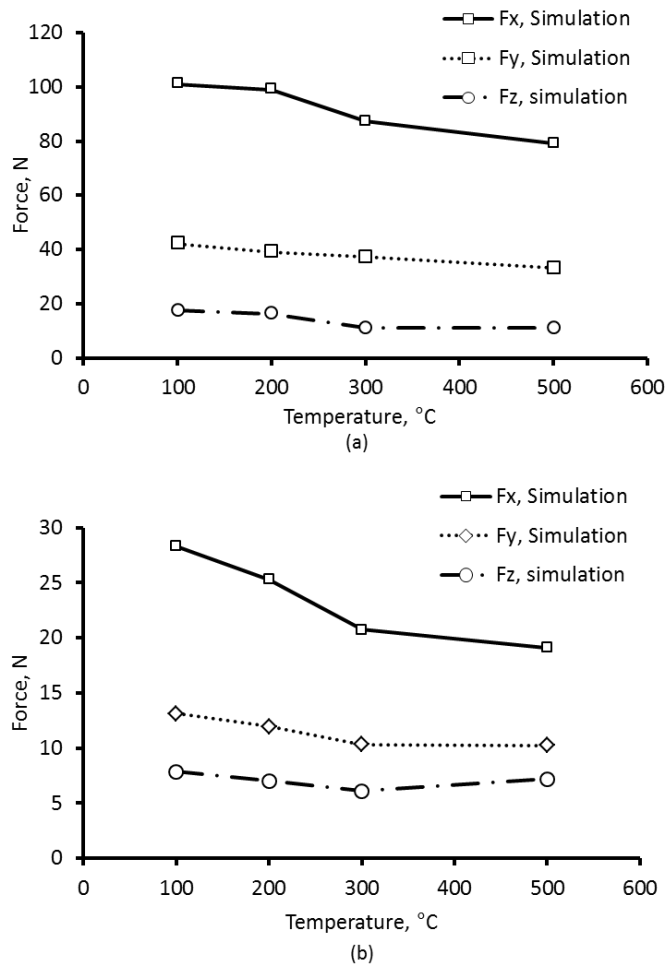


Figure 7-5: Cutting forces at various temperatures in (a) HCT and (b) HUAT ( $V = 10 \text{ m/min}$ ;  $f_r = 0.1 \text{ mm/rev}$ ;  $a_p = 0.3 \text{ mm}$ )

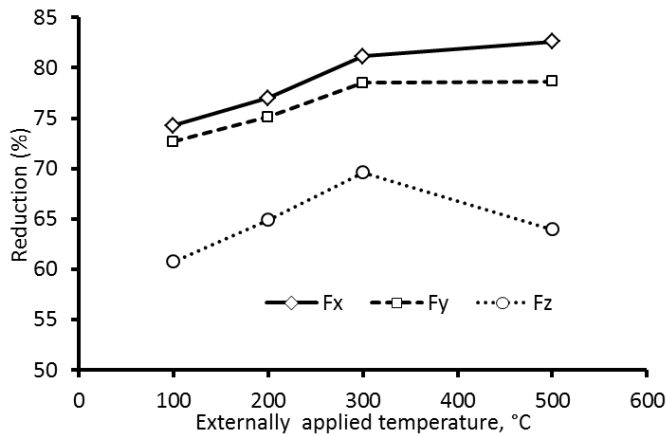


Figure 7-6: Force reduction in HUAT (as compared to CT) at various temperatures of workpiece materials

The studies indicated that an increased temperature in hot machining does not always yield tractable benefits with respect to force reductions. At 500°C, the reduction in cutting forces is

comparable to that for workpiece heating temperature of 300°C: there was some reduction in tangential component; the radial component was almost the same, whereas there was a slight increase in the axial component. The prime reason for the increased in the axial component was an excessive thermal softening of the workpiece material as shown in Figure 7-7. The decline in cutting force reduced due to the pile-up of material caused by excessive deformation. Thus, from the current study, a temperature of 300°C in HUAT of Ti-15333 can be recommended, for the studied cutting parameters.

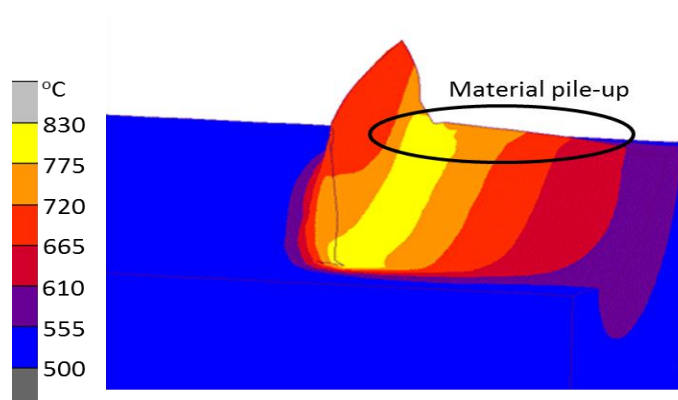


Figure 7-7: Material accumulation in HUAT at 500°C in axial direction

Hence, critical consideration should be given to the thermal heat generated during machining of conventional and assisted turning processes. The subsequent section demonstrates the thermal analysis of CT, HCT and HUAT.

### 7.3. Thermal Analysis

The efficient and precise prediction of temperature in conventional and hybrid oblique turning processes is in highly demand in the manufacturing industry. In experimentation, the accurate prediction of temperature at the tool-workpiece interaction zone is very difficult due to limitations of the equipment used for temperature measurements and a complex nature of the process. On the other hand, the numerical technique is an alternative approach to predict the process zone's temperature in the turning processes. To date, various modelling approaches were used in literature for this purpose [4, 7, 10, 112]. The modelling studies regarding temperatures in cutting can be categorised into two main groups: analytical and numerical techniques. The analytical modelling approach is the oldest among the available techniques. It is computationally less intensive when compared to numerical

methods. On the other hand, treating complex machining geometries in the oblique turning process is a significant challenge when using analytical approaches. However, the advancements in numerical simulation techniques and the availability of more powerful computational facilities enable the thermal modelling of the orthogonal and oblique turning processes. These models can be used for accurate prediction of cutting processes at various cutting conditions. Therefore, in the current study, the finite-element technique was used to analyse temperature in the process zone in the oblique turning process.

This was achieved with the developed 3D thermomechanically coupled finite-element oblique model in CT, HCT and HUAT as shown in Figure 7-8. In CT, a relatively lower temperature was observed along the contact area of the tool-workpiece interface. The amount of heat generated in CT is due to plastic deformation of the workpiece material and the frictional effect between the tool and chip. However, the frictional effect is less than 10% and the heat produced in the turning process is mostly due to the plastic deformation of the workpiece material.

The heat externally applied to the workpiece material increased temperature in the process zone significantly in both HCT and HUAT depending on the initial temperature of the workpiece. In HUAT, the process zone temperature was higher when compared to HCT as shown in Figure 7-8. This increase can be attributed to the additional energy of the cutting tool in the form of vibrations. The process zone temperature in both HCT and HUAT was significantly higher when compared to that in CT. The peak temperature value was observed in the region close to the tool-workpiece interaction zone that was not visible to the thermal camera during experiments. As a result, lower temperature levels were observed in experimentation for various cutting conditions. Hence, the FE models have the added advantage of elucidating the temperature characteristics in regions of the workpiece not visible to thermal imaging. In HUAT, a relatively high temperature was calculated for the process zone. The peak temperature was 680°C, in comparison to approx. 600°C measured in experiments.

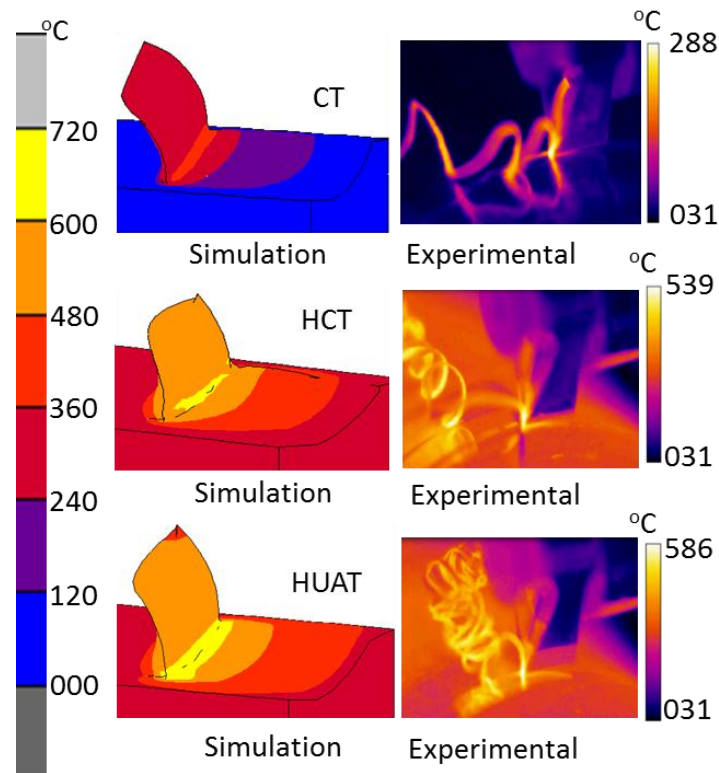


Figure 7-8: Calculated temperature distribution in cutting region for CT, HCT and HUAT ( $V = 10$  m/min;  $a_p = 0.3$  mm;  $f_r = 0.1$  mm/rev;  $T = 300^\circ\text{C}$  in hot machining)

Most of the heat produced at the process zone was removed with the chip in the turning process, whereas a portion of heat was transferred to the cutting tool. The distribution of heat along the cutting edge was calculated from FE simulation of CT, HCT and HUAT. The maximum temperature was observed at the centre point of the tool edge in contact with the workpiece material, with some drops towards the ends of the cutting length (Figure 7-9). This result can be attributed to the convective heat transfer from the rake surface of the tool to the environment.

A temperature distribution on the rake face of the tool changed with the tool position in HUAT. At the penetration stage, higher temperature of approx.  $303^\circ\text{C}$  was observed on the rake face due to severe plastic deformation and the frictional effect. Whereas in the retraction stage, the tool separated from the workpiece, and a marginally lower temperature with maxima of approx.  $295^\circ\text{C}$  on the rake face was found (see Figure 7-10). On the other hand, in CT and HCT, with the tool being in continuous contact with the workpiece, a steady distribution of temperature on the rake faces were obtained. The level of temperatures was

approx. 100°C and 290°C in CT and HCT, respectively. Hence, the temperature on the rake face in HUAT was higher when compared to HCT and CT.

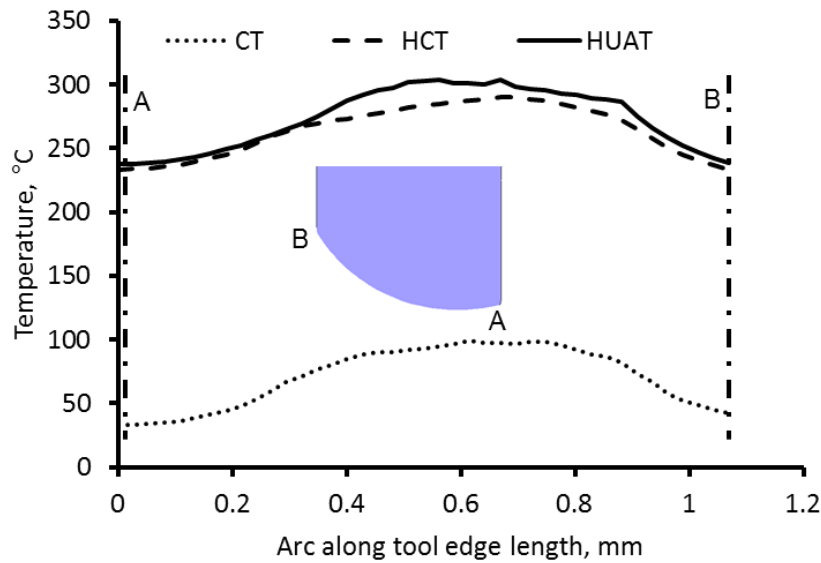


Figure 7-9: Temperature distribution along cutting edge in oblique turning of CT, HCT and HUAT ( $V = 10$  m/min;  $a_p = 0.3$  mm;  $f_r = 0.1$  mm/rev  $T = 300^\circ\text{C}$  in hot machining)

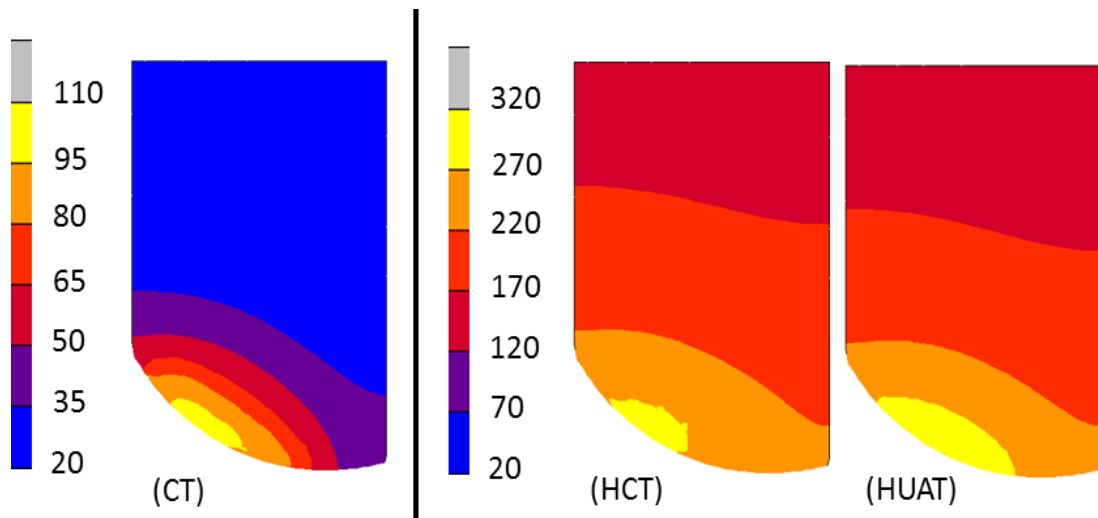


Figure 7-10: Temperature distributions on the rake face of the tool in CT, HCT and HUAT

The contour Plots of plastic strains are given in Figure 7-11 for both CT and HUAT, and results show a 33 % lower level of plastic strain in the HUAT case as compared to CT. The external heat supplied to the workpiece assisted its plastic deformation. As a result, lower plastic deformation was observed in HUAT when compared to CT.

The FE model was used for conventional and assisted turning processes and extended the experimental results obtained for cutting forces and temperature as discussed above. The

model was used for various cutting conditions and the effect of depth of cut, cutting speed and feed rate on cutting forces and temperature of the process zone are discussed in the subsequent sections in details.

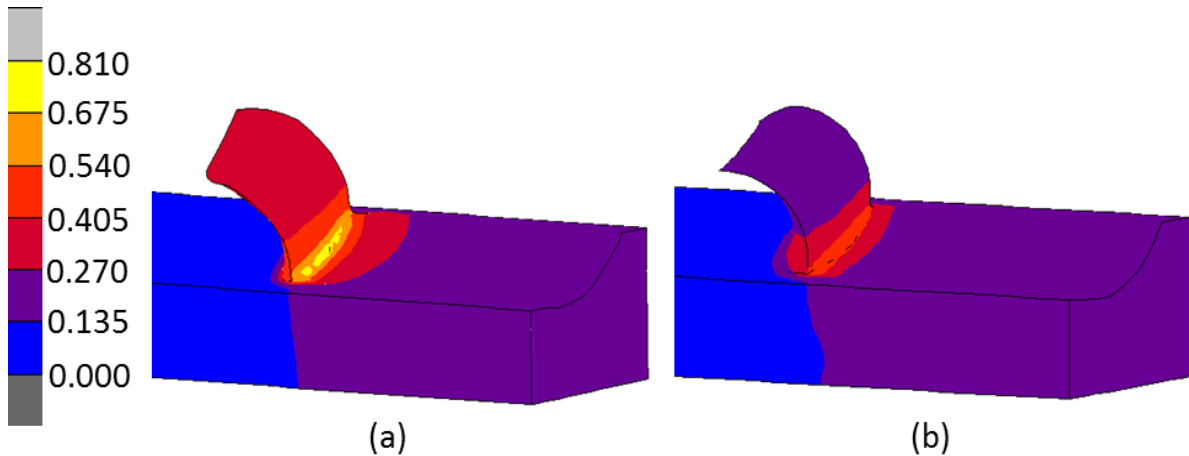


Figure 7-11: Calculated plastic strain distribution in cutting region for (a) CT and (b) HUAT

#### 7.4. Effect of Depth of Cut

The results presented in Figure 7-12 show the change in the cutting forces for varying depth of cuts. If the depth of cut increases, the section of material at the process zone to be removed requires larger energy. It is noticed in all simulations and experimentation for both CT and HUAT that the tangential force was dominant compare to both radial and axial components in turning of Ti-15333. The simulations were carried out for the depth of cuts between 300  $\mu\text{m}$  to 500  $\mu\text{m}$  in CT, HCT and HUAT. A nearly linear increase in cutting forces was observed with an increase in the depth of cut, as expected. The simulation results were in good agreement with experimental data obtained for the various turning processes as shown in Figure 7-12. A consistent reduction of approximately 80%, 76% and 68% in tangential, radial and axial component of forces was observed in HUAT when compared to CT for 300  $\mu\text{m}$  to 500  $\mu\text{m}$ . The reduction in cutting forces can be attributed to the tool separations form the workpiece and a reduction in the peak-force value due to thermal softening of the workpiece material in HUAT.

Similarly, the effect of depth of cut on the temperature of the process zone was also analysed and the temperature grew at higher depth of cuts. The growth in process zone temperature was a result of the increase in material removed from the workpiece, generating more plastic heat. Figure 7-13 shows a temperature distribution in the process zone in HUAT at 400  $\mu\text{m}$

depth of cut. Similarly, the cutting speed had also a pronounced effect on temperature generated during turning processes and cutting forces in HUAT. The simulation results obtained at various cutting speeds for cutting forces and temperature of the process zone are discussed in the following section.

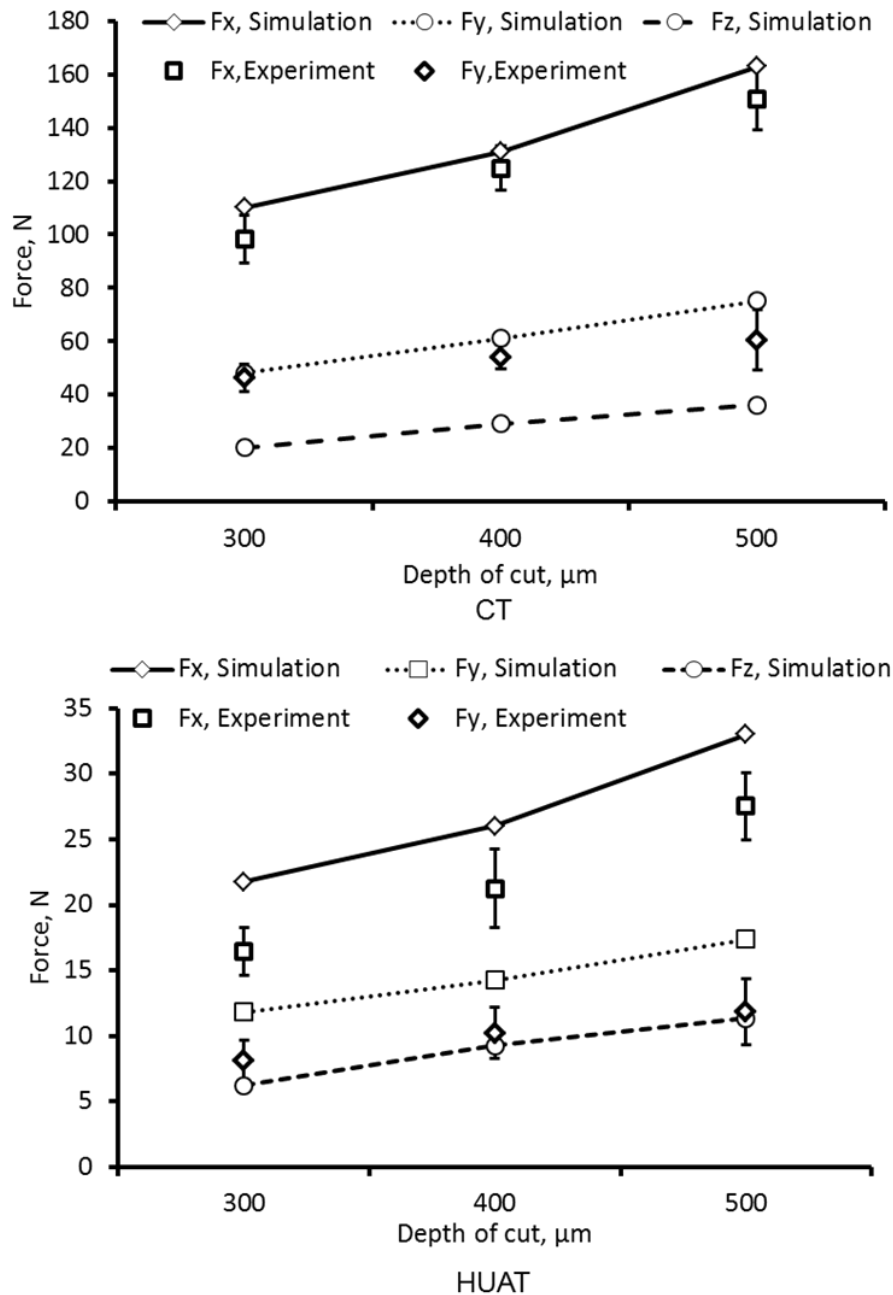


Figure 7-12: Three components of cutting forces at various depths of cut ( $V = 10$  m/min;  $f_r = 0.1$  mm/rev;  $T = 300^\circ\text{C}$ )

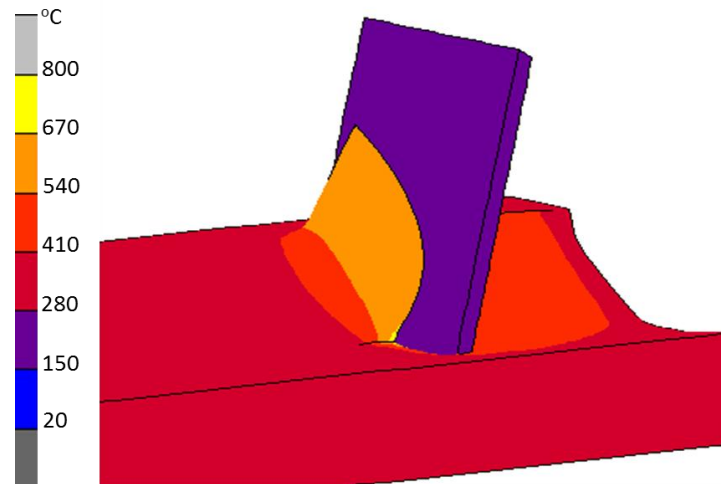


Figure 7-13: Temperature of process zone at higher depth of cut at  $t = 3$  ms

### 7.5. Effect of Cutting Speed

The cutting forces and temperature in HUAT are greatly affected by the level of cutting speed. Various cutting speeds ranging from 10 m/min to 70 m/min were used for the FE simulation of CT, HCT and HUAT. Figure 7-14 presents the cutting forces obtained at various cutting speeds. A constant level of cutting forces was observed at various cutting speeds in CT and HCT. However, the magnitude of average cutting forces increased in HUAT with growing cutting speed and, finally, the reduction in cutting forces vanished beyond 70 m/min. At 70m/min, the workpiece velocity was high enough to eliminate separation between the tool and workpiece in each cycle of vibration. The reduction in cutting forces above the critical speed (60 m/min) can be attributed to thermal softening caused by the amount of external heat supplied to the workpiece material and heat generated in the process zone due to plastic and frictional effects. In HUAT, the reduction in cutting forces at 70 m/min was negligible (less than 1 N) when compared to HCT at the same cutting conditions. However, a reduction of 21% was observed in HUAT when compared to CT and can be credited to the thermal softening effect due to external heat supplied. Thus the novel hybrid turning process improves the speed limit of vibro-impact machining of our setup beyond 70 m/min with a considerable reduction in cutting forces when compared to CT.

The current model predicted the magnitudes of all three components of cutting forces for a range of cutting speeds, and the same behaviour was found as discussed above for the radial and the axial components of cutting forces in HUAT, as expected.

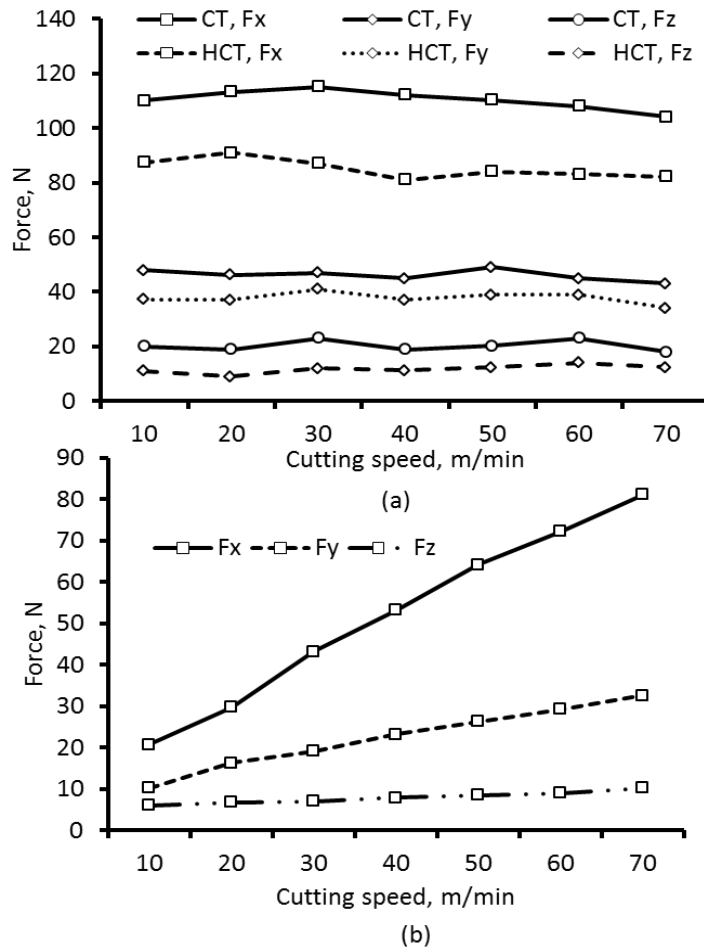


Figure 7-14: Effect of cutting speed on cutting forces: (a) CT and HCT; (b) HUAT

The effect of cutting speed on the heat generated in the process zone in HUAT was also investigated. A rise in temperature was observed with the increase of the cutting speed, as expected; Figure 7-15 demonstrates this effect of HUAT.

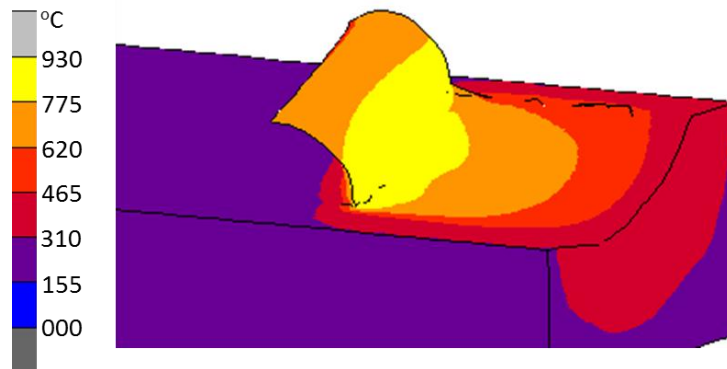


Figure 7-15: Temperature in process zone at higher cutting speed (70 m/min) in HUAT at  $t = 1$  ms

## 7.6. Effect of Feed Rate

The assessment of all components of cutting forces at various feed rates is presented in Figure 7-16. A nearly linear increase in all three components was observed with a growth in feed rate in CT, HCT and HUAT. The amount of material removed by the cutting tool at higher feed rate increases, resulting in higher cutting forces on the tool. The reduction in cutting forces was significantly higher in HUAT, even at higher feed rates. Reductions of approximately 74%-80% were observed at higher feed rates for tangential and radial cutting forces in HUAT. However, at higher feed rates in HUAT, the reduction in the axial cutting force diminished, and a reduction of 58% and 50% was observed at 0.2 mm/rev and 0.3 mm/rev, respectively. This drop in reduction in the axial component is due to a shorter separation of the tool in the retraction stage, resulting in a higher average force level on the cutting tool. The tool experienced some contact at the retraction stage with the workpiece material, resulting in a fraction of the axial and radial components of cutting forces. However, the reduction in cutting forces is significantly higher at the higher feed rate. Hence, HUAT is also effective at higher levels of depth of cut and feed rate, with a significant reduction in the cutting forces and improvement in surface roughness [97]. Similarly, a rise in temperature of the cutting region was observed with an increase in the feed rate in CT, HCT and HUAT, as expected.

## 7.7. Effect of Cutting-Edge Radius on Cutting Forces

The developed oblique turning model was also employed for the analysis of cutting forces using various magnitudes of the tool edge radius, ranging from 0  $\mu\text{m}$  to 100  $\mu\text{m}$ . It was observed that the cutting forces depended strongly on this parameter, particularly the radial component in conventional and assisted turning processes. The effect of the tool edge radius was investigated for CT and HUAT. The lowest cutting forces were observed for the sharp cutting edge in both CT and HUAT. The tangential, radial and axial cutting forces in CT were 102 N, 26 N and 14 N, respectively, whereas in HUAT, an average of 23 N, 7 N and 4 N of  $F_x$ ,  $F_y$  and  $F_z$ , respectively, were calculated. The effect of cutting edge radius was higher for the radial and axial components. In HUAT, an average reduction of 80-85% for all three components of cutting forces was observed for the sharp tool edge as shown in Figure 7-17. A nearly linear increase was observed above 25  $\mu\text{m}$  for all the components of cutting forces.

However, the tool edge radius had a more dominant effect on the radial component of cutting force when compared to tangential and axial component of forces in both CT and HUAT. The results demonstrated the effect of tool condition on cutting forces in turning of Ti-15333.

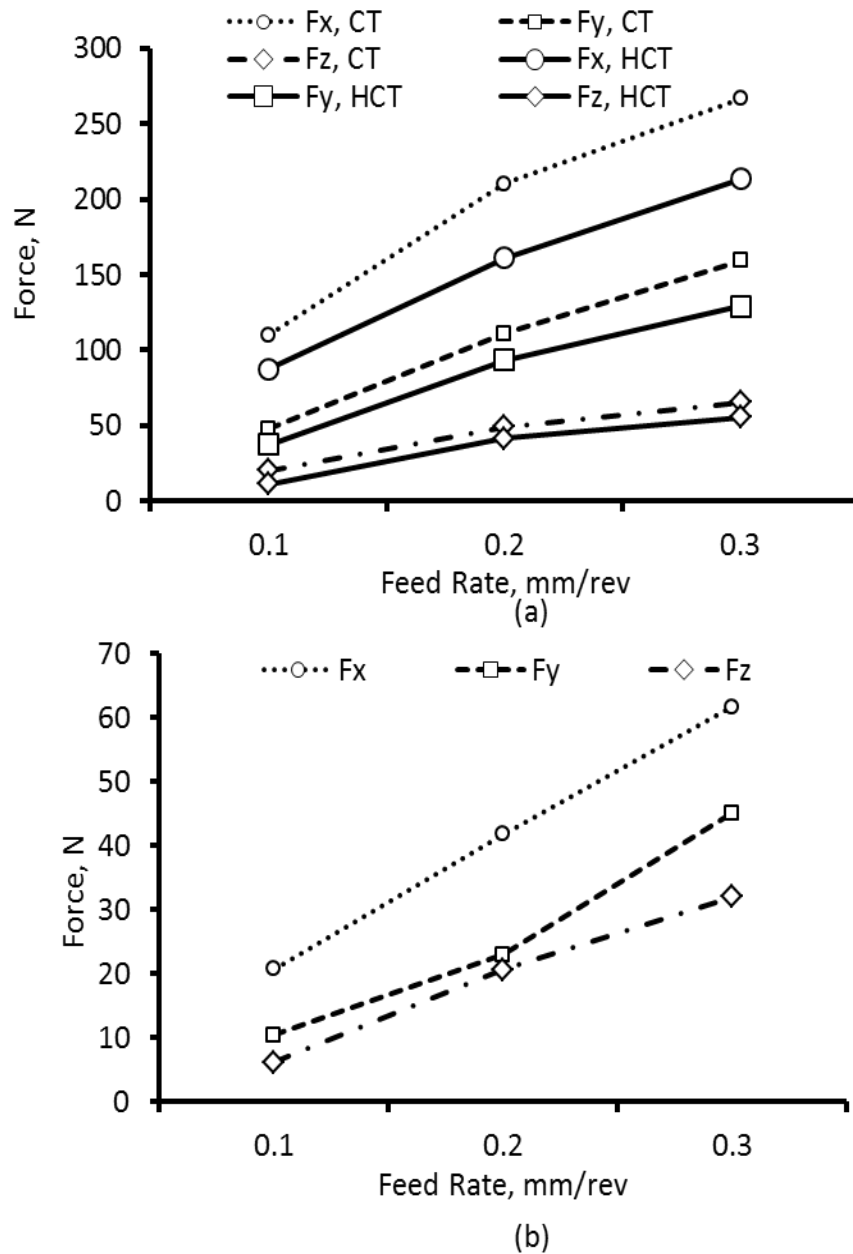


Figure 7-16: Effect of feed rate on cutting forces in (a) CT and (b) HUAT

## 7.8. Stresses in Process Zone

Results of FE simulations demonstrated that the level of stresses induced in HUAT was matching that in HCT at the penetration stage for identical cutting conditions. In HUAT, the

material response to the interaction of the tool with the workpiece material can be divided into four stages: (a) when the tool moves toward the workpiece in the forward direction called approach stage, (b) when the tool penetrates into the workpiece material called engagement stage (c) when the tool travelled away from the chip in backward direction still in contact with the chip is called disengagement stage and (d) when the tool separated from the chip and moves away from it called withdrawal stage . In the process zone of HUAT, dynamically changing stress distribution was observed for various cutting conditions. The character of stress distribution in the process zone for various stages of one complete cycle of vibration (0.05 ms) is shown in Figure 7-18c and Figure 7-18d for HUAT.

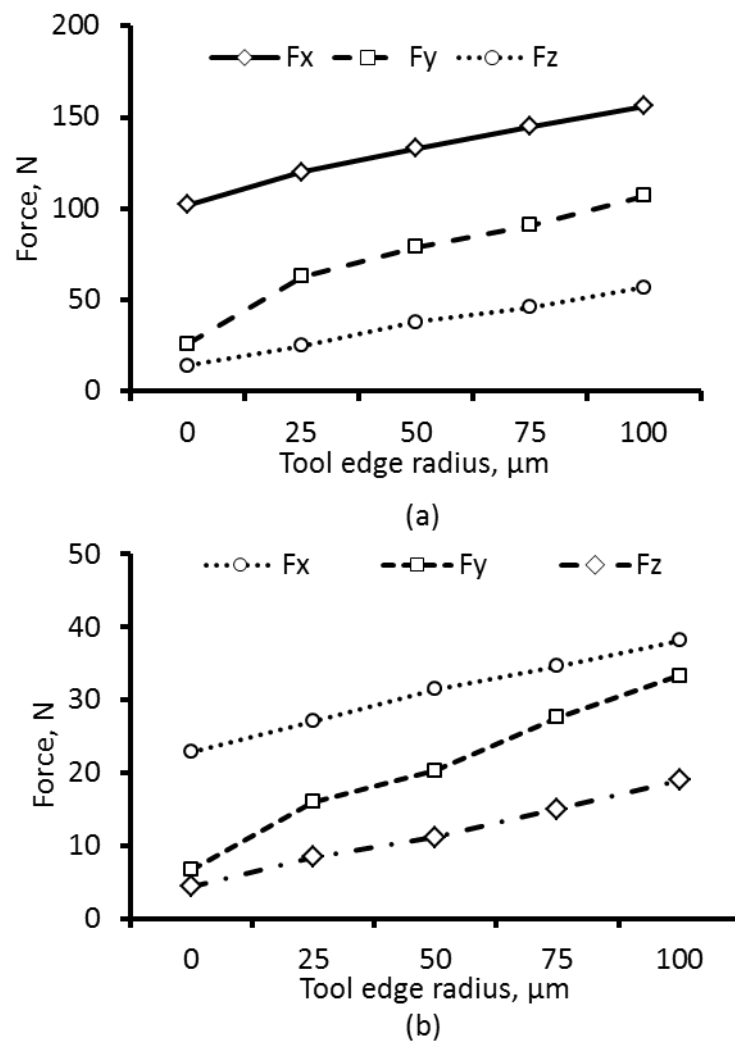


Figure 7-17: Cutting forces for various levels of cutting-edge radius: (a) CT and (b) HUAT ( $V = 10$  m/min;  $f_r = 0.1$  mm/rev;  $T = 300^\circ\text{C}$ ;  $\alpha = 0^\circ$ )

At the engagement stage in HUAT, the stress increased reaching a peak value of approximately 810 MPa near the tip of the tool. In HUAT, the stress level is significantly lower

(by approx. 200 MPa) when compared to CT. The application of external heat reduces the yield point of the workpiece material; hence, less energy is needed to remove it from the workpiece. When the tool moved in the opposite direction (in the disengagement stage), the level of maximum stress declined to an average value of 415 MPa in HUAT, (see in Figure 7-18). A transient stress level was observed in the process zone in HUAT, and the peak stress was reached only during the loading part (engagement stage) of the ultrasonic cycle in HUAT, the average over a cycle stress was considerably lower than that in CT and HCT.

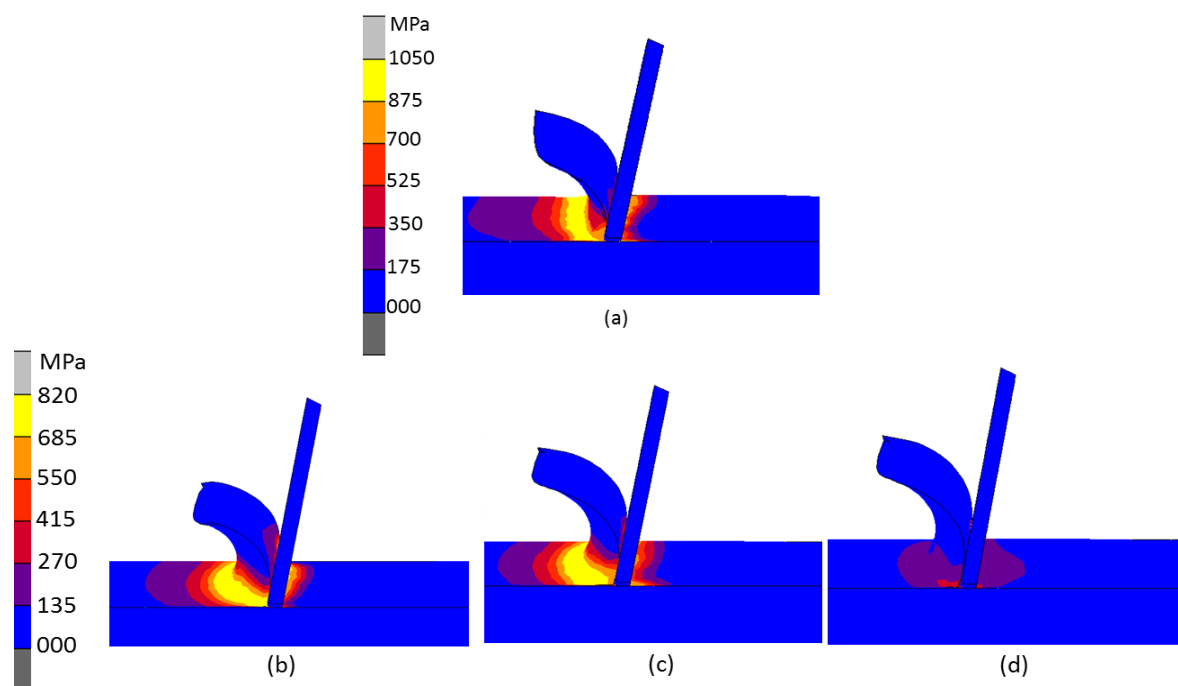


Figure 7-18: Stress distribution in process zone in (a) CT; (b) HCT; (c) HUAT at the engagement stage; (d) HUAT at retraction stage

## 7.9. Vibration in Axial and Radial Direction

Vibration superimposed on the cutting tool in HUAT can be applied either in tangential, radial or in the feed direction. The results obtained from experimentation demonstrated that the application of vibration in the tangential direction had a more promising effect compared to that for the radial and axial directions [124]. However, so far no attempt has been made to perform a comparison of vibration effects in applied different directions of a two-dimensional vibration mode called elliptical vibration using the FE model. The current model possesses the capability to apply vibration in any direction as well as to implement two-dimensional and three-dimensional vibration modes and to analyse the cutting forces. In the current study,

the analysis is limited to one dimensional and two-dimensional vibration modes superimposed on the cutting tool.

When ultrasonic vibration was applied in the radial and axial directions, the tool edge indented the machined surface and an un-removed part of the workpiece in the axial direction; as a result, an increase in peak forces in radial and axial direction was observed on the tool in both cases. During the withdrawal stage, the tool did not loose full contact as it did in case of tangential vibration. However, a marginal decline in the tangential force component was observed, whereas negative radial and axial force components were calculated for the radial and axial modes of vibration, respectively, as shown in Figure 7-19. This indenting of the workpiece material resulted in higher the radial and axial cutting forces. For HUAT with vibration in the feed and radial directions, when the tool was not in contact with the workpiece, the average tangential forces were equal to about 42 N and 52 N, respectively. Similarly, higher force levels were observed for the radial and axial directions for both modes of vibrations. Hence, tangential vibration leads to a greater force reduction in HUAT, thus it can be more beneficial for the cutting process. Still, the final conclusion on the efficiency of vibration directions cannot be based only on the force comparison, as other factors, such as quality of machined surfaces, should be analysed.

In addition to the study of one-dimensional vibration modes, the model was used for analysis of elliptical vibration analysis. The vibration superimposed on the cutting tool was defined using the following equations of motion:

$$x(t) = a \cos(2\pi ft), \quad (7.1)$$

$$y(t) = b \cos(2\pi ft + \varphi), \quad (7.2)$$

where  $a$  and  $b$  are the amplitudes in tangential and radial direction, respectively;  $f$ ,  $\varphi$  and  $t$  are the frequency, phase angle and time, respectively;

Vibration superimposed on the tool in the two-dimensional mode had the amplitude of 8  $\mu\text{m}$  in tangential direction and 4  $\mu\text{m}$  in radial direction. The superposition of elliptical vibration on the cutting tool resulted in a marginal decline in all three component of cutting forces when compared to the main studied modes (see Figure 7-19d and Figure 7-19e). These are the initial results obtained from the elliptical-vibration-assisted turning of Ti-15333. Apparently,

the model has the capability to impose vibrations in all three directions to investigate the response of material to various machining regimes.

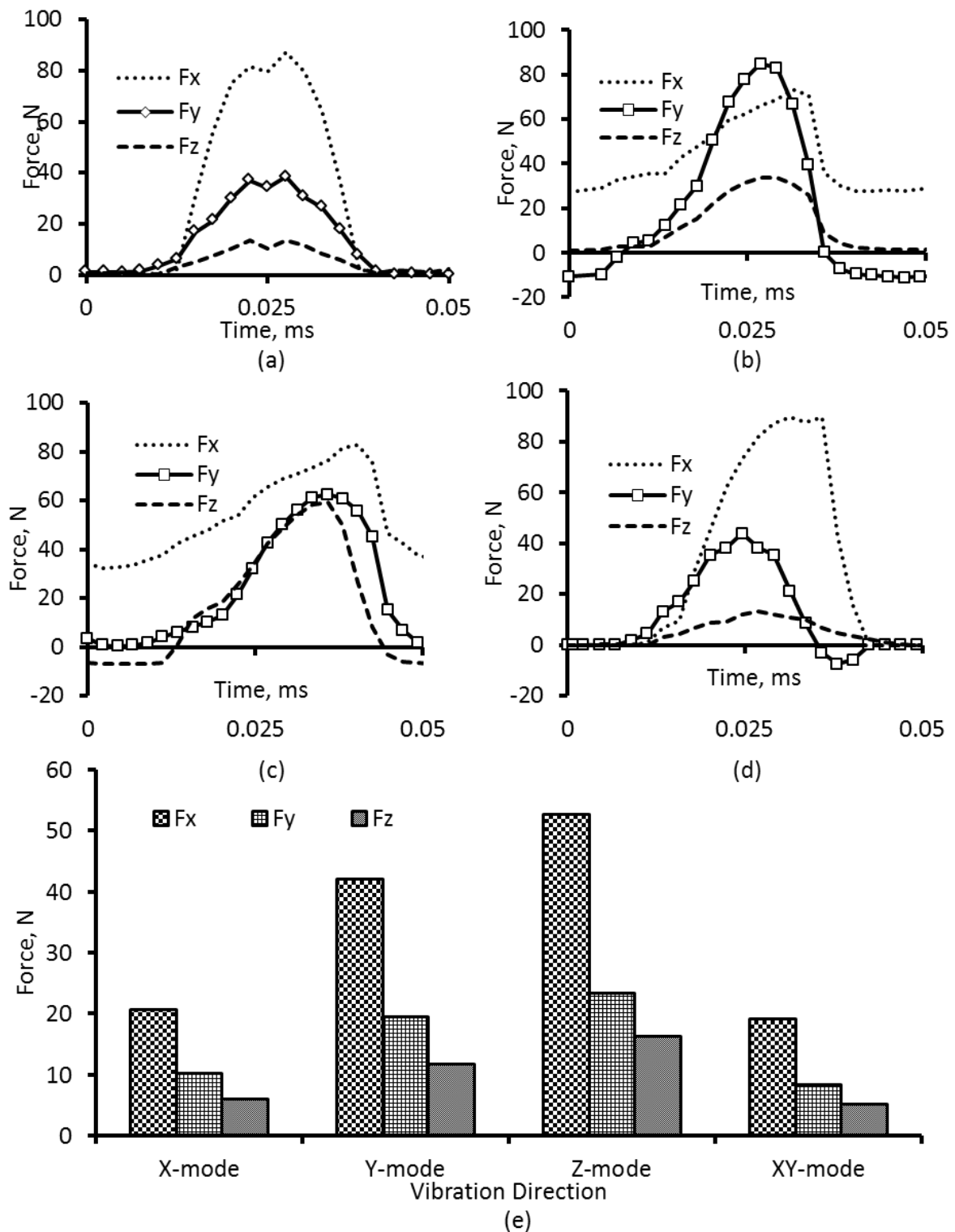


Figure 7-19: Cutting forces at various modes of vibrations (a) Tangential direction; (b) Radial direction; (c) Axial direction; (d) elliptical vibration (XY-mode); (e) Average cutting forces

## 7.10. Summary

The three-dimensional thermomechanically couple finite-element model of oblique turning was developed for CT, HCT and HUAT. The model was used to investigate the effect of various cutting parameters on the cutting forces and temperature in the process zone. The current model described the conventional and assisted turning processes with fewer assumptions involved compared to the previously developed model of orthogonal turning discussed in Chapter 6. The cutting-tool geometry used in this FE model was the same as those of the actual system; the workpiece had also the actual geometry in the FE simulations. The novel 3D model of oblique turning presented in this chapter, thus, overcame many if not all the shortcomings of the previously developed FE model because of its capability to represent a more realistic turning process.

The parts of the cutting tool and workpiece used in turning process were modeled to reduce the computational time. The model was used for CT, HCT and HUAT for various cutting conditions. Various modes of vibration were used in the analysis to investigate their effects on HUAT. A considerable reduction in cutting forces was observed in HUAT when compared to CT and HCT.

The novel model allowed the calculation of magnitudes of cutting forces at different cutting conditions. The model was used for various depths of cuts, and a significant improvement in cutting forces was observed for the studied range of this parameters. In additions to that, regimes with various cutting speeds were simulated in CT, HCT and HUAT using the developed model. The level of cutting forces in HUAT increased with an increase in the cutting speed. A non-permanent contact in the case of HUAT is the main reason for the force reduction as compared to CT and HCT. Thus, as the cutting speed increased in case of HUAT, the contact time between the tool and the workpiece increased resulting in the increased cutting forces. Hence, at the speed of 70 m/min, the reduction in cutting forces vanished in HUAT when compared to HCT. Still the novel turning process resulted in a significant reduction of 21% at the critical speed of 60 m/min (see Table 6-2). The effect of externally applied heat (100-500°C) on cutting forces and temperature in the process zone was also studied. A nearly linear reduction in cutting forces was observed with an increase in temperature of the workpiece material in HUAT. However, at 500°C, a slight increase in the axial component of cutting forces was observed whereas the radial component of cutting

forces was the same as at 300°C. The material became softer, and pile-up formation on the axial side of the workpiece was found causing a marginally rise in  $F_z$ . This effect was observed only in HUAT but not in HCT.

Keeping all other parameters – cutting speed, depth of cut and vibrational parameters – constant, the effect of feed rate was investigated using the developed model. A nearly linear increase in cutting forces was observed with a growth in feed rate in CT, HCT and HUAT.

The simulations were helpful in predicting the process zone temperature at various cutting conditions in CT, HCT and HUAT. A high process zone temperature was found in HUAT when compared to HCT and CT. The amount of heat supplied to the workpiece material increased this temperature. The amount of heat transfer from the process zone to the cutting increased in HCT and HUAT. The process zone temperature calculated in FE simulations showed a good agreement with the experimentally observed level. However, the temperature levels in the primary and secondary deformation zones were much higher than those in experiments due to limitation of the test method. The model predicted the temperature distributions for these regions that were not possible to obtain in experiments.

The model was also used to investigate the influence of the tool-edge radius on cutting forces. A significant increase in the cutting forces was found for higher magnitudes of this radius. However, the effect of the tool-edge radius was dominant on radial cutting forces in all the turning processes. In the case of the sharp edge, the minimum level of radial force components was observed. These results showed the importance of tool conditions for turning of Ti-15333.

The model has the capability to simulate vibrations in all three directions and even 2D and 3D elliptical vibration modes to investigate the effect of various types of vibration on cutting forces. Thus, the model was capable to get in-depth understanding of the deformation process in HUAT, HCT and CT using the actual geometry of the workpiece and tool.

Table 6-2: Cutting forces at various cutting conditions in conventional and assisted turning processes

Cutting conditions			Cutting Forces (N)									Reduction CT vs HUAT (%)			Reduction CT vs HCT (%)		
			CT			HUAT (300°C)			HCT (300°C)			Fx	Fy	Fz	Fx	Fy	Fz
$V$ (m/min)	$a_p$ (mm)	$f_r$ (mm/rev)	Fx	Fy	Fz	Fx	Fy	Fz	Fx	Fy	Fz	Fx	Fy	Fz	Fx	Fy	Fz
10	0.1	0.1	61.0	29.0	12.0	6.0	5.2	4.0	47.2	20.1	5.8	90.2	82.0	66.67	22.6	30.7	51.7
10	0.2	0.1	81.0	42.0	14.0	14.0	8.2	7.2	62.5	30.8	7.5	82.7	80.4	48.3	22.8	26.7	46.4
10	0.3	0.1	110.0	48.0	20.0	21.7	10.3	6.2	87.3	37.2	11.1	80.2	78.5	68.8	20.6	22.4	44.4
10	0.4	0.1	131.0	61.0	29.0	26.0	14.2	9.2	108.6	49.2	15.2	80.2	76.7	68.1	17.1	19.3	47.6
10	0.5	0.1	163.0	75.0	36.0	33.0	17.4	11.3	133.1	60.2	20.3	79.8	76.9	68.5	18.3	19.7	43.6
20	0.3	0.1	113.2	46.3	19.0	29.7	16.3	6.8	91.0	37.0	9.0	73.7	64.8	64.3	19.6	20.1	52.6
30	0.3	0.1	115.0	47.0	23.0	43.2	19.2	7.1	87.0	41.0	12.0	62.4	59.2	69.2	24.3	12.8	47.8
40	0.3	0.1	112.0	45.0	19.0	53.2	23.3	8.0	81.0	37.0	11.2	52.5	48.2	57.8	27.7	17.8	41.1
50	0.3	0.1	110.2	49.0	20.2	64.2	26.3	8.6	84.0	39.0	12.3	41.7	46.3	57.5	23.8	20.4	39.1
60	0.3	0.1	108.0	45.0	23.0	72.2	29.3	9.1	83.0	39.0	14.0	33.1	34.9	60.5	23.1	13.3	39.1
70	0.3	0.1	104.0	43.0	18.0	81.2	32.6	10.2	82.1	34.0	12.3	22.0	24.1	43.1	21.1	20.9	31.7
10	0.3	0.2	210.2	111.2	49.2	41.8	22.9	20.6	161.2	93.2	41.2	80.1	79.4	58.1	23.3	16.2	16.3
10	0.3	0.3	266.8	159.4	65.2	61.7	45.0	32.0	213.4	129.1	55.4	76.9	71.7	50.9	20.0	19.0	15
Cutting conditions			Initial Workpiece Temperature (°C)	HUAT			HCT			Reduction (%) CT vs HUAT			Reduction (%) CT vs HCT				
$V$ (m/min)	$a_p$ (mm)	$f_r$ (mm/rev)		Fx	Fy	Fz	Fx	Fy	Fz	Fx	Fy	Fz	Fx	Fy	Fz		
10	0.3	0.1	100	28.3	13.1	7.9	101.0	42.2	17.5	74.3	72.7	60.8	8.2	12.0	12.4		
10	0.3	0.1	200	25.3	12.0	7.0	99.0	39.2	16.3	77.0	75.1	64.9	10.0	18.3	18.4		
10	0.3	0.1	300	21.7	10.3	6.3	87.3	37.2	11.1	80.2	78.5	68.6	20.6	22.4	44.4		
10	0.3	0.1	500	19.1	10.2	7.2	79.1	33.2	11.1	82.6	78.7	64.0	28.1	30.8	44.4		

## CHAPTER-8

# Conclusions and Future Work

### 8.1. Introduction

In recent decades, titanium alloys have gained widespread application in the aerospace, power-generation, biomedical and chemical industries, primarily due to a balanced set of desirable properties, such as light weight, high strength, excellent fatigue behaviour, resistance to an aggressive environment and biocompatibility [2, 18, 203]. These alloys are difficult to machine using conventional machining processes due to their high strength and chemical reactivity with the tool material; hence, they require specialised coolants that lower the sustainability of the manufacturing processes. Over the last few decades, sustainable hybrid machining processes have attracted many researchers trying to improve the machining of these high-strength alloys by reducing the cutting forces [1].

In this sense, the current study was mainly aimed to introduce a new hybrid turning process called hot ultrasonically assisted turning (HUAT). In this process, vibration was superimposed on the cutting tool in tangential direction in order to separate it from the workpiece at the retraction stage, causing lower levels of average cutting forces, whereas external heat was supplied to the workpiece to make it easier for the cutting tool to remove the excess amount of material. It was accomplished by conducting a critical literature review followed by experimental and numerical studies. Various experiments were carried out to understand the difference between the novel HUAT with conventional and assisted turning processes considering force reduction, temperature in the process zone and hardness of the surface layer. A series of numerical studies were performed showing the development of the FE model of the orthogonal turning process and a more complex and adequate oblique turning model for conventional turning (CT), hot conventional turning (HCT), ultrasonically assisted turning (UAT) and HUAT. The developed novel model of oblique turning allowed predictions of stress distributions, the tool-penetration force for all three directions and temperature distribution in the turning processes. Most importantly, the developed model adequately reflected experimental results.

## 8.2. Conclusions

### 8.1.1. Experimentation of Novel Hybrid Turning Process

Substantial reduction in cutting forces was observed in HUAT for the same cutting conditions when compared to those in CT. The novel developed turning process resulted in a reduction of 80-85% at industrially applied cutting conditions. In addition to force reduction, a nearly full reduction of chatter was also observed as an interesting side effect in the newly developed HUAT process.

A relatively high chip temperature was observed in HUAT when compared to CT, HCT and UAT. The rise in temperature in HCT and HUAT depended on the level of initial temperature of the workpiece material. The newly developed HUAT produced continuous chip and no significant effect in metallurgy of the machined specimens were observed as reported in light microscopy and SEM analysis. A slight increase in hardness of the machined surface was observed in CT, HCT, UAT and HUAT. The rise in hardness of machined samples was insignificant compared to the virgin sample. Hence, the novel hybrid turning process (HUAT) resulted in a significant reduction in cutting forces without altering the properties of the machined surface, resulted high material removal rate (MRR) compared to CT. In addition to that, an improved surface roughness (approx. 70%) was also reported in HUAT when compared to CT [97].

### 8.1.2. Numerical Simulations of HUAT, CT, HCT and UAT

The developed 3D orthogonal turning model was used for the tangential cutting forces at various cutting conditions. One of the main limitations of the developed model was not incorporating the radial cutting force and simplification of the process zone in the model. A significant reduction in the tangential cutting forces was observed with the developed novel hybrid turning process. The observed cutting forces in HUAT were approx. 20% of the force level observed in CT. The model validated the claim that the reduction in cutting forces was due to tool separation from the process zone and decreased in peak force value due to thermal softening. A good prediction of the effect of cutting conditions and vibrational parameters on cutting forces, temperature in the process zone and stresses were observed

with the developed model. The contact time of the tool with the workpiece material in HUAT was approx. 40% of that in CT and HCT.

After successive attempts and parametric analysis of conventional and assisted turning processes with a simplified 3D model of orthogonal turning, a new model of hybrid oblique turning was developed for HUAT. The model was used for the analysis of CT, HCT, UAT and HUAT to investigate the effect of heat and vibration on the radial and the axial component of cutting forces. This model reflected the actual features of a turning setup more closely to the actual tool and workpiece geometries. With development of such a model, various hybrid turning processes were simulated to study the response of a material at various cutting conditions.

The model simulated the prime reason for a reduction in the radial and the axial cutting forces in UAT and HUAT. The reduction was observed due to the tool separation in the retraction stage and a reduction in peak force level due to thermal softening in HUAT. Small traces of forces in the retraction stage in the radial and the axial component of forces, less than 1 N was observed on the cutting tool. This indicate polishing of a machined surface in HUAT, resulted better surface finish [97] . The developed oblique turning model was used to determine the critical velocity of the novel HUAT. The reduction in cutting force vanished above 80 m/min. The reduction above the critical speed 60 m/min was attributed to the thermal softening due to the externally applied heat and process zone temperature in the workpiece material.

One of the main characteristics of the developed FE models was to explore those features of conventional and hybrid turning processes that were difficult to investigate with experimentations. The experimental thermal analysis performed had some limitations, primarily due to obstruction from the chip during the machining operation. The developed FE models for conventional and hybrid turning processes have the added advantage of elucidating the temperature characteristics in regions of the workpiece not visible to thermal imaging system. In addition to that, additional features like stresses, strain, the amount of heat transfer from the cutting region to the cutting tool, contact time, tool conditions, force and thermal histories in one complete cycle was investigated with the developed model. A good comparison of experimental and numerical simulation results was observed.

The model was also used to simulate HUAT for vibration applied in different directions and analysed its effect on cutting forces. The difference in cutting forces was studied on the basis of comparison to those in CT and HCT. The highest reduction in cutting forces was observed in a vibration case superimposed in the cutting direction. The newly developed oblique turning model was used for elliptical vibration analysis to estimate the cutting forces. A minor reduction in all components of cutting forces was observed in the analysis. This was one of the main features of the novel developed HUAT model to investigate different vibrational modes in hybrid turning processes.

The results obtained from the oblique turning model indicated that an increase in temperature of hot machining does not necessarily yield tractable benefits with respect to force reductions. At 500°C the reduction in cutting forces in the tangential and the radial component of forces was comparable to that for workpiece heating temperature of 300°C. However, a slight increase in the axial component of force was observed due to the pile up of material in HUAT. This observation was not possible with the previously developed 3D orthogonal turning model and a temperature of 300°C in HUAT of Ti-15333 was recommended in the current study. Thus, the obtained experimental and numerical results for HUAT and other turning processes will pose an interesting case for hybrid turning processes and an eventual widespread adoption of this technology in the industry.

### 8.3. Contribution to Knowledge

In the current study, conventional and assisted turning processes were used to investigate cutting forces and temperature of the process zone both experimentally and numerically. During the course of study, the following contributions to knowledge were made in the hybrid machining processes.

- A new hybrid turning process was investigated for the first time for cutting forces and process zone temperature.
- A novel hybrid FE turning model was developed for parametric analysis of the newly developed HUAT, conventional and assisted turning processes.
- The radial and axial cutting forces were investigated for the first time in UAT and HUAT.
- A significant reduction in cutting forces was achieved with the hybrid turning process

#### 8.4. Future Work

During the course of the current study, several challenges were treated successfully, yet there are some further research aims that can still be achieved in order to expand the recent study. Thus, some further investigations are suggested for experimentation and simulations.

- To Investigate the influence of crystallographic orientation of a workpiece on the chip-formation mechanism in turning of Ti-15333 using conventional and gradient polycrystalline plasticity theories.
- Analysis of residual stress in the machined sample at various cutting conditions to estimate the effect of a newly developed turning process compared to CT and other assisted turning processes.
- Development of a setup for 2D and 3D vibration assisted turning setups for the turning of modern alloys.
- Development of a fine-mesh algorithm for the machining of turning process to investigate the surface roughness of machined components.
- Economic analysis of the HUAT.

## References:

- [1]. C R Dandekar, Y C Shin and J Barnes: (2010), Machinability improvement of titanium alloy (Ti-6Al-4V) via LAM and hybrid machining, *International Journal of Machine Tools and Manufacture*, 50(2), pp: 174-182
- [2]. M J Donachie: (2004), *Titanium- A technical guide* ASM International, Ohio, USA
- [3]. E O Ezugwu, J Bonney and Y Yamane: (2003), An overview of the machinability of aeroengine alloys, *Journal of Materials Processing Technology*, 134(2), pp: 233-253
- [4]. N Ahmed, A V Mitrofanov, V I Babitsky and V V Silberschmidt: (2007), Analysis of forces in ultrasonically assisted turning, *Journal of Sound and Vibration*, 308(3-5), pp: 845-854
- [5]. A Shokrani, V Dhokia and S T Newman: (2012), Environmentally conscious machining of difficult-to-machine materials with regard to cutting fluids, *International Journal of Machine Tools and Manufacture*, 57 pp: 83-101
- [6]. F Klocke, G Eisenblätter and T Krieg: (2008), *Machining: Wear of tools* Encyclopaedia of Materials: Science and Technology, Elsevier, Oxford, UK
- [7]. N Ahmed, A V Mitrofanov, V I Babitsky and V V Silberschmidt: (2007), 3D finite element analysis of ultrasonically assisted turning, *Computational Materials Science*, 39(1), pp: 149-154
- [8]. N Ahmed, A V Mitrofanov, V I Babitsky and V V Silberschmidt: (2006), Stresses in ultrasonically assisted turning, *Applied Mechanics and Materials*, 5-6 pp: 351-358

- [9]. A V Mitrofanov, V I Babitsky and V V Silberschmidt: (2004), Finite element analysis of ultrasonically assisted turning of Inconel 718, *Journal of Materials Processing Technology*, 153–154(0), pp: 233-239
- [10]. A V Mitrofanov, V I Babitsky and V V Silberschmidt: (2003), Finite element simulations of ultrasonically assisted turning, *Computational Materials Science*, 28(3–4), pp: 645-653
- [11]. R Muhammad, A Maurotto, A Roy and V V Silberschmidt: (2012), Ultrasonically assisted turning of Ti-6Al-2Sn-4Zr-6Mo, *Journal of Physics: Conference Series* 382
- [12]. R Muhammad, N Ahmed, A Roy and V V Silberschmidt: (2012), Numerical modelling of vibration-assisted turning of Ti-15333, *Procedia CIRP*, 1 pp: 347-352
- [13]. A Maurotto, R Muhammad, A Roy, V I Babitsky and V V Silberschmidt: (2012), Comparing machinability of Ti-15-3-3-3 and Ni-625 alloys in UAT, *Procedia CIRP*, 1 pp: 330-335
- [14]. C Machai and D Biermann: (2011), Machining of  $\beta$ -titanium-alloy Ti-10V-2Fe-3Al under cryogenic conditions: Cooling with carbon dioxide snow, *Journal of Materials Processing Technology*, 211(6), pp: 1175-1183
- [15]. A Shokrani, V Dhokia, S T Newman and R Imani-Asrai: (2012), An Initial study of the effect of using liquid nitrogen coolant on the surface roughness of Inconel 718 Nickel-based alloy in CNC milling, *Procedia CIRP*, 3 pp: 121-125
- [16]. S Y Hong, Y Ding and W-c Jeong: (2001), Friction and cutting forces in cryogenic machining of Ti-6Al-4V, *International Journal of Machine Tools and Manufacture*, 41(15), pp: 2271-2285

- [17]. S M Yuan, L T Yan, W D Liu and Q Liu: (2011), Effects of cooling air temperature on cryogenic machining of Ti-6Al-4V alloy, *Journal of Materials Processing Technology*, 211(3), pp: 356-362
- [18]. O Ezugwu and M Wang: (1997), Titanium alloys and their machinability—a review, *Journal of Materials Processing Technology*, 68(3), pp: 262-274
- [19]. M C Shaw: (1991), *Metal cutting principle Oxford series on advanced manufacturing*, Oxford science publication, Clarendon press, Oxford, UK
- [20]. H El-Hofy: (2006), *Fundamental of machining processes: Conventional and non-conventional processes* Taylor and Francis Group, LLC, New York, USA
- [21]. B P Erdel: (2003), *High speed machining Society of Manufacturing Engineerings*, Michigan, USA
- [22]. M P Groover: (2010), *Fundamental of modern manufacturing materials, processes and systems* Jhon Wiley and Sons, Inc, New York, USA
- [23]. T Childs, K Maekawa, T Obikawa and Y Yamane: (2005), *Metal machining: Theory and applications* John Wiley & Sons, New York, USA
- [24]. H A Youssef: (2008), *Machining technology: Machine tools and operations* Taylor and Francis Group, London, UK
- [25]. M S Sun, Brandt, M.S.Dargusch: (2010), Thermally enhanced machining of hard-to-machine materials-A review, *International Journal of Machine Tools and Manufacture*, 50 pp: 663-680
- [26]. K Uehara and H Takeshita: (1986), Cutting ceramics with a technique of hot machining, *CIRP Annals - Manufacturing Technology*, 35(1), pp: 55-58
- [27]. C Brecher, M Emonts, C-J Rosen and J-P Hermani: (2011), Laser-assisted milling of advanced materials, *Physics Procedia*, 12, Part A(0), pp: 599-606

- [28]. M Mori, M Fujishima and O Yuhi: (2012), 5 Axis mill turn and hybrid machining for advanced application, CIRP Proceedia, 1 pp: 22-27
- [29]. M M Dhananchezian, P Kumar: (2011), Cryogenic turning of the Ti-6Al-4V alloy with modified cutting tool inserts, Cryogenics, 51 pp: 34-40
- [30]. A Shokrani, V Dhokia, P Muñoz-Escalona and S T Newman: (2013), State-of-the-art cryogenic machining and processing, International Journal of Computer Integrated Manufacturing, pp: 1-33
- [31]. R C Skelton: (1968), Turning with an oscillating tool, International Journal of Machine Tool Design and Research, 8(4), pp: 239-259
- [32]. DMG: DMG D4839/0210ND1; In: Ultrasonic Series; ULTRASONICS hard machining and milling on one machine. 2010; Available from: <http://en.dmgmorseiki.com/sites/en/home/>.
- [33]. Seco-Tool: Seco catalogue. 2013; Available from: <http://ecat.secotools.com/>.
- [34]. B.J.Ranganath: (1999), Metal cutting and tool design Vikas publishing house private limited
- [35]. J L Cantero, J Díaz-Álvarez, M H Miguélez and N C Marín: (2013), Analysis of tool wear patterns in finishing turning of Inconel 718, Wear, 297(1-2), pp: 885-894
- [36]. A Attanasio, E Ceretti, A Fiorentino, C Cappellini and C Giardini: (2010), Investigation and FEM-based simulation of tool wear in turning operations with uncoated carbide tools, Wear, 269(5-6), pp: 344-350
- [37]. B Rao, C R Dandekar and Y C Shin: (2011), An experimental and numerical study on the face milling of Ti-6Al-4V alloy: Tool performance and surface integrity, Journal of Materials Processing Technology, 211(2), pp: 294-304

- [38]. S Zhang, J F Li and Y W Wang: (2012), Tool life and cutting forces in end milling Inconel 718 under dry and minimum quantity cooling lubrication cutting conditions, *Journal of Cleaner Production*, 32 pp: 81-87
- [39]. N Tomac, K Tonnessen and F O Rasch: (1991), Formation of flank build-up in cutting magnesium alloys, *CIRP Annals - Manufacturing Technology*, 40(1), pp: 79-82
- [40]. N Fang and P Dewhurst: (2005), Slip-line modeling of built-up edge formation in machining, *International Journal of Mechanical Sciences*, 47(7), pp: 1079-1098
- [41]. T H C Childs: (2011), Towards simulating built-up-edge formation in the machining of steel, *CIRP Journal of Manufacturing Science and Technology*, 4(1), pp: 57-70
- [42]. S V Hosseini and M Vahdati: (2012), Modeling the effect of tool edge radius on contact zone in nanomachining, *Computational Materials Science*, 65 pp: 29-36
- [43]. K Iwata and K Ueda: (1980), Fundamental analysis of the mechanism of built-up edge formation based on direct scanning electron microscope observation, *Wear*, 60(2), pp: 329-337
- [44]. S Kitayama, T Nagata, M Nishimoto, Y Sugimoto and W W. Takahashi: (1992), Method for improving machinability of titanium and titanium alloys and free-cutting titanium alloys
- [45]. C Siemers, M Bäker, D Mukherji and J Rösler: (2003), Microstructure evolution in shear bands during the chip formation of Ti6Al4V in *Proceedings of Ti-2003 Wiley-VCH, Weinheim Germany*,
- [46]. M S Hussain, C Siemers and J Rösler: (2013), Development of a Free-machining Titanium Alloy based on Ti 6Al 2Sn 4Zr 6Mo, *Journal of Materials and Manufacturing Processes*, 28(5), pp: 545-549

- [47]. C Siemers, F Brunke, J Laukart, M S Hussain, J Rösler, K Saksl and B Zahra: (2012), in COM2012, Section Rare Earth Metals 2012 Niagara Falls, Canada, pp: 281-292
- [48]. C Siemers, F Brunke, M Stache, J Laukart, B Zahra, J Roesler, P Rokicki and K Saksl: (2011), Advanced titanium alloys containing micrometer-size particles in 12th World Conference on Titanium (Ti-2011) Beijing, China, 2 pp: 883-887
- [49]. C Siemers, J Laukart, B Zahra and J Rösler: (2011), Development of advanced and free-machining alloys by micrometer-size particle precipitation, Materials Science Forum, 690 pp: 262-265
- [50]. C Siemers, B Zahra, T Leemet and J Rösler: (2009), in 8th AMMT'09 Conference, St. Petersburg, Russia,
- [51]. M C Shaw and A Vyas: (1998), The mechanism of chip formation with hard turning steel, CIRP Annals - Manufacturing Technology, 47(1), pp: 77-82
- [52]. M A Elbestawi, A K Srivastava and T I El-Wardany: (1996), A model for chip formation during machining of hardened steel, CIRP Annals - Manufacturing Technology, 45(1), pp: 71-76
- [53]. W K Luk: (1970), Mechanics of the turning operation, International Journal of Machine Tool Design and Research, 10(3), pp: 351-360
- [54]. V Piispanen: (1948), Theory of formation of metal chips, Journal of Applied Physics, 19 pp: 876-881
- [55]. E J Krabacher, M E Marchant and C Ohio: (1951), Basic factors in hot-machining of metals, Transaction of American Society of Mechanical Engineers, 73 pp: 761-776
- [56]. W B Palmer: (1966), Metal cutting mechanics: N. N. Zorev: Pergamon Press (1966). pp. 526, £7, International Journal of Mechanical Sciences, 8(10), pp: 651

- [57]. P L B Oxley: (1988), Modelling machining processes with a view to their optimization and to the adaptive control of metal cutting machine tools, *Robotics and Computer-Integrated Manufacturing*, 4(1–2), pp: 103-119
- [58]. M C Shaw and A Vyas: (1993), Chip formation in the machining of hardened steel, *CIRP Annals - Manufacturing Technology*, 42(1), pp: 29-33
- [59]. M A Davies, Y Chou and C J Evans: (1996), On chip morphology, tool wear and cutting mechanics in finish hard turning, *CIRP Annals - Manufacturing Technology*, 45(1), pp: 77-82
- [60]. M E Merchant: (1945), Mechanics of the metal cutting process. I. Orthogonal cutting and a type 2 chip, *Journal of Applied Physics*, 16(5), pp: 267-275
- [61]. E H Lee and B W Shaffer: (1951), The theory of plasticity applied to the problem of machining, *Journal of Applied Mechanics*, 165 pp: 15-20
- [62]. P L B Oxley: (1962), An analysis for orthogonal cutting with restricted tool-chip contact, *International Journal of Mechanical Sciences*, 4(2), pp: 129-135
- [63]. N Fang: (1998), An improved model for oblique cutting and its application to chip-control research, *Journal of Materials Processing Technology*, 79(1–3), pp: 79-85
- [64]. Z-C Lin and Y-Y Lin: (1998), A study of an oblique cutting model, *Journal of Materials Processing Technology*, 86(1–3), pp: 119-130
- [65]. Z-C Lin and Y-Y Lin: (1999), Fundamental modeling for oblique cutting by thermo-elastic-plastic FEM, *International Journal of Mechanical Sciences*, 41(8), pp: 941-965
- [66]. G Fang and P Zeng: (2005), Three-dimensional thermo-elastic-plastic coupled FEM simulations for metal oblique cutting processes, *Journal of Materials Processing Technology*, 168(1), pp: 42-48

- [67]. H Razavi, M J Nategh and A Abdullah: (2012), Analytical modeling and experimental investigation of ultrasonic-vibration assisted oblique turning, part II: Dynamics analysis, *International Journal of Mechanical Sciences*, 63(1), pp: 12-25
- [68]. H Razavi, M J Nategh and A Abdullah: (2012), Analytical modeling and experimental investigation of ultrasonic-vibration assisted oblique turning, part III: Experimental investigation, *International Journal of Mechanical Sciences*, 63(1), pp: 26-36
- [69]. M J Nategh, H Razavi and A Abdullah: (2012), Analytical modeling and experimental investigation of ultrasonic-vibration assisted oblique turning, part I: Kinematics analysis, *International Journal of Mechanical Sciences*, 63(1), pp: 1-11
- [70]. P C Pandey and C K Singh: (1999), *Production engineering science*, Standard Publishers Distributors, Dehli, India
- [71]. Y Huang and S Y Liang: (2003), Cutting forces modeling considering the effect of tool thermal property—application to CBN hard turning, *International Journal of Machine Tools and Manufacture*, 43(3), pp: 307-315
- [72]. T I El-Wardany, E Mohammed and M A Elbestawi: (1996), Cutting temperature of ceramic tools in high speed machining of difficult-to-cut materials, *International Journal of Machine Tools and Manufacture*, 36(5), pp: 611-634
- [73]. W Grzesik: (2006), Determination of temperature distribution in the cutting zone using hybrid analytical-FEM technique, *International Journal of Machine Tools and Manufacture*, 46(6), pp: 651-658
- [74]. M Lazard and P Corvisier: (2004), Modelling of a tool during turning: Analytical prediction of the temperature and of the heat flux at the tool's tip, *Applied Thermal Engineering*, 24(5–6), pp: 839-849

- [75]. M Imran, R Muhammad, N Ahmed and V V Silberschmidt: (2009), Design and construction of dynamometer for cutting forces measurement in milling operation, *Journal of Engineering and Applied Sciences*, 28(1) pp: 25-32
- [76]. S E Oraby and D R Hayhurst: (1990), High-capacity compact three-component cutting force dynamometer, *International Journal of Machine Tools and Manufacture*, 30(4), pp: 549-559
- [77]. S Yıldız, F Ünsaçar, H Sağlam and H Işık: (2007), Design, development and testing of a four-component milling dynamometer for the measurement of cutting force and torque, *Mechanical Systems and Signal Processing*, 21(3), pp: 1499-1511
- [78]. S Karabay: (2007), Design criteria for electro-mechanical transducers and arrangement for measurement of strains due to metal cutting forces acting on dynamometers, *Materials & Design*, 28(2), pp: 496-506
- [79]. İ Korkut: (2003), A dynamometer design and its construction for milling operation, *Materials & Design*, 24(8), pp: 631-637
- [80]. HA.Youssef: (2008), *Machining technology: Machine tools and operations* Taylers and Francis Group
- [81]. R Muhammad: (2009), *Experimental and Numerical Analysis of Drilling Process of AISI 1020 Steel*, Faculty of Mechanical Engineering, Ghulam Ishaq Khan Institute of Engineering Sciences and Technology.
- [82]. M Imram: (2008), *Experimental and numerical study of slot milling*, Faculty of Mechanical Engineering, Ghulam Ishaq Khan Institute of Engineering Sciences and Technology.
- [83]. D A Stephenson and A Ali: (1992), Tool temperatures in interrupted metal cutting, *Journal of Engineering Industries*, 114 pp: 127-136

- [84]. B Alvelid: (1969), Cutting temperature thermo-electrical measurements, *CIRP Annals - Manufacturing Technology*, 18(1), pp: 547-554
- [85]. P Lezanski: (1990), Tool face temperatures in high speed milling, *Trans. ASME, Journal of Engineering for industry*, 112(2), pp: 132-135
- [86]. T Kitagawa, A Kubo and K Maekawa: (1997), Temperature and wear of cutting tools in high-speed machining of Inconel 718 and Ti-6Al-6V-2Sn, *Wear*, 202(2), pp: 142-148
- [87]. R Muhammad, N Ahmed, Y M Shariff and V V Silberschmidt: (2011), Effect of cutting conditions on temperature generated in drilling process: A FEA approach, *Advanced Materials Research*, 223 pp: 240-246
- [88]. P A Dearnley: (1983), New technique for determining temperature distribution in cemented carbide cutting tools, *Metals Technology*, 10(pt 6), pp: 205-214
- [89]. S Kato, K Yamaguchi, Y Watanabe and Y Hiraiwa: (1976), Measurement of temperature distribution within tool using powders of constant melting point, *Journal of Engineering for Industry*, 98(2), pp: 607-613
- [90]. B Müller and U Renz: (2003), Time resolved temperature measurements in manufacturing, *Measurement*, 34(4), pp: 363-370
- [91]. J Lin, S L Lee and C I Weng: (1992), Estimation of cutting temperature in high speed machining, *Journal of Engineering Material Technology*, 114 pp: 289-296
- [92]. R C Dewes, E Ng, K S Chua, P G Newton and D K Aspinwall: (1999), Temperature measurement when high speed machining hardened mould/die steel, *Journal of Materials Processing Technology*, 92–93(0), pp: 293-301
- [93]. M Alam, D E Peebles and D R Tallant: (1997), Diamond deposition onto WC-6%Co cutting tool material: coating structure and interfacial bond strength, *Thin Solid Films*, 300(1–2), pp: 164-170

- [94]. A Xing, Z Jun, H Chuanzhen and Z Jianhua: (1998), Development of an advanced ceramic tool material—functionally gradient cutting ceramics, *Materials Science and Engineering: A*, 248(1–2), pp: 125-131
- [95]. C Mao, H Zou, X Huang, J Zhang and Z Zhou: (2013), The influence of spraying parameters on grinding performance for nanofluid minimum quantity lubrication, *The International Journal of Advanced Manufacturing Technology*, 64(9-12), pp: 1791-1799
- [96]. S Sun, M Brandt and M S Dargusch: (2010), Thermally enhanced machining of hard-to-machine materials—A review, *International Journal of Machine Tools and Manufacture*, 50(8), pp: 663-680
- [97]. R Muhammad, A Maurotto, A Roy and V V Silberschmidt: (2012), Hot ultrasonically assisted turning of  $\beta$ -Ti alloy, *Procedia CIRP*, 1 pp: 336-341
- [98]. G Madhavulu and B Ahmed: (1994), Hot machining process for improved metal removal rates in turning operations, *Journal of Materials Processing Technology*, 44(3–4), pp: 199-206
- [99]. M A Lajis, A K M N Amin, A N M Karim, H C D M Radzi and T L Ginta: (2009), Hot machining of hardened steels with coated carbide inserts, *American Journal of Engineering and Applied Sciences*, 421-427
- [100]. D K Pal and S K Basu: (1971), Hot machining of austenitic manganese steel by shaping, *International Journal of Machine Tool Design and Research*, 11(1), pp: 45-61
- [101]. R Muhammad, N Ahmed, A Roy and V V Silberschmidt: (2012), Turning of advanced alloys with vibrating cutting tool, *Solid State Phenomena*, 188 pp: 277-284

- [102]. R Muhammad, M Demiral, N Ahmed, A Roy and V V Silberschmidt: (2011), Computational study of ultrasonically-assisted turning of Ti alloys, *Advanced Materials Research*, 223 pp: 30-36
- [103]. R Muhammad, A Maurotto, A Roy and V V Silberschmidt: (2011), Analysis of forces in vibro-impact and hot vibro-impact turning of advanced alloys, *Applied Mechanics and Materials*, 70 pp: 315-320
- [104]. M Murakawa, M Jin and P Kaewtatip: (1999), Utility of ultrasonic vibration applied to metal-forming processes, *Advanced Technology of Plasticity*, pp: 19-24
- [105]. E Shamoto, C Ma and T Moriwaki: (1999), Elliptical vibration cutting (3rd report) - Application to three-dimensional cutting and investigation of practical effects, *Seimitsu Kogaku Kaishi/Journal of the Japan Society for Precision Engineering*, 65(4), pp: 586-591
- [106]. E Shamoto and T Moriwaki: (1994), Study on elliptical vibration cutting, *CIRP Annals - Manufacturing Technology*, 43(1), pp: 35-38
- [107]. M Dhananchezian and M Pradeep Kumar: (2011), Cryogenic turning of the Ti-6Al-4V alloy with modified cutting tool inserts, *Cryogenics*, 51(1), pp: 34-40
- [108]. Y Yildiz and M Nalbant: (2008), A review of cryogenic cooling in machining processes, *International Journal of Machine Tools and Manufacture*, 48(9), pp: 947-964
- [109]. N A Dhar, S Paul and A B Chattopadhyay: (2002), The influence of cryogenic cooling on tool wear, dimensional accuracy and surface finish in turning AISI 1040 and E4340C steels, *Wear*, 249 pp: 932-942
- [110]. N A Dhar, S V N Kishore, S Paul and A B Chattopadhyay: (2002), The effects of cryogenic cooling on chips and cutting forces in turning AISI 1040 and AISI 4320 steel, *Journal of Engineering Manufacturing*, 216 Part B pp: 713-724

- [111]. S Paul, N R Dhar and A B Chattopadhyay: (2001), Beneficial effects of cryogenic cooling over dry and wet machining on tool wear and surface finish in turning AISI 1060 steel, *Journal of Materials Processing Technology*, 116(1), pp: 44-48
- [112]. A V Mitrofanov, V I Babitsky and V V Silberschmidt: (2005), Thermomechanical finite element simulations of ultrasonically assisted turning, *Computational Materials Science*, 32 pp: 463-471
- [113]. H Weber, J Herberger and R Pilz: (1984), Turning of machinable glass ceramics with an ultrasonically vibrated tool, *CIRP Annals - Manufacturing Technology*, 33(1), pp: 85-87
- [114]. T Moriwaki and E Shamoto: (1991), Ultraprecision diamond turning of stainless steel by applying ultrasonic vibration, *CIRP Annals - Manufacturing Technology*, 40(1), pp: 559-562
- [115]. J-D Kim and E-S Lee: (1994), A study of the ultrasonic-vibration cutting of carbon-fiber reinforced plastics, *Journal of Materials Processing Technology*, 43(2-4), pp: 259-277
- [116]. T Moriwaki and E Shamoto: (1995), Ultrasonic elliptical vibration cutting, *CIRP Annals - Manufacturing Technology*, 44(1), pp: 31-34
- [117]. J D Kim and I H Choi: (1997), Micro surface phenomenon of ductile cutting in the ultrasonic vibration cutting of optical plastics, *Journal of Materials Processing Technology*, 68(1), pp: 89-98
- [118]. E Shamoto and T Moriwaki: (1999), Ultraprecision diamond cutting of hardened steel by applying elliptical vibration cutting, *CIRP Annals - Manufacturing Technology*, 48(1), pp: 441-444
- [119]. C S Liu, B Zhao, G F Gao and F Jiao: (2002), Research on the characteristics of the cutting force in the vibration cutting of a particle-reinforced metal matrix composites SiCp/Al, *Journal of Materials Processing Technology*, 129(1-3), pp: 196-199

- [120]. M Xiao, S Karube, T Soutome and K Sato: (2002), Analysis of chatter suppression in vibration cutting, *International Journal of Machine Tools and Manufacture*, 42(15), pp: 1677-1685
- [121]. G F Gao, B Zhao, F Jiao and C S Liu: (2002), Research on the influence of the cutting conditions on the surface microstructure of ultra-thin wall parts in ultrasonic vibration cutting, *Journal of Materials Processing Technology*, 129(1–3), pp: 66-70
- [122]. M Xiao, K Sato, S Karube and T Soutome: (2003), The effect of tool nose radius in ultrasonic vibration cutting of hard metal, *International Journal of Machine Tools and Manufacture*, 43(13), pp: 1375-1382
- [123]. N Suzuki, S Masuda, M Haritani and E Shamoto: (2004), Ultraprecision micromachining of brittle materials by applying ultrasonic elliptical vibration cutting in Micro-Nanomechatronics and Human Science pp: 133-138
- [124]. V I Babitsky, A V Mitrofanov and V V Silberschmidt: (2004), Ultrasonically assisted turning of aviation materials: simulations and experimental study, *Ultrasonics*, 42(1–9), pp: 81-86
- [125]. C Ma, E Shamoto, T Moriwaki and L Wang: (2004), Study of machining accuracy in ultrasonic elliptical vibration cutting, *International Journal of Machine Tools and Manufacture*, 44(12–13), pp: 1305-1310
- [126]. A V Mitrofanov, N Ahmed, V I Babitsky and V V Silberschmidt: (2005), Effect of lubrication and cutting parameters on ultrasonically assisted turning of Inconel 718, *Journal of Materials Processing Technology*, 162–163(0), pp: 649-654
- [127]. E Shamoto, N Suzuki, E Tsuchiya, Y Hori, H Inagaki and K Yoshino: (2005), Development of 3 DOF Ultrasonic Vibration Tool for Elliptical Vibration Cutting of Sculptured Surfaces, *CIRP Annals - Manufacturing Technology*, 54(1), pp: 321-324

- [128]. C Ma, E Shamoto, T Moriwaki, Y Zhang and L Wang: (2005), Suppression of burrs in turning with ultrasonic elliptical vibration cutting, *International Journal of Machine Tools and Manufacture*, 45(11), pp: 1295-1300
- [129]. Z W Zhong and G Lin: (2005), Diamond turning of a metal matrix composite with ultrasonic vibrations, *Materials and Manufacturing Processes*, 20 pp: 727-735
- [130]. N Ahmed, A V Mitrofanov, V I Babitsky and V V Silberschmidt: (2006), Analysis of material response to ultrasonic vibration loading in turning Inconel 718, *Materials Science and Engineering: A*, 424(1–2), pp: 318-325
- [131]. X Zhang, A Senthil Kumar, M Rahman, C Nath and K Liu: (2011), Experimental study on ultrasonic elliptical vibration cutting of hardened steel using PCD tools, *Journal of Materials Processing Technology*, 211(11), pp: 1701-1709
- [132]. T Moriwaki, E Shamoto and K Inoue: (1992), Ultraprecision ductile cutting of glass by applying ultrasonic vibration, *CIRP Annals - Manufacturing Technology*, 41(1), pp: 141-144
- [133]. V K Astashev and V I Babitsky: (1998), Ultrasonic cutting as a nonlinear (vibro-impact) process, *Ultrasonics*, 36(1–5), pp: 89-96
- [134]. V I Babitsky, V K Astashev and A Meadows: (2007), Vibration excitation and energy transfer during ultrasonically assisted drilling, *Journal of Sound and Vibration*, 308(3–5), pp: 805-814
- [135]. V K Astashev and V I Babitsky: (2007), *Ultrasonic processes and machines: dynamics, control and applications*, SpringerVerlag, Berlin Heidelberg, Germany
- [136]. V I Babitsky, A N Kalashnikov and F V Molodtsov: (2004), Autoresonant control of ultrasonically assisted cutting, *Mechatronics*, 14(1), pp: 91-114

- [137]. V I Babitsky, A N Kalashnikov, A Meadows and A A H P Wijesundara: (2003), Ultrasonically assisted turning of aviation materials, *Journal of Materials Processing Technology*, 132(1–3), pp: 157-167
- [138]. S Sun, J Harris and M Brandt: (2008), Parametric investigation of laser-assisted machining of commercially pure titanium, *Advanced Engineering Materials*, 10(6), pp: 565-572
- [139]. L Ozler, A Inan and C Ozel: (2001), Theoretical and experimental determination of tool life in hot machining of austenitic manganese steel, *International Journal of Machine Tools and Manufacture*, 41(2), pp: 163-172
- [140]. K P Maity and P K Swain: (2008), An experimental investigation of hot-machining to predict tool life, *Journal of Materials Processing Technology*, 198(1–3), pp: 344-349
- [141]. N N S Chen and K C Lo: (1974), Factors affecting tool life in hot machining of alloy steels, *International Journal of Machine Tool Design and Research*, 14(2), pp: 161-173
- [142]. G S Kainth and M N Chaturvedi: (1975), Theoretical investigation of temperature in hot machining, *International Journal of Machine Tool Design and Research*, 15(4), pp: 241-256
- [143]. E G Loewen and M C Shaw: (1954), On the analysis of cutting tool temperatures, *Trans. ASME*, 76 pp: 217-231
- [144]. K Uehara, M Sakurai and H Takeshita: (1983), Cutting performance of coated carbides in electric hot machining of low machinability metals, *CIRP Annals - Manufacturing Technology*, 32(1), pp: 97-100
- [145]. B K Hinds and S M De Almeida: (1981), Plasma arc heating for hot machining, *International Journal of Machine Tool Design and Research*, 21(2), pp: 143-152

- [146]. C E Leshock, J Kim and C Y Shin: (2001), Plasma enhanced machining of Inconel 718: modeling of workpiece temperature with plasma heating and experimental results, *International Journal of Machine Tools and Manufacture*, 41(6), pp: 877-897
- [147]. C Zhang and Y C Shin: (2002), A novel laser-assisted truing and dressing technique for vitrified CBN wheels, *International Journal of Machine Tools and Manufacture*, 42(7), pp: 825-835
- [148]. P Dumitrescu, P Koshy, J Stenekes and M A Elbestawi: (2006), High-power diode laser assisted hard turning of AISI D2 tool steel, *International Journal of Machine Tools and Manufacture*, 46(15), pp: 2009-2016
- [149]. S Sun, J Harris and M Brandt: (2008), Parametric investigation of laser-assisted machining of commercially pure titanium, *Advanced Engineering Materials*, 10 pp: 565-572
- [150]. G Germain, P Dal Santo and J L Lebrun: (2011), Comprehension of chip formation in laser assisted machining, *International Journal of Machine Tools and Manufacture*, 51(3), pp: 230-238
- [151]. M F Zaeh, R Wiedenmann and R Daub: (2010), A thermal simulation model for laser-assisted milling, *Physics Procedia*, 5, Part B(0), pp: 353-362
- [152]. M Anderson, R Patwa. and Y C Shin: (2006), Laser-assisted machining of Inconel 718 with an economic analysis, *International Journal of Machine Tool and Manufacture*, 46 pp: 1879-1891
- [153]. A K M N Amin, S B Dolah, M B Mahmud and M A Lajis: (2008), Effects of workpiece preheating on surface roughness, chatter and tool performance during end milling of hardened steel D2, *Journal of Materials Processing Technology*, 201(1–3), pp: 466-470

- [154]. Z Y Wang, K P Rajurkar, J Fan, S Lei, Y C Shin and G Petrescu: (2003), Hybrid machining of Inconel 718, *International Journal of Machine Tools and Manufacture*, 43(13), pp: 1391-1396
- [155]. Y Tian and Y C Shin: (2006), Thermal modelling for laser-assisted machining of silicon nitride ceramics with complex features, *Journal of Manufacturing Science and Engineering (Trans ASME)*, 128 pp: 425-434
- [156]. J Hua and R Shivpur: (2005), A cobalt diffusion based model for predicting crater wear of carbide tools in machining titanium alloys, *Journal Of Engineering Materials and Technology*, 127(1) pp: 136-144
- [157]. M Calamaz, D Coupard and F Girot: (2008), A new material model for 2D numerical simulation of serrated chip formation when machining titanium alloy Ti-6Al-4V, *International Journal of Machine Tools and Manufacture*, 48(3-4), pp: 275-288
- [158]. T H C Childs: (2006), Numerical experiments on the influence of material and other variables on plane strain continuous chip formation in metal machining, *International Journal of Mechanical Sciences*, 48(3), pp: 307-322
- [159]. K Li, X L Gao and J W Sutherland: (2002), Finite element simulation of the orthogonal metal cutting process for qualitative understanding of the effects of crater wear on the chip formation process, *Journal of Materials Processing Technology*, 127(3), pp: 309-324
- [160]. J I Carroll and J Strenkowski: (1988), Finite element models of orthogonal cutting with application to single point diamond turning, *International Journal of Mechanical Science*, 30 pp: 899-920
- [161]. K Komvopoulos and S A Erpenbeck: (1991), Finite element modeling of orthogonal metal cutting, *Journal of Engineering for Industry*, 113(3), pp: 253-267

- [162]. C Shet and X Deng: (2000), Finite element analysis of the orthogonal metal cutting process, *Journal of Materials Processing Technology*, 105(1–2), pp: 95-109
- [163]. A G Mamalis, M Horvath, A S Branis and D E Manolakos: (2001), Finite element simulation of chip formation in orthogonal metal cutting, *Journal of Materials Processing Technology*, 110(1), pp: 19-27
- [164]. A J Shih and H T Y Yang: (1993), Experimental and finite element predictions of residual stresses due to orthogonal metal cutting, *International Journal for Numerical Methods in Engineering*, 36 pp: 1487-1507
- [165]. L J Xie, J Schmidt, C Schmidt and F Biesinger: (2005), 2D FEM estimate of tool wear in turning operation, *Wear*, 258(10), pp: 1479-1490
- [166]. P J Arrazola and T Ozel: (2010), Investigations on the effects of friction modeling in finite element simulation of machining, *International Journal of Mechanical Sciences*, 52(1), pp: 31-42
- [167]. S L Soo, D K Aspinwall and R C Dewes: (2004), 3D FE modelling of the cutting of Inconel 718, *Journal of Materials Processing Technology*, 150(1–2), pp: 116-123
- [168]. S Lei, Y C Shin and F P Incropera: (1999), Thermo-mechanical modeling of orthogonal machining process by finite element analysis, *International Journal of Machine Tools and Manufacture*, 39(5), pp: 731-750
- [169]. E Bagci: (2011), 3-D numerical analysis of orthogonal cutting process via mesh-free method *International Journal of the Physical Sciences* 6(6), pp: 1267-1282
- [170]. A Zahedi, S Li, A Roy, V Babitsky and V V Silberschmidt: (2012), Application of smooth-particle hydrodynamics in metal machining, *Journal of Physics: Conference Series*, 382

- [171]. T Özel, M Sima, A K Srivastava and B Kaftanoglu: (2010), Investigations on the effects of multi-layered coated inserts in machining Ti-6Al-4V alloy with experiments and finite element simulations, *CIRP Annals - Manufacturing Technology*, 59(1), pp: 77-82
- [172]. R Muhammad, N Ahmed, M Abid and V V Silberschmidt: (2010), 3D modeling of drilling process of AISI 1010 steel, *Journal of Machining and Forming Technologies*, 2(3/4) pp: 201-216
- [173]. T H C Childs: (2006), Friction modelling in metal cutting, *Wear*, 260(3), pp: 310-318
- [174]. H Ding and Y C Shin: (2013), Multi-physics modeling and simulations of surface microstructure alteration in hard turning, *Journal of Materials Processing Technology*, 213(6), pp: 877-886
- [175]. X C. Shet, Deng: (2000), Finite element analysis of orthogonal metal cutting process, *Journal of Materials Processing Technology*, 105 pp: 95-109
- [176]. P G. Fang, Zeng: (2004), Three dimensional thermo elastic-plastic coupled FEM simulations for metal oblique cutting processes., *Journal of Materials Processing Technology*, 168 pp: 42-48
- [177]. T Özel and E Zeren: (2004), Determination of work material flow stress and friction for FEA of machining using orthogonal cutting tests, *Journal of Materials Processing Technology*, 153-154(0), pp: 1019-1025
- [178]. M S. Bahi, Nouari, A. Moufki, M. El Mansori, A. Molinari: (2011), A new friction law for sticking and sliding contacts in machining, *Tribology International*, 44 (7-8) pp: 764-771
- [179]. G R Johnson and W H Cook: (1985), Fracture characteristics of three metals subjected to various strains, strain rates, temperatures and pressures, *Engineering Fracture Mechanics*, 21(1), pp: 31-48

- [180]. A Molinari and D Dudzinski: (1992), Stationnary shear band in high-speed machining, C.R. Academy of Sciences Paris, 315(2) pp: 399-405
- [181]. M I Sadik and B Lindström: (1993), The role of tool-chip contact length in metal cutting, Journal of Materials Processing Technology, 37(1-4), pp: 613-627
- [182]. G S Gad, E J A Armarego and A J R Smith: (1992), Tool-chip contact length in orthogonal machining and its importance in tool temperature predictions, International Journal of Production and Research, 30(3) pp: 485-501
- [183]. Y-C Yen, A Jain and T Altan: (2004), A finite element analysis of orthogonal machining using different tool edge geometries, Journal of Materials Processing Technology, 146(1), pp: 72-81
- [184]. M C Cakir and Y I Sik: (2005), Finite element analysis of cutting tools prior to fracture in hard turning operations, Materials & Design, 26(2), pp: 105-112
- [185]. A K M N Amin and N V Talantov: (1986), Influence of instability of chip formation and preheating of work on tool life in machining high temperature resistance steel and titanium alloy, Mechanical Engineering Research Bulletin, 9 pp: 52-62
- [186]. T Kitagawa and K Maekawa: (1990), Plasma hot machining for new engineering materials, Wear, 139 pp: 251-167
- [187]. G Chryssolouries, N Anifantis and S Karagiannis: (1997), Laser assisted machining: an overview, Journal of Manufacturing Science and Engineering, Transactions of the ASME, 119 pp: 766-769
- [188]. A Maurotto, R Muhammad, A Roy and V V Silberschmidt: (2013), Enhanced ultrasonically assisted turning of a  $\beta$ -titanium alloy, Ultrasonics, 53(7), pp: 1242-1250

- [189]. A Dodonov, C Siemers and J Rosler: (2009), Analysis of the processing and machining characteristics of Ti15V3Al3Sn3Cr alloy in 7th International Conference on Modern Practice in Stress and Vibration Analysis Cambridge, UK, pp: 1-14
- [190]. R Muhammad, N Ahmed, Y M Shariff and V V Silberschmidt: (2012), Finite-element analysis of forces in drilling of Ti-alloys at elevated temperature, Solid State Phenomena, 188 pp: 250-255
- [191]. M Korzynski, T Zarski and K Korzynska: (2011), Surface layer condition and the fatigue strength of an AZ91 alloy after ball peening, Journal of Materials Processing Technology, 211(12), pp: 1982-1988
- [192]. E S Gadelmawla, M M Koura, T M A Maksoud, I M Elewa and H H Soliman: (2002), Roughness parameters, Journal of Materials Processing Technology, 123(1), pp: 133-145
- [193]. M Hokka, T Leemet, A Shrot, M Bäker and V-T Kuokkala, Dynamic behavior and numerical modeling of titanium 15-3-3-3 alloy, in Dynamic Behavior of Materials, Volume 1, V. Chalivendra, B. Song and D. Casem, Editors. 2013, Springer New York. p. 235-242.
- [194]. M Demiral, A Roy and V V Silberschmidt: (2012), Deformation processes of advanced alloy in indentation and turning, Computer, Material and Continua, 169(1), pp: 1-15
- [195]. Z Li and J Lambros: (1999), Determination of the dynamic response of brittle composites by the use of the split Hopkinson pressure bar, Composites Science and Technology, 59(7), pp: 1097-1107
- [196]. J Shi and C L Richard: (2004), The Influence of material models on finite element simulation of machining, Journal of Manufacturing Science and Engineering (Trans ASME), 126 pp: 849-857

- [197]. M Demiral, A Roy and V V Silberschmidt: (2010 ), Effects of loading conditions on deformation process in indentation, *Computers Materials and Continua*, 475(1) pp: 1-18
- [198]. G Shi, X Deng and C Shet: (2002), A finite element study of the effect of friction in orthogonal metal cutting, *Finite Elements in Analysis and Design*, 38(9), pp: 863-883
- [199]. M Baker, J Rosler and C Siemers: (2002), A finite element model of high speed metal cutting with adiabatic shearing, *Computers and Structures*, 80 pp: 495-513
- [200]. H Fassi, L Bousschine, A Chaaba and A Elharif: (2003), Numerical simulation of orthogonal cutting by incremental elsto-plastic analysis and finite element methods, *Journal of Materials Processing Technology*, 141 pp: 181-188
- [201]. J T Oden and E B Pires: (1983), Nonlocal and Nonlinear friction laws and variational principles for contact problems in elasticity, *Journal of Applied Mechanics*, 50 pp: 67-76
- [202]. Marc User's Guide Version 2012. MSC Software Corporation LA, USA
- [203]. M Peters and C Leyens: (2002), *Titanium and titanium alloys* Wiley-VCH, Germany